

University of St Andrews



Full metadata for this thesis is available in
St Andrews Research Repository
at:

<http://research-repository.st-andrews.ac.uk/>

This thesis is protected by original copyright

Structure and Electrochemistry of Cathode Materials

Tracey E. Quine



Thesis submitted for the degree of Doctor of Philosophy
of the University of St Andrews

September 28, 2001



DECLARATION

I, Tracey E. Quine, hereby certify that this thesis, which is approximately 35 000 words in length, has been written by me, that it is the record of work carried out by me and that it has not been submitted in any previous application for a higher degree.

Date: 28.09.01

Signature of Candidate:

I was admitted as a research student in October 1997 and as a candidate for the degree of Doctor of Philosophy in September 1998; the higher study for which this is a record was carried out in the University of St. Andrews between 1997 and 2001.

Date: 28.09.01

Signature of Candidate:

Certification

I hereby certify that the candidate has fulfilled the conditions of the Resolution and Regulations appropriate for the degree of Doctor of Philosophy in the University of St. Andrews and that the candidate is qualified to submit this thesis in application for the degree.

Date:

28/9/2001

Signature of Supervisor:

Library declaration

In submitting this thesis to the University of St. Andrews I understand that I am giving permission for it to be made available for use in accordance with the regulations of the University Library for the time being in force, subject to any copyright vested in the work not being affected thereby. I also understand that the title and abstract will be published, and that a copy will be made available to any *bona fide* library or research worker.

Date: 28.09.01

Signature of Candidate:

ACKNOWLEDGEMENTS

My thanks go to Professor Peter Bruce for his help and supervision throughout this work, and to the Engineering and Physical Science Research Council for a research scholarship award. Thanks also to the past and present members of the PGB group, Morven Duncan and Dr. Alastair Robertson for their help, Dr. Amelia Jennings for her help with GSAS refinement, and Dr. Rob Armstrong for the neutron refinement data. Thankyou also to Sylvia Williamson for the chemical analysis results, Dr. Steve Francis for XPS data and Dr. Paul Connor for proof reading.

The last four years would not have been half as much fun without my friends here in St. Andrews, thanks especially to Iain, Steph, Kate, Shiobhaún, Aled, Jonathan, Ineke and John for their friendship and support. Thankyou to everybody in St. Andrews University Mountaineering Club, for providing quality time out through an endless supply of adventures. Thanks also to the benchball guys for many crazy games, and to Caroline, for her great company during lunchtime runs.

And finally, thankyou to all my family,
and to Charlie for explaining everything.

ABSTRACT

Single phase $\text{Li}_x\text{M}_y\text{Mn}_{1-y}\text{O}_2$, where M = Ni or Mg replace a small amount of Mn, were prepared by a low temperature solution synthesis route, coupled with ion exchange from sodium precursors. Three different ion exchange conditions, 25 °C, 78 °C and 156 °C, were investigated, for the compositions $0 < y < 0.2$. X-ray and neutron powder diffraction confirmed that all $\text{Li}_x\text{M}_y\text{Mn}_{1-y}\text{O}_2$ materials have layered structures, $\alpha\text{-NaFeO}_2$ type, (space group R-3 m). Chemical analysis revealed that materials possess cation vacancies, and the amount was sensitive to the conditions of ion exchange. As a result the lattice parameters varied significantly with ion exchange conditions. Materials were also characterised by scanning electron microscopy, and x-ray photoelectron spectroscopy confirmed that in Ni doped materials, Ni is divalent.

The suitability of $\text{Li}_x\text{M}_y\text{Mn}_{1-y}\text{O}_2$, for use as cathode materials in lithium batteries, was investigated using galvanostatic cycling at medium to high rates. The electrochemical performance, in terms of capacity and capacity retention, was sensitive to the level and type of dopant as well as the conditions of ion exchange. The best performance was obtained for low M substitution levels, $y \approx 0.025$ and 0.5, prepared in ethanol at 78 °C. For a level of $y = 0.025$ Ni substitution, an initial discharge capacity of 220 mA h g^{-1} was obtained, and the capacity loss over 50 cycles was only 0.2 mA h g^{-1} per charge-discharge cycle, at a current density of 25 mA g^{-1} .

A conversion to a spinel-like structure is observed on cycling these materials, this was clearly observed in x-ray diffraction patterns taken of cycled materials, and also from incremental capacity measurements. This conversion occurs later for materials ion exchanged in ethanol compared to hexanol, and for materials with higher dopant levels of Ni and Mg. However, the performance of these spinel-like materials, prepared *in-situ* on cycling, remains markedly superior to the cycling performance of directly prepared spinels.

CONTENTS

CHAPTER 1. INTRODUCTION

1.1	Introduction to lithium ion batteries	1
1.2	History of intercalation	2
1.3	Requirements for intercalation electrodes	3
1.4	Methods of synthesis of cathode materials	7
1.5	Sites for ions	9
1.6	Layered structures	11
1.7	Cathode materials and electrochemical performance	13
1.7.1	Layered LiCoO_2 and LiNiO_2	13
1.7.2	Manganese based materials	14
1.7.2.1	Introduction	14
1.7.2.2	LiMn_2O_4 spinel	14
1.7.2.3	Layered LiMnO_2	18
1.8	Conclusions and outline of this thesis	20
1.9	References	21

CHAPTER 2. PREPARATION AND EXPERIMENTAL TECHNIQUES

2.1	Introduction	25
2.2	Preparation of compounds	25
2.2.1	Preparation of layered sodium precursors by solution synthesis reaction	25
2.2.2	Ion exchange reaction	26
2.2.3	Preparation of Ni doped spinel	26
2.3	Methods for characterisation	28
2.3.1	Powder x-ray diffraction	28
2.3.1.1	Introduction	28
2.3.1.2	The x-ray source	28
2.3.1.3	X-ray diffraction	30
2.3.2	Crystal structure identification and refinement	31
2.3.2.1	Crystal structure identification	31
2.3.2.2	Rietveld refinement	32
2.3.2.3	Criteria of fit	34
2.3.2.4	Peak shapes	35
2.3.3	Powder neutron diffraction	35
2.3.3.1	Introduction	35
2.3.3.2	The neutron source	36
2.3.4	Chemical analysis	37
2.3.5	Redox titration	37
2.3.6	Thermogravimetric analysis (TGA)	38
2.3.7	Scanning electron microscopy (SEM)	38
2.3.8	X-ray photoelectron spectroscopy (XPS)	38
2.3.9	Surface area measurement	39
2.4	Electrochemical cell preparation	39
2.4.1	Introduction	39
2.4.2	Cathode construction	40
2.4.3	Cell construction	40
2.4.4	Electrochemical techniques	41
2.5	Kinetic properties of solids	42
2.6	References	44

CHAPTER 3. PREPARATION AND CHARACTERISATION OF $A_xNi_yMn_{1-y}O_2$, $A = Na, Li$.

3.1	Introduction	45
3.2	Sodium phases $Na_xNi_yMn_{1-y}O_2$	45
3.2.1	Introduction	45
3.2.2	X-ray diffraction simulation of the layered sodium phase.	46
3.2.3	Synthesis of the sodium phase, $Na_xNi_{0.05}Mn_{0.95}O_2$.	47
3.2.3.1	TGA	48
3.2.3.2	X-ray diffraction	49
3.2.4	Characterisation of the sodium phases $Na_xNi_yMn_{1-y}O_2$	53
3.2.4.1	Introduction	53
3.2.4.2	X-ray diffraction	53
3.2.4.3	Nickel Oxide impurity	56
3.2.4.4	Chemical analysis	57
3.2.4.5	Rietveld refinement and lattice parameters	58
3.2.4.6	Particle morphology	62
3.2.5	Conclusions of sodium phases	62
3.3	Lithium phases $Li_xNi_yMn_{1-y}O_2$	64
3.3.1	Introduction	66
3.3.2	Ion exchange of $Na_xNi_yMn_{1-y}O_2$	67
3.3.3	Characterisation of the Li phases $Li_xNi_yMn_{1-y}O_2$	67
3.3.3.1	Introduction	67
3.3.3.2	XPS measurements	67
3.3.3.3	X-ray diffraction	70
3.3.3.4	Chemical analysis	73
3.3.3.5	Rietveld refinement	75
3.3.3.5.1	Introduction	75
3.3.3.5.2	X-ray diffraction	75
3.3.3.5.3	Neutron diffraction	77
3.3.3.6	Lattice parameters	79
3.3.3.7	Particle morphology and surface area	83
3.3.4	Mechanism of ion exchange	85
3.4	Conclusions	86
3.5	References	88

CHAPTER 4. ELECTROCHEMICAL PERFORMANCE OF $\text{Li}_x\text{Ni}_y\text{Mn}_{1-y}\text{O}_2$

4.1	Introduction	89
4.2	The first cycle of layered $\text{Li}_x\text{Ni}_y\text{Mn}_{1-y}\text{O}_2$	89
4.2.1	Voltage profile	89
4.2.2	First cycle charge capacity	92
4.2.3	First cycle discharge capacity	94
4.2.4	Influence of ion exchange conditions on the first cycle	96
4.2.5	Structural changes in the first cycle	98
4.2.5.1	Introduction	98
4.2.5.2	X-ray diffraction	98
4.2.5.3	Rietveld refinement	101
4.2.5.4	Lattice parameters	101
4.2.6	First cycle conclusions	104
4.3	Extended cycling of $\text{Li}_x\text{Ni}_y\text{Mn}_{1-y}\text{O}_2$	105
4.3.1	Introduction	105
4.3.2	$\text{Li}_x\text{Ni}_y\text{Mn}_{1-y}\text{O}_2$ prepared in hexanol at 156 °C	105
4.3.2.1	Electrochemical performance at 25 mA g ⁻¹	105
4.3.2.2	Electrochemical performance at 100 mA g ⁻¹	109
4.3.2.3	Structural changes on cycling	110
4.3.3	$\text{Li}_x\text{Ni}_y\text{Mn}_{1-y}\text{O}_2$ prepared in ethanol at 78 °C	116
4.3.3.1	As prepared material	116
4.3.3.2	Electrochemical performance at 25 mA g ⁻¹	116
4.3.3.3	Structural changes on cycling	119
4.3.4	$\text{Li}_x\text{Ni}_y\text{Mn}_{1-y}\text{O}_2$ prepared in ethanol at 25 °C	123
4.3.5	Rate capability	128
4.4	Conclusions	131
4.5	References	132

CHAPTER 5. STRUCTURE AND ELECTROCHEMISTRY OF $\text{Li}_x\text{Mg}_y\text{Mn}_{1-y}\text{O}_2$

5.1	Introduction	133
5.2	Sodium phases $\text{Na}_x\text{Mg}_y\text{Mn}_{1-y}\text{O}_2$	133
5.2.1	X-ray diffraction	133
5.2.2	Rietveld refinement and lattice parameters	136
5.3	Lithium phases $\text{Li}_x\text{Mg}_y\text{Mn}_{1-y}\text{O}_2$	140
5.3.1	Ion exchange	140
5.3.2	X-ray diffraction	141
5.3.3	Chemical analysis	144
5.3.4	Rietveld refinement and lattice parameters	144
5.3.5	Particle morphology	149
5.4	Electrochemical performance of $\text{Li}_x\text{Mg}_y\text{Mn}_{1-y}\text{O}_2$	150
5.4.1	Introduction	150
5.4.2	First cycle: practical charge and discharge capacities	150
5.4.2.1	Introduction	150
5.4.2.2	Effect of magnesium substitution level	150
5.4.2.3	Effect of ion exchange conditions	152
5.4.3	Extended cycling of $\text{Li}_x\text{Mg}_y\text{Mn}_{1-y}\text{O}_2$	155
5.4.3.1	$\text{Li}_x\text{Mg}_y\text{Mn}_{1-y}\text{O}_2$ prepared in ethanol at 78 °C	155
5.4.3.2	Structural changes on cycling	158
5.4.3.3	Effect of ion exchange conditions	160
5.4.3.4	Rate capability	162
5.4.3.5	Comparison of different voltage windows	165
5.5	Comparison with Ni doping	165
5.6	Conclusions	167
5.7	References	168

CHAPTER 6. CONCLUSIONS AND FURTHER WORK

6.1	Introduction	169
6.2	Sodium phases	169
6.3	Lithium phases	170
6.4	Electrochemistry	172
6.4.1	Nickel doped materials	172
6.4.2	Magnesium doped materials	174
6.5	Further work	174

CHAPTER 1. INTRODUCTION

1.1 INTRODUCTION TO LITHIUM ION BATTERIES

Lithium ion batteries are state of the art among advanced batteries and about 500 million are produced worldwide every year.¹ They have reduced the size and weight of portable devices such as mobile telephones and laptop computers, and currently represent one of the fastest growing high technology products.² Lithium ion batteries employ intercalation materials as positive electrodes and research in this field is vast.

The introduction by Sony in 1990 of the world's first commercially successful rechargeable lithium battery represented a revolution in the power source industry.^{3,4,5,6} The essential elements of the Sony cell are shown schematically in Figure 1.1. It's operation is a true expression of solid state intercalation chemistry, involving the flow of lithium ions between two intercalation hosts. The cell is constructed in the discharged state and consists of a thin layer of powdered LiCoO_2 , mounted on aluminium foil, and a negative electrode formed from a thin layer of powdered graphite, mounted on copper foil. The two electrodes are separated by a porous plastic film soaked, typically, in LiPF_6 dissolved in a mixture of dimethyl carbonate and ethylene carbonate. Charging the cell involves diffusion of lithium ions within the LiCoO_2 particles towards their interface with the electrolyte. The lithium ions then cross the electrolyte and are intercalated between the carbon layers in the graphite electrode. Charge balance requires that the equivalent number of electrons must pass around the external circuit. Discharge reverses the process moving lithium out of the graphite and reforming LiCoO_2 . This cell greatly improved earlier designs, which employed lithium metal rather than graphite as the negative electrode. The reactivity of lithium metal and the difficulty of plating and stripping it with high efficiency resulted in concerns over safety performance. Although LiCoO_2 has

molecules. There are also many kinds of hosts, the most promising candidates having either 'layer' or 'open channel framework' lattices, which allow the easy extraction and insertion of lithium.¹⁰

A number of transition-metal oxides and sulphides in which the metal occurs in a high oxidation state, have open covalent structures and are capable of incorporating alkali metals under mild conditions. In 1959, Rudorff and Sick first reported the formation of intercalation compounds between alkali metals and layered metal dichalcogenides.¹¹ Early work focussed upon TiS_2 , which has the layered structure and the reaction with lithium is the perfect intercalation reaction, as the reactant and product have the same structure over the entire range of reaction $0 < x < 1$ in Li_xTiS_2 . The single-phase behaviour with a slight expansion of the crystalline lattice allows the reaction to be completely reversible, as no energy needs to be expended to nucleate new phases.

1.3 REQUIREMENTS FOR INTERCALATION ELECTRODES

The design and synthesis of new improved intercalation compounds as positive electrodes requires the special chemical and structural features listed in Table 1.1.

Some of these attributes and their relationship to the solid state chemistry are considered further:

2) The voltage of the cell is a crucial parameter; it should be large in order to minimise the loss in energy density introduced by the non-zero voltage of the anode. The voltage between two intercalation electrodes is related to the work the cell can deliver on transferring electrons around an external circuit, and to the free energy change on transferring the guest lithium ions from one electrode to the other.

- 1 Must be an intercalation host for lithium
- 2 Low Fermi level and lithium ion site energy → high open circuit voltage (OCV)
- 3 Electrode potential varies little with lithium content
- 4 Capable of accommodating large quantities of lithium per formula unit → high capacity
- 5 Low formula mass → high gravimetric energy density
- 6 Low molar volume → high volumetric energy density
- 7 Sustain high rates of lithium intercalation and deintercalation → high cell charge/discharge rates
- 8 Highly reversible lithium intercalation → many charge/discharge cycles
- 9 Avoid cointercalation of solvent
- 10 Stable in contact with candidate electrolytes
- 11 Adequate electronic conductivity
- 12 Low cost
- 13 Easily fabricated into electrode
- 14 Environmentally friendly

Table 1.1 Criteria for intercalation compounds as positive electrodes.¹²

The work done on the cell for the transfer of one electron through a potential difference E is $-eE$ Joules, and this must equal the difference in the Gibbs free energy, ΔG , between lithium in each intercalation electrode. Chemical potential, $\mu = \delta G / \delta n$ describes the change in G with n , the number of intercalated Li^+ ions. For the transfer of one ion and one electron, $\mu_{\text{Li}}^{\text{int}} - \mu_{\text{Li}}^{\text{graph}} = -eE$, where $\mu_{\text{Li}}^{\text{int}}$ is the chemical potential of lithium in the cathode and $\mu_{\text{Li}}^{\text{graph}}$ is the chemical potential of lithium in the anode. The chemical potential of lithium in each electrode varies with the lithium concentration in each. For the transfer of one mole of ions and electrons the open circuit potential of the cell is

$$E = -(\mu_{\text{Li}}^{\text{int}} - \mu_{\text{Li}}^{\text{graph}}) / N_{\text{A}}e,$$

or,

$$E = -\Delta G / F.$$

Where F is the Faraday constant ($9.6 \times 10^4 \text{ C mol}^{-1}$) and N_A is the Avogadro constant ($6 \times 10^{23} \text{ mol}^{-1}$). This equation shows that a low $\mu_{\text{Li}}^{\text{int}}$ will achieve a large cell voltage. Upon discharge, lithium ions are transferred from a high-energy state (high $\mu_{\text{Li}}^{\text{graph}}$) in the anode to a low energy state (low $\mu_{\text{Li}}^{\text{int}}$) in the cathode and as a result, work is done by the cell.

Insertion of lithium into a transition metal oxide involves ionisation of lithium. As a result, the chemical potential of lithium in the cathode can be separated into an ion chemical potential, $\mu_{\text{Li}^+}^{\text{int}}$, and an electron chemical potential, μ_e^{int} , as $\mu_{\text{Li}}^{\text{int}} = \mu_{\text{Li}^+}^{\text{int}} + \mu_e^{\text{int}}$. The chemical potential of electrons μ_e^{int} is also known as the Fermi energy E_F .

It follows that design of an intercalation compound with maximised cell voltage requires low lithium ion site energies (high stability). This will be discussed further in section 1.4. Additionally, low energy levels or bands for the electron to occupy (Fermi energies) are required. To achieve electron insertion at the lowest Fermi energy, the energy at the top of the valence band must be low. In transition-metal oxides, the Fermi energy is set by the position of the cation d-levels which lie just above the top of the oxygen valence band. Therefore, charge neutrality is achieved by introducing Li 1s electrons into d bands of the host. These are lowest in Cr, Fe, Mn, Co, and Ni ions. The oxygen environment of the host also significantly affects the electronic structure.

3) Mutual repulsions between intercalated lithium ions also affect the cell voltage. Repulsions result in an increased value of $\mu_{\text{Li}}^{\text{int}}$ and, the net effect is that the electrode potential will decrease with increasing lithium concentration. A lattice gas model can be described as:

$$\mu = \varepsilon + kT \log[x/(1+x)] + Ux,$$

which shows how the lithium ions and electrons are distributed in an intercalation host.¹³ Where k is Boltzmann's constant, ϵ is the lithium site energy, U is the total interaction energy and x is the fraction of occupied sites. The electrode potential of an intercalation compound varies as a function of Li content x in an s-shape. However, such a relation does not exist when there are two phases associated with intercalation. In this situation, intercalation results in the conversion of one phase of fixed composition into another, also of fixed composition. This results in a fixed change of chemical potential due to a fairly fixed free energy of formation and hence, an invariant electrode potential.

4) The amount of charge stored is equivalent to the amount of lithium that can be accommodated within the lithium intercalation host. The theoretical capacity (Q_T) is defined as, $Q_T = xF$, where x is the theoretical number of moles associated with the complete discharge of the cell.¹⁴ The specific gravimetric capacity is defined as the capacity divided by the mass of the cell, in units of mA h g⁻¹ or alternatively, a specific volumetric capacity is used (mA h dm⁻³). A high capacity to store lithium should ideally be reversible. If utilisation of electrode material is not 100%, a practical capacity is delivered. A reason for the reduced capacity may be side reactions occurring within the cell, which consume some of the reactants and thus prevent their utilisation.

5) and 6) As described in 2), the work done on the cell is $-eE$ joules per ion transferred. As reactants are continually converted into products, theoretically the available energy (W) for complete discharge of a cell is given by, $W = xFE = EQ$. The energy density of a battery is an important parameter, for electric vehicles, batteries are required which provide a high gravimetric energy density, whereas for implantable medical devices, volumetric energy density is more important. The rate at which work is done defines the power (P) delivered by a cell, *i.e.* the product of the current flowing, (i), and the associated cell voltage.

7) To facilitate transport of the guest, the host lattice must contain interconnected vacant sites, to provide continuous diffusion paths of suitable size. The rate at which a cell can be discharged or charged is an important parameter, limited by the rate of lithium intercalation or deintercalation.

8) The host lattice must have a structurally stable network of atoms remaining intact throughout the insertion and extraction of lithium. This is a key property to ensure that an electrochemical cell operates reversibly, providing good electrochemical efficiency.

10) The electrode material should be capable of forming stable interfaces with the electrolyte used, and, transfer across the electrode/electrolyte interface should be rapid. The surfaces of transition-metal oxides provide an ideal environment for catalytic decomposition of many electrolytes and this can present problems.

12) The starting materials used to prepare the intercalation electrode should be of low cost as should the preparation method.

1.4 METHODS OF SYNTHESIS OF CATHODE MATERIALS

Powdered solids for use as cathode materials can be prepared by many different methods. For some, preparation is possible by a variety of routes, while others may be more sensitive and require special methods. The electrochemical performance of oxide materials is affected by the preparation concurrently through composition, structure and morphology. This is a short review of some of the main methods used to synthesise cathode materials.

1) Solid state reactions

This is the oldest, simplest and most commonly used method for the production of polycrystalline samples.¹⁵ Powdered reactants are mixed together and heated in a furnace for

prolonged periods. It is effective, but intrinsically slow because although the reactants may be well mixed at the level of individual particles, on the atomic scale they are very inhomogeneous.

2) Solution synthesis

A solution synthesis approach enables a lower firing temperature compared to a solid state reaction, due to the materials having a more homogeneous composition and particle morphology. The goal in such 'soft chemistry' techniques, is to precipitate new solids which may have different structures from the thermodynamically stable phases formed under high temperature synthesis conditions. For example, in LiNiO_2 , a lower synthesis temperature of 700 °C reduces intrinsic disorder in the layers.¹⁶

3) Ion exchange

Ion exchange operates in solution and is another soft chemistry technique where a low temperature route can control the resulting structure.¹⁷ Ion exchange occurs when a soluble lithiation agent reacts with an insoluble solid host. The ability of the reagent to exchange the ions depends upon its reduction potential. From thermodynamics, a reagent can reduce a host if its redox potential is lower than that of the host. According to the Nernst equation it is also possible to adjust the reducing power of a reagent, by controlling the reaction temperature and concentration of the reagent.¹⁵

4) Electrolysis methods

If the host structure of interest is the cathode in a cell, phases of precisely known stoichiometry of a guest species can be prepared. An electrolyte transports the guest ion from an anode either of the metal guest, or a suitable source of the metal. The current controls the reaction rate and the state of reaction is related to the cell potential.

1.5 SITES FOR IONS

Taking into account the results of section 1.2 and considering both the electrode potential and capacity, a metal oxide of the form LiMO_2 , from which all the lithium may be reversibly deintercalated, would seem optimal.¹⁸ Ideally, M is a light element in a high oxidation state ($\text{M}^{4+/3+}$ couple), and the oxygen ions are in a close packed structure. Therefore, it is no coincidence that the positive electrode in the Sony cell is layered LiCoO_2 . Layered transition metal oxides, which have the flexibility of the two dimensional structure to expand or contract, constitute an interesting, much studied, and often successful class of intercalation compounds.

The cell voltage depends on the lithium ion site energy. The sites available for ions depend on the structure, and a given structure can contain different types of sites. The structure of layered AMO_2 oxides can be considered as the stacking of strongly bonded two dimensional sheets containing a layer of transition metal ions, M, octahedrally coordinated between two oxygen layers. In Figure 1.3, the MO_2 layers are displayed clearly, small black spheres represent M and the large grey spheres represent oxygen. Sites available for guest alkali cations, A, are in the van der Waals gap, represented by the small grey spheres. The guests are surrounded by the oxygen anions and distance themselves as far as possible from the M cations.

Layered structures form in response to incompatible size or bonding requirements, to alleviate excessive stresses which would otherwise occur. The layered structure is stable when the ratio of transition to alkali metal radius is less than 0.9.¹⁹ However, substitution by other metals can significantly change the stability limits.

The site for the guest alkali cations depends on the relative position of the MO_2 sheets and may be in either a tetrahedral site, (surrounded by four anions), an octahedral site, (surrounded by six anions), or a trigonal prismatic site (which is found when one close packed layer sits directly over another). The sites are shown in Figure 1.2, where the light grey spheres represent

the guest alkali ions. Lithium prefers octahedral or tetrahedral sites, while larger ions like sodium, may occupy trigonal prismatic sites.

The ABC notation is the simplest system of nomenclature to describe the relative positions of all atoms within and between MO_2 layers. The three sites in the plane of a hexagonally close packed sheet of atoms are designated A, B or C to indicate the oxygen, a , b or c to indicate the transition metal position and α , β or γ to indicate the intercalated guest alkali metal.¹³

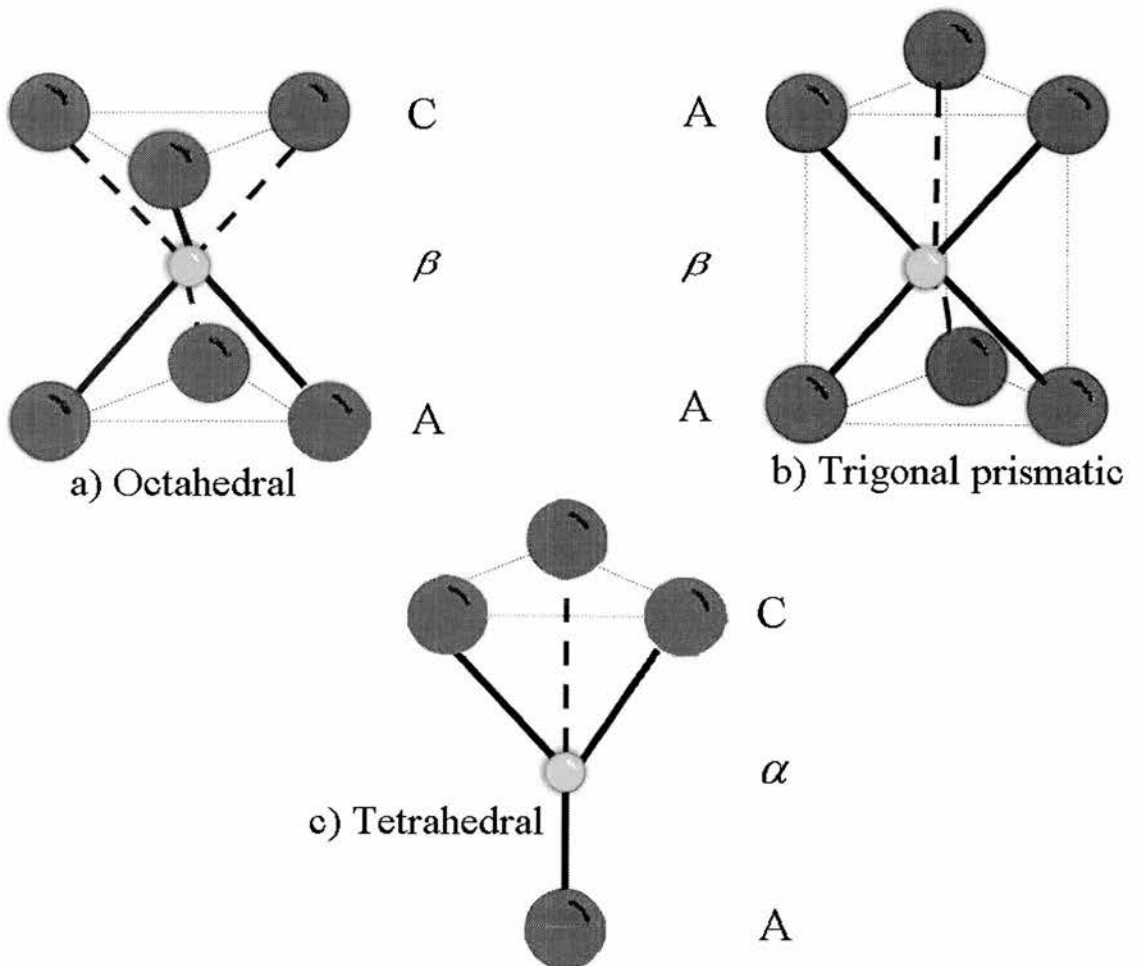


Figure 1.2 Sites for alkali ions (light grey spheres), between close-packed layers of oxygen atoms (dark grey spheres).¹³

1.6 LAYERED STRUCTURES

A full description of the layer disposition is achieved by indicating the number of MO_2 layers in the c -direction of the unit cell, and the symmetry of the oxygen atoms around the guest alkali metal ion by O (octahedral) or P (trigonal prismatic).

The layered transition metal oxides (A_xMO_2) show a rich variety of structures, based on close packed oxygen layers. A given compound is sometimes found with different polytypes, which may differ in the coordination of the transition metal or the stacking of the layers. There are many permutations of relative layer position within stacks of several layers, and thus, the structures of this class of compounds are numerous and complicated. For example, the range of different polytypes existing for a material is well demonstrated in bronzes, which are thermodynamically stable over a range of alkali metal compositions x .²⁰ In Na_xCoO_2 the amount of sodium can range from 0.55 to 0.64 in P3 structure, from 0.64 to 0.8 in P2 structure and from 0.8 to 1 in O'3 structure.²¹ The range of compounds formed depends mainly on the stoichiometry x , reaction conditions and ionic size. Four different types of oxygen packings are commonly found in layer oxides: P2, P3, O2 and O3.²²

The O3 oxygen packing sequence is $(\text{AcB})\alpha(\text{CbA})\gamma(\text{BaC})$ and is shown in Figure 1.3. Alkali ions (light grey spheres) are inserted into octahedral sites between MO_2 layers, (M = small dark spheres and O = large dark spheres). There are three MO_2 sheets in the unit cell, this structure is generally related to the α - NaFeO_2 type²³. O3 structure is usually obtained for phases with low vacancy content, and small size ions. The AO_6 and MO_6 octahedra share only edges. The intercationic electrostatic repulsions are then minimised and highly stabilised materials are obtained.

The P3 oxygen packing sequence is $(AcB)\alpha/\gamma(BaC)\alpha/\beta(CbA)$. In this structure alkali ions are inserted in trigonal prisms, which share one face with one MO_6 octahedron in one layer, and three edges with three other MO_6 octahedra, belonging to the other layer. The trigonal prismatic coordination is highly unfavoured electrostatically, having a high repulsion energy between adjacent oxide layers. This must be reduced by increasing the relative distance (using large alkali ions) or by filling the Van der Waals gap with cations.

Since the stacking sequence depends on the size and quantity of guest alkali ions, it follows that both intercalation and ion exchange reactions can induce transitions between polytypes. It is the ionocovalent character of the M-O and A-O bonds that is sufficiently high to provide a bonding anisotropy. As a result MO_2 layers can be considered as independent units, able to move

with respect to other layers. This behaviour is well illustrated by the intersheet distance modifications (vertical dilation of the Van der Waals gap to accommodate the guest species) and a lateral movement of an MO_2 layer to form a different polytype. Unlike normal solid state processes, intercalation reactions avoid the large kinetic barriers of defect diffusion, extensive bond breaking, nucleation and growth. It is possible for certain transitions to occur even at room temperature. For example, P3 and O3 structures are related to each other only by a

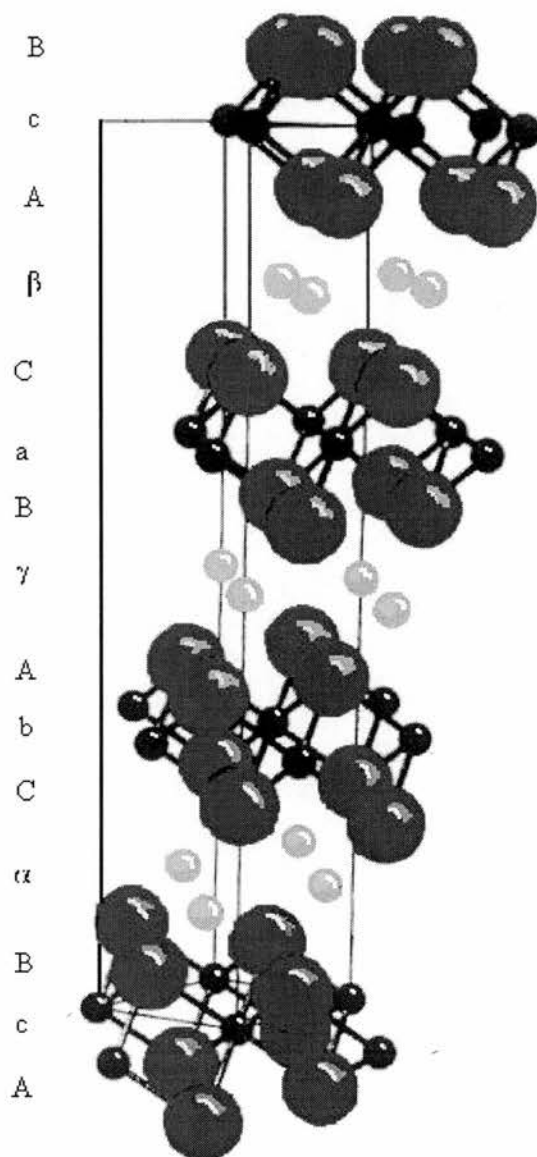


Figure 1.3 Layered O3 structure consisting of rigid MO_2 sheets

gliding of the MO_2 layers. However, a transformation of O2 or P2 to O3 or P3 is not possible by gliding since it involves breaking M-O bonds.

The layered compounds prepared in this project possess the P3 and O3 structures. Dahn's group is exploring different layered oxides based on the O2 stacking of oxide layers (*i.e.* ACAB).²⁴

1.7 CATHODE MATERIALS AND ELECTROCHEMICAL PERFORMANCE

1.7.1 LAYERED LiCoO_2 AND LiNiO_2

The most common 'high voltage' cathode materials are the layered lithium manganese oxides LiCoO_2 and LiNiO_2 . LiCoO_2 is currently the material of choice, despite its high cost because it is relatively easy to prepare a high quality electrode with an essentially layered structure. Preparation involves heating a mixture of LiOH and CoCO_3 at $850\text{ }^\circ\text{C}$ in air.^{3,4,6} LiNiO_2 is more difficult to synthesise, and the true formula is $\text{Li}_{1-z}\text{Ni}_{1+z}\text{O}_2$.^{25,26,27,28,29}

LiCoO_2 and LiNiO_2 have a layered O3 structure, (Figure 1.3), based on close-packed oxygen ions with lithium and the transition metal ions ordering on alternate (111) planes of the cubic rock salt structure. They are isostructural with $\alpha\text{-NaFeO}_2$, and crystallise in the space group $R\bar{3}m$. Ordering introduces a slight distortion of the lattice to hexagonal symmetry, so the oxygen ion array is not ideally cubic-close-packed. The c/a ratio of about 4.989 is significantly larger than that of an ideal ccp lattice where $c/a = 4.899$.

LiNiO_2 has an average voltage several hundred mV lower compared with LiCoO_2 , due to its higher energy t_{2g} orbitals.¹² About 140 mA h g^{-1} of capacity can be utilised as further removal degrades the cyclability and causes exothermic decomposition at elevated temperatures, which poses safety hazards.²⁵⁻²⁹ On cycling, LiCoO_2 goes through three reversible phase transitions, accompanied by lattice distortions as the lithium content varies. However, a fourth transition is

irreversible and limits the practical cyclability to only about $\text{Li}_{0.5}$. The capacity in this composition range is 130 mA h g^{-1} and the cycle life is good.³³⁰

1.7.2 MANGANESE BASED MATERIALS

1.7.2.1 INTRODUCTION

In the last ten years much attention has been focussed on manganese because of its low cost, low toxicity and familiarity to the battery field. This has centred on the spinel LiMn_2O_4 and on several layered manganese oxides.

The synthesis of layered LiMnO_2 was motivated by the success displayed by layered LiCoO_2 . LiMnO_2 is particularly attractive since it has the potential to deliver a theoretical capacity of 285 mA h g^{-1} . However, solid state reaction at high temperature to prepare layered LiMnO_2 , has been unsuccessful since the non-layered structures, LiMnO_2 (orthorhombic), LiMn_2O_4 (spinel), or Li_2MnO_3 (rock salt) are more thermodynamically stable.

LiMnO_2 is one of only a few ternary oxides that are known to form in the orthorhombic corrugated layer structure. Strong antiferromagnetic interactions between Mn^{3+} ions contribute to stabilisation of the orthorhombic structure.³¹ It consists of double slabs of edge sharing MnO_6 octahedra, alternating with double slabs of edge sharing LiO_6 octahedra. Cycling this material easily changes the structure to a spinel-related form.^{32,33,34,35,36,37,38,39}

1.7.2.2 LiMn_2O_4 SPINEL

Wickham and Croft discovered the three dimensional spinel structure, LiMn_2O_4 in 1958.⁴⁰ It was found to act as an intercalation host for lithium in the early eighties by Goodenough.⁴¹

The cubic spinel structure is shown in Figure 1.4. The anions form a cubic close packed, (ccp), array occupying the 32e sites of the space group Fd-3m. The Mn cations occupy half the octahedral sites, 16d, and the Li cations occupy 1/8 of the tetrahedral sites 8a. The interstitial octahedral sites, 16c, are interconnected by sharing common edges with six like near neighbours exactly as the 16d sites, but shifted by half a lattice parameter in space. Each 16c site shares two common faces, on opposite sides, with occupied 8a sites; the other faces are shared with empty interstitial tetrahedral sites 48f. The final empty tetrahedral sites 8b share faces with four occupied 16d octahedral sites. With a spinel Mn_2O_4 framework, the interstitial space represents a 'diamond' network of tetrahedral 8a and surrounding octahedral 16c sites that offers conduction pathways for lithium ions.

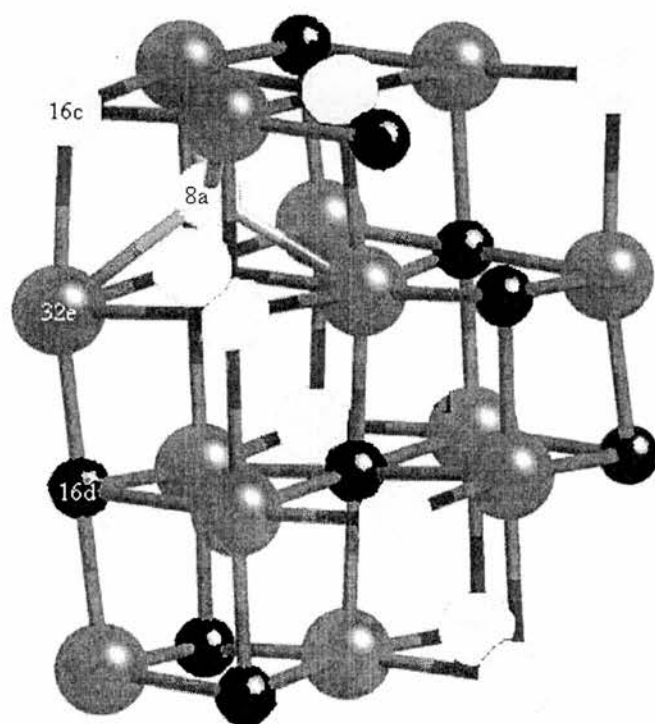


Figure 1.4 Structure of the spinel $LiMn_2O_4$ lattice showing the location of the octahedral (16d), tetrahedral (8a) and interstitial octahedral (16c) sites which are represented by small black spheres, small white spheres and light grey spheres respectively. Large grey spheres represent the oxygen atoms in 32e sites.

The cubic spinel is a cathode material of interest for both 3 V and 4 V lithium batteries. The electrode operates at 3 V for lithium insertion into the interstitial $16c$ sites, $\text{Li}_x\text{Mn}_2\text{O}_4$ ($1 < x < 2$), whereas lithium extraction from the $8a$ sites begins at 4 V over the range ($0 < x < 1$).

The tetrahedral coordination defines a particularly stable environment for lithium ions, resulting in higher potentials during lithium insertion or extraction compared to sites with octahedral coordination. Sufficient Mn also exists in every layer to provide, on delithiation, a sufficiently high binding energy to maintain an ideal ccp array. Full deintercalation yields a polymorph of MnO_2 that cannot be prepared by other means, thus providing another example of soft chemistry.⁴² The performance of the spinel in the 4 V region appears to occur over a continuous range of solid solutions for $0.5 < x < 1$.^{43,44,45} Further extraction causes lithium ion ordering, involving occupancy of half the tetrahedral $8a$ sites. Deintercalation below this composition involves coexistence of two cubic spinel phases of approximate composition $x = 0$ and 0.5. A small step of around 100 mV between two essentially flat voltage profiles is observed at about 0.5. The cycling performance over 4 V was disappointing, although significantly better than in the 3 V region.

Several possible mechanisms have been proposed as playing a part in the 4 V capacity loss:

- 1) A slow dissolution of Mn^{2+} from the spinel electrode surface into the electrolyte according to the disproportionation reaction $2\text{Mn}^{3+} \rightarrow \text{Mn}^{4+} + \text{Mn}^{2+}_{(\text{solution})}$.^{46 47}
- 2) An instability (oxidation) of the organic based electrolyte at high voltages.⁴⁸
- 3) The unstable two-phase coexistence of λ - MnO_2 and $\text{Li}_{0.5}\text{Mn}_2\text{O}_4$, which leads to a cell volume change and loss of particle contact.⁴⁹

Lithium insertion into LiMn_2O_4 proceeds at 3 V into the $16c$ sites without displacement of the $8a$ Li^+ ions into $16c$ positions. The Li-Li electrostatic forces between $8a$ and $16c$ are not strong enough to displace a Li^+ ion from an $8a$ to a $16c$ site. The coexistence of Li on $8a$ and $16c$ positions also provides continuous lithium diffusion pathways. Insertion reduces the Mn^{4+} to

Mn^{3+} and a continuous solid solution is obtained up to $x = 1.1$. At this composition, the Jahn-Teller active Mn^{3+} ions are present in sufficient concentration to promote a cooperative distortion of the octahedral sites to a tetragonal symmetry. Associated with this, the cubic crystal symmetry of LiMn_2O_4 is lowered to tetragonal. For $1.1 < x < 2$, a mixture of the cubic and tetragonal spinels coexist and, intercalation involves the continuous conversion, within each particle, of the former phase to the latter. As a result, the voltage does not vary with the lithium content in this composition range. Accompanying the cubic-to-tetragonal phase change, is an abrupt change in unit cell volume, (6.5 %), which has a deleterious effect on the cyclability. Cubic spinel accumulates at the end of discharge and this is the primary cause of the significant capacity loss on cycling the spinel electrodes. The capacity loss arises because the particles contract on deintercalation, resulting in a loss of mutual contact. Some particles may become isolated from the rest of the electrode and are unable to act as host for lithium insertion on subsequent discharge. Early LiMn_2O_4 compounds were prepared by the solid state reaction between lithium carbonate and Mn_2O_3 at $850\text{ }^\circ\text{C}$ in air. It has since been found that lower temperature firing can prepare materials with improved capacity retention on cycling.^{50 51}

52,53

Careful control of the composition can dramatically improve the cycling performance, for example, by replacing a small amount of the Mn on the $16d$ octahedral sites by lithium in $\text{Li}_{1+x}\text{Mn}_{2-x}\text{O}_4$.^{54 55 56} Foreign ions such as Mg, Zn, Ti, Ni, Co, Cr, Fe, Al, Ge, Li and Ga have also been used to replace a small amount of Mn.⁵⁷⁻⁷² They may or may not take part in the redox processes and there is also the possibility of tailoring the energy potentials of the cathode. Such solid solutions also reduce dissolution of Mn and promote a single phase composition over the range $0 < x < 1$. The Jahn-Teller distortion may also be prevented. However, the capacity drops substantially as the amount of stabilising dopant increases. So far, no agreement has been obtained regarding both the best dopant ion and the optimum composition.

The cubic spinel LiMn_2O_4 has certainly proved to be far more complex than was thought when it was introduced as an intercalation host in 1983. It is also evident that the performance, in contrast to LiCoO_2 , is very sensitive to the preparation conditions. At present the NEC Moli Energy Corporation is the only commercial producer of the spinel lithium ion battery.⁷³

1.7.2.3 LAYERED LiMnO_2

LiMnO_2 of the almost ideal layered O3 type, was first prepared indirectly in 1996. The synthesis involved ion exchanging the mobile sodium ions in layered O3 $\alpha\text{-NaMnO}_2$ with lithium, using LiBr dissolved in hexanol.^{74,75} This 'soft chemical' route is required to access the thermodynamically metastable, but kinetically stable layered LiMnO_2 phase.

In the sodium phase, lattice strain is reduced by the large sodium ions residing in different layers compared to the Mn^{+3} , and therefore results in a strictly two dimensional layered NaMnO_2 . On ion exchange, the sodium precursor phase acts as a templating agent and the layered structure is retained. This material is structurally analogous to LiCoO_2 except that the electronic structure of Mn^{3+} ($3d^4$) adopts a high spin configuration (t_{2g}^3, e_g^1) and is strongly Jahn-Teller active.¹⁵ As a result of the Jahn-Teller effect, the stabilisation of the electron in the d_{z^2} orbital leads to a lower crystal symmetry, caused by the formation of two long Mn-O bonds (2.27 Å) and four short Mn-O ones (1.92 Å). The cooperative character of this distortion is very easily extended over the whole of the layer. Therefore layered LiMnO_2 has a monoclinic unit cell with space group C 2/m. The unit cell dimensions are $a \approx 5.4387$ Å, $b \approx 2.8086$ Å, $c \approx 5.3878$ Å, $\beta \approx 116.006^\circ$. The monoclinic unit cell still has the same three layer structure as the original hexagonal unit cell.

On heating to 150 °C, layered LiMnO_2 slowly converts to spinel and orthorhombic LiMnO_2 , which demonstrates its metastable nature. From the relative amounts present the lithiated spinel

is formed more easily than orthorhombic LiMnO_2 , but both phases are more stable than the layered structure.

It was possible to extract 90 % of the lithium from layered LiMnO_2 , corresponding to a high initial charge capacity of 250 mA h g^{-1} . Unfortunately, it is not structurally stable on cycling, and gradually converts to a thermodynamically more stable spinel-like phase.^{76,77} This conversion is connected with a rapid decrease in cell capacity with cycle number. The transformation is enabled by the close similarity of the spinel structure and the layered O3 structure, as they both have the same close packed oxygen sublattice. Electrochemical results indicate that spinel-like regions are formed during the first charge to $\text{Li}_{0.5}\text{MnO}_2$.

To improve the cycling performance of layered LiMnO_2 researchers have drawn on the experience gained from optimising the spinel material. Replacing 10 % of the Mn in LiMnO_2 by Co^{3+} dramatically improves the capacity retention, displaying a discharge capacity of 200 mA h g^{-1} after 20 cycles.^{78,79,80} X-ray and neutron diffraction data collected on Co doped materials may be indexed on a rhombohedral cell, isostructural with LiCoO_2 . There is no evidence of a monoclinic distortion arising from the Jahn-Teller active Mn^{3+} ion. Electrochemical data indicate conversion to a spinel like structure on cycling and the conversion is progressively slower with increasing Co content.^{81,82} Monoclinic $\text{Li}_x\text{Al}_{0.05}\text{Mn}_{0.95}\text{O}_2$ also exhibits stable cycling and a high discharge capacity.^{83, 84,85}

1.8 CONCLUSIONS AND OUTLINE OF THIS THESIS

This chapter intended to give a brief insight into the development, variety, and performance of some transition metal oxide cathode materials for rechargeable lithium batteries. Especially over the last decade, a large proportion of the current literature in this field of study has concentrated on aspects of the layered system. A manganese based material with the layered structure is optimal but unfortunately, the main operating problem of layered LiMnO_2 is capacity fade, arising from an irreversible change to a spinel-like structure during cycling. To try to understand and reduce this problem, research is mainly focussed on modifying the structural and electrochemical properties, by varying parameters such as composition, cation distribution and crystallinity. The solid-solutions $\text{Li}_x\text{M}_y\text{Mn}_{1-y}\text{O}_2$, ($\text{M} = \text{Ni}, \text{Mg}$), for $0.01 < y < 0.2$, have been proposed as layered cathode materials for lithium batteries.

Chapter 2 describes the method used to prepare the layered compounds $\text{Na}_x\text{M}_y\text{Mn}_{1-y}\text{O}_2$ and $\text{Li}_x\text{M}_y\text{Mn}_{1-y}\text{O}_2$. The characterisation methods used and some background theory are also included.

Chapter 3 presents the results from preparing and characterising $\text{A}_x\text{Ni}_y\text{Mn}_{1-y}\text{O}_2$, ($\text{A} = \text{Na}$ or Li), as a function of Ni content, ($0 < y < 0.2$) and ion exchange conditions.

Chapter 4 presents the electrochemical performance of $\text{Li}_x\text{Ni}_y\text{Mn}_{1-y}\text{O}_2$ materials, as a function of ion exchange conditions and Ni content.

Chapter 5 presents the results from preparing and characterising the Mg doped materials, $\text{A}_x\text{Mg}_y\text{Mn}_{1-y}\text{O}_2$, ($\text{A} = \text{Na}$ or Li), ($0 < y < 0.2$), together with their electrochemical performance.

Chapter 6 is the conclusions of this work and further work.

1.9 REFERENCES

-
- ¹ C. A. Vincent, *Solid State Ionics*, **134**, (2000), 159.
- ² M. Broussely, P. Biensan and B. Simon, *Electrochimica Acta*, **45**, (1999) 3.
- ³ T. Nagaura, Extended Abstracts, Third International Rechargeable Battery Seminar, Deerfield Beach, FL, USA, (1990).
- ⁴ T. Nagaura and K. Tazawa, *Prog. Batteries Col. Cells*, **9**, (1990), 20.
- ⁵ P. G. Bruce, *Philos. Trans. R. Soc. Lond. A*, **354**, (1996), 1577.
- ⁶ K. Ozawa, *Solid State Ionics*, **69**, (1994), 212.
- ⁷ F. G. Fowler and H. W. Fowler, *The Oxford Dictionary of Current English*. Clarendon Press, Oxford, (1984).
- ⁸ B. Laufer, *Beginnings of Porcelain in China*, ARC Press, (1917).
- ⁹ C. Schaffhautl, *J. Prakt Chem*, **3** (1840), 129.
- ¹⁰ M. M. Thackeray, *J. Electrochem. Soc.*, **8**, (1995), 2558.
- ¹¹ W. Rudorff and H. H. Sick, *Agnew. Chem.*, **71**, (1959), 127.
- ¹² P. G. Bruce, *Chem. Commun.* (1997) 1817.
- ¹³ W. R. McKinnon, Ed. P. G. Bruce, *Solid State Electrochemistry*, Cambridge University Press, (1995).
- ¹⁴ C. A. Vincent and B. Scrosati, *Modern Batteries*, Second edition, Arnold Publ. Ltd., London, (1997).
- ¹⁵ A. R. West, *Basic Solid State Chemistry*, Second edition, John Wiley and Sons, (1999)
- ¹⁶ R. Kanno, T. Shirane, Y. Kawamoto, Y. Takeda, M. Takano, M. Ohashi and Y. Yamaguchi, *J. Electrochem. Soc.*, 1996, **143**, 2435.
- ¹⁷ C. Delmas, J. J. Braconnier, A. Maazaz and P. Hagenmuller, *Revue de Chimie minerale*, **19**, (1982), 343.
- ¹⁸ S. Megahed and B. Scrosati, *J. Power Sources*, **51** (1994) 79.
- ¹⁹ E. J. Wu, P. D. Tepesch, C. G. Ceder, *Philos. Mag. B*, **77**, (1998), 1059.
- ²⁰ K. West, *Mat. Res. Bull.* **10** (1975), 447.

-
- ²¹ J. J. Braconnier, *Mat. Res. Bull.* **15** (1980) 1797.
- ²² A. Mendibourne, C Delmas and P. Hagenmueller, *Mater. Res. Bull.*, **19**, (1984), 1383.
- ²³ S. Goldsztaub, *Comp. Rend.* **196** (1933), 280.
- ²⁴ J. M. Paulsen and J. R. Dahn, *Solid State Ionics*, **3**, (1999), 126.
- ²⁵ J. R. Dahn, U. von Sacken, M. W. Juzkow and H. Al-Janaby, *J. Electrochem. Soc.*, **8**, (1991), 2207.
- ²⁶ T. Ohzuku, A. Ueda and M. Nagayama, *J. Electrochem. Soc.*, **7**, (1993), 1862.
- ²⁷ J. R. Dahn, E. W. Fuller, M. Obrovac, U. von Soacken, *Solid State Ionics*, **69**, (1994), 265.
- ²⁸ M. Broussely, F. Perton, P. Biensan, J. M. Bodet, J. Labat, A. Lecerf, C. Delmas, A Rougier and J. P. Peres, *J. Power Sources*, **54**, (1995), 109.
- ²⁹ A. Rougier, P. Gravereau and C. Delmas, *J. Electrochem. Soc.*, **4**, (1996), 1168.
- ³⁰ K. Mizushima, P. C. Jones and J. B. Goodenough, *Mater. Res. Bull.*, **15**, (1980), 783.
- ³¹ G. Ceder and S. K. Mishra, *Electrochem. and Solid-State Lett.*, **2** (11) (1999).
- ³² J. N. Reimers, E. W. Fuller, E. Rossen and J. R. Dahn, *J. Electrochem. Soc.* **140** 3396 (1993).
- ³³ R. J. Gummow, D. C. Liles and M. M. Thackeray, *Mat. Res. Bull.* **28**, (1993), 1249.
- ³⁴ R. J. Gummow and M. M. Thackeray, *J. Electrochem. Soc.*, **141**, (1994), 1178.
- ³⁵ I. Koetschau, M. N. Richard and J. R. Dahn, *J. Electrochem. Soc.*, **142**, (1995), 2906.
- ³⁶ I. J. Davidson, R. S. McMillan, J. J. Murray and J. E. Greedan, *J. Power Sources*, **54**, (1995), 232.
- ³⁷ I. M. Kotschau and J. R. Dahn, *J. Electrochem. Soc.*, **145**, (1998), 2672.
- ³⁸ Y. Jang, B. Huang, H. Wang, D. Sadoway and Y. Chiang, *J. Electrochem. Soc.*, **146**, (9), (1999).
- ³⁹ L. Congruennec, P. Deniard and R. Brec, *J. Electrochem. Soc.*, **144**, (1997), 3323.
- ⁴⁰ D. G. Wickham and W. J. Croft, *J. Phys. Chem. Solids*, **7** (1958) 351
- ⁴¹ M. M. Thackeray, W. I. F. David, P. G. Bruce, and J. B. Goodenough, *Mat. Res. Bull.*, **18** (1983) 461.
- ⁴² J. C. Hunter, *J. Solid State Chem.*, 1981, **39**, 142.

-
- ⁴³ M. M. Thackeray, P. J. Johnson, L. A. de Picciotto, W. I. F. David, P. G. Bruce and J. B. Goodenough, *Mat. Res. Bull.*, 1984, 19, 179.
- ⁴⁴ J. B. Goodenough, M. M. Thackeray, W. I. F. David and P. G. Bruce, *Rev. Chim. Minér.*, **21**, (1984), 435.
- ⁴⁵ T. Ohzuku, M Kitagawa and T. Hirai, *J. Electrochem. Soc.*, 1990, 137, 769.
- ⁴⁶ J. M. Tarascon, F. Coowar, G. Amatucci, F. K. Shokoohi and D. G. Guyomard, *J. Power Sources*, 1995, 54, 103.
- ⁴⁷ R. J. Gummow, A. de Kock and M. M. Thackeray, *Solid State Ionics*, 1994, 69,59.
- ⁴⁸ G. Pistoia, A. Antonni, R. Rosati and D. Zane, *Electrochim. Acta*, 1996, 41, 2683.
- ⁴⁹ Y. Xia and M. Yoshio, *J. Electrochem. Soc.*, 1996, 143, 825.
- ⁵⁰ P.G. Bruce, A. R. Armstrong and H. Huang, *J. Power Sources*, **68**, (1997), 19.
- ⁵¹ H. Huang and P. G. Bruce, *J. Electrochem. Soc.*, **141**, (1994), L76.
- ⁵² H. Huang and P. G. Bruce, *J. Power Sources*, **54**, (1995), 52.
- ⁵³ P. Barboux, J. M. Tarascon and F. K. Shokoohi, *J. Solid State Chem.*, **94** (1991), 185.
- ⁵⁴ H. Huang and P. G. Bruce, *J. Electrochem. Soc.*, **141**, (1994), L106
- ⁵⁵ R. J. Gummow, A. de Kock and M. M. Thackeray, *Solid State Ionics*, **69**, (1994), 59.
- ⁵⁶ Y. Gao and J. R. Dahn, *J. Electrochem. Soc.*, **143**, L106, (1996).
- ⁵⁷ J. M. Tarascon, E. Wang and F. K. Shokoohi, *J. Electrochem. Soc.*, **138**, (1991), 2859.
- ⁵⁸ G. Pistoia and G. Wang, *Solid State Ionics*, **66** (1993) 135.
- ⁵⁹ R. J. Gummow, A. de Kock and M. M. Thackeray, *Solid State Ionics* **69** (1994), 59.
- ⁶⁰ I. J. Davidson, R.S. McMillan and J. J. Murray, *J. Power Sources*, **54** (1995), 205.
- ⁶¹ C. Sigala, D. Guyomard, A. Verbaere, Y. Piffard and M. Tournoux, *Solid State Ionics*, **81** (1995) 167.
- ⁶² Guohua, H. Ikuta, T. Uchida and M. Wakihara, *J. Electrochem. Soc.*, **143**, (1996),.
- ⁶³ L. Hernan, J. Morales, L Sanchez and J. Santos. *J. Electrochem. Soc.*, **144**, (1997).
- ⁶⁴ A. D. Robertson, S.H. Lu, W.F. Verill and W. F. Howard *J. Electrochem. Soc.*, **144**, (1997).
- ⁶⁵ G. Pistois, A. Antonini and R. Rosati, *Chem. Mater*, **9**, (1997), 1443.

-
- ⁶⁶ Q. Zhong, A. Bonakdarpour, M. Zhang, Y. Gao and J. R. Dahn, *J. Electrochem. Soc.*, **144**, (1997).
- ⁶⁷ M. Song and D. Ahn, *Solid State Ionics* **112**, (1998) 245.
- ⁶⁸ M. Hosoya, H. Ikuta and M. Wakihara, *Solid State Ionics*, (1998), 153.
- ⁶⁹ P. Arora, B. N. Popov and R. E. White, *J. Electrochem. Soc.*, **145**, (1998).
- ⁷⁰ J. R. Dahn, T. Zheng and C. L. Thomas, *J. Electrochem. Soc.*, **145**, (1998).
- ⁷¹ J. Cho and B. Park, *Electrochem. and Solid State Lett.*, **3** (8) (2000)
- ⁷² J. M. Amarilla, J. L. Martin de Vidales and R. M. Rojas. *Solid State Ionics* **127** (2000), 73.
- ⁷³ *Japan Electronics*, March 6th, (1996).
- ⁷⁴ A. R. Armstrong and P. G. Bruce, *Nature*, 1996, **381**, (1996), 499.
- ⁷⁵ F. Capitaine, P. Gravereau and C. Delmas, *Solid State Ionics*, **89**, (1996), 197.
- ⁷⁶ P. G. Bruce, A. R. Armstrong, R. L. Gitzendanner, *J. Mat. Chem.*, **9**, (1999), 193.
- ⁷⁷ G. Vitins and K. West, *J. Electrochem. Soc.*, **144**, (1997), 2587.
- ⁷⁸ A. R. Armstrong, R. Gitzendanner, A. D. Robertson and P. G. Bruce, *Chem. Comm.*, **198**, (1998), 1833.
- ⁷⁹ A. R. Armstrong, A. D. Robertson and P. G. Bruce, *Electrochimica Acta*, **45**, (1999) 285.
- ⁸⁰ A. R. Armstrong, A. D. Robertson, R. Gitzendanner and P. G. Bruce, *J. Solid-State Chem.*, **145**, (1999), 549.
- ⁸¹ A. D. Robertson, A. R. Armstrong and P. G. Bruce, *Chem. Commun.*, (2000), 1997.
- ⁸² A. D. Robertson, A. R. Armstrong, A. J. Fowkes and P. G. Bruce, *J. Mater. Chem.*, **11**, (2001), 113.
- ⁸³ Y. I. Jang, B. Huang, H. Wang, Y. Chiang, and D. R. Sadoway. *Electrochem. and Solid-State Lett.*, **1**, (1998), 13.
- ⁸⁴ Y. Chiang, D. Sadoway, Y. Jang, B. Huang and H. Wang, *Electrochem. and Solid State Lett.* **2** (3), (1999), 107.
- ⁸⁵ G. Ceder, Y. M. Chiang, D. R. Sadoway, M. K. Aydinol, Y. I. Jang, B. Huang, *Nature*, **392**, (1998), 694.

CHAPTER 2. PREPARATION AND EXPERIMENTAL TECHNIQUES

2.1 INTRODUCTION

This chapter includes the experimental details for preparation of layered $\text{Li}_x\text{M}_y\text{Mn}_{1-y}\text{O}_2$, ($\text{M} = \text{Ni}$ or Mg). The methods used for characterisation are described, together with some background theory.

2.2 PREPARATION OF COMPOUNDS

2.2.1 PREPARATION OF LAYERED SODIUM PRECURSORS BY SOLUTION SYNTHESIS REACTION

Several $\text{Na}_x\text{M}_y\text{Mn}_{1-y}\text{O}_2$ ($\text{M} = \text{Ni}, \text{Mg}$) were prepared by a coprecipitation solution synthesis reaction. Stoichiometric amounts of manganese (II) acetate tetrahydrate (99% Aldrich) and M ($\text{M} = \text{Ni}, \text{Mg}$) acetate tetrahydrate (99% Aldrich) were dissolved and heated to 70 °C in distilled water to obtain clear solutions. Upon addition of a clear aqueous solution of a stoichiometric amount of Na_2CO_3 (99.5% Fisons) to the acetate solution, a coloured suspension resulted. A rotary evaporator was used at a temperature of 70 °C (to remove the solvent). The resultant precipitates were collected and then ground before being subjected to further heat treatments.

A two step heating procedure was applied to all samples; first the solid product of rotary evaporation was heated at 200 °C in air, overnight for 12 hours to burn off the acetates. The resulting brown powder was ground and covered and heated in air, at 400 °C hr^{-1} , to 600 °C,

when it was quenched to room temperature after an hour. Phase evolution, as well as the structure of the quenched powders was studied using x-ray diffraction and thermogravimetric analysis. An important advantage of this solution synthesis procedure over solid state synthesis methods is that it can be carried out in air. However the samples produced are moisture sensitive and transform to a birnessite phase ($\text{Na}_4\text{Mn}_{14}\text{O}_{27}\cdot 9\text{H}_2\text{O}$) unless kept in a dessicator or vacuum oven at 70 °C.

2.2.2 ION EXCHANGE REACTION

Sodium ions in $\text{Na}_x\text{M}_y\text{Mn}_{1-y}\text{O}_2$ were exchanged with lithium ions. Typically 5 g of $\text{Na}_x\text{M}_y\text{Mn}_{1-y}\text{O}_2$ was dissolved in a solution of LiBr (40 g) in alcohol (150 ml). This corresponds approximately to a 5 M solution, 7-8 times excess of lithium. The reaction was conducted, at the boiling point of the solution *i.e.* reflux at 156 °C, for 8 hours in hexanol or at 78 °C for 8 hours in ethanol. A milder ion exchange condition by stirring in ethanol at 25 °C was also used but one week was required to obtain a complete reaction.

Following ion exchange, the solids were filtered under suction and washed with water and ethanol before drying. Figure 2.1 is a flow chart showing the procedure followed for synthesizing the doped lithium manganese oxides $\text{Li}_x\text{M}_y\text{Mn}_{1-y}\text{O}_2$.

2.2.3 PREPARATION OF Ni DOPED SPINEL

For use as a comparison, both structurally and electrochemically, the ordered spinels $\text{LiNi}_y\text{Mn}_{2-y}\text{O}_4$, ($y = 0.05$ and 0.15), were synthesised by reacting Li_2CO_3 , MnCO_3 and Ni acetate at 420 °C in air, for 12 hours.

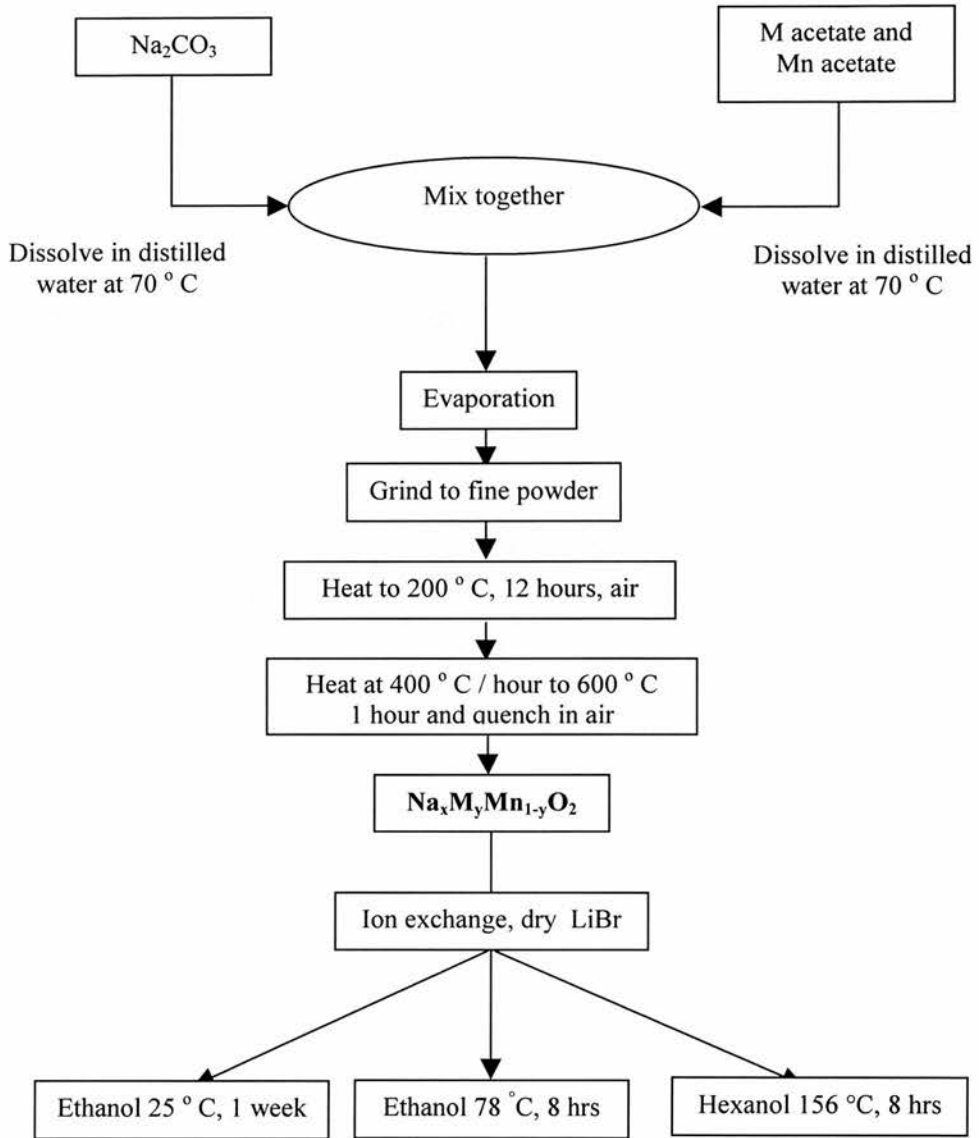


Figure 2.1. Schematic of preparation of $\text{Na}_x\text{M}_y\text{Mn}_{1-y}\text{O}_2$ and $\text{Li}_x\text{M}_y\text{Mn}_{1-y}\text{O}_2$

2.3 METHODS FOR CHARACTERISATION

The principal analytical techniques used to characterise the as-prepared compounds were: powder x-ray diffraction, neutron diffraction, chemical analysis, redox titration, thermogravimetric analysis (TGA), scanning electron microscopy (SEM), x-ray photoelectron spectroscopy (XPS) and surface area measurements.

2.3.1 POWDER X-RAY DIFFRACTION

2.3.1.1 INTRODUCTION

X-rays, so named because their nature was at first unknown, were discovered in 1895 by Röntgen. X-rays are a form of electromagnetic radiation, and powder x-ray diffraction is one of the best methods for a versatile and non-destructive identification of crystal structure. It is particularly valuable in the study of intercalation compounds where single crystals are often not available. In an x-ray diffraction pattern, the positions of the peaks show the phases that are present and peak heights show the phase concentration.

2.3.1.2 THE X-RAY SOURCE

X-rays are produced when an electron beam collides with a target material, such as copper or iron. The electron beam can penetrate deep into the lowest energy levels of the target material atoms, and displace the electrons there. These energy levels have a full complement of electrons and x-rays originate from electronic transitions between these levels. For example, if a K-shell electron is ionised an electron in an outer L-shell orbital can immediately drop down to occupy the vacant level. The energy released during this transition appears as x-ray radiation, the wavelength of which will be given by $\lambda = hc/(E_1 - E_2)$, where h is Planck's constant, c the speed of light and E_1 and E_2 are the higher and lower energy levels of the shell electrons. The

output from an iron x-ray tube consists of various peaks derived from transitions between various shells. For most x-ray crystallographic purposes, monochromatic radiation is required and filters are used to eliminate the unwanted radiation. Target materials are used with the wavelengths of their $K\alpha_1$ radiation.¹

The output from an iron x-ray tube, operating at 35 000 V has a $K\alpha_1$ wavelength of 1.936 Å. All oxide powders prepared in this project were analysed by x-ray $FeK\alpha_1$ radiation, since manganese rich compounds exhibit fluorescence when irradiated by copper x-ray radiation. A curved crystal primary monochromator, a focussing geometry in transition mode and a small angle position sensitive detector are employed on a Stoe STADI/P diffractometer, as shown in Figure 2.2. Such arrangement delivers high resolution and minimises preferred orientation, which can be particularly severe when examining layered compounds using Bragg-Brentano (reflection geometry). The two theta range over which data were collected was typically from 10° to 120°, over 12 hours.

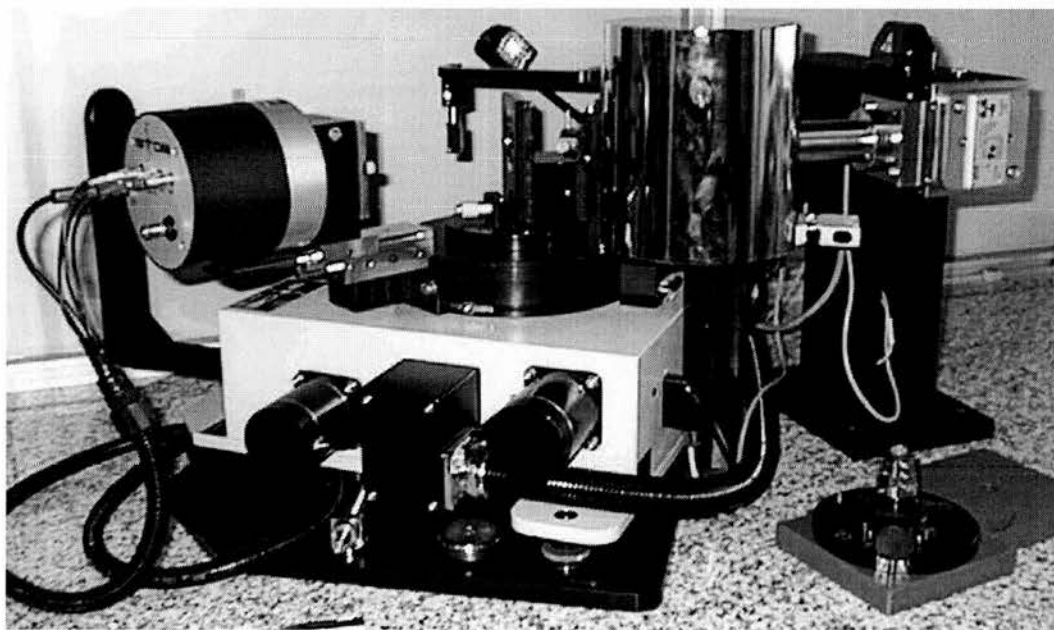


Figure 2.2 Stoe transmission diffractometer used in these studies.

2.3.1.3 X-RAY DIFFRACTION

Within any sample, lattice planes exist in a number of different orientations, each with their own specific d -spacing. When x-rays fall on planes of atoms in a crystal, each atom scatters a small fraction of the incident beam due to oscillations generated in the electrons of the atoms. The atoms may be regarded as the source of a weak secondary wavelet of x-rays and in most directions destructive interference occurs. However, if the path difference, $(AB + BC)$, between successive planes is a whole number of wavelengths of the incident radiation, the resultant reflected beam is strong. From Figure 2.3 the reflected beam has maximum intensity when Bragg's law, $n\lambda = 2d\sin\theta$, is satisfied, for a monochromatic beam with wavelength λ incident at a glancing angle θ on lattice planes.²

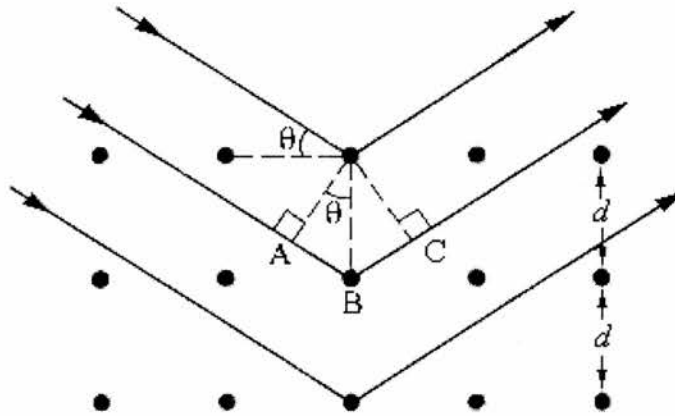


Figure 2.3. Each lattice plane reflects the incident radiation. Two reflected beams will only interfere constructively when the difference in path lengths $AB + BC$ is equal to an integral

number of wavelengths $n\lambda$.³

In a powdered sample the crystallites all have different orientations relative to the direction of the incident beam. The full powder diffraction pattern for a sample is formed by the cones corresponding to reflections from all sets of planes satisfying Bragg's law, as shown in Figure 2.4.

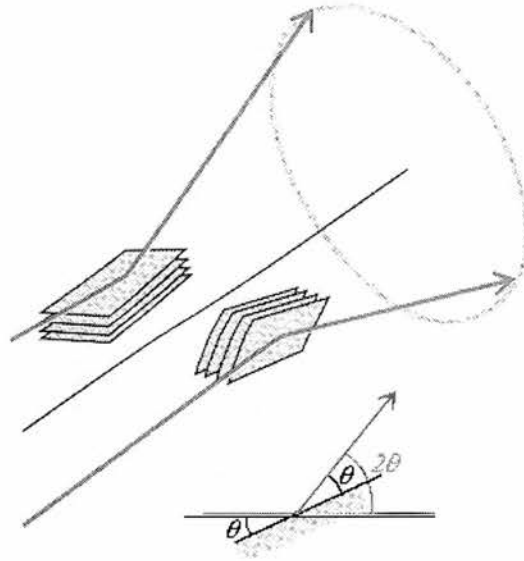


Figure 2.4 The same set of planes in two crystallites give diffracted rays for a glancing angle θ that lie on a cone of half-angle 2θ .³

2.3.2 CRYSTAL STRUCTURE IDENTIFICATION AND REFINEMENT

2.3.2.1 CRYSTAL STRUCTURE IDENTIFICATION

Identification of a sample involves comparing the diffraction peak positions and their intensities with an internationally recognised database, containing reference patterns of many phases. The database used in this work was the JCPDS International Centre for Diffraction Data (ICDD).⁴ An x-ray diffraction pattern can be indexed from the standard pattern by assigning Miller indices hkl for each diffraction line. Miller indices are a set of three numbers, h , k and l , which identify each lattice plane (*i.e.* the diffraction plane) according to Bragg's Law.

Using a refinement process, the lattice parameters of a unit cell can be calculated from the positions of diffraction peaks, when the pattern has been indexed. Lattice parameters were obtained from x-ray diffraction data by Rietveld refinement, using the General Structure Analysis System, (GSAS), suite of programs.⁵

2.3.2.2 RIETVELD REFINEMENT

In the 1960's, Rietveld developed the first computer-based analytical procedures to make use of the full information provided by a powder diffraction pattern. He subsequently published the work and freely shared his computer program, so that the method most commonly used to solve structures in recent years has been called the Rietveld method.⁶

In the Rietveld method, a mathematical least squares procedure simultaneously refines atomic positions, thermal vibrational parameters, lattice parameters and line profile shapes. These are all modified until the best fit is obtained between the observed powder diffraction pattern taken as a whole, and the entire calculated pattern. During this procedure, continuous feedback is used to improve the knowledge of the structure and to improve the allocation of the observed intensity to partially overlapping Bragg reflections.

In all cases, the 'best-fit' is simultaneously the least-squares fit to all of the thousands of intensities y_i , at step i in the diffraction pattern. The quantity minimised in the least-squares refinement is the residual S_y :

$$S_y = \sum_i w_i (y_i - y_{c_i})^2,$$

where

$$w_i = 1/y_i$$

with,

y_i = observed intensity at i th step and

y_{ci} = calculated intensity at i th step.

The summation is over all data points.

A powder diffraction profile for a crystalline material is essentially a collection of individual reflection profiles, each of which has a peak height, a peak position, a breadth, tails which decay gradually with distance from the peak position and an integrated area which is proportional to the Bragg intensity, I_K . K stands for the Miller indices, h, k, l and I_K is proportional to the square of the absolute value of the structure factor, $|F_K|^2$. In powder patterns, these are not all resolved but overlap to some degree and hence, the Rietveld method is required to fit the data.

For the Rietveld method to be successfully applied to the refinement of a structure, a good starting model is required. The procedure is a structure refinement method and not a structural solution. Typically, many Bragg reflections contribute to the intensity, y_b , observed at any point, i , in the pattern. The calculated contributions from neighbouring Bragg reflections and the background are summed, to determine the calculated intensities y_{ci} from the $|F_K|^2$ values calculated from the structural model:

$$y_{ci} = y_{bi} + s \sum_K L_K |F_K|^2 \phi(2\theta_i - 2\theta_K) P_K A,$$

where

s = scale factor,

L_K = Lorentz, polarisation and multiplicity factors,

ϕ = reflection profile function,

P_K = preferred orientation function,

A = absorption factor,

y_{bi} = background intensity at the i th step,

2.3.2.3 CRITERIA OF FIT

The Rietveld refinement process adjusts the refinable parameters until the residual is minimised, *i.e.* the ‘best fit’ obtained will depend on the adequacy of the model and on whether a global minimum as opposed to a local minimum has been reached. To assist making these judgements, there are a number of criteria that show, as the refinement cycles progress, how well the model is behaving. The R-value used in this work to enable the user to judge the fit, is defined as

the R-weighted pattern

$$R_{wp} = \left\{ \frac{\sum w_i (y_i(\text{obs}) - y_i(\text{calc}))^2}{\sum w_i (y_i(\text{obs}))^2} \right\}^{1/2}$$

In R_{wp} , the numerator is being minimised and so mathematically this R factor is the most meaningful and the one that best reflects the progress of the refinement.

Another useful criterium for the quality of the fit is χ^2 ,

$$\chi = \frac{R_{wp}}{R_e},$$

$$\text{where } R_e = \left[\frac{(N - P)}{\sum w_i y_{oi}^2} \right]^{1/2} = \text{‘R-expected’},$$

with N the number of observations,

P the number of variables and

y_{oi} the observed intensity.

A value of χ^2 of 1 is aimed for in the refinement.

2.3.2.4 PEAK SHAPES

For an ideal single crystal, the diffraction pattern should consist of a collection of infinitely sharp Bragg peaks. However, the resolution and instrumental effects will broaden the signal to some extent. Peak broadening is in many cases intrinsic to the sample. For samples with very small crystallite domains, or where there are significant distortions in the unit cell, the observed Bragg peaks are often significantly broader than expected.

In this work, the pseudo-Voigt function was used exclusively to model the peak shape.^{7,8} This function allows the refinement of a mixing parameter, determining the fraction of the Lorentzian and Gaussian components of the peak shape. The pseudo-Voigt is symmetric but allows for a flexible variation of the broad Gaussian to the narrow Lorentzian.

2.3.3 POWDER NEUTRON DIFFRACTION

2.3.3.1 INTRODUCTION

In 1932, Chadwick discovered the neutron and shortly after, Elasser first suggested that neutron motion would be governed by wave mechanics.⁹ Neutrons have a mass, (m_n) of 1.660437×10^{-27} kg and wavelengths similar to interatomic distances. 0.5-3 Å. As a result, they are diffracted by crystalline materials. Because their interactions with the sample are weak, neutrons are penetrating, and this allows the bulk of a material to be probed, unlike x-rays which only tend to probe the surface. Bragg's law also governs neutron diffraction and when neutrons are scattered, it is the nucleus that is solely responsible for the scattering, as electrons are too small to deflect neutron beams. Therefore, the scattering powers of atoms towards neutrons are quite different from those towards x-rays. The structures of several $\text{Li}_x\text{Ni}_y\text{Mn}_{1-y}\text{O}_2$ materials were characterised using neutron diffraction, time of flight data were collected on the GEM diffractometer at ISIS, Rutherford Appleton Laboratory.

2.3.3.2 THE NEUTRON SOURCE

Protons are used to produce the pulsed neutron beam at ISIS. Each proton chips about 30 neutrons from a heavy atom nucleus, usually depleted uranium or tantalum and this process is known as spallation. The production of protons which are sufficiently energetic to produce efficient spallation, involves the acceleration of H⁺ ions to 70 MeV. Subsequently they enter the synchrotron where the electrons are stripped from the H⁺ ions. This produces a circulating beam of protons and the 52 m diameter proton synchrotron accelerates 2.5×10^3 protons per pulse to 800 MeV. The protons are then extracted and sent to the heavy metal target. This process is repeated 50 times per second. The high energy neutrons are slowed down for neutron diffraction studies by using moderators. The resulting neutron beam is directed down a number of different beam guide lines to a variety of diffractometers and spectrometers. In this work, the high intensity, high resolution, general materials diffractometer (GEM) was used.¹⁰ Vanadium sample cans were loaded with sample and sealed with PTFE tape.

At a spallation source, the neutron beam is pulsed so that neutrons with different wavelengths can be discriminated by their time of arrival at a detector, and different *d*-spacings are measured at fixed θ , $\lambda_{hkl} = 2d_{hkl}\sin\theta$. There are banks of detectors at different scattering angles allowing access to a large number of *d*-spacings.

Structural refinement was carried out by Dr. A. R. Armstrong using the program 'TF12LS' based on the Rietveld method using programs based on the Cambridge Crystallographic Subroutine Library (CCSL) at the ISIS facility.^{11,12} Neutron scattering lengths of -0.19, -0.373, 1.03 and 0.5803 (all $\times 10^{-12}$ cm) were assigned to Li, Mn, Ni and O respectively.¹³

2.3.4 CHEMICAL ANALYSIS

As-prepared materials were submitted for chemical analysis in the University of St. Andrews chemistry department. Flame emission, and atomic absorption spectroscopy were performed on a PU 9400 instrument. The former technique was used for the alkali metals and the latter for the transition metals. The true sodium content present in sodium phases was determined by subtraction of the Na_2CO_3 content, which was measured by carbon microanalysis.

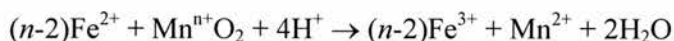
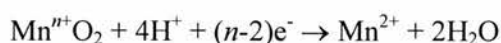
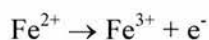
2.3.5 REDOX TITRATION

The oxidation state of manganese in all transition metal oxides was determined using a potentiometric titration method.¹⁴ A Mettler DL 40 RC auto titrator was used.

The redox titrations procedure was as follows:

- 1) Dissolution of oxide powders, $\text{A}(\text{M}_y\text{Mn}_{1-y})\text{O}_2$, with excess $\text{Fe}(\text{II})\text{SO}_4$, to reduce all Mn to Mn(II).

Standard equations:



- 2) Potentiometric titration of the remaining Fe^{2+} with a standardised KMnO_4 solution to oxidise the excess Fe^{2+} ions which remain after Na phase dissolution.



2.3.6 THERMOGRAVIMETRIC ANALYSIS (TGA)

TGA is a dynamic technique for measuring the change in weight of a substance, as a function of temperature or time. Use of thermal analysis in solid state science includes the study of solid state reactions, thermal decompositions and phase transitions. A TA Instruments SDT 2960 thermal gravimetric analyser was used. Typically, 25 mg of powder was placed in an alumina crucible. The measurement was made in a flow of high purity dry laser air (no CO₂ or water, BOC). A sweep rate of 2 °C min⁻¹ was used and the data were corrected for the change in the buoyant force of air with temperature. The data necessary for the correction were obtained by performing the TGA experiment on 25 mg of inert Al₂O₃ powder.

2.3.7 SCANNING ELECTRON MICROSCOPY (SEM)

Electron microscopy is a versatile technique capable of providing microstructural information over a wide range of magnification. SEM studies the texture, topography and surface features of powders. Features up to tens of micrometers in size can be observed and, because of the depth of focus of SEM instruments, the resulting pictures have a definite three-dimensional quality. Selected samples were examined using a JOEL JSM – 840 SEM. It was necessary to place the sample in a thin layer of silver paint in order to prevent the build-up of charge on the surface.

2.3.8 X-RAY PHOTOELECTRON SPECTROSCOPY (XPS)

Electron spectroscopy techniques measure the kinetic energy of electrons that are emitted from matter, as a consequence of bombarding it with ionising radiation or high energy particles. The kinetic energy is equal to the difference between the energy of the incident radiation and the binding energy or ionising potential of the electron. For a given atom, a range of binding

energies are possible, corresponding to the ionisation of electrons from different inner and outer valence shells, which are characteristic for each element.

Investigation of the nickel oxidation states was carried out using XPS on a VG.ESCALAB 3 instrument. The surface science group in the St. Andrews University chemistry department performed the experiments. The photoelectron spectrometer was equipped with a magnesium anode (1254 eV) and operated at 12 kV, 20 mA. The instrument was operated in constant energy analyser mode, with the vacuum in the analysis chamber continuously smaller than 5×10^{-9} mbar. Non-stoichiometric nickel oxide (Ni_{1-x}O) was used as an energy standard for both Ni^{2+} and Ni^{3+} . High resolution spectra were recorded of the O(1s) and Ni(2p) regions. Binding energy values were referenced to the O (1s) peak at 540.2 eV.

2.3.9 SURFACE AREA MEASUREMENT

The Catalyst Evaluation and Optimisation Service at Edinburgh University determined the surface areas of selected powder samples. The Brunauer-Emmett-Teller (BET)¹⁵ method was used on a micromeritics Gemini 2360 instrument using N_2 at 77 K.

2.4 ELECTROCHEMICAL CELL PREPARATION

2.4.1 INTRODUCTION

Electrochemical cycling is a powerful technique for obtaining structural, thermodynamic and kinetic data on insertion compounds. This section discusses the preparation of the composite cathodes and electrochemical cells used to enable lithium cycling of the cathode materials. Some kinetic aspects of electrode reactions are presented in section 2.5.

2.4.2 CATHODE CONSTRUCTION

In order to evaluate the electrochemical performance of the layered materials, electrochemical cells were constructed. Cathodes were made from the active cathode materials, $\text{Li}_x\text{M}_y\text{Mn}_{1-y}\text{O}_2$, super S carbon and Kynar Flex 2801 binder (Elf Atochem). These materials, in an 85:10:5 mixture, by weight, were stirred in tetrahydrofuran (THF) for 24 hours. The surface of a 0.05 mm thick aluminium foil, (Aldrich, 99.8 %), was prepared by roughening with a scourer and then cleaning with acetone. A layer (40 μm thick) of the cathode material slurry was cast onto the prepared aluminium foil using the doctor blade technique, at a speed of 5 mm s^{-1} . After evaporation of the THF and drying under vacuum overnight at 70 $^\circ\text{C}$, the cast material was pressed under 100 kg cm^{-1} pressure. Disc-shaped cathodes 13 mm in diameter were cut, and then dried again overnight, prior to cell assembly. To calculate the mass of cathode material, the mass of the aluminium disc is obtained by weighing 10 discs and taking the average.

2.4.3 CELL CONSTRUCTION

The coin cells were assembled and crimp sealed in a dry box, filled with argon. Cells employed to cycle material for the electrochemical results are two electrode coin cells, having 23 mm diameter and 2.5 mm height. The components are made by the National Research Council, Canada (NRC) and Figure 2.5 is an exploded view of the coin cell assembly. Stainless-steel disc springs, and disc spacers were needed to establish enough force on the electrode, to ensure reliable internal contact. The working electrode is the previously prepared, aluminium backed intercalation compound, cathode material disc. The mass of active material contained in each cathode was calculated as

$$(\text{total mass of cathode disc} - \text{mass of aluminium disc}) \times 0.85,$$

this was usually of the order of 5 mg. Anodes were punched from a 0.38 mm thick ribbon of clean lithium metal and had a diameter of 13 mm. The electrodes are separated from one

another by a glass fibre pad, soaked with a 1 molal solution of LiPF_6 , (Battery grade, Morita), in propylene carbonate, (Merck), as the standard electrolyte solution. The electrolyte was prepared and stored in the glove box.

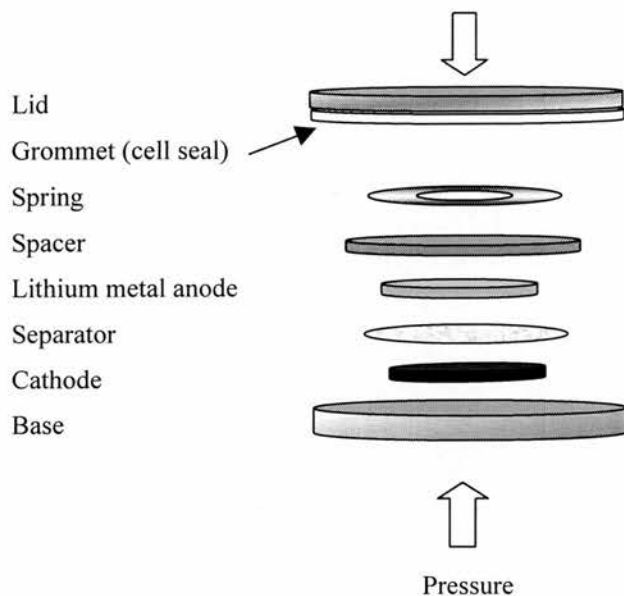


Figure 2.5 Exploded view of coin cell assembly used for these studies

2.4.4 ELECTROCHEMICAL TECHNIQUES

To investigate the effect of repeated lithium extraction, and reinsertion, in the new cathode materials, cells were cycled between the potential limits of interest. Cycling tests were carried out at 30 °C and controlled by a Macpile II multichannel cycler (Biologic, France). All the potentials indicated in this report refer to Li/Li^+ .

The cycling method most often used in this project was galvanostatic cycling, where a constant current is applied through the cell. Data were logged whenever the cell voltage changed by more than 0.005 V. It was assumed that all the current passed can be related to lithium ion insertion/extraction. The current was varied, based on the mass of active cathode material, to

give a constant current density in mA g^{-1} . Current densities were adjusted to be 10, 25, 50, 100 or 200 mA g^{-1} of active material, which corresponded approximately to full discharge times of $t = 20, 9, 4, 2$ and 1 hours, respectively. The C-rate is a way of expressing the current, and is defined as the discharge capacity divided by t .

An alternative method of characterising the redox behaviour of materials is potentiostatic cycling. A linear change in potential with time causes a change in current, and a voltammogram shows the current's response to the changing voltage. The rate of potential step used was 2.5 mV every 4 minutes, such a relatively slow rate should allow slow processes to be observed, such as lithium ion diffusion in the intercalation electrode.

For structural analysis of the cathode materials at different stages of cycling, cells were first stabilized at the desired potential for one hour. In order to minimise exposure to moisture in the air, the cells were disassembled in a glove box, and dried in an argon atmosphere for several days. The cathode material was scraped from the aluminium foil current collector, and evenly spread onto a thin layer of vacuum grease, smeared on the transmission foil, for x-ray analysis.

2.5 KINETIC PROPERTIES OF SOLIDS

Thermodynamic laws, as discussed in section 1.3, govern the behaviour of electrochemical cells during equilibrium, but it is kinetics which dictate their behaviour when current is passed. Movement of charged species determines the amount of current a cell is capable of sustaining at a particular voltage. Regrettably, a cell is never able to maintain its equilibrium potential due to the generation of forces opposing the passage of current. These forces manifest themselves as polarisation overpotential, a voltage loss which is a function of current density. It consists of three separate terms,¹⁶

η_a = activation overpotential, connected with the charge-transfer step,

η_c = concentration overpotential, connected with mass-transfer, and

η_0 = Ohmic overpotential, due to the internal resistance of all components.

Since an electrode process consists of several steps the rate of overall reaction will depend on the slowest step. Activation polarisation in classical solution electrochemistry, is a measure of the ease of charge-transfer between different phases. If mass transfer is fast, the overall kinetics are controlled by the reaction at the surface, *i.e.* the Butler-Volmer equation.¹⁶ During the charge-transfer step, materials are consumed or formed. The process of mass transfer is essential for a continuing chemical change as it supplies the electrode surface with reactant and removes the product. Concentration polarisation is due to the mass-transport limitations of the ions. There are three forms of mass transfer, diffusion, convection and migration. In the electrolyte, the solution phase is characterised by a very large concentration of mobile ions. Thus, concentration gradients, (diffusion), must be small, and ion transport occurs predominantly through migration. The situation is reversed, however, for the electrode phase, where charge transport takes place via the motion of electronic species. Internal electric fields are small, and therefore ionic flux is due mainly to a local ionic concentration gradient (diffusion) within the solid phase.

2.6 REFERENCES

- ¹ M. M. Woolfson, *An Introduction to x-ray crystallography*, second edition, Cambridge University Press, (1997).
- ² W. L. Bragg, *Proc. Camb. Phil. Soc.*, **17**, (1912), 43.
- ³ P. W. Atkins, *Physical Chemistry*, 5th Edition, Oxford University Press (1994)
- ⁴ JCPDS, ICDD, Newton Square, PA 19073, USA.
- ⁵ A. C. Larson and R. B. von Dreele, *General Structure Analysis System*, Los Alamos National Laboratory, (1995).
- ⁶ H. M. Rietveld, *Acta Cryst.* **2**, (1969), 65.
- ⁷ C. J. Howard, *J. Appl. Cryst.*, **15**, (1982), 615.
- ⁸ P. Thomson, D. E. Cox, J. B. Hastings, *J. Appl. Cryst.*, **20**, (1987), 79.
- ⁹ W. M. Elasser, *C.r. hebd. Seanc. Acad. Sci. Paris*, **202**, (1936), 1029.
- ¹⁰ W.G.Williams, R.M.Ibberson, P.Day and J.E.Enderby, *Physica B*, **241-243**, (1998), 234.
- ¹¹ J. C. Matthewman and P. Thompson, *J. Appl. Cryst.* **15**, (1982), 167.
- ¹² P. J. Brown and J. C. Matthewman, Rutherford Appleton Laboratory Report, RAL-87-010, (1987).
- ¹³ V. F. Sears, *Neutron News*, **3**, (1992), 26.
- ¹⁴ M. J. Katz, R. C. Clarke and W. F. Nye, *Anal. Chem.* **28**, (1956), 507.
- ¹⁵ S. Brunauer, *Physical Adsorption*, Princeton University Press, Princeton, N. J., (1945).
- ¹⁶ C. A. Vincent and B. Scrosati, *Modern Batteries*, Second Edition, Arnold Publ. Ltd., London, (1997).

CHAPTER 3. PREPARATION AND

CHARACTERISATION OF $A_xNi_yMn_{1-y}O_2$, $A =$

Na, Li.

3.1 INTRODUCTION

In this research, doped layered manganese phases, $Li_x(Mn_{1-y}Ni_y)O_2$, for $0 < y < 0.2$, are obtained from the analogous Na phases by ion exchange, as described in chapter two. The first half of this chapter concerns the investigation of the synthesis, and structural and compositional characterisation, of the solid solution $Na_xNi_yMn_{1-y}O_2$ precursors. The second half of this chapter characterises the materials obtained after ion exchanging the sodium for lithium. Ion exchange is performed at three different temperatures. The effect of nickel substitution and ion exchange temperature on the electrochemical properties will be presented in chapter four.

3.2 SODIUM PHASES $Na_xNi_yMn_{1-y}O_2$

3.2.1 INTRODUCTION

The aim is to prepare a sodium precursor $Na_xNi_yMn_{1-y}O_2$, which will successfully ion exchange to form a layered O3, α - $NaFeO_2$, structure type, $Li_xNi_yMn_{1-y}O_2$. Investigation of the crystal chemistry of the Na_xMnO_2 system by classical high temperature synthesis has shown the existence of several phases in the range $0 < x < 1$, Figure 3.1.¹ Structures are three dimensional for the lower x values and two dimensional as x increases. The average manganese oxidation state in equilibrium with the gas phase also changes with temperature, for example, MnO_2 is stable up to 415 °C, Mn_2O_3 between 415 and 910 °C, while above 910 °C, $(Mn^{+2.67})_3O_4$ is

stable. The same general trend is observed for Na_xMnO_2 , however the Na cations within the structure stabilise a higher oxidation state of manganese compared to the pure oxides. For example $\beta-Na_{0.7}(Mn^{+3.4})O_{2.05}$ is stable to 1000 °C.

Below 600 °C a P3 phase exists in the composition range $Na_{0.7+x}MnO_2$. P3 structures are easier to ion exchange than P2 or O3 because of the physical amount of space for ion diffusion due to the difference in the oxygen stacking sequence, P3 having more room than P2 or O3. In the P3 structure the sodium layer is approximately 2/3 filled, leaving open pathways for the coupled diffusion of lithium and sodium. It is on this composition that we shall base our synthesis of the Ni doped material.

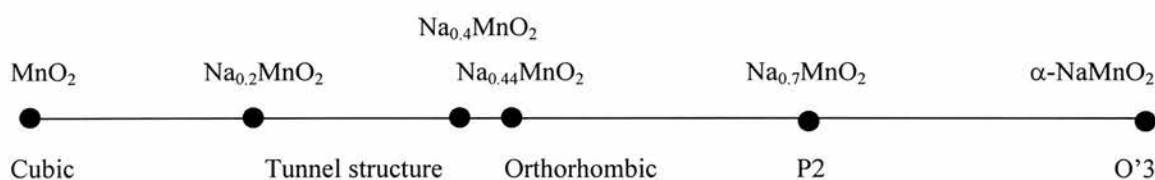


Figure 3.1 Na_xMnO_2 phase compositions above 600 °C.

3.2.2 XRD SIMULATION OF THE LAYERED SODIUM PHASE

The P3 structure for $Na_xNi_yMn_{1-y}O_2$ has the space group R3m. The crystallographic details in Table 3.1 were used to simulate a model diffraction pattern for $y = 0.05$ in $NaNi_yMn_{1-y}O_2$ using Fe ($\lambda = 1.936 \text{ \AA}$) radiation is shown in Figure 3.2.³ The pattern is characteristic of a layered P3 structure; the first diffraction line at $d_{003} \approx 5.6 \text{ \AA}$ corresponds to the interslab distance.

	Wyckoff symbol	x/a	y/b	z/c	Occupancy
Na	3b	0	0	0.8300	0.7
Mn	3a	0	0	0	0.95
Ni	3a	0	0	0	0.05
O1	6c	0	0	0.5996	1
O2	6c	0	0	0.3548	1

Table 3.1. Crystallographic details used to simulate of the sodium phase $Na_{0.7}Ni_{0.05}Mn_{0.95}O_2$, space group $R3m$.

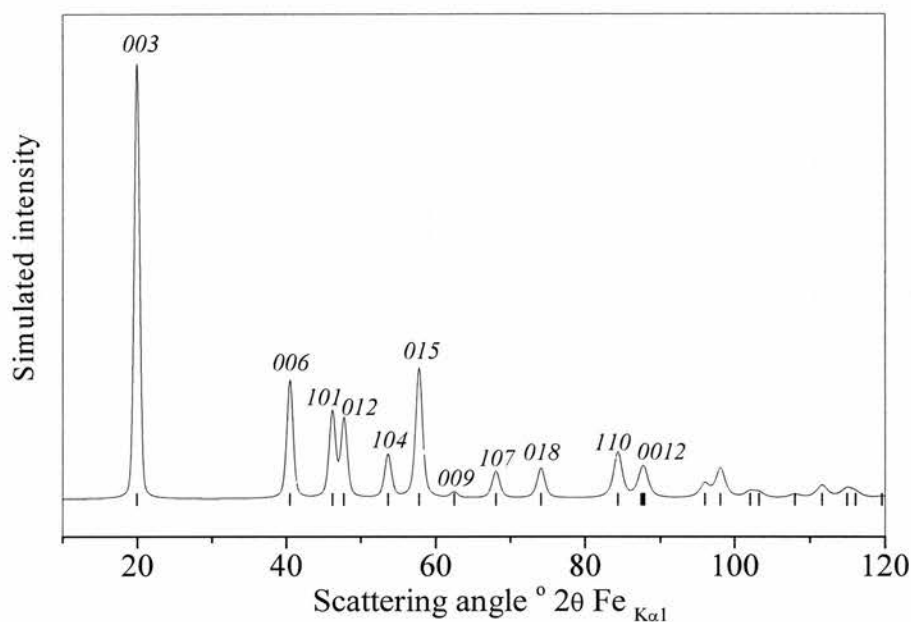


Figure 3.2 Simulated diffraction pattern for the composition $Na_{0.7}Ni_{0.05}Mn_{0.95}O_2$. Space group $R3m$

3.2.3 SYNTHESIS OF THE SODIUM PHASE, $Na_xNi_yMn_{1-y}O_2$.

$Na_xNi_yMn_{1-y}O_2$ was synthesised via a solution technique as described in chapter two. Intimate mixing of the reagents favours high reactivity due to a more even distribution during thermal treatment. This method also has the advantage of lower temperature reaction and provides the possibility of homogeneously adding differing amounts of the metal dopant.

The product of rotary evaporation with composition $Na_xNi_{0.05}Mn_{0.95}O_2$ is precalcined at 200 °C for 12 hours. The heating process was initially investigated with a single TGA experiment to highlight the temperatures of interest in the range 200 to 900 °C. The structural changes throughout the heating process were then observed from *ex-situ* x-ray diffraction patterns to find the optimum temperature for forming the desired P3 phase.

3.2.3.1 TGA

The weight change was recorded while heating the sample at a rate of 2 °C min⁻¹ in high purity dry air to 900 °C where it was held for an hour. Cooling was at a rate of -2 °C min⁻¹. Figure 3.3 is a plot of the weight loss (%) against temperature and the labels (a) to (g) correspond to temperatures at which significant weight loss occurs, these are most likely to be phase changes.

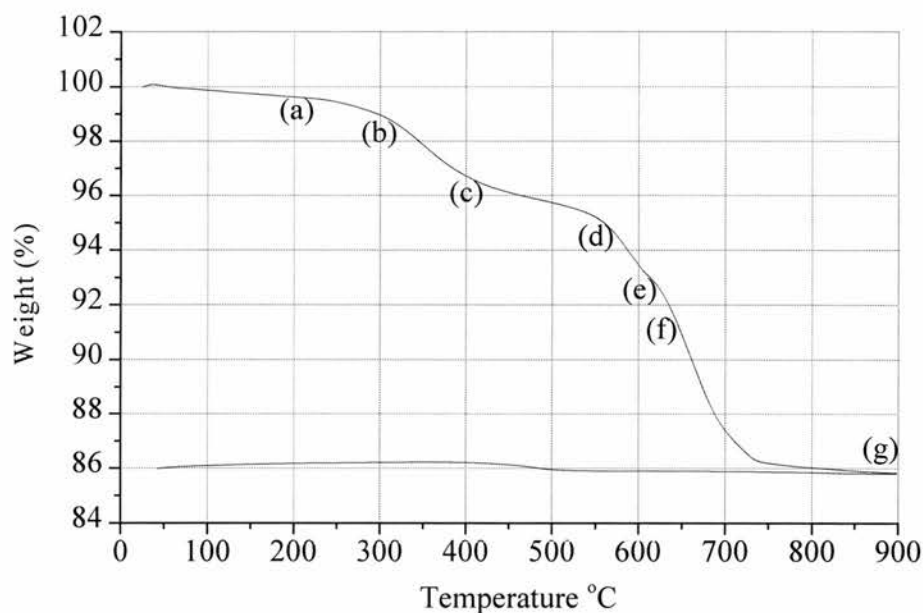


Figure 3.3 TGA plot for heating $NaNi_{0.05}Mn_{0.95}O_2$ at 2 °C min⁻¹. (precalcined at 200 °C for 12 hours) Labels (a) to (g) indicate the temperatures of interest, later investigated by x-ray diffraction, see text.

The mass versus temperature during heating initially shows a small weight loss, (1 %), Figure 3.3(a), prior to 300 °C, which is attributed to the loss of moisture absorbed by the prepared powder prior to its analysis. At 300 °C, Figure 3.3(b), the TGA curve starts to fall more steeply until 400 °C, 3.3(c). The weight loss slows at 400 °C and extends until 550 °C, 3.3(d). At 600 °C in the TGA there is a subtle change in slope observed, 3.3(e). The final decomposition commenced at a temperature of 630 °C, 3.3(f). The final plateau at 740 °C corresponds to the weight of the residue.

3.2.3.2 X-RAY DIFFRACTION

To investigate the phase evolution observed by TGA six identical precalcined materials, (all sample (a)), with composition $Na_xNi_{0.05}Mn_{0.95}O_2$, were heated in air at 400 °C hr^{-1} . Each new sample was quenched to room temperature after one hour at a temperature in the range 300 to 900 °C, (Table 3.2) and investigated by x-ray diffraction.

Sample	Quenching temperature (°C)	Time (h)
(a)	200	12
(b)	300	1
(c)	400	1
(d)	550	1
(e)	600	1
(f)	630	1
(g)	900	1

Table 3.2. Heating conditions for $Na_xNi_{0.05}Mn_{0.95}O_2$, (b) to (g) all initially precalcined at 200 °C for 12 hours.

The x-ray diffraction patterns taken immediately after quenching each sample are presented in Figure 3.4 (b) to (g). Figure 3.4(a) is the x-ray diffraction pattern of $Na_xNi_{0.05}Mn_{0.95}O_2$ after precalcination at 200 °C. Comparing Figure 3.4(b) with the model of Figure 3.2, the broad peak observed at a d -spacing of 5.6 Å suggests that small particles of the desired layered phase are

already forming at this temperature. Sharp peaks in Figure 3.4(a) and (b) at d -spacings of 4.92, 3.08, 2.76 and 2.49 Å can be attributed to γ - Mn_3O_4 .⁴

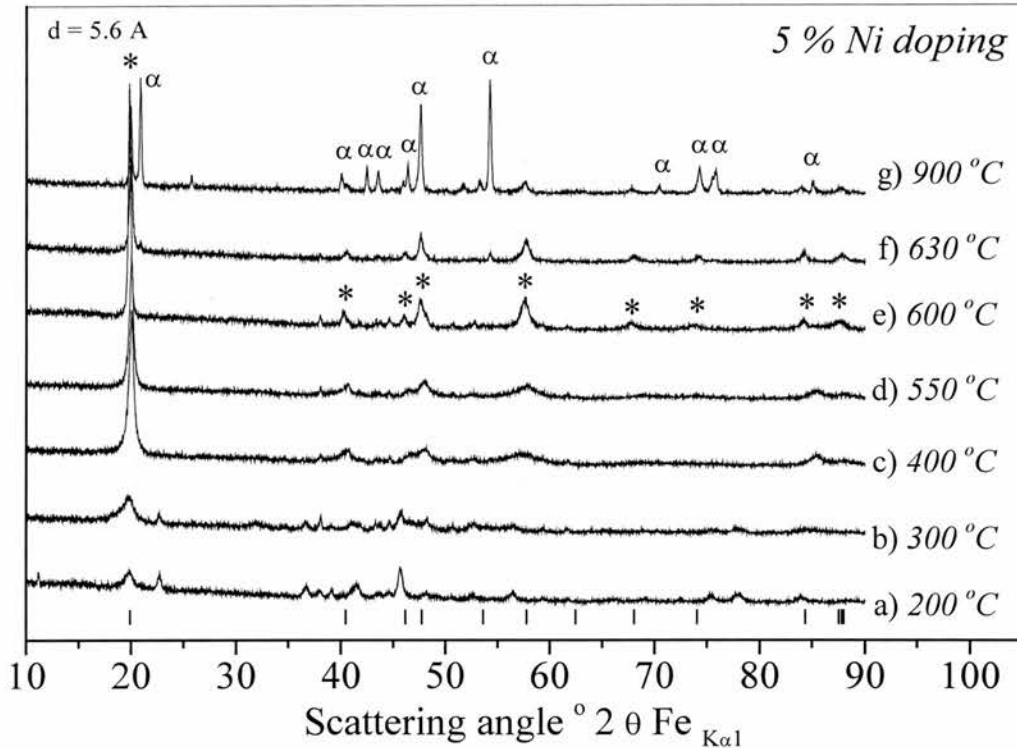


Figure 3.4 Evolution of the x-ray diffraction patterns taken after heating $Na_xNi_{0.05}Mn_{0.95}O_2$. All samples were prepared by the solution route and precalcined in air at 200 °C for 12 hours (a). Subsequent heat treatments carried out in air for one hour were : (b) 300 °C, (c) 400 °C, (d) 550 °C, (e) 600 °C, (f) 630 °C, (g) 900 °C, as indicated in Table 4.2. The positions of the reflections of the desired P3 phase are indicated by tic marks and * indicate the peaks in (e) which correspond to this phase. Reflections marked α in (g) correspond to the peak positions for α - $NaMnO_2$.

Heating to 400 °C, (Figure 3.3(c)), alters the structure further to resemble the simulated P3 x-ray diffraction data, but the materials still remain poorly crystalline with broad peaks in the positions where the true reflections should occur. This structure change before 400 °C is in agreement with the TGA plot where a relatively large weight loss (2.5 %) was observed up to

point (c) in Figure 3.3. The x-ray patterns of the material remains similar in the temperature range 400 to 550 °C indicating that no phase changes take place, (Figure 3.4(c)-(d)). The lack of structural changes observed in this temperature range correspond to the plateau between (c) and (d) in Figure 3.3. As the temperature was increased to 600 °C the diffraction pattern alters significantly to display much sharper peaks, indicating that the crystallinity of the compound is much greater (indicated by asterisks 3.3(e)).

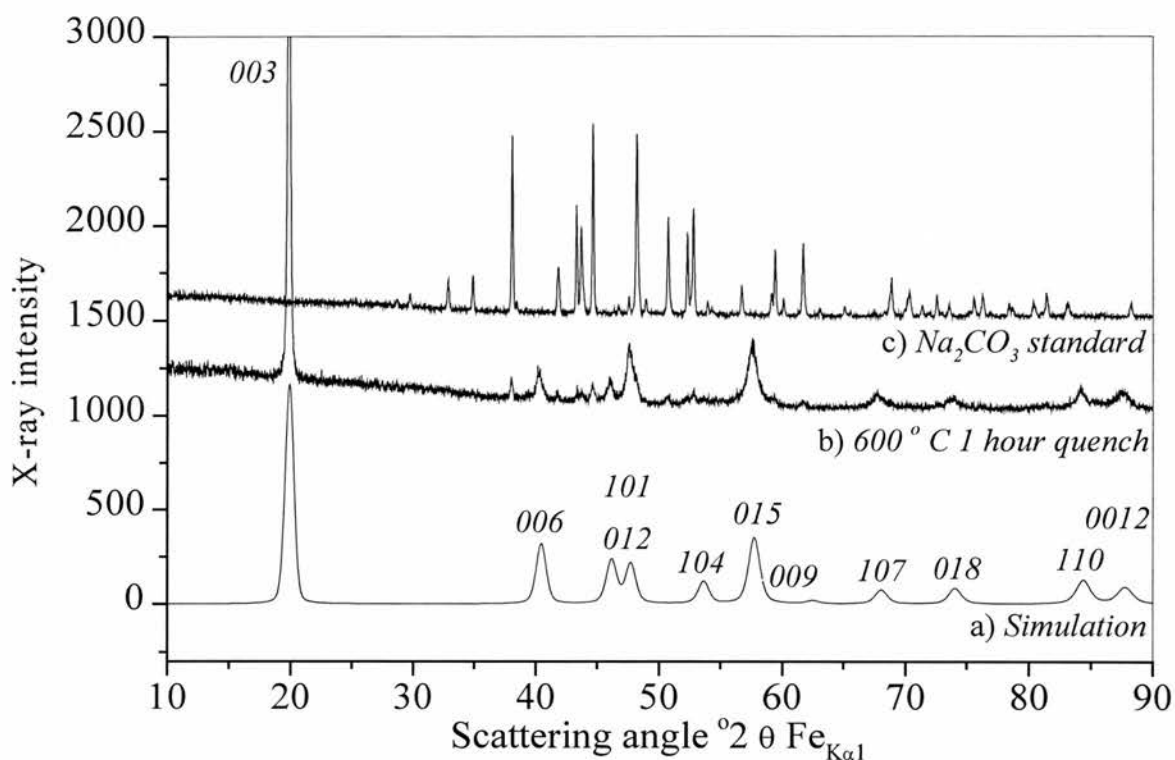


Figure 3.5 Comparison of a) the simulated layered phase model with b) $Na_xNi_{0.05}Mn_{0.95}O_2$ obtained from a 600 °C quench.. The peaks are indexed in the space group of the $P3$ structure, $R3m$. c) is a standard Na_2CO_3 pattern.

The x-ray pattern of Figure 3.4(e) is shown in Figure 3.5(b) together with the layered phase simulation. This comparison shows that the desired layered phase has been formed after one hour at 600 °C. The remaining peaks in Figure 3.5(b) correspond to the more intense peaks for Na_2CO_3 and could be washed out with water. A standard Na_2CO_3 pattern is shown in Figure

3.4(c) for comparison. Figure 3.9 shows a washed sodium phase displaying no Na_2CO_3 peaks. This suggests that the layered phase is deficient in sodium compared with the composition of the starting material.

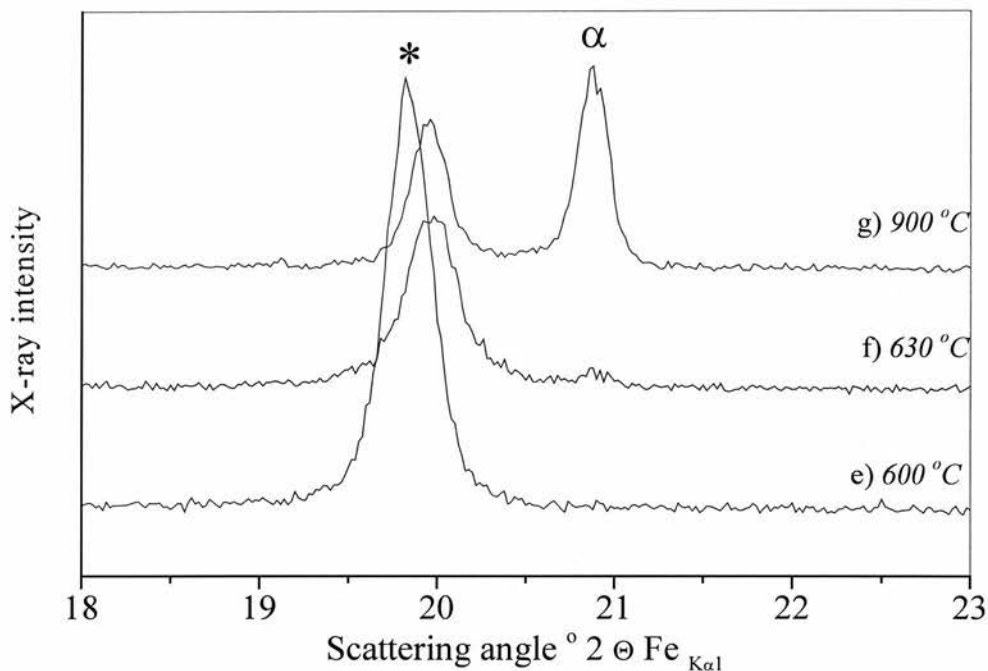


Figure 3.6 Enlargement of Figure 3.3 to show the metastable nature of $NaNi_yMn_{1-y}O_2$ P3 phase above 600 °C.

Returning to the TGA plot, the feature at (e) in Figure 3.3 must correspond to the formation of the more crystalline P3 phase.

If the heat treatment was continued to temperatures above 600 °C a new phase was seen to appear in the x-ray diffraction pattern. Heating to just 630 °C for one hour, Figure 3.3(f), was sufficient. This is shown more clearly in Figure 3.6, an enlargement of Figure 3.4. On heating to 900 °C this new phase dominates, Figure 3.4(g) and 3.6(g), and can be identified as O'3 α - $NaMnO_2$, which is a monoclinic distortion of the layered O3 structure. The peaks for this

phase are indicated by α . At 900 °C the peaks from Na_2CO_3 are no longer present, it has all reacted to form the stoichiometric distorted phase.

The importance of the solution based technique has been demonstrated. It yields homogeneous intermediate precursors which, even after precalcining at only 200 °C for 12 hours, 3.3(a) contain some crystallites already corresponding to the layered phase. As a result only a relatively low heating temperature at 600 °C is required, for just one hour, to prepare the desired layered crystalline phase.

3.2.4 CHARACTERISATION OF THE SODIUM PHASES $Na_xNi_yMn_{1-y}O_2$

3.2.4.1 INTRODUCTION

Having prepared the $y = 0.05$ phase, other $Na_xNi_yMn_{1-y}O_2$ in the range $0 < y < 0.3$ were prepared similarly. The samples were then characterised by powder x-ray diffraction. Elemental and oxidation state analysis (the latter obtained by $KMnO_4$ iron(II) ammonium sulphate titration) confirmed the compositions. The results from chemical analysis were also used in powder x-ray refinements for all y . SEM was used to investigate particle morphology.

3.2.4.2 X-RAY DIFFRACTION

Figure 3.7 shows powder x-ray diffraction patterns for the sodium precursors $Na_xNi_yMn_{1-y}O_2$ with nickel compositions in the range $0 < y < 0.3$. In spite of the moderate temperature of synthesis (600 °C), and the short reaction time (one hour), all samples up to $y = 0.2$ were obtained as single phase, fairly crystalline compounds. The peaks could be indexed using a hexagonal unit cell of the layered sodium phase. With all reflections fitting the criteria $-h + k + l = 3n$ the structure is rhombohedral with space group R3m.

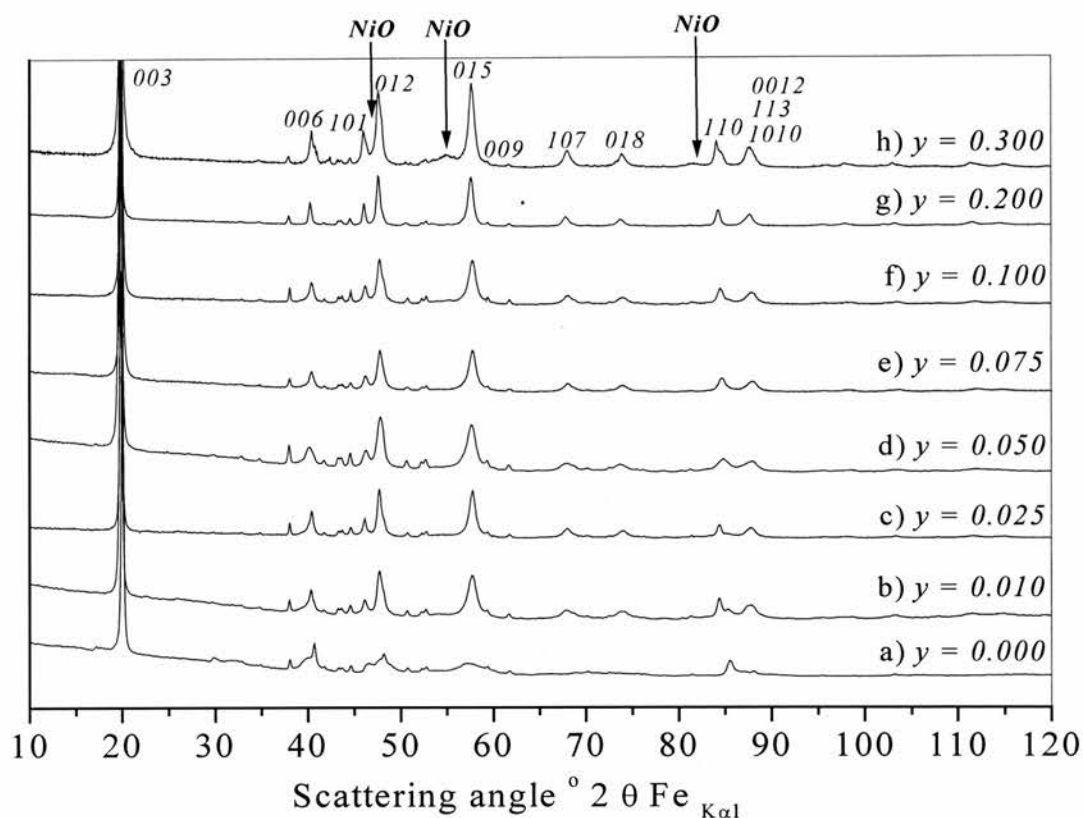


Figure 3.7 X-ray diffraction patterns as a function of nickel content for $Na_xNi_yMn_{1-y}O_2$

($0 < y < 0.3$) 'NiO' arrows indicate the theoretical positions of Nickel Oxide peaks at 47, 55 and 82°.

The unreacted sodium carbonate observed in these precursor materials can be washed out with water. Following washing the sample must be dried at 150 °C overnight to eliminate birnessite formation. Figure 3.8 is an x-ray diffraction pattern obtained from a washed material with $y = 0.075$, it shows no evidence of the sodium carbonate phase. The tick marks indicate where Na_2CO_3 would be observed.

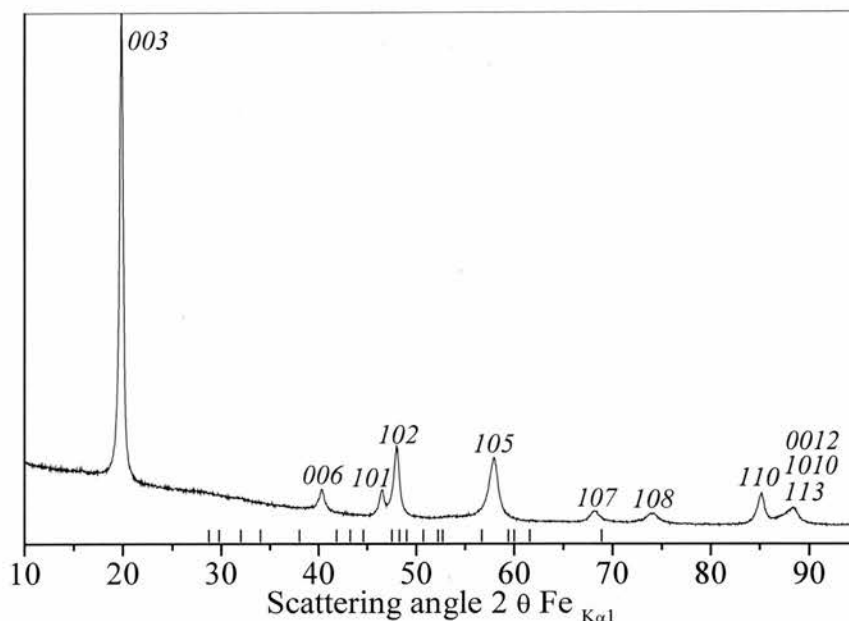


Figure 3.8 X-ray diffraction pattern of $Na_{0.51}Ni_{0.075}Mn_{0.925}O_2$ washed with water and dried. The tick marks indicate the position of Na_2CO_3 peaks.

Layered, stoichiometric $NaMnO_2$ has a monoclinic unit cell (space group $C2/m$) whereas the x-ray patterns shown in Figure 3.7 are rhombohedral ($R3m$) with $P3$ structure. The higher crystal symmetry of these new materials is due to the sodium deficiency, Na_xMnO_2 , leading to an increased manganese oxidation state and therefore a reduced concentration of high-spin, Jahn-Teller active trivalent Mn ($t_2^3 e^1$) ions. The Jahn-Teller distortion of the octahedral Mn environment in $NaMnO_2$ is a local effect and whether it results in a macroscopic deformation of the unit cell depends on the interaction of neighbouring Jahn-Teller active sites, the temperature and the concentration of Jahn-Teller ions. A cooperative distortion typically occurs at a *ca.* 50% occupancy of the transition metal octahedral sites by Mn^{3+} . In $Na_xMn_x^{3+}Mn_{1-x}^{4+}O_2$ this would correspond to $x < 0.5$ to suppress the distortion. Chemical composition and manganese oxidation state analysis will show the exact proportion of Mn^{3+} ions in these materials.

3.2.4.3 NICKEL OXIDE IMPURITY

X-ray diffraction reveals that the composition $y = 0.3$ contains a nickel oxide impurity. The most intense peaks of this impurity phase are observed at $2\theta = 47, 55$ and 82° , (indicated in figure 3.7(h) by 'NiO' labels). The standard x-ray diffraction pattern of nickel oxide is presented in Figure 3.8 by the thin dotted line. Figure 3.9 shows the presence of nickel oxide in an early sample with $y = 0.2$ (thin line, Figure 3.9) where the Ni acetate was dissolved in cold water. Preparation of a 20% Ni doped material using nitrates as starting materials was later performed in an attempt to reduce the amount of NiO but there was no improvement. Finally it was found that dissolution of the acetates at $80^\circ C$ resulted in a material with no nickel oxide impurity observable by x-ray diffraction, shown by large dots in Figure 3.9.

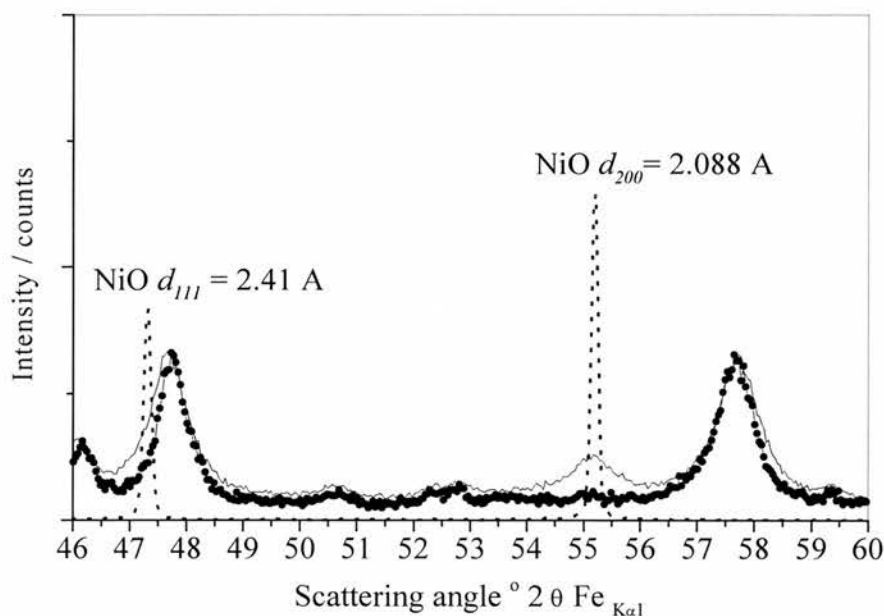


Figure 3.9 Powder X-ray diffraction patterns showing the elimination of NiO in $NaNi_{0.2}Mn_{0.8}O_2$. — acetates dissolved at $20^\circ C$, —●— acetates dissolved at $80^\circ C$, and ... standard NiO pattern.

3.2.4.4 CHEMICAL ANALYSIS

Chemical analysis provides confirmation of the stoichiometry, as well as the oxidation state of manganese. The proportion of Mn^{3+} and Mn^{4+} can also therefore be calculated, assuming that nickel exists in the divalent state for our samples, (see section 3.3.3.2). Two runs were performed for each sample and the results averaged. Chemical analysis for sodium was carried out by flame emission, and for manganese and nickel by atomic absorption spectroscopy. Oxidation states for manganese were obtained by $KMnO_4/Fe(II)$ ammonium sulphate titration. See chapter two for experimental details.

The ratio of sodium to transition metal in the starting materials was always 1:1, yet x-ray diffraction patterns of all the products clearly indicate unreacted Na_2CO_3 (Figures 3.5 and 3.7). As a result, the Na detected by chemical analysis does not all belong to the $Na_xNi_yMn_{1-y}O_2$ phase, some will be due to excess sodium carbonate. Using $y = 0.075$ as an example, a total sodium analysis of this sample detected $x = 0.73$, (Table 3.3(a)) indicating that some has been lost during heating. To deduce the amount of the remaining sodium that belongs to the layered phase, carbon analysis was performed on the same material. From the amount of carbon detected, the exact amount of sodium due to Na_2CO_3 can be deducted from the total sodium content to give a true sodium content. In this case the amount of sodium in the layered phase was found to be $Na_{0.42}$, assuming all carbon is due to Na_2CO_3 , (Table 3.3(b)).

$Na_xNi_{0.075}Mn_{0.925}O_2$	Sodium content x
(a) Na analysis (total, as prepared Figure 4.7(e))	$Na_{0.73}$
(b) Taking into account Na_2CO_3 after C analysis	$Na_{0.42}$

Table 3.3 Sodium content in $Na_xNi_{0.075}Mn_{0.925}O_2$ by different methods.

Detailed chemical analysis of the sodium phases for $0.025 < y < 0.2$ are presented in Table 3.4.

The results reveal vacancies on the transition metal sites, as well as a large number of vacancies on the alkali metal (A) sites. To satisfy the electroneutrality condition the equivalent number of Mn^{4+} ions must exist. The solid solution mechanism requires the replacement of $2Mn^{3+}$ by a Mn^{4+} and a Ni^{2+} ion and hence an increase in manganese oxidation state with increase in Ni content is expected. The results in Table 3.4 do not display a clear trend illustrating this. However, the presence of vacancies on the sodium sites as well as dopant ions substituting for Mn has conspired to reduce the occupancy of the octahedral sites by Mn^{3+} to a level where they can no longer promote a Jahn Teller distortion. This is in agreement with the lack of distortion in the x-ray patterns of Figure 3.7.

y	Chemical analysis	Mn OS	Mn^{3+} occupancy	% of TM vac	% of A vac
0.000	$Na_{0.66}[]_{0.34}\{Mn_{0.902}[]_{0.098}\}O_2$	3.71	26.8 %	10%	34 %
0.025	$Na_{0.42}[]_{0.48}\{Mn_{0.926}Ni_{0.024}[]_{0.050}\}O_2$	3.75	23.2 %	5 %	48 %
0.050	$Na_{0.46}[]_{0.54}\{Mn_{0.950}Ni_{0.044}[]_{0.010}\}O_2$	3.63	34.8 %	1 %	54 %
0.075	$Na_{0.42}[]_{0.58}\{Mn_{0.894}Ni_{0.077}[]_{0.028}\}O_2$	3.83	15.4 %	3 %	58 %
0.100	$Na_{0.47}[]_{0.53}\{Mn_{0.890}Ni_{0.100}[]_{0.010}\}O_2$	3.72	23.0 %	1 %	53 %
0.200	$Na_{0.45}[]_{0.55}\{Mn_{0.800}Ni_{0.195}[]_{0.010}\}O_2$	3.84	12.0 %	1 %	55 %

Table 3.4 Chemical analysis for layered sodium manganese oxide doped with Ni. Na_2CO_3 content determined by carbon analysis, thereby allowing the amount of Na_2CO_3 and Na in the main phase to be calculated.

3.2.4.5 RIETVELD REFINEMENT AND LATTICE PARAMETERS

Crystallographic lattice parameters were obtained by fitting the x-ray diffraction patterns of Figure 3.7 to a two phase model comprising an R3m layered phase and reflections associated with unreacted sodium carbonate using the GSAS suite of programs.⁵ Table 3.5 shows the crystallographic details, used to initiate each refinement, and Table 3.6 shows the crystallographic details for sodium carbonate. The material with $y = 0.3$ was fitted to a three phase model including NiO, Table 3.7.

In refining the data the lattice constants a and c , the z coordinate of the O1, O2 and Na sites were allowed to vary, as were the five thermal parameters and the phase fractions. The sodium and transition metal ion site occupancies were fixed at the values obtained from chemical analysis where data were available. Parameters describing the background function and the variation of the halfwidth of the pseudo Voigt peaks with scattering angle were also refined for all phases. A calculated pattern assuming the layered structure and the difference between calculated and observed patterns is given in Figure 3.10 for the sample $Na_xNi_{0.2}Mn_{0.8}O_2$. The lattice parameters were obtained in this way for all y and the results are presented in Table 3.8, and as a plot in Figure 3.11.

The presence of vacancies on both cation sites helps to explain the differences observed between the simulated model and the x-ray patterns of the sodium phases, (Figure 3.5). For example the reduced occupancies reduce the intensity of the 101 and 104 reflections.

Atom	Wyckoff symbol	x/a	y/b	z/c	Occupancy
Na	$3b$	0	0	0.8300	x
Ni	$3a$	0	0	0	y
Mn	$3a$	0	0	0	$1-y$
O1	$6c$	0	0	0.5996	1
O2	$6c$	0	0	0.3548	1

Table 3.5 Crystallographic details of the sodium phase, space group $R\bar{3}m$.

Atom	x/a	y/a	z/c	Occupancy
Na ₁	0.0	0.018	0	0.5
Na ₂	0.0	0.022	0.500	0.5
Na ₃	0.172	0.544	0.749	0.5
O1	0.123	0.255	0.314	0.5
O2	0.291	0.491	0.173	0.5
O3	0.079	0.676	0.255	0.5
C1	0.0	0.488	0.251	0.5

$$a = 8.907 \text{ \AA}, b = 5.24 \text{ \AA}, c = 6.04 \text{ \AA}, \beta = 101.2^\circ$$

Table 3.6 Crystallographic data for Na_2CO_3 monoclinic $C2/m^6$

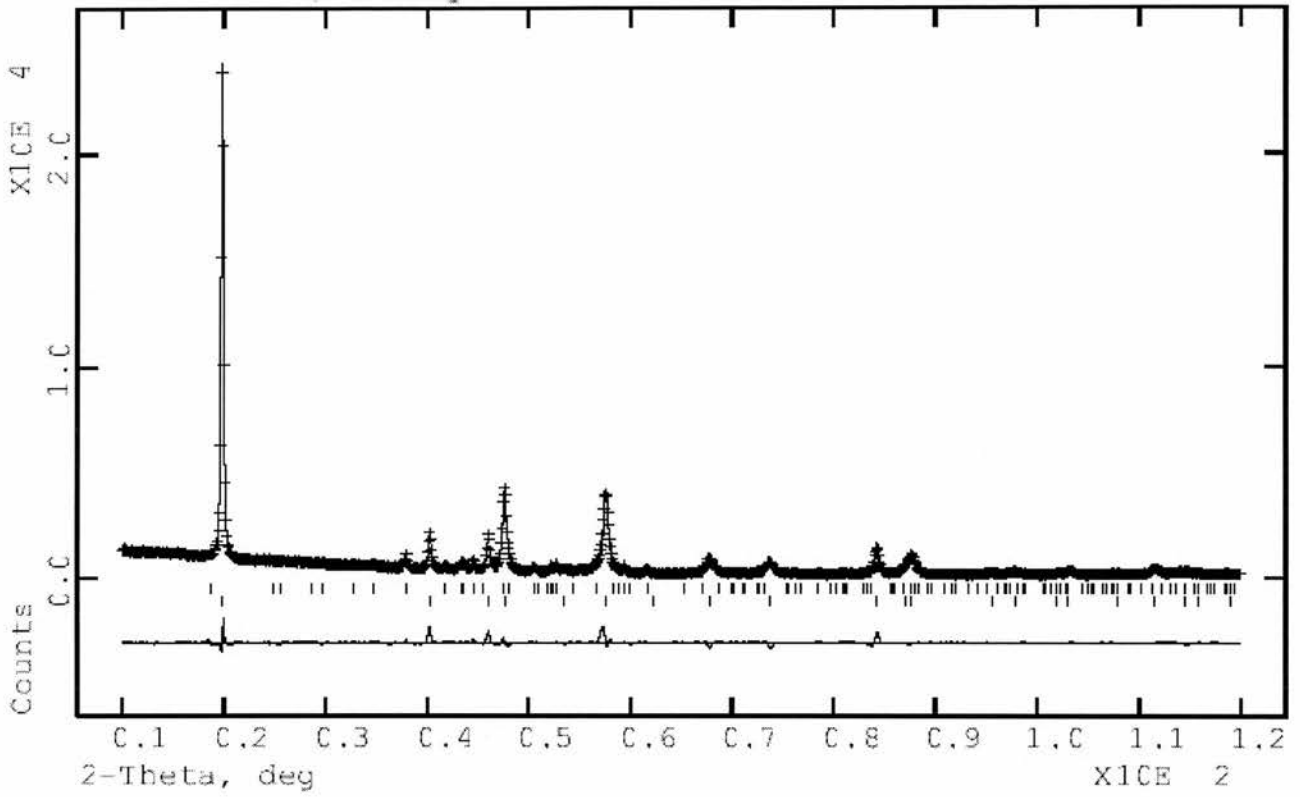


Figure 3.10 X-ray diffraction pattern of $Na_{0.42}Mn_{0.71}Ni_{0.017}O_2$ (crosses) and a calculated pattern (thin line). The difference plot is below. $\chi^2 = 5.2$. The tic marks show the allowed reflections for sodium carbonate and for the layered phase.

Atom	Wyckoff symbol	x/a	y/b	z/c	Occupancy
Ni		0	0	0	1
O		0.5	0.5	0.5	1

$a = 4.1769 \text{ \AA}$

Table 3.7 Crystallographic data for NiO, cubic, $Fm3m$.⁷

y	a (Å)	c (Å)
0.000	2.8784 ± 0.0005	16.748 ± 0.003
0.010	2.8809 ± 0.0006	16.840 ± 0.002
0.025	2.8711 ± 0.0003	16.685 ± 0.002
0.050	2.8774 ± 0.0006	16.701 ± 0.003
0.075	2.8781 ± 0.0008	16.777 ± 0.002
0.100	2.8803 ± 0.0009	16.785 ± 0.002
0.200	2.8869 ± 0.0002	16.853 ± 0.001
0.300	2.8858 ± 0.0002	16.800 ± 0.002

Table 3.8 Lattice parameters of layered $Na_xNi_yMn_{1-y}O_2$ from refinement of a two-phase model comprising a rhombohedral cell $R3m$ and Na_2CO_3 .

The a and c lattice parameters are presented in Figure 3.11 and show no clear trend with nickel content. The a lattice parameter lies in the basal plane of the layered structure and is particularly sensitive to changes in the average transition metal to oxygen bond length. The average distance would be expected to shorten when the average valence state of manganese increases, *i.e.* when the average radii shrink. a is not seen to vary with y because substitution of Mn^{+3} , (HS d^4 , $r = 0.645$ Å), with Ni^{+2} , (d^8 , $r = 0.69$ Å), and Mn^{+4} , ($3d^3$, $r = 0.53$ Å), results in an average radii of 0.61, this is very similar to the radius of Mn^{+3} at 0.645.⁸

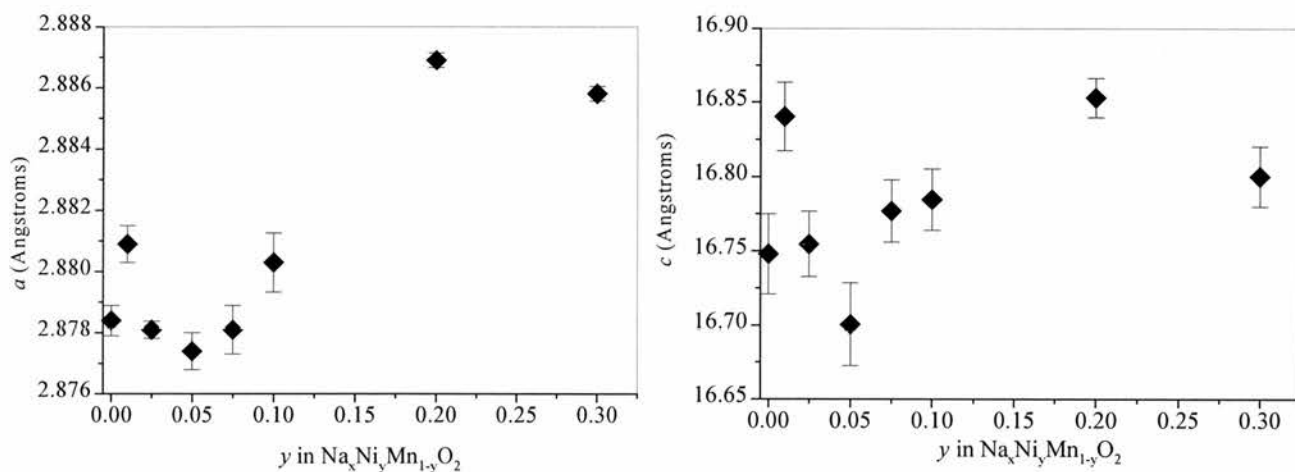


Figure 3.11 Plots of lattice parameters from Rietveld refinement for $Na_xNi_yMn_{1-y}O_2$ prepared with different y contents.

3.2.4.6 PARTICLE MORPHOLOGY

In order to investigate the particle morphology, scanning electron micrographs (SEM) were obtained from various samples. Figure 3.12 is the micrograph of the sample $Na_{0.42}Ni_{0.077}Mn_{0.894}O_2$, and as observed in x-ray diffraction patterns, Na_2CO_3 is also present. Particles are irregularly shaped and consist of porous nanocrystalline agglomerates. There is a large agglomerate size distribution, the average agglomerate size is between 10 and 100 μm .

Section 3.2.4.2 mentioned the preparation of a sample using nitrates in an attempt to eliminate the NiO impurity problem. The material prepared by this method was identical by x-ray diffraction to the other sodium phases, yet SEM investigation shows a less porous morphology, (Figure 3.13) and is free from Na_2CO_3 .

3.2.5 CONCLUSIONS OF SODIUM PHASES

Comparison of x-ray diffraction patterns with a rhombohedral R3m model, showed that a layered sodium phase $Na_xNi_yMn_{1-y}O_2$ with P3 structure is formed at 600 °C in air. Quenching from this temperature after one hour is critical to the success of the synthesis because at higher temperatures the P3 phase is unstable. For $y > 0.2$ a NiO impurity was present which gives the limit of the solid solution. It was possible to eliminate the NiO impurity by stirring the acetates at 80 °C prior to rotary evaporation of the acetate solution. Chemical analysis revealed the existence of sodium and transition metal vacancies, about 50 % and 4 % respectively. The lattice parameters of $Na_xNi_yMn_{1-y}O_2$ did not change consistently with nickel content, $a \approx 2.88 \text{ \AA}$ and $c \approx 16.80 \text{ \AA}$. This is due to the invariance of the average transition metal radius on substitution of $2Mn^{3+}$ with a Ni^{2+} and a Mn^{4+} , (0.645 \AA vs. 0.61 \AA).

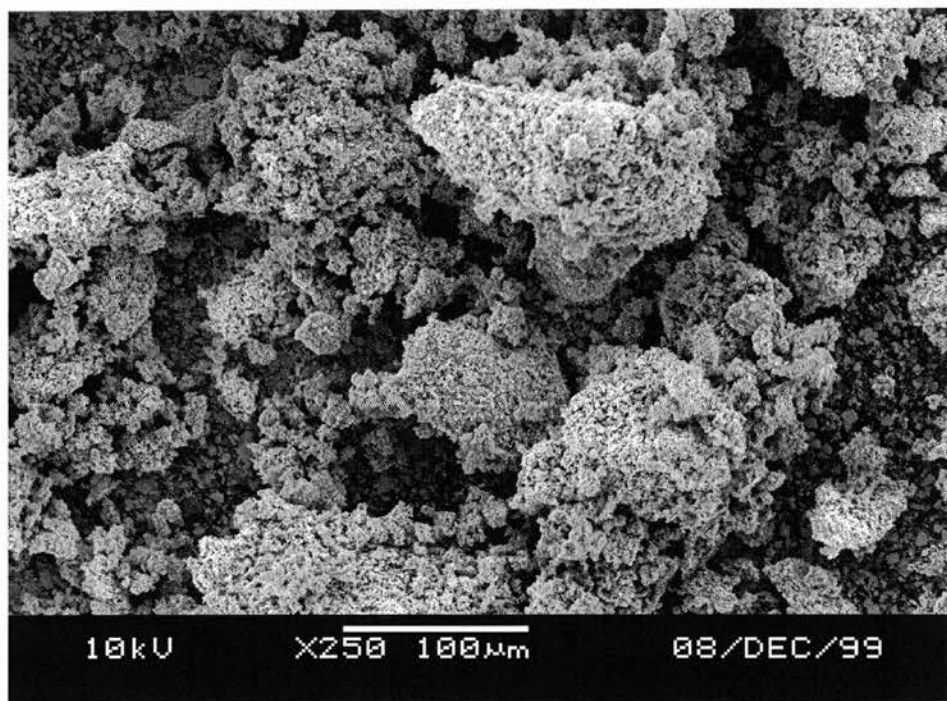


Figure 3.12 $Na_xNi_{0.075}Mn_{0.925}O_2$ prepared at 600 °C and containing residual sodium carbonate.

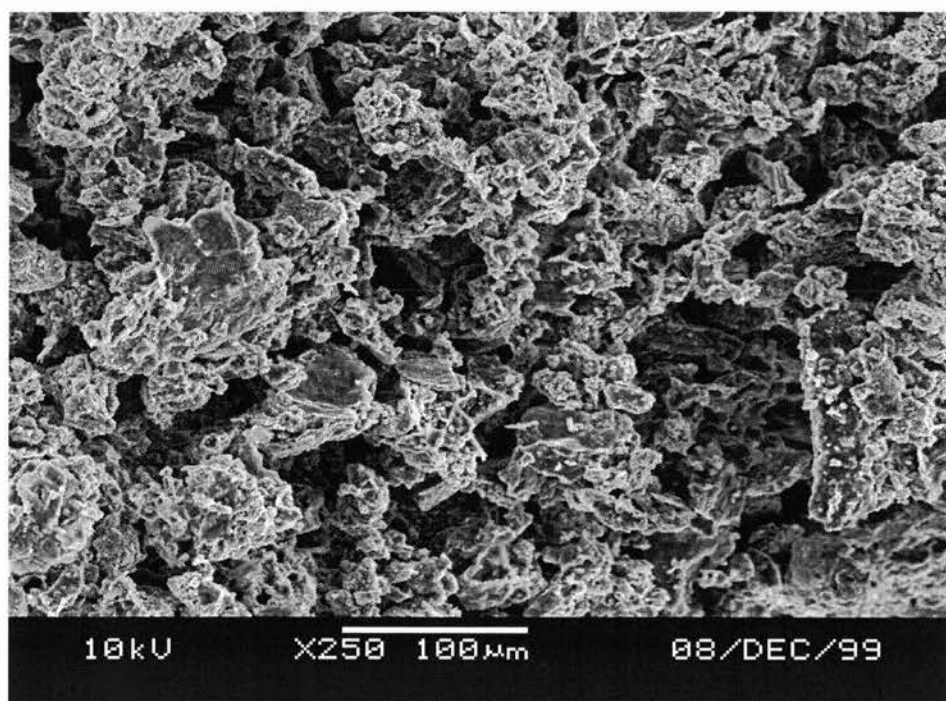


Figure 3.13 $Na_xNi_{0.2}Mn_{0.8}O_2$ prepared at 600 °C and containing residual sodium nitrate.

3.3 LITHIUM PHASES $Li_xNi_yMn_{1-y}O_2$

3.3.1 INTRODUCTION

The preparation of nickel doped sodium manganese oxide resulted in a P3-type $Na_xNi_yMn_{1-y}O_2$ layered phase for $0 < y < 0.2$ at 600 °C. The Na-O bonds are relatively weak compared to those in the MO_2 sheets and so allow easy slab gliding. Consequently it is possible to exchange the sodium ions for lithium even at room temperature while the structure of the MO_2 sheets will remain essentially unchanged. Lithium prefers octahedral sites and so a shift from P3 to O3 during ion exchange is favourable. This phase change is depicted in Figure 3.14. Displayed are two MO_2 layers above and below an alkali metal layer. In the original P3 structure the oxygen positions either side of the Na are in orientation B. The O3 structure is achieved by gliding of the upper layer, M glide from orientation a to b, perpendicular to the 110 direction of the hexagonal cell. This gliding makes an octahedral site for lithium. As a result the ion exchange of P3 $Na_xNi_yMn_{1-y}O_2$ produces O3 $Li_xNi_yMn_{1-y}O_2$.

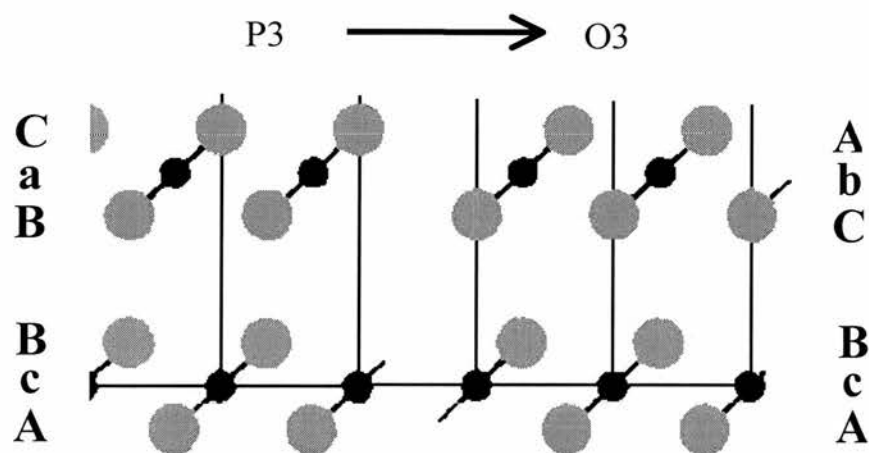


Figure 3.14 Layered structures consisting of rigid MO_2 sheets viewed from the 110 direction

The $Li_xNi_yMn_{1-y}O_2$ is a metastable phase, which cannot be directly obtained from classical solid state chemistry, only by ion exchange. Preparing a metastable phase by ion exchange requires that the temperature be sufficiently high to allow a fast ion exchange whilst still being

sufficiently low to prevent the phase transition to the equilibrium phase. It is well known that the cubic spinel $LiMn_2O_4$ structure is thermodynamically favoured in oxides with Li:Mn ratios close to 1:2. Only the migration of $\frac{1}{4}$ of the manganese ions into the octahedral lithium sites is required since the oxygen lattice in layered Li_xMnO_2 and cubic spinel $LiMn_2O_4$ is identical. Attempts to form the lithium phase by exchange in molten salts, such as $LiNO_3/LiCl$ proved unsuccessful,⁵ as the temperature was too high (300 °C) and caused a collapse of the layered structure to the stable spinel structure.

Figures 3.15(a) and (b) show how the x-ray diffraction patterns are indistinguishable by diffraction techniques for a cubic spinel $LiMn_2O_4$ structure and a layered rhombohedral structure with ideal hexagonal close packed anions. An undistorted O3 structure has a c/a ratio of $\sqrt{24} \approx 4.9$.^{9,10}

A layered material with a lattice distortion along the c direction can be seen in Figure 3.15(c). The distortion can be measured by considering the c/a ratio and the main difference is in the positions and relative intensities of peaks in the 2θ 80° to 90° range. The distorted layered phase exhibits (018) and (110) peaks at 82.3° and 84.9° respectively. The crystallographic parameters for Li_xMnO_2 are shown in Table 3.9.

Atom	Wyckoff symbol	X/a	y/b	z/c	Occupancy
Li	$3b$	0.0	0.0	0.5	x
Mn	$3a$	0.0	0.0	0.0	1
O	$6c$	0.0	0.0	0.25	1

Table 3.9 Crystallographic details of the layered lithium phase, Li_xMnO_2 space group $R-3m$.

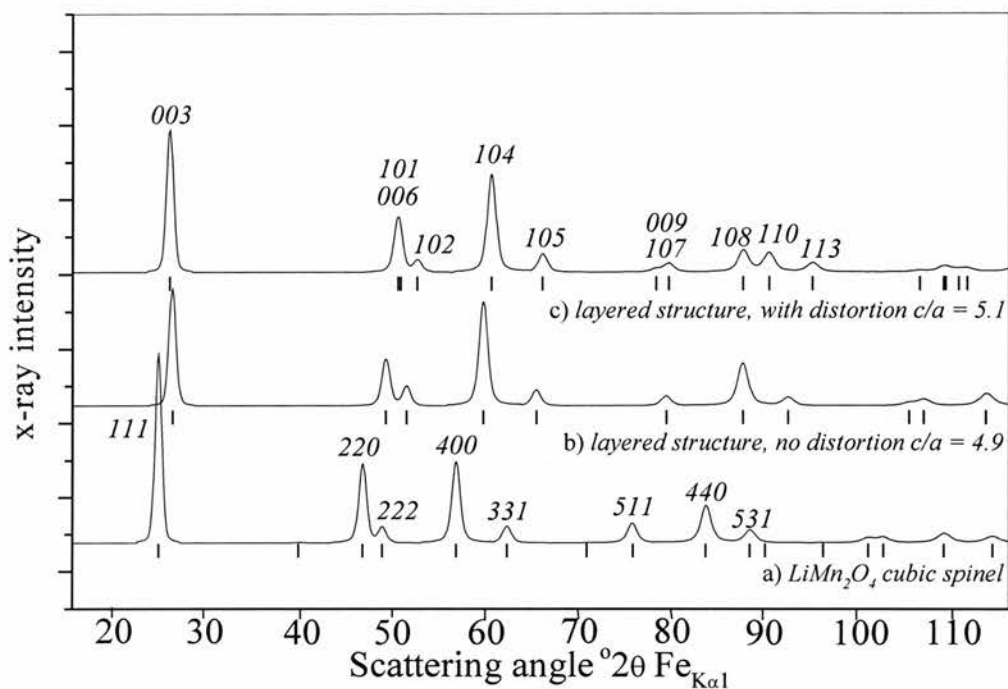
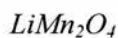


Figure 3.15 Simulated powder x-ray diffraction patterns for layered Li_xMnO_2 and spinel



3.3.2 ION EXCHANGE OF $Na_xNi_yMn_{1-y}O_2$

Ion exchange of the sodium phases $Na_xNi_yMn_{1-y}O_2$ ($0 < y < 0.2$) in an excess of LiBr was made under three different conditions.

- i) Ion exchange by stirring in ethanol at room temperature (25 °C) for one week.
- ii) Reflux for 8 hours in ethanol (78 °C)
- iii) Reflux for 8 hours in hexanol (156 °C)

Following ion exchange the product was filtered under suction while still warm, washed with ethanol and water and dried at 70 °C. The experimental details are given in chapter two.

3.3.3 CHARACTERISATION OF THE LITHIUM PHASES $Li_xNi_yMn_{1-y}O_2$

3.3.3.1 INTRODUCTION

In order to characterise the physical and chemical properties of the lithiated materials the experimental techniques of x-ray photoelectron spectroscopy (XPS), x-ray diffraction, chemical analysis, Scanning electron microscopy (SEM), and oxidation state analysis were used. Characterisation by electrochemical methods will be described in Chapter 4.

3.3.3.2 XPS MEASUREMENTS

XPS measurements were conducted to obtain information on the nickel valance state. An XPS measurement on a non-stoichiometric nickel oxide ($Ni_{1-x}O$) was performed to provide a standard for both Ni^{2+} and Ni^{3+} , (Figure 3.16). Figure 3.16 shows the two peaks observed in the Ni ($2p_{3/2}$) region corresponding to Ni^{2+} and Ni^{3+} , the binding energy values obtained are 864.9 and 866.8 eV respectively. For $Ni_{1-x}O$ the peak in the O (1S) region had a binding energy value of 540.2 eV. These results are listed in Table 3.10.

The Ni ($2p_{3/2}$) emission spectrum from $LiNi_{0.2}Mn_{0.8}O_2$ prepared by hexanol reflux is shown in Figure 3.17. It shows one sharp peak at low binding energy, (861.3 eV), and an associated broad satellite peak (867.8 eV). Compared to $Ni_{1-x}O$, the binding energy value for the $2p_{3/2}$ electron is shifted to a lower value, this might be caused by an interaction between nickel and manganese that leads to a shift of the Ni ($2p_{3/2}$) electron to lower values.

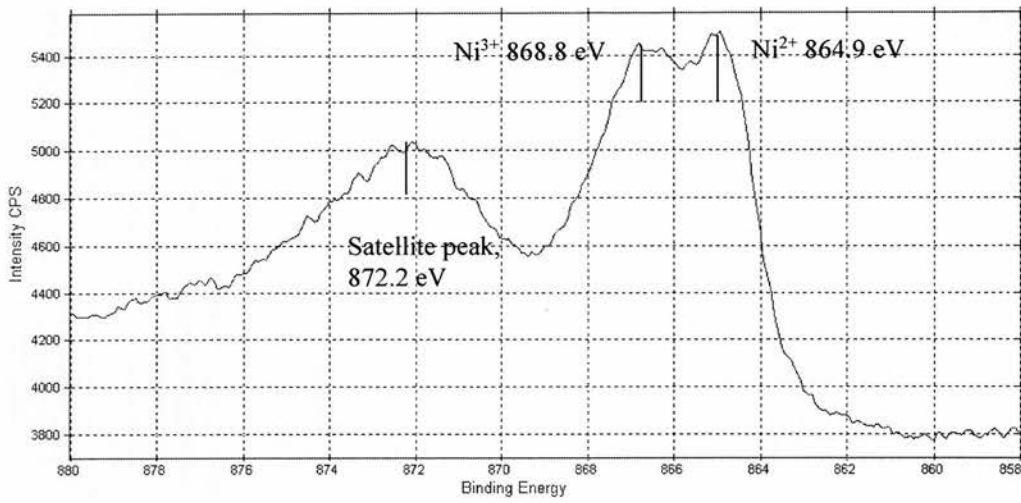


Figure 3.16 XPS Ni 2p_{3/2} emission spectra of a Ni_{1-x}O

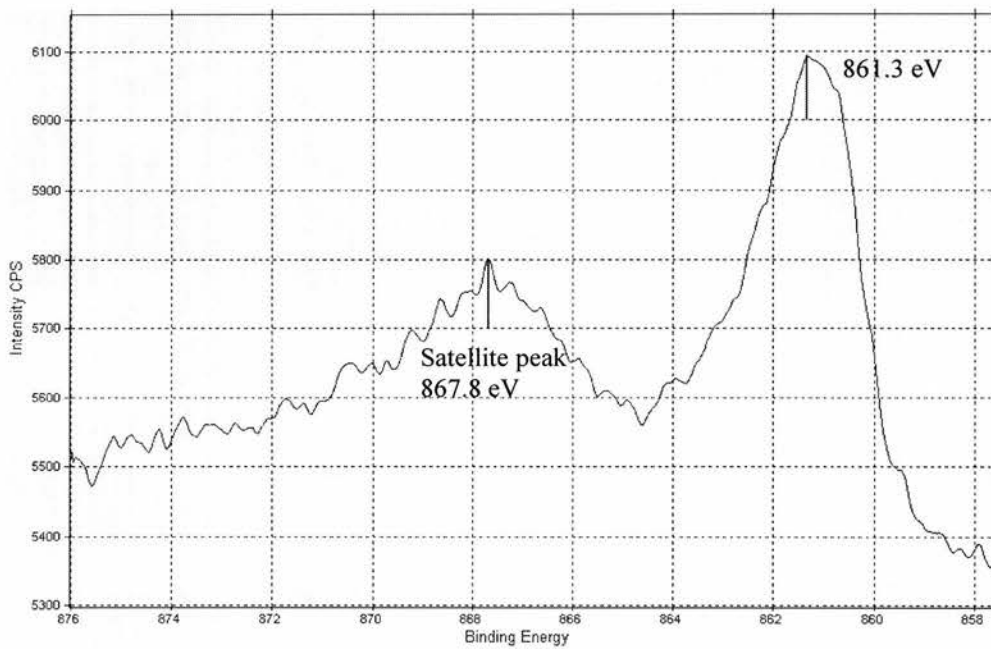


Figure 3.17 XPS Ni (2p_{3/2}) emission spectra of LiNi_{0.2}Mn_{0.8}O₂

The binding energy of electrons from the Ni (2p_{3/2}) level must be measured relative to that of electrons from the O (1s) level, to enable comparison with the energy levels in Ni_{1-x}O. The spectrum for LiNi_{0.2}Mn_{0.8}O₂ displayed a peak in the O (1s) region with a binding energy value of 536.6 eV. The results from XPS characterisation of LiNi_{0.2}Mn_{0.8}O₂ are given in Table 3.10.

For $LiNi_{0.2}Mn_{0.8}O_2$ this difference is 324.7 eV and for $Ni_{1-x}O$ the 864.9 eV energy corresponding to Ni^{2+} is exactly 324.7 eV above the O 1s level at 540.2 eV. This is taken as evidence that nickel is divalent in all these materials and therefore they can be written as $Li^+_x(Ni^{2+}_yMn^{3+}_{x-2y}Mn^{4+}_{1+y-x})O_2$ implying the following solid solution mechanism as nickel increases: $2Mn^{3+} \rightarrow Mn^{4+} + Ni^{2+}$. These results are in agreement with those reported by Neudecker *et. al.*¹¹ Whose XPS measurements on $Li_x(Mn_yNi_{1-y})_{2-x}O_2$ gave evidence for Mn^{4+} and Mn^{3+} , but no indication was found for Ni valance states other than Ni^{2+} . Identical binding energies were obtained for all y in $LiNi_yMn_{1-y}O_2$.

Energy state	Binding energy (eV)		
	$Ni_{1-x}O$		$LiNi_yMn_{1-y}O_2$
	Ni^{2+}	Ni^{3+}	
Ni ($2p_{3/2}$)	864.9	866.8	861.3
O (1s)	540.2		536.6
Energy difference referenced to O(1s)	324.7	326.6	324.7

Table 3.10 Electron binding energies obtained for the oxides $LiNi_yMn_{1-y}O_2$ and $Ni_{1-x}O$.

Ni^{2+} has an exchange splitting which is smaller than the crystal field splitting and is in the low spin configuration.¹²

3.3.3.3 X-RAY DIFFRACTION

The compositions $Li_xNi_yMn_{1-y}O_2$ with various y were refluxed under the conditions shown in Table 3.11. In most cases there were several batches of each material made.

Ni content y	Ethanol 25 °C	Ethanol 78 °C	Hexanol 156 °C
0.000	✓	✓	✓
0.001	✗	✓	✓
0.025	✓	✓	✓
0.050	✓	✓	✓
0.075	✓	✓	✓
0.100	✓	✓	✓
0.200	✓	✓	✓

Table 3.11 Sample preparation, Ni content y in $Li_xNi_yMn_{1-y}O_2$ and ion exchange conditions.

The x-ray diffraction patterns from materials ion exchanged in hexanol, ethanol at 78 °C and ethanol at 25 °C are presented in Figures 3.18, 3.19 and 3.20 respectively. They show no evidence of the sodium precursor phase, an indication that the ion exchange has essentially gone to completion. The x-ray diffraction patterns also show that the materials are free from any lithium carbonate impurity, which can occur if the materials are not sufficiently washed.

Peak positions in the x-ray diffraction patterns agree with the peaks in the model of Figure 3.15. The patterns present broader peaks compared to the sodium precursor phases indicating that they are less crystalline and more disordered. Under all ion exchange conditions reported here, the x-ray diffraction data for the lithium phases may be indexed on a rhombohedral unit cell in space group R-3m, typical of phases with the O3 α -NaFeO₂ structure type. The first diffraction line, $d_{003} \approx 4.8$ Å indicates that the structure has changed to a smaller interslab distance from that of the precursor sodium phases where $d_{003} \approx 5.6$ Å.

Comparing Figures 3.18 and 3.19 it can be seen how the degree of the splitting of the peak pair (018/110) increases as the temperature of ion exchange decreases.

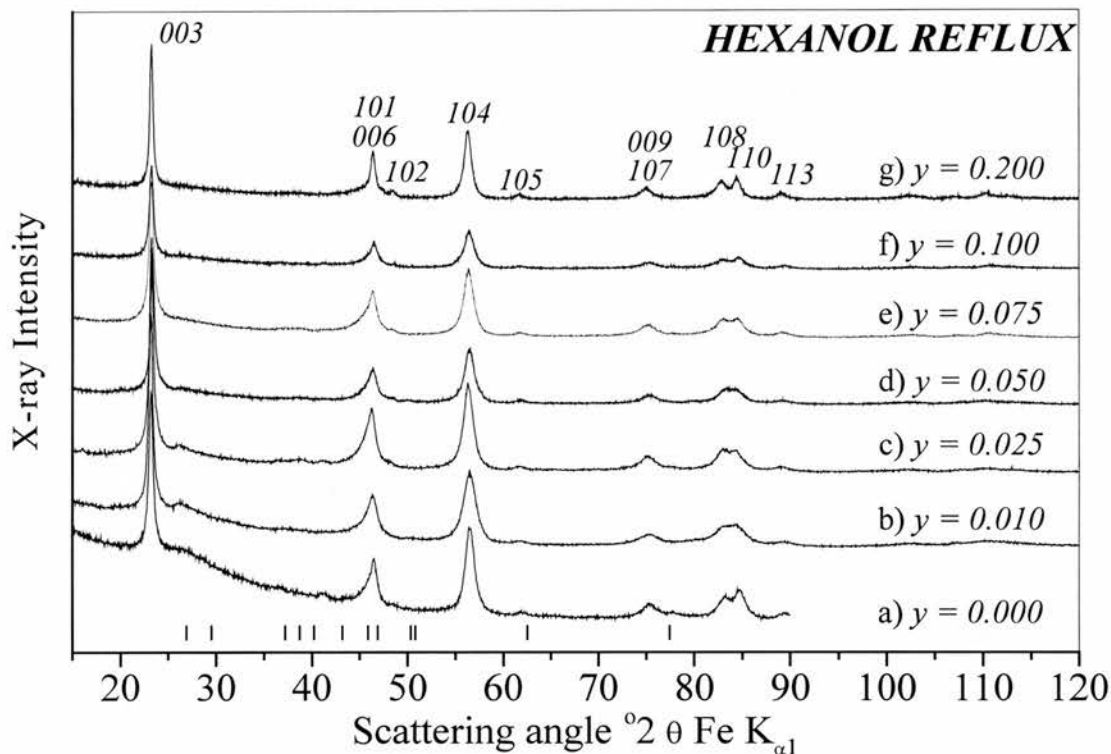


Figure 3.18 X-ray diffraction patterns of $\text{Li}_x\text{Ni}_y\text{Mn}_{1-y}\text{O}_2$ refluxed in hexanol at 156°C for 8 hours. The tic marks indicate where peaks due to Li_2CO_3 would occur¹³.

The weak broad peaks seen near 27° in some of the samples coincides with the position of a strong peak from Li_2CO_3 but other strong peaks from this compound are missing suggesting it is absent. It is possible that this peak arises from partial ordering of the Ni and Mn on an in-plane superlattice as is found in the $\text{Li}_{1/3}\text{Mn}_{2/3}$ layers of Li_2MnO_3 . The peak position falls exactly where expected¹⁴ for such a superlattice, the peak is broad because only short-ranged correlations are present.

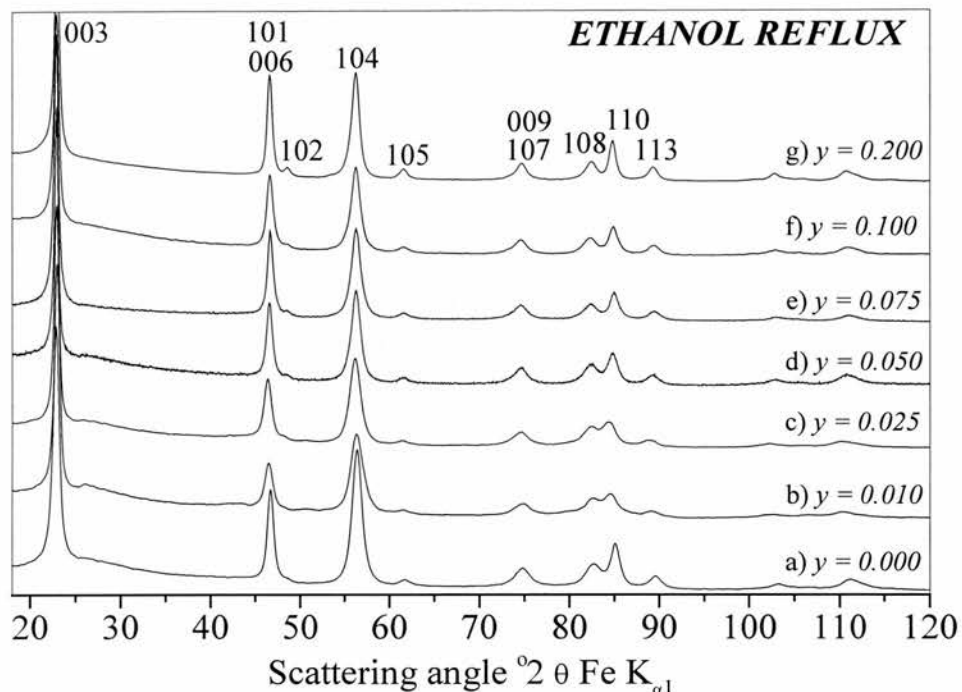


Figure 3.19 X-ray diffraction patterns of $Li_xNi_yMn_{1-y}O_2$ refluxed in ethanol at $78^\circ C$ for 8 hours.

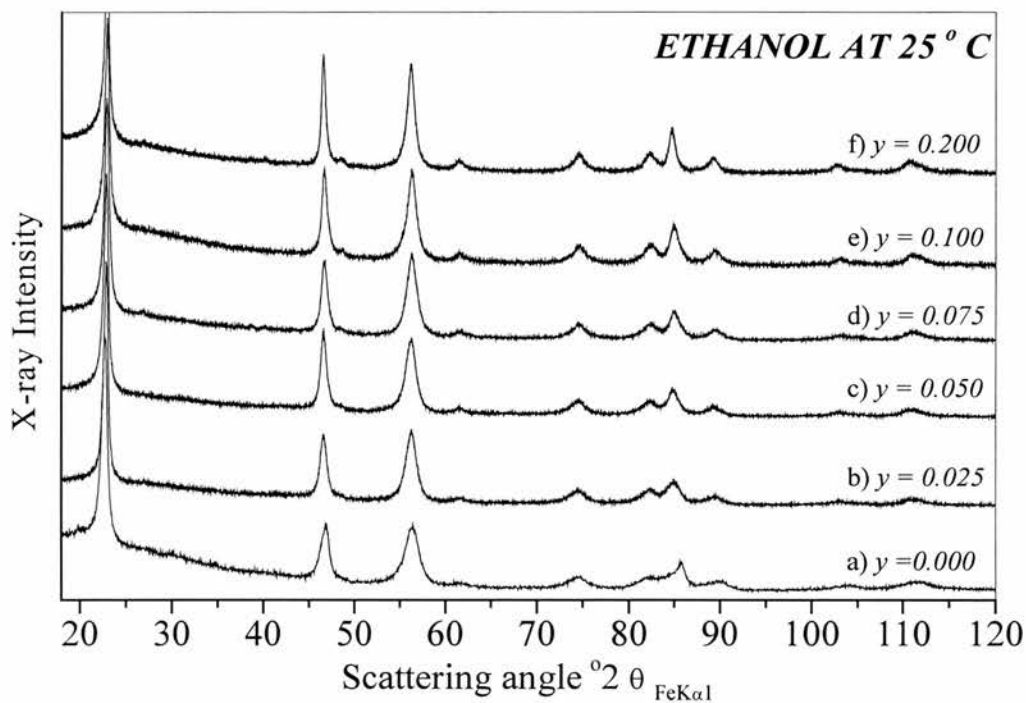


Figure 3.20 X-ray diffraction patterns of $Li_xNi_yMn_{1-y}O_2$ ion exchanged in ethanol at $25^\circ C$ for 1 week.

3.3.3.4 CHEMICAL ANALYSIS

Chemical analysis for lithium and sodium were carried out by flame emission, and for nickel and manganese by atomic absorption spectroscopy. The results from detailed chemical analysis on the ion exchanged materials are presented in Tables 3.12 to 3.14. The most important observations will be the manganese oxidation state, (Mn OS), reflecting the proportion of Mn^{3+} and the alkali, (A vac), and transition metal, (TM vac), vacancies.

The total alkali metal content A is significantly less than unity in all cases and this is consistent with the sodium deficiency in the sodium phases prior to ion exchange, (Table 3.4). The deficiency is carried through into the lithium phases on ion exchange. The remaining alkali metal vacancies are slightly more in number, (average 39 %), for materials prepared at the lower ion exchange temperatures of 25 °C and 78 °C, compared to those prepared at 156 °C (average 34 %). In all cases the total alkali metal content, A, is significantly higher ($0.57 < A < 0.69$) after the exchange than before where $A \approx 0.42$. The conditions are sufficiently reducing in all cases for LiBr in alcohol to act as an intercalating agent as well as a source for ion exchange¹⁵ and materials prepared at the highest ion exchange temperature have an increased lithium content. In addition, it can be seen that some sodium has remained after exchange, the amount is larger in the case of samples prepared in ethanol (4 %), than those prepared in hexanol (1 %).

Turning to the transition metal occupancies, in the case of the material prepared in hexanol, the Ni and Mn contents are close to those anticipated from the nominal composition and there are vacancies (< 2 %) on the transition metal sites. In contrast, the ethanol derived materials are somewhat transition metal deficient and as a result have significant vacancy concentrations on the transition metal sites (average 6 %). The increased number of alkali and TM metal vacancies for the lower temperature ion exchanges explains the significantly higher manganese

oxidation states displayed by these materials. (3.7 vs. 3.45 for materials ion exchanged in ethanol and hexanol respectively).

A summary of the general trends observed as the ion exchange conditions change from ethanol to hexanol preparation is: a decrease in residual sodium, manganese oxidation state and the numbers of alkali and transition metal vacancies, and an increase in lithium content.

Ni content y	Composition	Mn OS	Occupancy of TM sites (%)		TM vac (%)	A vac (%)
			Mn ³⁺	Mn ⁴⁺		
0.025	$Na_{0.01}Li_{0.643}[]_{0.338}\{Mn^{+3}_{0.486}Mn^{+4}_{0.470}Ni^{+2}_{0.025}[]_{0.019}\}O_2$	3.45	49	47	2	34
0.050	$Na_{0.01}Li_{0.652}[]_{0.338}\{Mn^{+3}_{0.478}Mn^{+4}_{0.452}Ni^{+2}_{0.048}[]_{0.022}\}O_2$	3.49	48	45	2	34
0.075	$Na_{0.01}Li_{0.650}[]_{0.340}\{Mn^{+3}_{0.490}Mn^{+4}_{0.430}Ni^{+2}_{0.073}[]_{0.007}\}O_2$	3.47	49	43	0	34
0.100	$Na_{0.01}Li_{0.676}[]_{0.314}\{Mn^{+3}_{0.570}Mn^{+4}_{0.353}Ni^{+2}_{0.096}[]_{0.000}\}O_2$	3.38	57	35	0	31
0.200	$Na_{0.02}Li_{0.643}[]_{0.337}\{Mn^{+3}_{0.443}Mn^{+4}_{0.405}Ni^{+2}_{0.194}[]_{0.042}\}O_2$	3.48	44	41	0	34

Table 3.12 Results from composition analysis of $Li_xNi_yMn_{1-y}O_2$ prepared in hexanol at 156 °C.

Ni content y	Composition	Mn OS	Occupancy of TM sites (%)		TM vac (%)	A vac (%)
			Mn ³⁺	Mn ⁴⁺		
0.000	$Na_{0.06}Li_{0.587}[]_{0.343}\{Mn^{3+}_{0.397}Mn^{4+}_{0.538}[]_{0.06}\}O_2$	3.58	40	54	7	34
0.025	$Na_{0.02}Li_{0.592}[]_{0.388}\{Mn^{+3}_{0.244}Mn^{+4}_{0.652}Ni^{+2}_{0.024}[]_{0.080}\}O_2$	3.75	24	65	8	39
0.050	$Na_{0.03}Li_{0.575}[]_{0.395}\{Mn^{+3}_{0.223}Mn^{+4}_{0.659}Ni^{+2}_{0.045}[]_{0.073}\}O_2$	3.75	22	66	7	40
0.075	$Na_{0.02}Li_{0.635}[]_{0.345}\{Mn^{+3}_{0.280}Mn^{+4}_{0.600}Ni^{+2}_{0.070}[]_{0.050}\}O_2$	3.69	28	60	5	38
0.100	$Na_{0.03}Li_{0.555}[]_{0.415}\{Mn^{+3}_{0.339}Mn^{+4}_{0.555}Ni^{+2}_{0.089}[]_{0.017}\}O_2$	3.62	34	56	2	42
0.020	$Na_{0.02}Li_{0.620}[]_{0.360}\{Mn^{+3}_{0.235}Mn^{+4}_{0.561}Ni^{+2}_{0.205}[]_{0.001}\}O_2$	3.71	24	56	0	36

Table 3.13 Results from composition analysis of $Li_xNi_yMn_{1-y}O_2$ prepared in ethanol at 78 °C.

Ni content y	Composition	Mn OS	Occupancy of TM sites (%)		TM vac (%)	A vac (%)
			Mn ³⁺	Mn ⁴⁺		
0.000	$Na_{0.07}Li_{0.534}[]_{0.398}\{Mn^{3+}_{0.394}Mn^{4+}_{0.554}[]_{0.05}\}O_2$	3.59	39	55	5	40
0.025	$Na_{0.05}Li_{0.571}[]_{0.383}\{Mn^{+3}_{0.357}Mn^{+4}_{0.566}Ni^{+2}_{0.024}[]_{0.053}\}O_2$	3.61	36	57	5	38
0.050	$Na_{0.06}Li_{0.510}[]_{0.427}\{Mn^{+3}_{0.307}Mn^{+4}_{0.602}Ni^{+2}_{0.049}[]_{0.042}\}O_2$	3.66	31	60	4	43
0.075	$Na_{0.04}Li_{0.570}[]_{0.390}\{Mn^{+3}_{0.234}Mn^{+4}_{0.639}Ni^{+2}_{0.067}[]_{0.060}\}O_2$	3.73	23	64	6	39
0.100	$Na_{0.03}Li_{0.583}[]_{0.388}\{Mn^{+3}_{0.246}Mn^{+4}_{0.617}Ni^{+2}_{0.091}[]_{0.046}\}O_2$	3.72	25	62	9	39
0.200	$Na_{0.04}Li_{0.639}[]_{0.325}\{Mn^{+3}_{0.127}Mn^{+4}_{0.639}Ni^{+2}_{0.194}[]_{0.040}\}O_2$	3.83	13	64	4	33

Table 3.14 Results from composition analysis of $Li_xNi_yMn_{1-y}O_2$ prepared in ethanol at 25 °C.

3.3.3.5 RIETVELD REFINEMENT

3.3.3.5.1 INTRODUCTION

All the Ni doped materials have been examined by x-ray diffraction and their lattice parameters refined. Neutron diffraction however, is a more superior technique, but only a limited number of Ni doped materials were analysed by neutron diffraction and submitted for refinement. Where possible the refined lattice parameters gained from both techniques will be compared.

3.3.3.5.2 X-RAY DIFFRACTION

X-ray diffraction patterns of the various $Li_xMn_{1-y}Ni_yO_2$ for $0 < y < 0.2$, were presented in Figures 3.19, 3.20 and 3.21 respectively. The layered α - $NaFeO_2$ structure of $LiCoO_2$ was used as the starting hypothesis for refinement by the Rietveld method. The structural parameters of the layered O3 structure are shown in Table 3.15, with oxygen atoms adopting a ccp arrangement. In this structure lithium and manganese ions are in fixed positions: Li (3b) [0, 0, 0.5], Mn/Ni (3a) [0, 0, 0], while oxygen ions occupy (6c) [0, 0, 0.25]. In refining the compounds the occupancies for all atoms were fixed at the values obtained from the chemical analysis. The lattice constants a and c , and the z coordinate of the O site were allowed to vary as were the four thermal parameters. Parameters describing the background function and the variation of the halfwidth of the pseudo-Voigt peaks with scattering angle were also refined. No account was taken of any transition metal vacancy ordering that may occur or any clustering of sodium ions with the vacancies. It would be difficult to refine such complex ordering.

The experimental and calculated x-ray diffraction pattern is given in Figure 3.21 for $Li_xNi_{0.05}Mn_{0.95}O_2$ formed by ion exchange in ethanol at 25 °C. Results for this material are presented in Table 3.16 and Table 3.18 presents the results from refining the lattice parameters for all y .

Atom	Wyckoff symbol	x/a	y/b	z/c	Occupancy
Li	$3b$	0	0	0.5	x
Ni	$3a$	0	0	0	y
Mn	$3a$	0	0	0	$1-y$
O	$6c$	0	0	0.25	1

Table 3.15 Crystallographic details of the lithium phase, space group $R-3m$

$a = 2.8651 (5) \text{ \AA}$, $c = 14.6879 (9) \text{ \AA}$; $\chi^2 = 14.1$					
Atom	Wyckoff symbol	x/a	y/b	z/c	Occupancy
Li/Na	$3b$	0.0	0.0	0.5	0.51/0.06
Mn/Ni	$3a$	0.0	0.0	0.0	0.91/0.05
O	$6c$	0.0	0.0	0.26279 (6)	1

Table 3.16 Results of Rietveld refinement of x-ray data assuming layered $R-3m$ for

$Li_xNi_{0.05}Mn_{0.95}O_2$ prepared in ethanol at 25 °C.

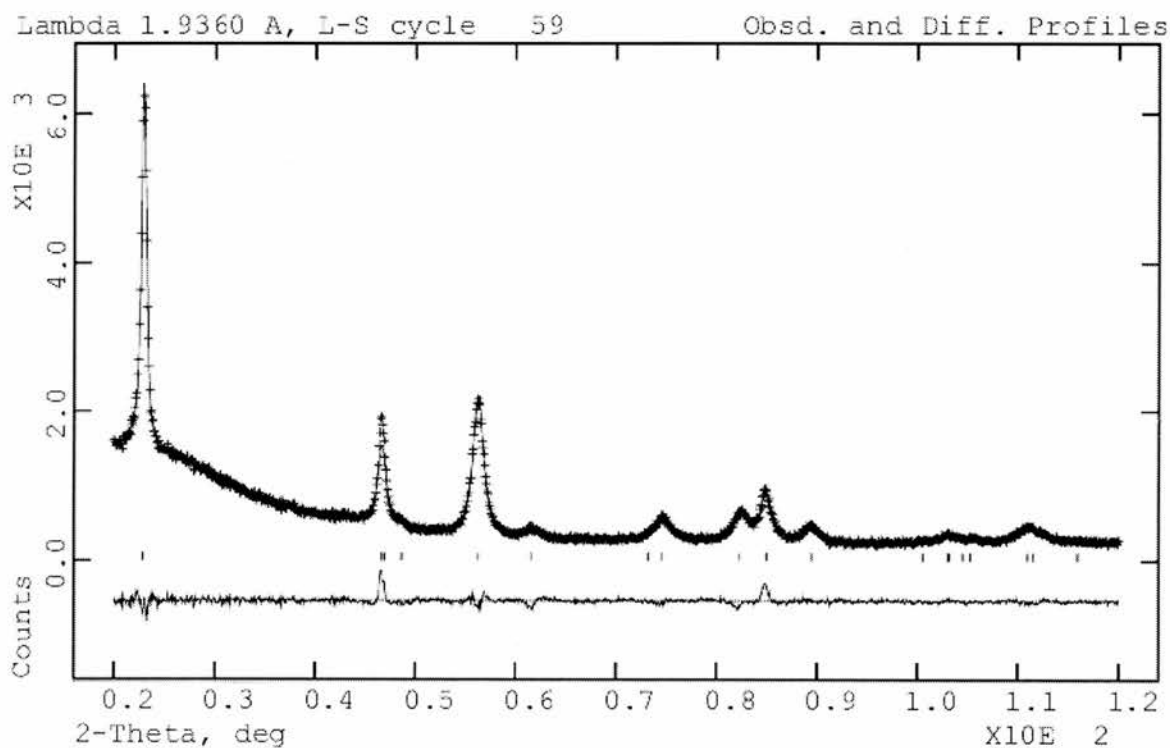


Figure 3.21 Comparison of the (+) experimental and (-) calculated x-ray diffraction patterns

for $Li_xNi_{0.05}Mn_{0.95}O_2$ ion exchanged in ethanol at 25 °C.

3.3.3.5.3 NEUTRON DIFFRACTION

The structure of materials with $y = 0.05$ was probed further by Rietveld refinement on neutron diffraction data. The experimental details are given in chapter two. The data for the 5 % nickel doped material ion exchanged under three different conditions is presented in Figure 3.22. A good fit to the data may be obtained based on the layered O3 structure, R-3m. The Rietveld refinement was carried out with the sodium and nickel contents fixed at the values obtained from the chemical analysis, and the lithium and manganese occupancies were allowed to vary freely. Crystallographic data and R factors are given in Table 3.17. It is evident that the refined lithium and transition metal vacancy contents are in good agreement with the chemical analysis. The lithium content refined by neutron diffraction is always appears slightly higher than from chemical analysis, this may be due to a small amount of Mn on the Li sites.

Atom	Wyckoff symbol	x/a	y/a	z/c	B_{iso}	Occupancy
a) $Li_xNi_{0.05}Mn_{0.95}O_2$ Hexanol 156 °C						
$a = 2.8822 (2) \text{ \AA}$, $c = 14.3666 (6) \text{ \AA}$; $R_{exp} = 1.0\%$, $R_{wp} = 3.5\%$, $R_p = 3.2\%$. $R_I = 4.1\%$.						
Li/Na	3b	0.0	0.0	0.5	1.5 (2)	0.64 (2)/0.01
Mn/Ni	3a	0.0	0.0	0.0	-	0.878/0.048 (2)
O ₁	6c	0.0	0.0	0.26184 (8)	-	1
Mn/Ni $B_{11} = B_{22} = 0.15 (7)$ $B_{33} = 0.5 (2)$ $B_{12} = 0.07 (4)$						
O ₁ $B_{11} = B_{22} = 1.06 (3)$ $B_{33} = 0.94 (5)$ $B_{12} = 0.53 (1)$						
b) $Li_xNi_{0.05}Mn_{0.95}O_2$ Ethanol 78 °C						
$a = 2.8666 (2) \text{ \AA}$, $c = 14.5940 (6) \text{ \AA}$; $R_{exp} = 1.1\%$, $R_{wp} = 2.1\%$, $R_p = 1.9\%$. $R_I = 1.8\%$.						
Li/Na	3b	0.0	0.0	0.5	0.55(14)	0.672 (13)/0.029
Mn/Ni	3a	0.0	0.0	0.0	-	0.843/0.045 (2)
O ₁	6c	0.0	0.0	0.26239 (6)	-	1
Mn/Ni $B_{11} = B_{22} = 0.19 (8)$ $B_{33} = 1.1 (2)$ $B_{12} = 0.10 (4)$						
O ₁ $B_{11} = B_{22} = 0.84 (2)$ $B_{33} = 1.07 (3)$ $B_{12} = 0.42 (1)$						
c) $Li_xNi_{0.05}Mn_{0.95}O_2$ Ethanol 25 °C						
$a = 2.8624 (2) \text{ \AA}$, $c = 14.6255 (6) \text{ \AA}$; $R_{exp} = 0.9\%$, $R_{wp} = 2.3\%$, $R_p = 1.9\%$. $R_I = 2.3\%$.						
Li/Na	3b	0.0	0.0	0.5	0.6 (2)	0.551 (14)/0.035
Mn/Ni	3a	0.0	0.0	0.0	-	0.873/0.046 (2)
O ₁	6c	0.0	0.0	0.26279 (6)	-	1
Mn/Ni $B_{11} = B_{22} = 0.15 (7)$ $B_{33} = 0.5 (2)$ $B_{12} = 0.07 (4)$						
O ₁ $B_{11} = B_{22} = 1.06 (3)$ $B_{33} = 0.94 (5)$ $B_{12} = 0.53 (1)$						

Table 3.17 Structural parameters obtained from neutron diffraction refinement of

$Li_xNi_{0.05}Mn_{0.95}O_2$ prepared at three different ion exchange temperatures.

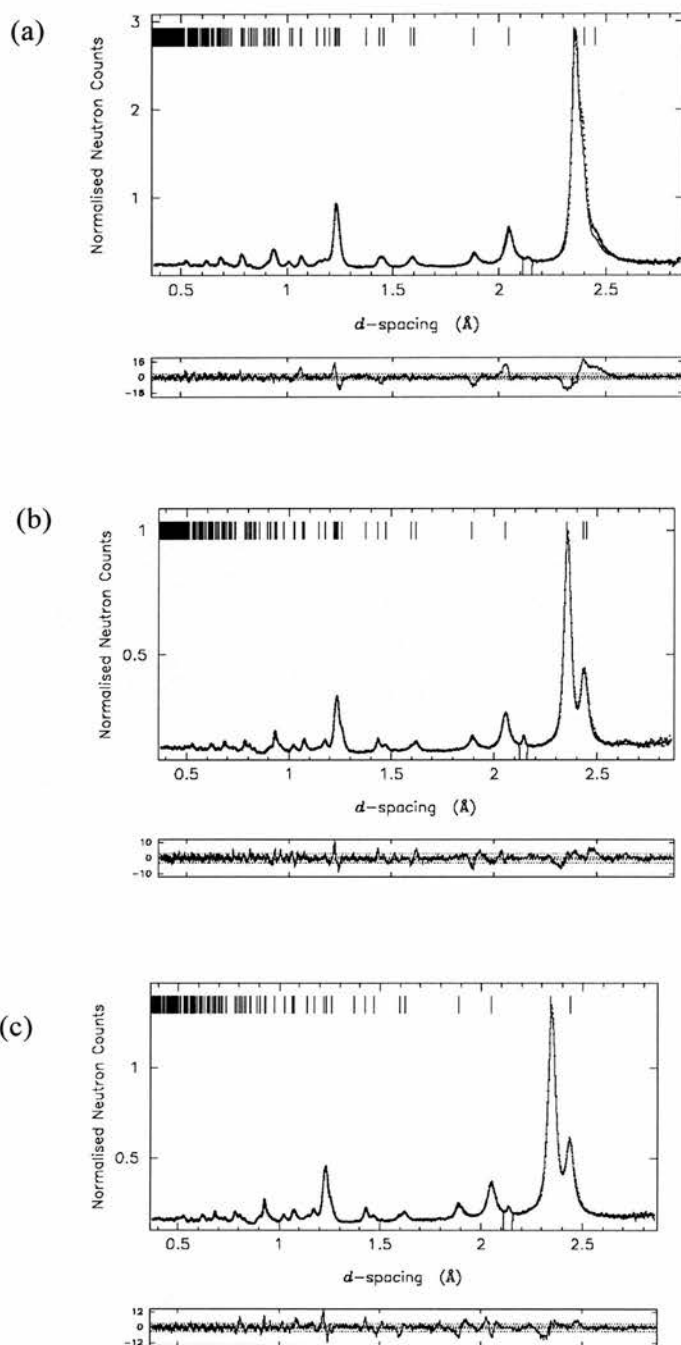


Figure 3.22 Powder neutron diffraction patterns for $Li_xNi_{0.05}Mn_{0.95}O_2$ prepared in a) hexanol 156 °C, b) ethanol 78 °C and c) ethanol at 25 °C. Dots = experimental data, solid line = best fit, lower curve = difference/e.s.d. Upper tick marks indicate position of reflections in $R-3m$.

3.3.3.6. LATTICE PARAMETERS

The lattice parameters and c/a ratios obtained from x-ray diffraction data refinement are presented in Table 3.18 and as plots in Figure 4.23. Black squares represent the materials prepared in ethanol at 25 °C, triangles the materials prepared by ethanol reflux and circles the materials prepared in hexanol. The lattice parameters for $y = 0.05$ obtained from neutron diffraction data are also presented in Figure 3.23, as open shapes, and are in good agreement with the lattice parameters derived from x-ray data. Companion batches were prepared for all compositions and the lattice parameters from x-ray data were refined to demonstrate consistency between batches.

Ni content y	Ion exchange	$a/\text{Å}$	$c/\text{Å}$	$c/a \pm 0.01$
0.000	Ethanol 25 °C	2.8511 ± 0.006	14.646 ± 0.002	5.14
	Ethanol 78 °C	2.8605 ± 0.005	14.635 ± 0.002	5.12
	Hexanol 156 °C	2.8837 ± 0.004	14.438 ± 0.002	5.03
0.010	Ethanol 78 °C	2.8681 ± 0.003	14.586 ± 0.002	5.08
	Hexanol 156 °C	2.8721 ± 0.002	14.460 ± 0.002	5.03
0.025	Ethanol 25 °C	2.8656 ± 0.008	14.691 ± 0.006	5.13
	Ethanol 78 °C	2.8764 ± 0.002	14.565 ± 0.003	5.06
	Hexanol 156 °C	2.8828 ± 0.004	14.417 ± 0.002	5.00
0.050	Ethanol 25 °C	2.8651 ± 0.008	14.688 ± 0.005	5.13
	Ethanol 78 °C	2.8697 ± 0.003	14.617 ± 0.002	5.09
	Hexanol 156 °C	2.8874 ± 0.005	14.399 ± 0.002	4.99
0.075	Ethanol 25 °C	2.8623 ± 0.004	14.647 ± 0.003	5.12
	Ethanol 78 °C	2.8652 ± 0.003	14.549 ± 0.001	5.08
	Hexanol 156 °C	2.8791 ± 0.005	14.421 ± 0.002	5.00
0.100	Ethanol 25 °C	2.8633 ± 0.005	14.636 ± 0.003	5.11
	Ethanol 78 °C	2.8713 ± 0.003	14.601 ± 0.005	5.08
	Hexanol 156 °C	2.8847 ± 0.004	14.438 ± 0.003	5.01
0.200	Ethanol 25 °C	2.8697 ± 0.008	14.647 ± 0.007	5.10
	Ethanol 78 °C	2.8731 ± 0.007	14.587 ± 0.005	5.08
	Hexanol 156 °C	2.8864 ± 0.008	14.475 ± 0.003	5.02

Table 3.18 Lattice parameters for layered $Li_xNi_yMn_{1-y}O_2$ obtained from Rietveld refinement of x-ray diffraction patterns.

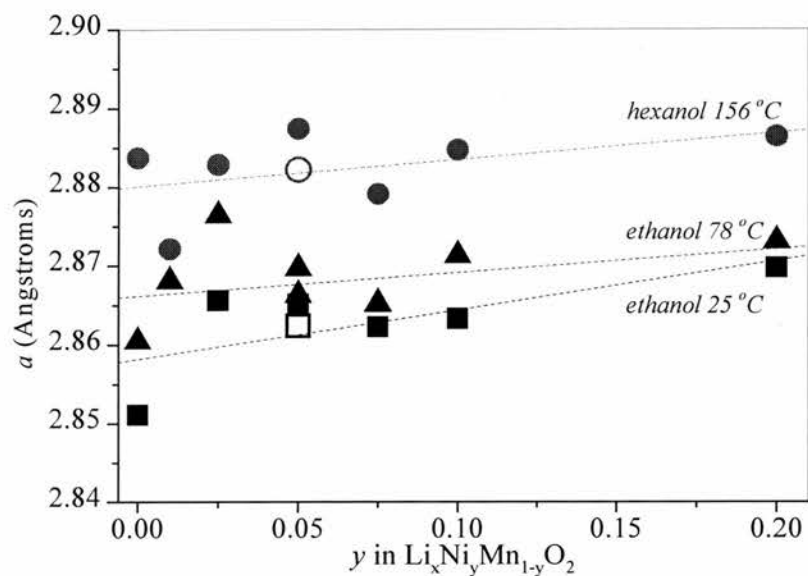
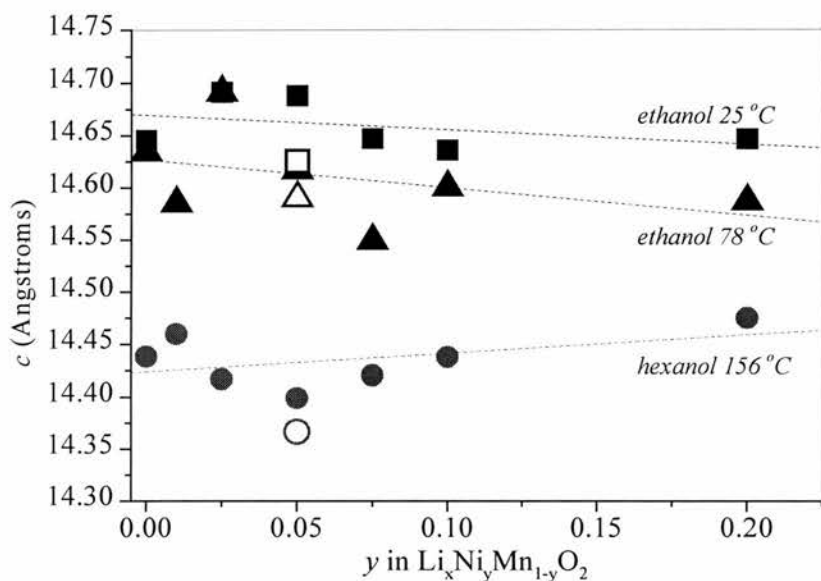


Figure 3.23 a) and b) Evolution of the lattice parameters a and c , for nickel doped materials $Li_xNi_yMn_{1-y}O_2$. Open shapes at $y = 0.05$ represent lattice parameters obtained from neutron data.



■ = Ethanol 25 °C,
 ▲ = Ethanol 78 °C
 ● = Hexanol 156 °C

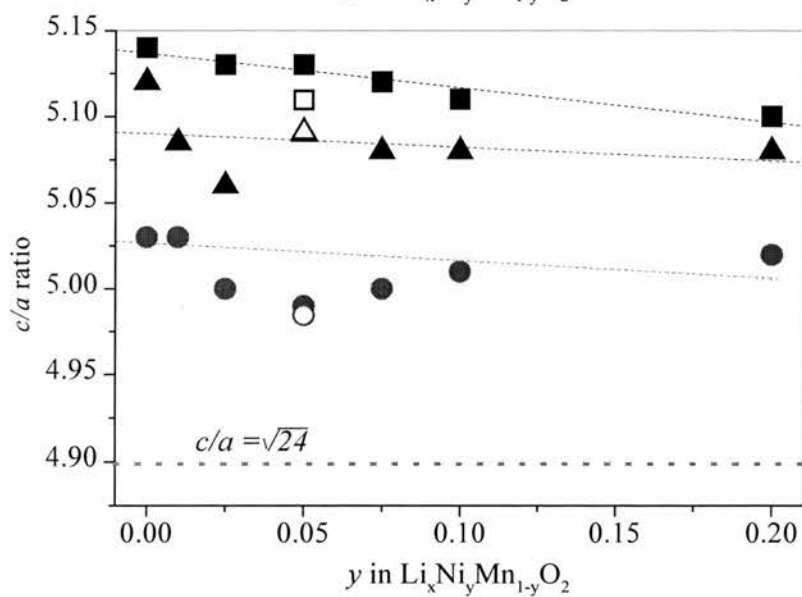


Figure 3.23c) Distortion of the hexagonal unit cell c/a . The dotted line shows $c/a = \sqrt{24} = 4.898$ for the ideal cubic rocksalt structure.

The trend in lattice parameters with ion exchange conditions displays an increase in the a lattice parameter and a reduction in the c lattice parameter with an increase in ion exchange temperature. Lines of best fit for each data set have been added to Figure 3.23 to show the trends more clearly and they are seen to hold for all y . The relative invariance in a and c with nickel content y is consistent with the sodium phase results in section 3.2.4.5.

The trends observed from chemical analysis of these materials with ion exchange conditions were introduced in section 3.3.3.4. In summary there was found to be a decrease in residual sodium, manganese oxidation state and cation vacancies with increasing ion exchange temperature. These chemical analysis results, presented in Tables 3.13 to 3.15, help to explain the lattice parameter data presented in Figure 3.23.

The increase in the a lattice parameter for a change in ion exchange conditions from ethanol to hexanol is due to the presence of less cation vacancies in the compounds prepared at the higher ion exchange temperature. This leads to a decrease in the average manganese oxidation state compared to the samples prepared in ethanol. The higher oxidation state for the samples prepared in ethanol reflects a greater proportion of Mn^{4+} ($\approx 58/60\%$) compared with the hexanol samples ($\approx 42\%$). Since Mn^{4+} (ionic radius = 0.53 Å) is smaller than high spin Mn^{3+} (ionic radius = 0.645 Å) this results in a shorter average transition metal to oxygen bond length. The effect of this is to reduce the a lattice parameter for the ethanol samples, as observed in Figure 3.23. In Tables 3.14 and 3.15 the manganese oxidation states were very close for materials prepared in ethanol at two different temperatures. This is consistent with the trend lines in Figure 3.23(a) being close to each other for the materials prepared in ethanol.

It is clear in Figure 3.23(b) that there is a reduction in the c lattice parameter for a change in ion exchange conditions from ethanol to hexanol. The c axis parameter of layered compounds is particularly sensitive to the size and quantity of the guest metal species in the alkali metal layers. The weak Van der Waal's bonding between adjacent oxide ion sheets in layered oxides

can lead to a general expansion of the c axis with decreasing alkali metal content. Larger guests will also lead to a c axis expansion. For the samples prepared in ethanol, the alkali metal content is lower and the quantity of the sodium higher and this is consistent with the longer c axis observed in the case of the ethanol samples compared with those prepared in hexanol.

Analysis of the sodium phases prior to ion exchange reveals that they possess vacancies on the transition metal sites, these vacancies are retained in samples prepared at the lower ion exchange temperatures of 25° and 78 °C. Such vacancies inevitably carry, in the language of defect chemistry as introduced by Kröger-Vink,¹⁶ a high negative effective charge and this will pin a proportion of the sodium ions and they will be less mobile. This can explain the retention of a small amount of sodium during the ethanol exchanges. The more aggressive conditions of reflux in hexanol at 156 °C caused a greater reduction of the host, with the associated elimination of the transition metal vacancies. Without the transition metal vacancies to trap sodium ions, the ion exchange process is more complete. It is therefore not a coincidence that the persistence of transition metal vacancies in the materials exchanged in ethanol is accompanied by incomplete exchange of sodium ions by lithium.

The sodium precursor materials were very crystalline in comparison to materials after ion exchange. The x-ray patterns of ion exchanged materials are typical of stacking faulted structures. Examination of the powder x-ray diffraction patterns reveals that there is a variation in the full width at half maximum (FWHM) of the peaks as a function of their hkl values³. This effect is dependent on the l component of the reflection suggesting disorder in the c direction, possibly arising from the incomplete exchange of the sodium ions by lithium ions. Disorder in the c direction results in the 110 peak being the only reflection not affected by the disorder. The absence of vacancies and sodium ions in the lithium phases after exchange in hexanol is consistent with the lack of hkl dependent peak disordering in the x-ray data. As expected, the hkl dependent peak broadening is found to be particularly marked for the samples prepared in ethanol at 25 °C, Figure 3.20.

3.3.3.7 PARTICLE MORPHOLOGY AND SURFACE AREA

The particle size of battery electrode materials is an important parameter influencing performance. Large particles ($> 100 \mu\text{m}$) can break the separator and short the cell, while small particles ($< 5 \mu\text{m}$) with relatively high surface area result in diminished capacity attributed to poor microcrystalline contact and the resultant ionic mobility. However, it is also possible that a smaller particle size can increase the number of sites for insertion. The particle morphology was investigated by scanning electron microscopy and the surface area by the BET method.

Figures 3.24 and 3.25 are scanning electron micrographs of the $y = 0.075$ material, ion exchanged by reflux in hexanol and ethanol respectively and magnified 250 times. After ion exchange the particle morphology has not changed greatly compared to the precursor Na phase of Figure 3.11. These materials appeared to have an irregular random surface, size and shape. It is difficult to see plate like formations indicative of the layered microstructure.

Figure 3.26 is a scanning electron micrograph of the $y = 0.075$ material, ion exchanged at 25°C in ethanol and magnified 1000 times. Comparing the SEM micrographs for the different ion exchange temperatures the particles are possibly less broken up for the lower temperature ion exchange. It is possible that the more vigorous conditions break the particles up more. This is in agreement with BET measurements where the materials prepared by a hexanol reflux had a slightly larger surface area of $16 \text{ m}^2 \text{ g}^{-1}$ compared to ethanol refluxed materials with a surface area of $10 \text{ m}^2 \text{ g}^{-1}$. SEM was also obtained on materials with different nickel contents but there was no observable difference between these materials.

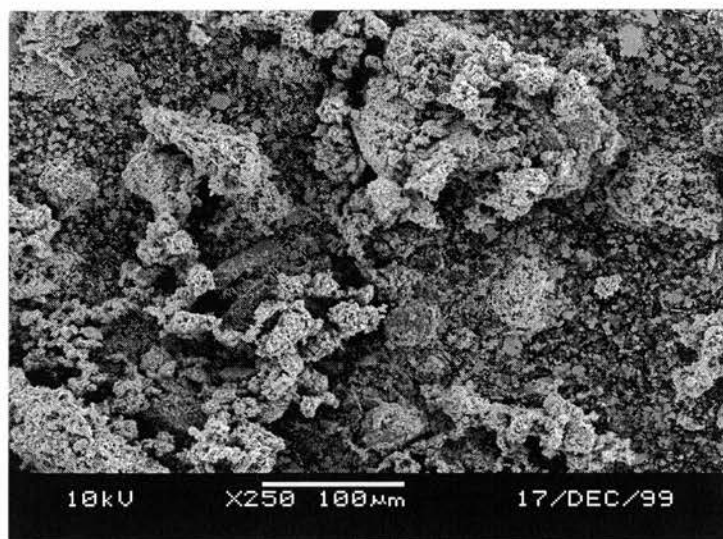


Figure 3.24 $Li_xNi_{0.075}Mn_{0.925}O_2$ refluxed in hexanol, magnified 250 times.

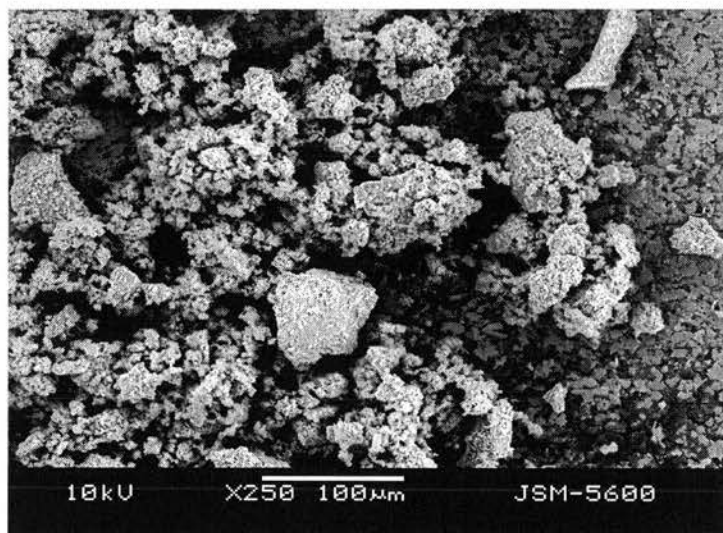


Figure 3.25 $Li_xNi_{0.075}Mn_{0.925}O_2$ refluxed in ethanol, magnified 250 times.

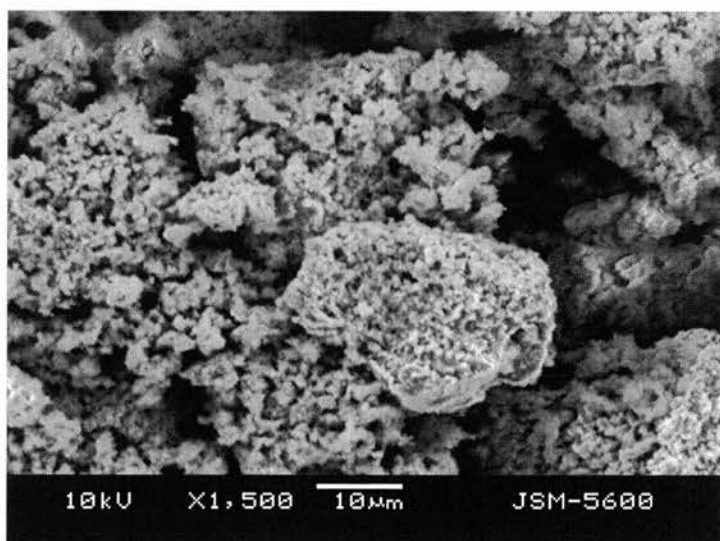


Figure 3.26 $LiNi_{0.075}Mn_{0.925}O_2$ prepared by ion exchange at 25 °C, magnified 1,500 times.

3.3.4 MECHANISM OF ION EXCHANGE

Here, the ion exchange of $P3-Na_xNi_{0.05}Mn_{0.95}O_2$ to $O3-Li_xNi_{0.05}Mn_{0.95}O_2$ at 25 °C is studied by x-ray diffraction as a function of time. Partly ion exchanged samples were prepared by stirring $Na_xNi_{0.05}Mn_{0.95}O_2$ in ethanol with dry LiBr at 25 °C for 5, 60 and 120 minutes, one week and three weeks. In all cases 5 lithium atoms for each Na atom in $Na_xNi_{0.05}Mn_{0.95}O_2$ were used. Following ion exchange the solids were filtered under suction and washed with ethanol and water before drying at 70 °C overnight.

Figure 3.27(a) is the x-ray diffraction pattern of the sodium precursor phase, Figures 3.27(b)-(d) are x-ray diffraction patterns of the partially ion exchanged materials showing remnants of the main peaks of the layered sodium phase. As the time of ion exchange and hence the lithium content increases, the new phase is formed giving a two phase region that exists between 5 and 120 minutes. Figure 3.27(b) is an example of a material dried at 70 °C for only a few hours. The peaks marked *B* in Figure 3.27 are due to the impurity phase birnessite, ($Na_4Mn_{14}O_{27} \cdot 9H_2O$), often appearing following washing in water but with incomplete drying at 70 °C.¹⁷

Normally lithium and sodium do not coexist in one layer because their sizes and chemistries differ significantly. So in the layered compound during exchange it is expected that any given layer is likely to be almost completely occupied by Li or Na. This minimises lattice strain that would otherwise arise if ions of very different radii were to be accommodated within the same layers.

After one week of stirring in ethanol with LiBr the x-ray diffraction pattern of Figure 3.27(e) is achieved and indicates that the ion exchange is essentially complete. Figure 3.27(f) shows no change in the x-ray pattern between ion exchange for one week and three weeks. However chemical analysis in section 3.3.3.4 has shown that small amounts of sodium do remain even after ion exchange for one week.

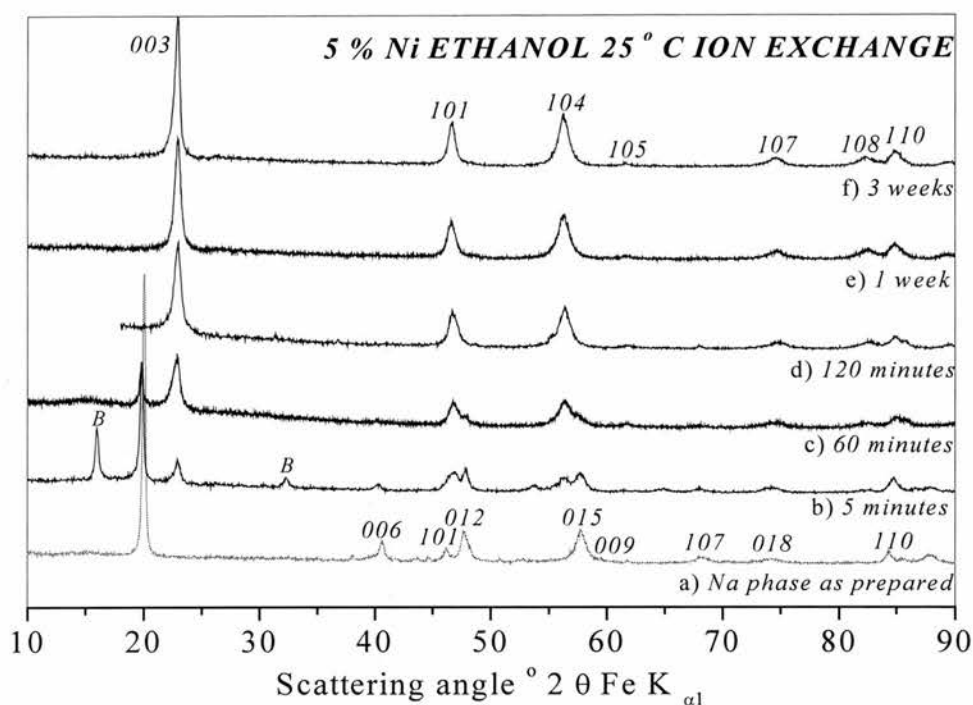


Figure 3.27 X-ray diffraction patterns to show the evolution of the lithiated phase after different times stirring $Na_xNi_{0.05}Mn_{0.95}O_2$ in ethanol at 25 °C. *B* = birnessite impurity phase.

3.4 CONCLUSIONS

Ion exchange of the sodium precursors was successfully performed under three different conditions, hexanol at 156 °C, ethanol at 78 °C and ethanol at 25 °C. X-ray and neutron diffraction confirmed that $LiNi_yMn_{1-y}O_2$ for $0 < y < 0.2$ materials were single phase. Analysis of XPS measurements showed that there was no evidence for nickel valence state other than Ni^{2+} . The refined lattice parameters of rhombohedral $Li_xNi_yMn_{1-y}O_2$ (space group R-3m) showed no significant change with y . Lattice parameters were dependent more on ion exchange temperature.

The x-ray diffraction patterns of $LiNi_yMn_{1-y}O_2$ show the widening of 018/110 peak pair, increase of the c lattice parameter and decrease of the a lattice parameter as the temperature of ion exchange decreased. The c/a ratio subsequently increased from 4.96 to 5.13.

About 6 % of the transition metal vacancies present in the sodium phase still remain in materials prepared by the ethanol ion exchange. It is thought that these vacancies pin some sodium ions, (about 4 %), in the layers and this is consistent with the longer c axis observed in the case of the ethanol samples compared with those prepared in hexanol. Transition metal vacancies and residual sodium ions are minimised on refluxing at 156 °C in hexanol, resulting in a lower valence state of manganese. This is consistent with the increased a lattice parameter observed with ion exchange temperature.

The presence of residual sodium in the layered lithium materials hinders the ion exchange and also induces disorder perpendicular to the layers. It is also observed that the ion exchange conditions are significantly reducing for lithium intercalation to accompany ion exchange. Analysis of SEM micrographs showed that the particle morphology changes little during the ion exchange reaction.

Overall it is evident that the ion exchange process is not restricted to the anticipated simple exchange of sodium by lithium. As well it plays a critical role in controlling the defect chemistry of the transition metal host.

3.5 REFERENCES

- ¹ J. Parant, R. Olazcuaga, M. Devalette, C. Fouassier and P. Hagenmuller, *J. Solid-State Chem.* **3**, (1971), 1.
- ² L. Zhonghua, R. A. Donaberger, and J. R. Dahn, *Chem. Mater.*, **12**, (2000), 3583.
- ³ J. M. Paulsen and J. R. Dahn, *Solid State Ionics*, **126**, (1999), 3.
- ⁴ PDF number 18-0803 JCPDS ICDD International Centre for Diffraction Data, Version 2.16.
- ⁵ A. C. Larson and R. B. von Dreele, *General Structure Analysis system*, Los Alamos National Laboratory, (1995).
- ⁶ PDF number 19-1130 JCPDS ICDD International Centre for Diffraction Data, Version 2.16.
- ⁷ PDF number 04-0835 JCPDS ICDD International Centre for Diffraction Data, Version 2.16.
- ⁸ R. D. Shannon, *Acta. Cryst.*, **A 32**, (1976), 751.
- ⁹ J. N. Reimers, W. Li, E. Rossen, and J. R. Dahn, *Mat. Res. Soc. Symp. Proc.*, **293**, (1993), 3.
- ¹⁰ R. J. Gummow, D. L. Liles and M. M. Thackeray, *Mat. Res. Bull.* **28**, (1993), 235.
- ¹¹ B. J. Neudecker, R. A. Zuhr, B. S. Kwak and J. B. Bates, *J. Electrochem. Soc.*, **145**, (1998).
- ¹² Q. Zhong, A. Bonakdarpour, M. Zhang, Y. Gao and J. Dahn, *J. Electrochem. Soc.*, **144**, (1997).
- ¹³ PDF number 22-1141 JCPDS ICDD International Centre for Diffraction Data, Version 2.16.
- ¹⁴ J. M. Paulsen, R.A. Donaberger, and J. R. Dahn, *Chem. Mater.* **12**, (2000), 2257.
- ¹⁵ A. D. Robertson, A. R. Armstrong, A. Fowkes and P. G. Bruce, *J. Mater. Chem.*, **11**, (2001), 118.
- ¹⁶ A. R. West, *Basic Solid State Chemistry*, Second Edition, John Wiley and Sons, (1999).
- ¹⁷ PDF number 23-10460 JCPDS ICDD International Centre for Diffraction Data, Version 2.16.

CHAPTER 4. ELECTROCHEMICAL PERFORMANCE OF $\text{Li}_x\text{Ni}_y\text{Mn}_{1-y}\text{O}_2$

4.1 INTRODUCTION

The previous chapter described the synthesis and structure determination of $\text{Li}_x\text{Ni}_y\text{Mn}_{1-y}\text{O}_2$. The purpose of preparing these layered materials was to establish if the Ni doping could enhance the ability to sustain the reversible removal and reinsertion of lithium compared to LiMnO_2 . Galvanostatic and potentiostatic measurements will be used to obtain phase, thermodynamic and kinetic information on cycling.

4.2 THE FIRST CYCLE OF LAYERED $\text{Li}_x\text{Ni}_y\text{Mn}_{1-y}\text{O}_2$

4.2.1 VOLTAGE PROFILE

The variation of voltage with x during the passage of current is called a 'load' curve and can be easily collected using galvanostatic measurements. For layered materials such as $\text{Li}_x\text{Ni}_y\text{Mn}_{1-y}\text{O}_2$ close to equilibrium, a lattice gas model predicts smooth, symmetrical load curves with no large step in voltage. The solid line in Figure 4.1 shows the typical load curve obtained for the first cycle of a layered material, with nominal composition, $\text{Li}_x\text{Ni}_{0.075}\text{Mn}_{0.925}\text{O}_2$, prepared by refluxing in ethanol for 8 hours, (78 °C). The voltage range used was between 2.4 and 4.8 V, at a constant current density of 25 mA g⁻¹ (C/9 rate). The maximum voltage used was 4.8 V because above this potential the electrolyte may not be stable in contact with the electrode. The surfaces of transition metal oxides provide an ideal environment for decomposition of many electrolytes. The net effect of this would be that the effective current used to deintercalate lithium is smaller than the set current, because some current is used to decompose electrolyte.

The dotted line shown in Figure 4.1 is the load curve obtained for a directly prepared spinel $\text{Li}_1\text{Ni}_{0.15}\text{Mn}_{1.85}\text{O}_4$. This has the same Ni content as layered $\text{Li}_x\text{Ni}_{0.075}\text{Mn}_{0.925}\text{O}_2$ and was cycled under exactly the same conditions. The curves in Figure 4.1, for the two different structure types, are quite different. The layered material shows no distinct plateaus, while the spinel material exhibits two distinct plateaus at 3 V and 4 V, indicating lithium extraction and insertion on two distinct sites, octahedral and tetrahedral respectively.¹

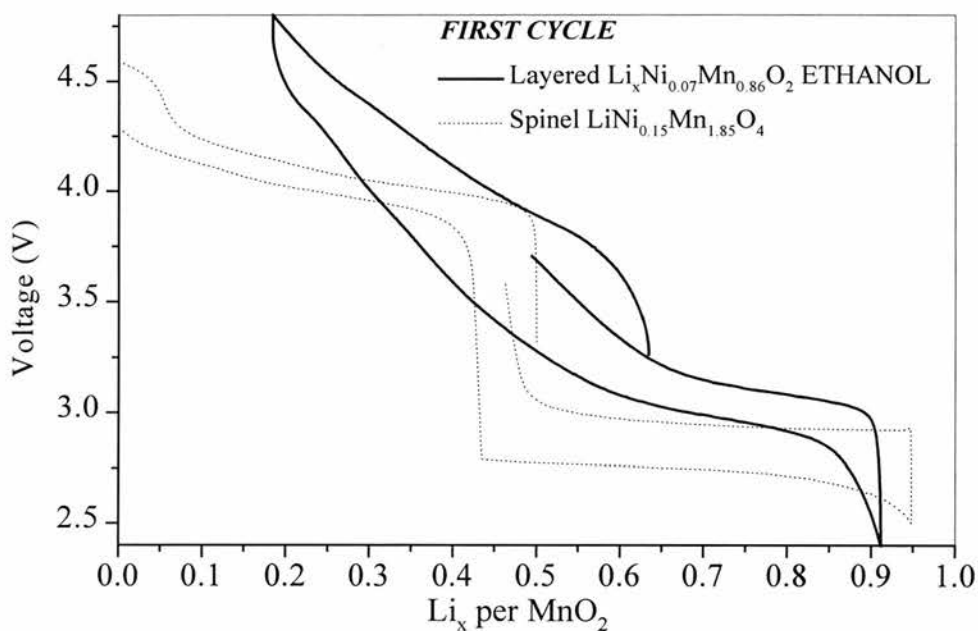


Figure 4.1 First cycle variation of potential with lithium content x for layered $\text{Li}_x\text{Ni}_{0.07}\text{Mn}_{0.86}\text{O}_2$, (solid line). Compositions are expressed in terms of Li_xMnO_2 . The characteristic voltage profile of spinel $\text{LiNi}_{0.15}\text{Mn}_{1.85}\text{O}_4$ is shown by the dotted line. Current density = 25 mA g^{-1} , voltage range 2.4 to 4.8 V, electrolyte = 1 M LiPF_6 in PC, temperature = $30 \text{ }^\circ\text{C}$.

Features in the load curve reveal a great deal about the thermodynamics of a system, provided the insertion rate is sufficiently slow. The voltages at which plateaus occur in load curves correspond to the energetics of the intercalation process, specifically the energies of lithium ions in their sites, and the charge compensating Li 1s electrons in the d-bands of the host. Solid

solutions, (*i.e.* a single phase), display a continuous variation of voltage with composition x (step). Defined compounds, separated from one another by biphased domains, display a constant voltage with composition, (plateau). The fine structure of the potential variation in plateaus is easier to observe in the first derivative, and a plot of $-dx/dV$, (or $-dQ/dV$), is called an incremental capacity plot. The first cycle incremental capacity plot corresponding to the layered material of Figure 4.1 is presented in Figure 4.2. Plateaus in the load curve are transformed into peaks in the derivative plot. It can be seen that significant capacity is present at 3 V, but there are also features at higher voltage, which exhibit some capacity. The labels (a) to (j) on Figure 4.2 correspond to compositions which are investigated later by x-ray diffraction throughout the first cycle.

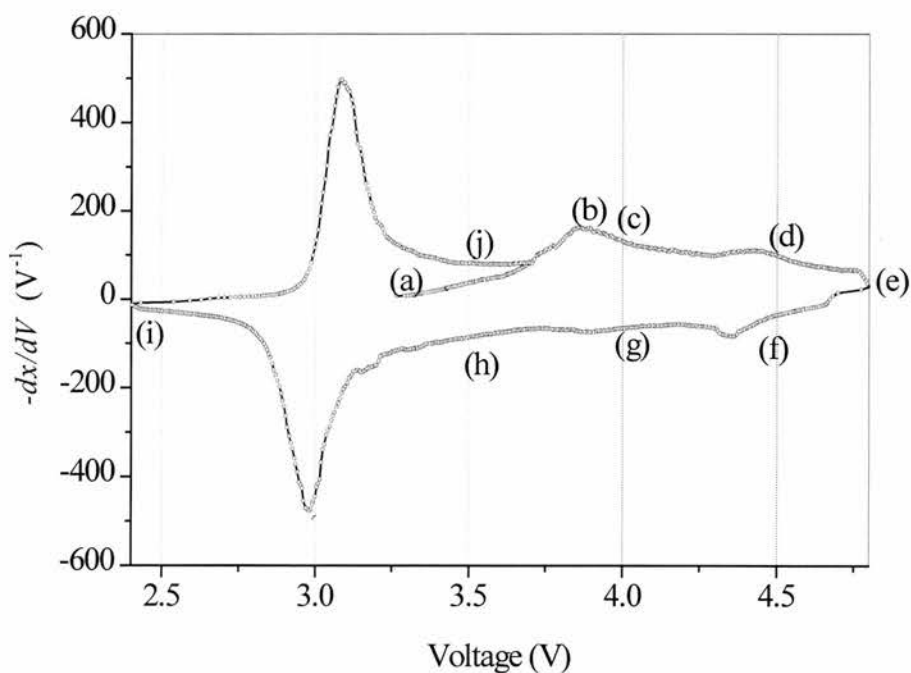


Figure 4.2 The incremental capacity plot for the first cycle of a lithium cell with a layered $\text{Li}_x\text{Ni}_{0.07}\text{Mn}_{0.86}\text{O}_2$ electrode (ethanol reflux). Current density = 25 mA g^{-1} , voltage range = 2.4 to 4.8 V. Labels (a)-(j) indicate compositions of interest, later investigated by x-ray diffraction, see section 4.2.5.

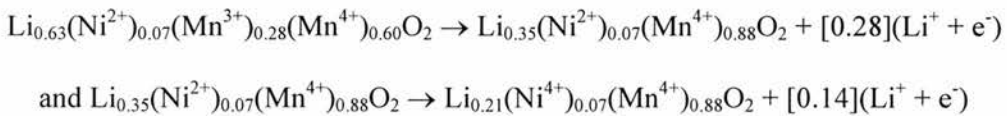
4.2.2 FIRST CYCLE CHARGE CAPACITY

As shown in Chapter 3 nickel is in the divalent state in $\text{Li}_x\text{Ni}_y\text{Mn}_{1-y}\text{O}_2$ materials. As a result the substitution of Ni^{2+} for a Mn^{3+} involves a second Mn^{3+} converting to Mn^{4+} , *i.e.* $2\text{Mn}^{3+} \rightarrow \text{Ni}^{2+} + \text{Mn}^{4+}$. Also, allowing for lithium deficiency, a general formula may be considered to describe the species present: $\text{Li}_x\text{Ni}^{2+}_y\text{Mn}^{3+}_{x-2y}\text{Mn}^{4+}_{1+y-x}\text{O}_2$. However compositional analysis of the as prepared materials, Tables 3.12 to 3.14, showed that the total Mn content was less than $1-y$. For a compound with nominal Ni content $y = 0.075$ the ordered formula was:



The fact that samples are lithium deficient, yet Ni is still divalent, and this has been compensated by $\text{Mn}^{3+} \rightarrow \text{Mn}^{4+}$, suggests that on extraction of further lithium, Mn^{3+} will first be oxidised to Mn^{4+} before oxidation of Ni^{2+} .

As lithium ions are removed, the corresponding electrons are removed from the top of the valence band, which is made up of metal 3d levels². In an octahedral site the Mn^{3+} ions in high-spin configuration d^4 , have the electron configuration $t^3_{2g} e_g^1$. Once the Mn^{3+} 3d e_g^1 electrons are removed, the next electrons available are from the Ni 3d e_g , which according to the work of Zhong *et al.* on $\text{Li}_x\text{Ni}_y\text{Mn}_{2-y}\text{O}_4$ spinel has a 0.5 eV higher binding energy.³ Following this work the authors showed that Ni^{2+} was oxidised always to Ni^{4+} and at a potential of 4.6 V vs. Li^+ . Thus, in the fully charged state, (4.8 V), we expect Ni^{2+} to be oxidised to Ni^{4+} , in which case the electrochemical reaction on the first charge may be summarised as:



Assuming all Mn can oxidise to Mn^{4+} and all Ni to Ni^{4+} , the total theoretical first charge capacity is 120 mA h g^{-1} .

The load curve of Figure 4.1 has been reproduced in Figure 4.3. It demonstrates a first charge practical capacity of 126 mA h g^{-1} on lithium extraction, (a)-(e), which is in excess of the theoretical value.

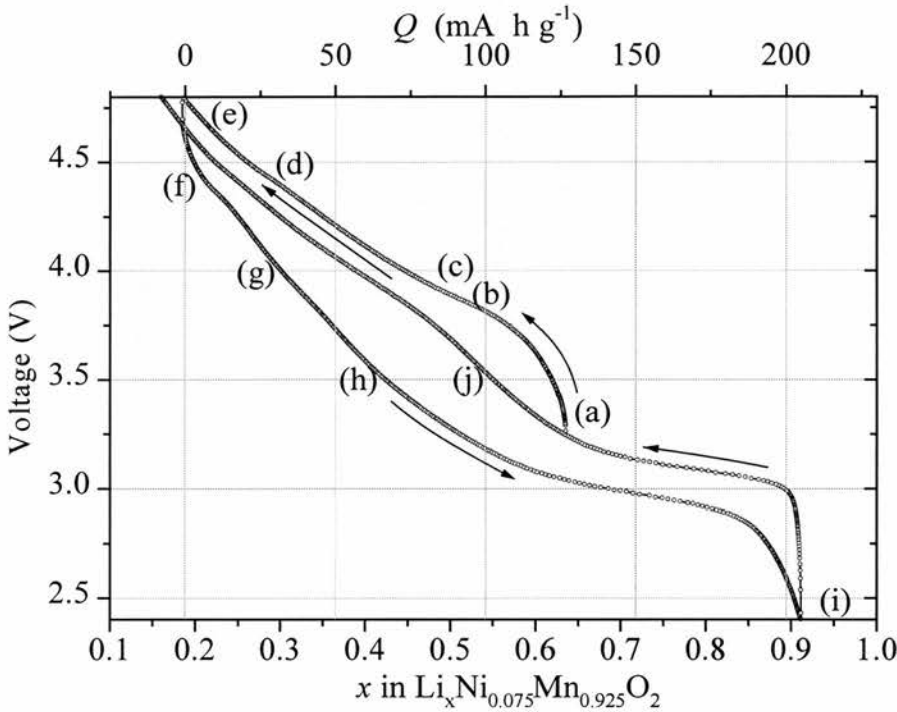
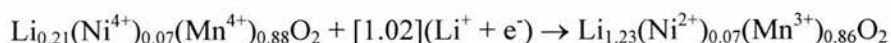


Figure 4.3 The load curve for the first cycle of a lithium cell with a layered $\text{Li}_x\text{Ni}_{0.07}\text{Mn}_{0.88}\text{O}_2$ electrode (ethanol reflux). Current density = 25 mA g^{-1} , voltage range = 2.4 to 4.8 V. Labels (a)-(j) indicate compositions of interest, later investigated by x-ray diffraction, see section

4.2.5.

4.2.3 FIRST CYCLE DISCHARGE CAPACITY

Once all the Mn^{3+} have been oxidised to Mn^{4+} and all the Ni^{2+} to Ni^{4+} the Mn^{4+} are available for reduction to Mn^{3+} and $y\text{Ni}^{4+}$ to Ni^{2+} . The electrochemical reaction on discharge can be summarised as:



The theoretical discharge capacity increases with Ni content y , for the composition with $y = 0.07$ it is therefore 291 mA h g^{-1} . The load curve of Figure 4.3 demonstrates a practical capacity to insert lithium of 208 mA h g^{-1} , 71 % of the theoretical capacity. It can also be seen from Figure 4.3 that 214 mA h g^{-1} (74 % of the theoretical capacity) can be extracted on the subsequent charge, suggesting that this extraction and insertion of lithium is highly reversible.

The results of the first discharge capacity obtained for all y , ($0.0 < y < 0.2$), prepared by three different ion exchange conditions, are presented in Table 4.1. All cells were cycled under the same conditions at a current density of 25 mA g^{-1} , and between the voltage limits of 4.8 and 2.4 V. The cell with $y = 0$, prepared at $25 \text{ }^\circ\text{C}$, was an exception, data was only available from cycling between 4.6 and 2.4 V.

For all materials the capacity is nearly always in excess of 200 mA h g^{-1} . This represents an increase of almost 50 % compared with the earlier stoichiometric LiMnO_2 which has a practical capacity of 130 mA h g^{-1} . There is no trend seen in first discharge capacity with ion exchange conditions. For samples prepared in by ion exchange in ethanol at $25 \text{ }^\circ\text{C}$ for one week, with $0.0 < y < 0.2$, the expected increase in discharge capacity with Ni content y is seen clearly. But for compositions refluxed in ethanol and hexanol for 8 hours, there is no obvious increase in discharge capacity with y . The theoretical discharge capacities, (Q_T), were calculated from the

chemical analysis results presented in chapter 3, the practical capacities are expressed terms of these in brackets in Table 4.1.

Ni content y in $\text{Li}_x\text{Ni}_y\text{Mn}_{1-y}\text{O}_2$	First cycle discharge capacity (mA h g^{-1})					
	Ethanol 25 °C		Ethanol 78 °C		Hexanol 156 °C	
	1 week	% of Q_T	8 hours	% of Q_T	8 hours	% of Q_T
0.000	181	(67)	227	(85)	225	-
0.010	-	-	223	-	212	-
0.025	192	(69)	220	(81)	203	(71)
0.050	199	(69)	225	(81)	208	(71)
0.075	200	(70)	208	(71)	212	(70)
0.100	205	(69)	220	(72)	213	(67)
0.200	223	(68)	228	(66)	197	(56)

Table 4.1 First cycle discharge capacities of $\text{Li}_x\text{Ni}_y\text{Mn}_{1-y}\text{O}_2$ for $0.0 < y < 0.2$, prepared under different ion exchange conditions. Voltage range 4.8 to 2.4 V, current density 25 mA g^{-1} .

The first cycle incremental capacity plots of the Ni doped materials prepared in ethanol at 25 °C are compared in Figure 4.4. The increase in discharge capacity with increasing Ni content can be seen immediately in the discharge profile, in the high voltage range $3.5 \text{ V} < V < 4.8 \text{ V}$. More specifically, it can be seen that the reversible peaks at 4.37 and 3.92 V become more prominent as the Ni content increases. These peaks are therefore probably due to Ni redox processes. More precisely, the capacity due Ni should increase as $2y$ because there are 2 electrons per nickel atom in the lowest e_g level. Zhong observed this in the 4.6 V plateau for $\text{LiNi}_x\text{Mn}_{2-x}\text{O}_4$.³ Increased capacity observed at these values of potential, for the materials prepared at 78 °C and 156 °C had less effect on the total discharge capacity, compared to materials prepared at 25 °C. There is an observed decrease in capacity in the range $2.4 \text{ V} < V < 3.5 \text{ V}$, as the Ni content increases. It is not possible to separate the capacities due to Ni and Mn because of the peak overlap, especially close to 3.9 V.

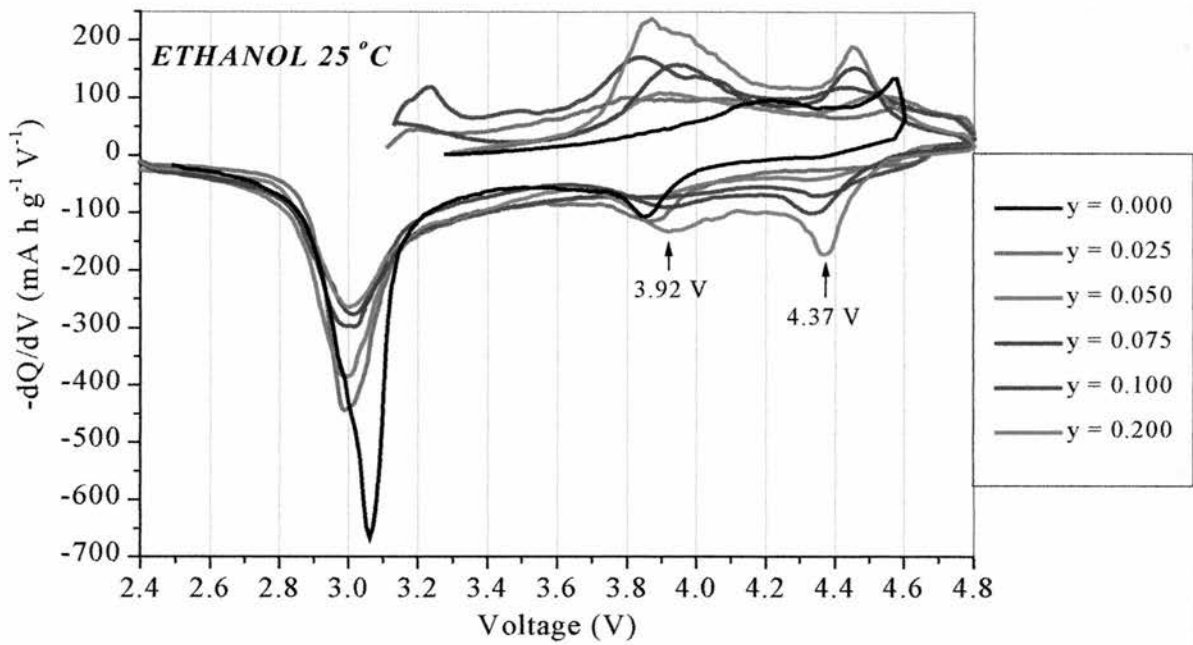


Figure 4.4 First cycle incremental capacity plots of $\text{Li}/\text{LiNi}_y\text{Mn}_{1-y}\text{O}_2$ cells vs. potential, the layered materials were prepared in ethanol at 25 °C. Current density = 25 mA g^{-1} .

4.2.4 INFLUENCE OF ION EXCHANGE CONDITIONS ON THE FIRST CYCLE

To compare the first cycle behaviour of two different ion exchanges, the cyclic voltammograms of $\text{Li}_x\text{Ni}_{0.025}\text{Mn}_{0.975}\text{O}_2$, (ethanol 78 °C and hexanol 156 °C), electrodes were obtained. Voltammetric measurements were made at a step rate of 2.5 mV every four minutes, between the potential limits of 2.4 and 4.8 V.

Figure 4.5 shows the 4 V region, and compares the first cycle voltammograms, for two materials with the same composition. For comparison, the cyclic voltammogram was also obtained for a spinel structure with the same composition, and is shown by the dotted line. The spinel material exhibits two pairs of redox peaks at 4.04 and 4.16 V on oxidation, and 4.13 and 3.98 V on reduction, are characteristic of LiMn_2O_4 spinel.⁴

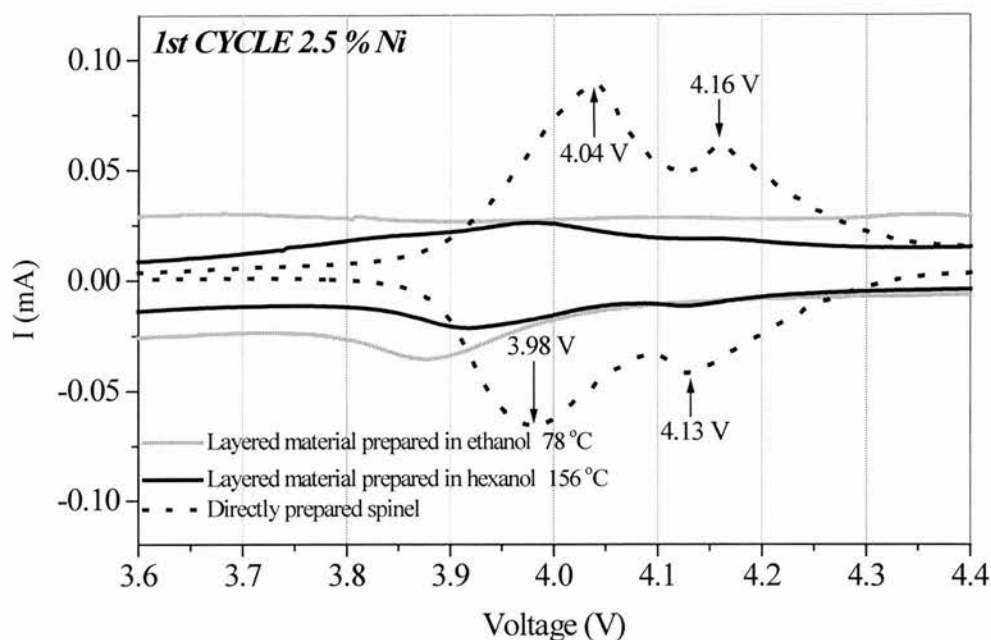


Figure 4.5 First cycle voltammograms for layered and spinel compounds with $y = 0.025$, highlighting the 4 V region. Step rate 2.5 mV every 4 minutes, voltage range 2.4 to 4.8 V.

Examination of the cyclic voltammogram for the layered compound prepared in hexanol, (black line), already reveals the presence of oxidation peaks at about 3.98 and 4.15 V, and reduction peaks at 4.13 and 3.92 V, in the first cycle. These correspond quite well with the voltage peaks of the spinel phase, and suggest some lithium in tetrahedral sites for the material prepared in hexanol. There are no such peaks observed in the first cycle for the material prepared in ethanol, (grey line).

A 4 V peak occurs when, in order to minimise the lattice energy, Li deintercalation displaces some transition metal ions from 3a octahedral sites, into empty octahedral 3b sites in the lithium layers. Such a displacement has been observed with vanadium ions in the structurally similar layered compound LiVO_2 , upon extraction of lithium.⁵ The presence of transition metal ions in the lithium layers will then result in displacement of Li^+ ions from their octahedral 3b sites, (which share edges with the transition metal 3a octahedra), into tetrahedral 8a sites

(which share only corners with the transition metal $3a$ octahedra). In this way the Li-Mn repulsions will be minimised. Further lithium extraction will then involve removal of some lithium from the tetrahedral $8a$ sites, which in LiMn_2O_4 spinel occurs at 4 V. Site energies are determined, to a first approximation, by the local environment and will be the same in regions with the local structure of spinel as they are in large crystals. For occupancies of more than 50% Li on the tetrahedral $8a$ sites, a double 4 V process is observed due to Li ordering.

4.2.5 STRUCTURAL CHANGES IN THE FIRST CYCLE.

4.2.5.1 INTRODUCTION

A series of cells were made to electrochemically prepare $\text{Li}_x\text{Ni}_{0.07}\text{Mn}_{0.88}\text{O}_2$, (prepared in ethanol at 78 °C), with various Li compositions x . Lithium was removed from the as-prepared material by charging the cell from 3.1 V at 25 mA g^{-1} . The four compositions prepared were $x =$ (b) 0.55, (c) 0.45, (d) 0.25 and (e) 0.18, corresponding to the labels in Figures 4.2 and 4.3. Five identical cells were then fully charged to 4.8 V ($x = 0.18$) and then discharged so that cathodes were prepared with $x =$ (f) 0.22, (g) 0.30, (h) 0.43 and (i) 0.91. Sample (j) underwent one complete cycle and was stopped at 3.5 V on the second charge. Compositions were determined by coulometric titration from the amount of charge passed during cycling, this was based on the as-prepared material $x = 0.63$, obtained from chemical analysis. X-ray diffraction patterns were then collected from the ten cycled materials, (b) to (j).

4.2.5.2 X-RAY DIFFRACTION

The sequence of powder diffraction patterns obtained as a function of Li composition x throughout the first cycle is shown in Figure 4.6.

The pattern in Figure 4.6(a) was indexed on the rhombohedral cell, (Section 3.3.3.3.). Powder patterns (b) to (e) are obtained throughout the charging process. The 2θ range between 80° and 90° will include the most important changes, in particular the changes in the 018 and 110 reflections. X-ray diffraction patterns recorded from deintercalated samples as far as $\text{Li}_{0.25}\text{Ni}_{0.07}\text{Mn}_{0.88}\text{O}_2$, Figure 4.6(d), can be indexed on the same rhombohedral phase as the as-prepared material Figure 4.6(a). This shows that the rhombohedral phase persists over a wide composition range in agreement with the voltage profile of Figure 4.3. Oxidation to 4.8 V results in a material with the composition $\text{Li}_{0.18}\text{Ni}_{0.07}\text{Mn}_{0.88}\text{O}_2$. In Figure 4.6(e) the 018 peak has virtually vanished and the emergence of peaks that correspond roughly to a cubic phase, (like LiMn_2O_4) are observed.

A standard spinel pattern was compared with two layered patterns in Figure 3.15. Distinguishing between layered and spinel phases using diffraction data can be problematical because of the similarity between their powder diffraction patterns. It can be seen in Figures 4.6(d) and (e) that the 018 and 110 peaks appear to merge, with the 108 peak continuously decreasing in intensity on extraction of lithium. Even although Figure 4.6(e) may look spinel-like, the absence of a 4V peak in Figure 4.2 suggests no tetrahedral lithium and no $3b$ transition metal ions at this stage of cycling.

On reintercalation the rhombohedral single phase persists up to at least $\text{Li}_{0.43}$, Figure 4.6(f)-(h). Beyond $\text{Li}_{0.43}$ the powder x-ray data of Figure 4.6(i) indicates the formation of some tetragonal Jahn-Teller distorted phase, as expected at this level of intercalation. Electrons compensating the lithium ion insertion reduce Mn^{4+} to Mn^{3+} , and the magnitude of the cooperative Jahn-Teller distortion, in a first approximation, is a function of the concentration of octahedral site Mn^{3+} ions. The distortion is observed when the Mn^{3+} content is greater than 50%.

The x-ray diffraction pattern in Figure 4.6(j) is from a material after one full cycle. The data look identical to that of as-prepared $\text{Li}_x\text{Ni}_{0.07}\text{Mn}_{0.88}\text{O}_2$ in figure 4.6(a) indicating that the

rhombohedral phase is recovered after a charge-discharge cycle. The broad and high background at low angles is observed for all cycled materials and is due to the presence of amorphous components of the composite electrode.

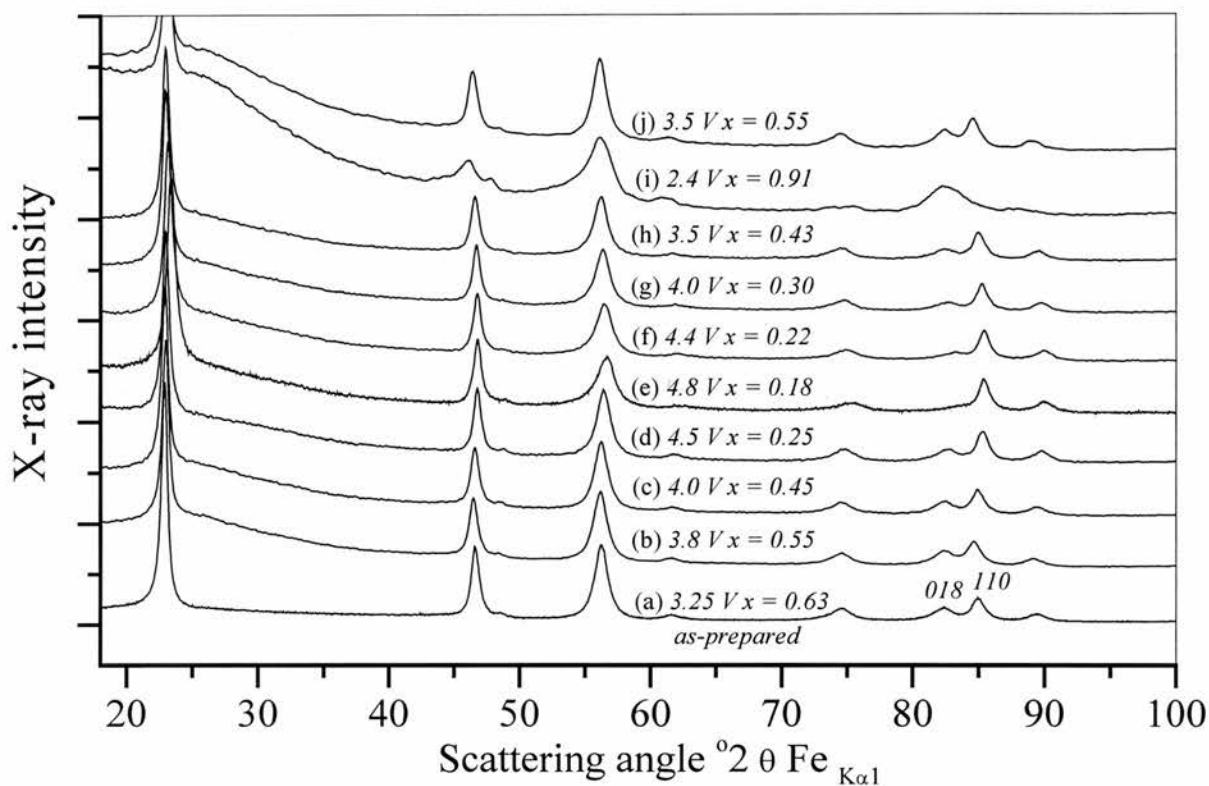


Figure 4.6 Ex-situ x-ray diffraction patterns of $\text{Li}_x\text{Ni}_{0.0}\text{Mn}_{0.88}\text{O}_2$ (ethanol reflux) prepared electrochemically with different lithium contents x . A typical load curve for the cells is shown in Figure 4.3. (a) is the as prepared material, (b)-(e) are the x-ray diffraction patterns obtained from the charge process and (f)-(i) on the discharge process. (j) is the x-ray diffraction pattern obtained after one full cycle returning to 3.5 V.

4.2.5.3 RIETVELD REFINEMENT

Lattice parameters throughout the first cycle of $\text{Li}_x\text{Ni}_{0.07}\text{Mn}_{0.88}\text{O}_2$ were refined using the GSAS suite of programs.⁶ The crystallographic details of the layered rhombohedral structure, R-3m, are shown in Table 4.2 and all Rietveld refinements were carried out based on this model. The occupancies of the 3a Mn and Ni sites were fixed at 0.88 and 0.07 respectively from chemical analysis. The lithium ion occupancy of the 3b octahedral sites was fixed for each x at the value obtained from coulometric titration, x-ray diffraction is not sensitive enough to detect the lithium site occupancy.

Atom	Wyckoff symbol	x/a	y/b	z/c	Occupancy
Li	3b	0	0	0.5	x
Ni	3a	0	0	0	0.07
Mn	3a	0	0	0	0.88
O	6c	0	0	0.25	1

Table 4.2 Crystallographic details of $\text{Li}_x\text{Ni}_{0.07}\text{Mn}_{0.88}\text{O}_2$, R-3m.

4.2.5.4 LATTICE PARAMETERS

The refined lattice parameters obtained for rhombohedral $\text{Li}_x\text{Ni}_{0.07}\text{Mn}_{0.88}\text{O}_2$, on the first charge/discharge cycle, are presented in Figure 4.7(a) and (b) as a function of lithium composition x . The c/a ratios are plotted in Figure 4.7(c). Filled circles represent the charging process and open circles the discharge process. The points are labeled (a) to (j) and correspond to Figures 4.2, 4.3 and 4.6.

The reversible shrinkage of the unit cell, along the a axis as x decreases, is caused by the decreasing average ionic radius of the transition metal ions within the MO_6 octahedra, that results from an increase in the average ionic valence state.⁷

The reduction in the c lattice parameter as lithium is extracted indicates a reversible contraction of the lattice due to the reduced lithium in the layers. However, Li insertion above about $\text{Li}_{0.5}$ also causes a contraction, probably due to increased van der Waals forces in the layers.

Examination of the c/a ratio shows that a lattice distortion exists for all x , with c/a always > 4.98 . The dotted line in 4.7(c) represents $c/a = \sqrt{24} = 4.898$ for a cubic spinel lattice. The variation of c/a ratio on the first charge and discharge is clearly seen to be reversible for $x < 0.6$. The c/a ratio of the two cells exactly one cycle apart, (b) and (j), where $x = 0.55$, are identical. This indicates that the lattice contraction is reversible, which is believed to be an important prerequisite for good cycle stability. It also suggests that the lattice parameter changes observed are more related to the contraction and expansion of the c -axis within the layered structure, than any conversion to spinel.

Another important feature in Figure 4.7 is between (a) and (b), a divergence of the c/a ratios between the charge and discharge processes suggests some irreversible structural transformation on the first extraction of lithium.

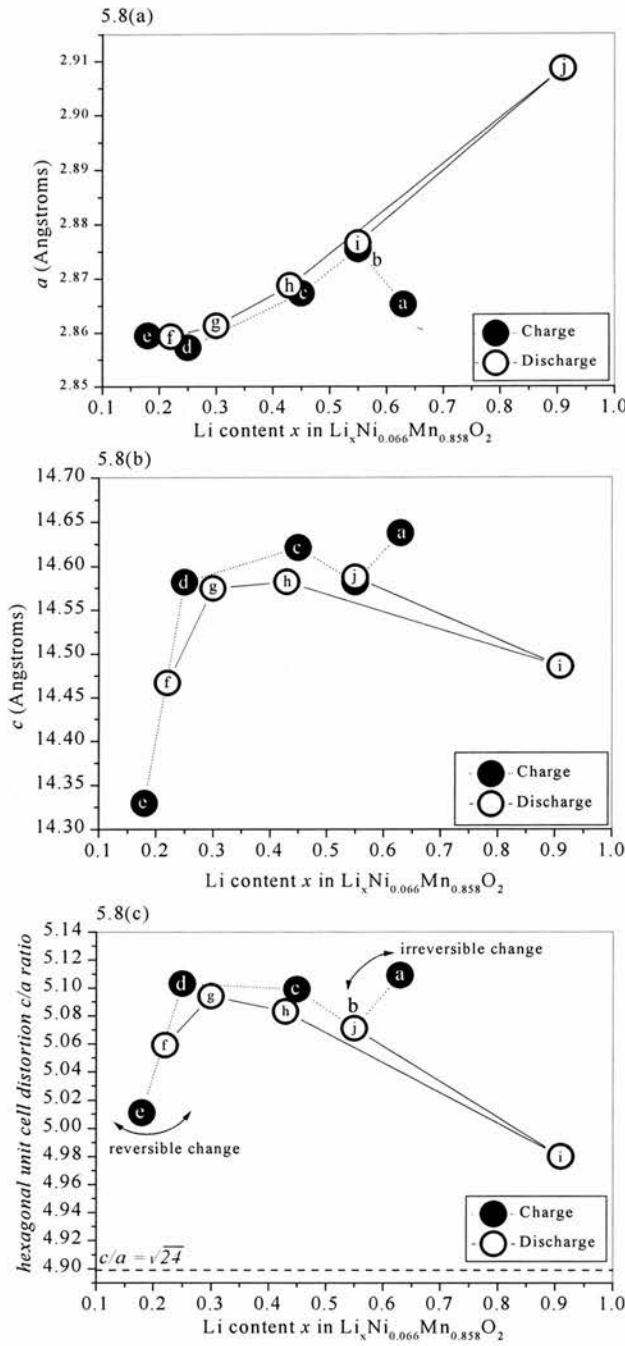


Figure 4.7 Unit cell parameters a and c , and variation of the c/a ratio as a function of x in $\text{Li}_x\text{Ni}_{0.07}\text{Mn}_{0.88}\text{O}_2$ in the first cycle. Lattice parameters presented as solid circles were obtained for the charge process, and open circles for the discharge process. Labels (a) to (i) indicate compositions corresponding to the x-ray diffraction patterns in Figure 4.6.

4.2.6 FIRST CYCLE CONCLUSIONS

Between the potential limits of 2.4 and 4.8 V, all layered Ni doped $\text{Li}_x\text{Ni}_y\text{Mn}_{1-y}\text{O}_2$ materials displayed significant capacity at 3 V, and some capacity at higher voltages. The reversible extraction and insertion of about 70% of the lithium was possible. The Ni ions were found to be active in this potential region and incremental capacity plots displayed increased capacity at 4.37 and 3.92 V for the materials doped with more Ni. The increase in first discharge capacity with y was most clearly observed in the materials prepared by ion exchange at 25 °C, where the capacity increased from 192 mA h g⁻¹ for $y = 0$ to 223 mA h g⁻¹ for $y = 0.2$. This is in good agreement with the expected increase in capacity if Ni^{2+} are oxidised to Ni^{4+} in the higher potential region.

The ion exchange conditions were also found to influence the first cycle behaviour. In a material prepared in hexanol at 156 °C with $y = 0.025$, a subtle double 4 V process was observed, suggesting that there is some lithium in the tetrahedral sites within the first cycle. This process was not observed for the same material prepared in ethanol at 78 °C.

Structural changes observed in the first cycle of a material with $y = 0.07$, (prepared in ethanol), show a rhombohedral phase at all compositions. The unit cell parameters are highly reversible throughout the first cycle charge-discharge process.

4.3 EXTENDED CYCLING OF $\text{Li}_x\text{Ni}_y\text{Mn}_{1-y}\text{O}_2$

4.3.1 INTRODUCTION

The performance of the Ni doped layered materials will be studied, together with associated structural and electrochemical changes, as the materials are cycled. Incremental capacity plots track the electrochemical behaviour of a material throughout cycling, and information can be obtained for any cycle. These will be correlated with x-ray diffraction patterns obtained from cycled materials.

4.3.2 $\text{Li}_x\text{Ni}_y\text{Mn}_{1-y}\text{O}_2$ PREPARED IN HEXANOL AT 156 °C

4.3.2.1 ELECTROCHEMICAL PERFORMANCE AT 25 mA g⁻¹

The evolution of the discharge capacities, during galvanostatic cycling of $\text{Li}_x\text{Ni}_y\text{Mn}_{1-y}\text{O}_2$ prepared in hexanol, is shown in Figure 4.8. The voltage range used was between 4.8 and 2.4 V at 25 mA g⁻¹. The capacity fade per cycle over 50 cycles is indicated on each plot. Crosses indicate the discharge capacity of a directly prepared spinel material, $\text{LiNi}_{0.15}\text{Mn}_{1.85}\text{O}_4$, cycled under the same conditions.

Ultimately, it is desired to have a high first discharge capacity, followed by good capacity retention over a large number of cycles. Except for $y = 0$, the materials show an increase in capacity initially and then a gradual capacity loss. The capacity retention is calculated between the cycle number at which the maximum capacity occurs, and cycle 50.

It is clear that the Ni doped materials can be cycled in the 4.8 to 2.4 V region with an improved capacity retention compared to both spinel and undoped layered ($y = 0$) Li_xMnO_2 . The undoped sample exhibits a high initial capacity of 225 mA h g⁻¹, but this falls rapidly to 120 mA h g⁻¹

after 35 cycles, with almost the same fade as the directly prepared spinel material. A high initial capacity that then fades substantially is of little use in the context of rechargeable batteries.

The data demonstrate that as little as 2.5% Ni is required to improve the cycling performance, and the cathode materials doped with 2.5 % and 7.5 % Ni display the lowest capacity fade rate, 0.7 $\text{mA h g}^{-1} \text{ cycle}^{-1}$. The highest Ni substitution levels with $y = 0.1$ and 0.2 show higher capacity fade rates.

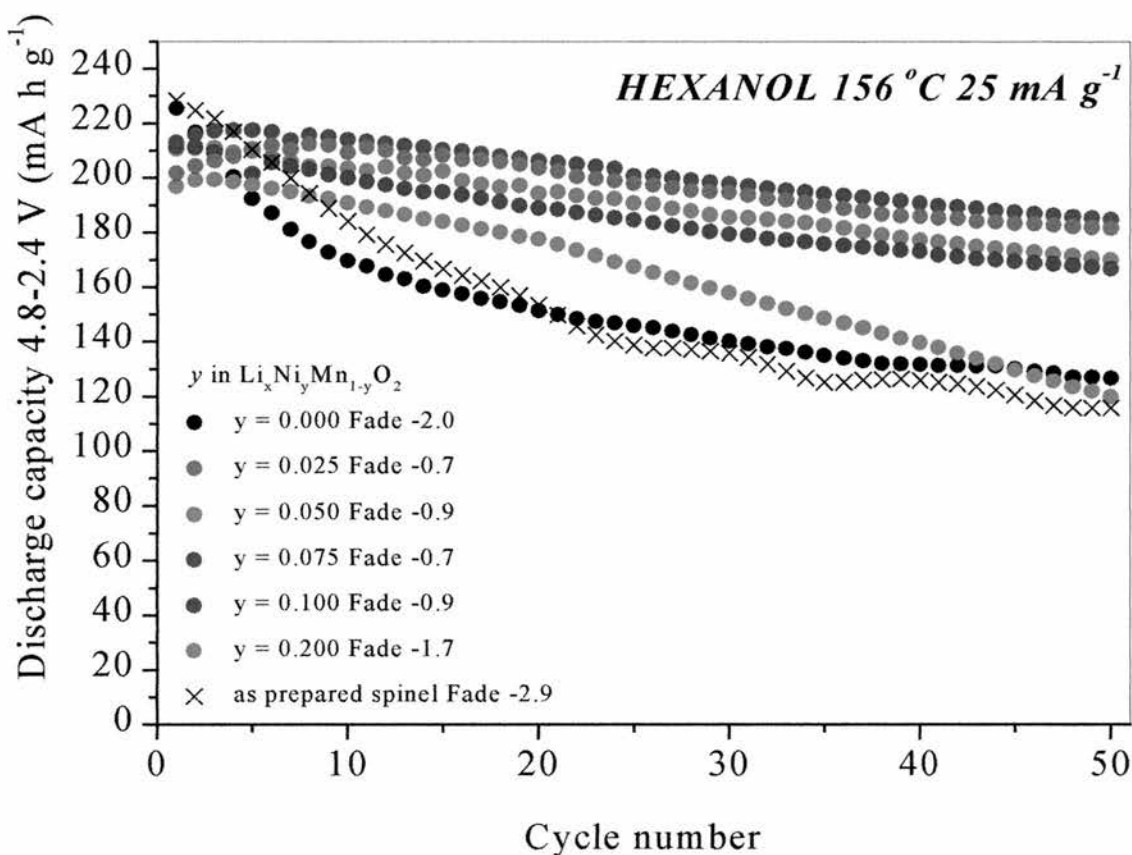


Figure 4.8 Discharge capacities of $\text{Li}_x\text{Ni}_y\text{Mn}_{1-y}\text{O}_2$ (refluxed in hexanol) as a function of the number of charge-discharge cycles. Voltage range 4.8 to 2.4 V, current density 25 mA g^{-1} . Fade rates are indicated in $\text{mA h g}^{-1} \text{ cycle}^{-1}$, between the cycle number at maximum capacity and cycle 50.

It was shown in Figure 4.2 that the available capacity is split between two potential regions close to 3V and 4V. The cycling performance of Figure 4.8 is therefore the combination of the performance within these separate regions. To understand the origin of the discharge capacity behaviour between 4.8 and 2.4 V, the separate discharge capacities over 4 V (between 4.8 and 3.5 V) and 3 V (between 3.5 and 2.4 V) have been examined. These voltage limits correspond to minimum values of the differential capacity ($|dQ/dV|$) during discharge, for example in Figure 4.4.

The origin of the capacity losses in Figure 4.8 are made clearer in Figure 4.9, where the capacity from each potential range is presented. Capacity is lost immediately for the undoped and spinel materials over both 3 and 4 V. The loss for the undoped layered material is however, more significant over 3 V than it is over 4V. This observation is consistent with a degradation mechanism at an early stage of cycling that is associated with a severe Jahn-Teller effect, indicating that the electrode was discharge substantially into the tetragonal region. However, beyond about cycle 15, while the 3 V region capacity continues to fade, the capacity of the 4 V region remains essentially unchanged. The tetragonal phase change, large lattice change, and subsequent electrical disconnection from the electrode, cannot be responsible for the capacity loss on cycling after 15 cycles, because this would not explain the constant capacity at 4 V.

All doped systems display a rising 3 V capacity and then a fade from 10 cycles onwards. However, this 3 V fade is improved compared to that displayed by the undoped material. The 4 V capacity drops initially and is then very stable, displaying no fade. In fact, the 4 V capacity is most stable, and has the highest value for $y = 0.05$ and 0.075 .

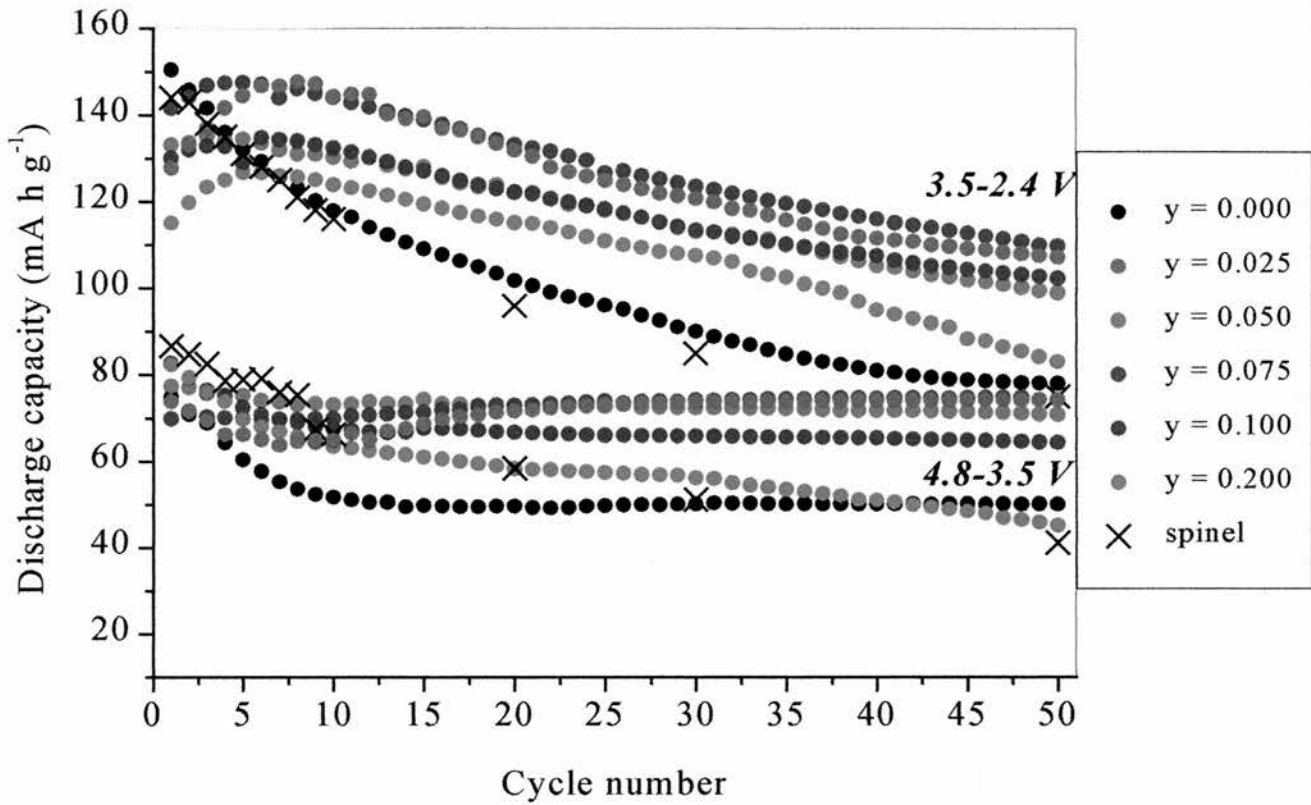


Figure 4.9 The separate 4 and 3 V discharge capacities vs. cycle number for $\text{Li}_x\text{Ni}_y\text{Mn}_{1-y}\text{O}_2$ in the voltage ranges of 4.8 to 3.5 V and 3.5 to 2.4 V respectively. Data was derived from Figure 4.8; the current density used was 25 mA g^{-1} .

4.3.2.2 ELECTROCHEMICAL PERFORMANCE AT 100 mA g^{-1}

A set of cycling data was also obtained, for $0 < y < 0.1$, at the higher current density of 100 mA g^{-1} . The discharge capacities obtained are shown in Figure 4.10, together with the separate discharge capacity contributions from each potential range, 4.8 to 3.5 V and 3.5 to 2.4 V. The discharge capacity fade per cycle is also included.

The results of cycling at 100 mA g^{-1} show similar trends to Figures 4.8 and 4.9. The undoped material displays the worst overall capacity retention, and doping with Ni clearly improves this.

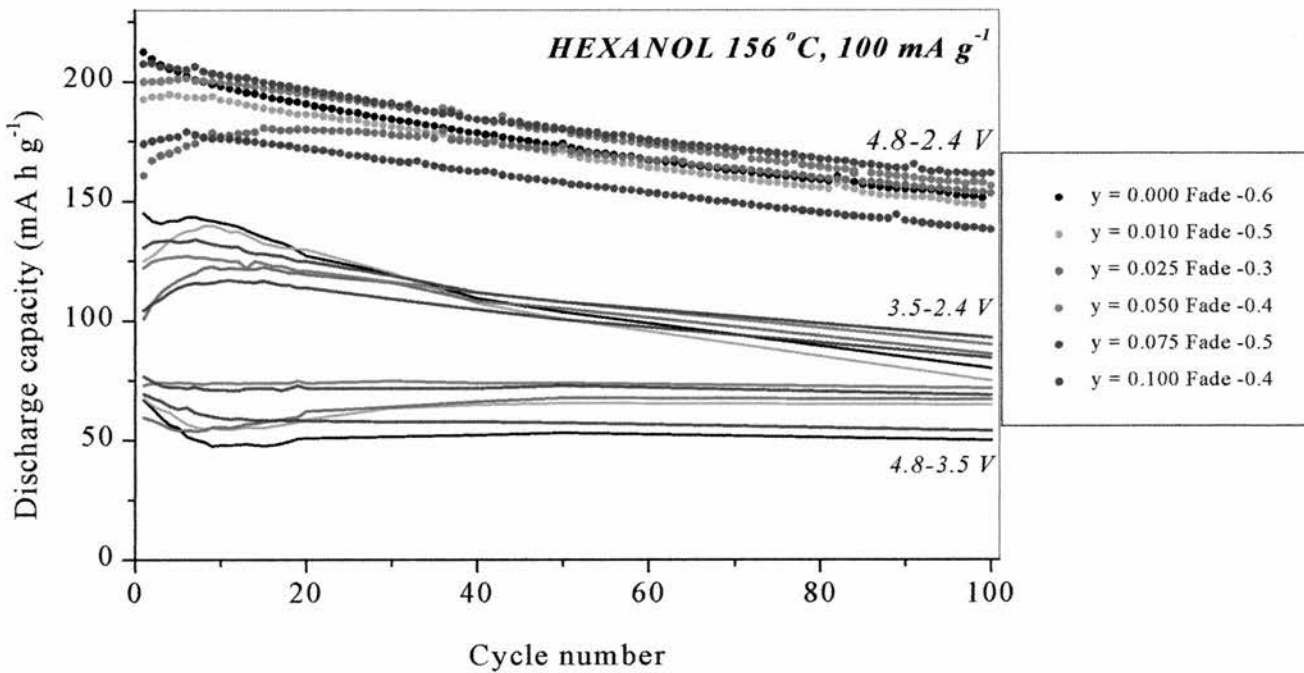


Figure 4.10 Discharge capacities of $\text{Li}_x\text{Ni}_y\text{Mn}_{1-y}\text{O}_2$ refluxed in hexanol as a function of the number of charge-discharge cycles, (circles). Current density 100 mA g^{-1} . Fade rates are indicated in $\text{mA h g}^{-1} \text{ cycle}^{-1}$. The lines represent the separate discharge capacities in the voltage ranges 4.8 to 3.5 V and 3.5 to 2.4 V.

4.3.2.3 STRUCTURAL CHANGES ON CYCLING

The evolution of structural and electrochemical characteristics, on extended cycling of the Ni doped materials prepared in hexanol, is presented. Figure 4.11 shows the 1st, 3rd, 5th, 8th, 12th and 30th cycle incremental capacity plots for the material with $y = 0.075$. It is clear that the first charge is markedly different from subsequent charges. A large part of the capacity during the first charge is possibly due to electrolyte decomposition as the capacity exceeds the amount of lithium initially present in the oxide. This composition does not show signs of a double 4 V process in the electrochemistry until the 5th cycle, (blue line), and there is more evidence for this by cycle 8, (green line). The establishment of spinel-like regions by cycle 8 is later than was observed for 2.5 % Ni doping, where there was the suggestion of a double 4 V process in the first cycle, Figure 4.5. It is also evident from Figure 4.11 that the establishment of spinel-like regions is irreversible, and once formed the structure remains spinel-like on subsequent cycling, since the position of the 4 V peak is invariant for all cycles.

Another feature exists in addition to the signature for spinel transformation. There is a well defined capacity peak at 3.68 V on oxidation, and this is observed in all materials. It has previously been seen in spinels cycled in a wide voltage range,⁸ including Co doped spinels.⁹ There is so far no explanation for this peak.

Evidence for the evolution of the spinel like characteristics has also been observed by *ex-situ* x-ray diffraction data. Figure 4.12 shows the patterns obtained from materials with $y = 0.075$ after 3, 5, 8 and 12 cycles, these cycle numbers correspond to the incremental capacity plots of Figure 4.11. Patterns of the pristine layered $\text{Li}_x\text{Ni}_{0.07}\text{Mn}_{0.88}\text{O}_2$, (black line) and a manganese oxide spinel, (grey line), are also presented for comparison in 4.12(a) and (f) respectively.

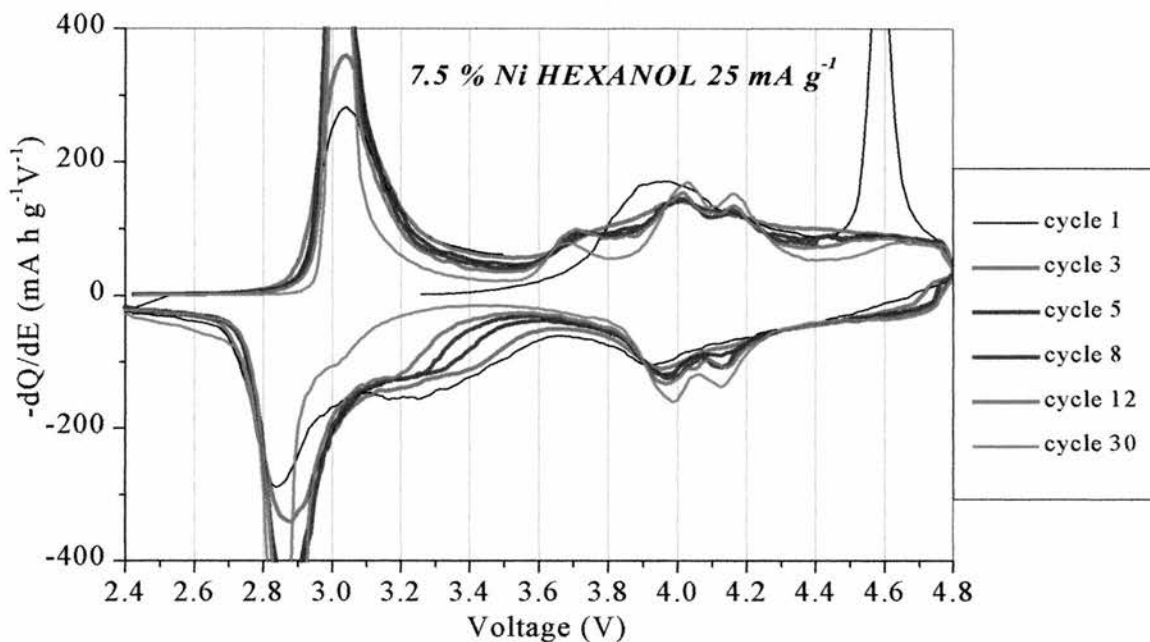


Figure 4.11 Incremental capacity plots from the cycling of a 7.5% Ni doped material, prepared by ion exchange in hexanol, 25 mA g^{-1} . Data derived from Figure 4.8.

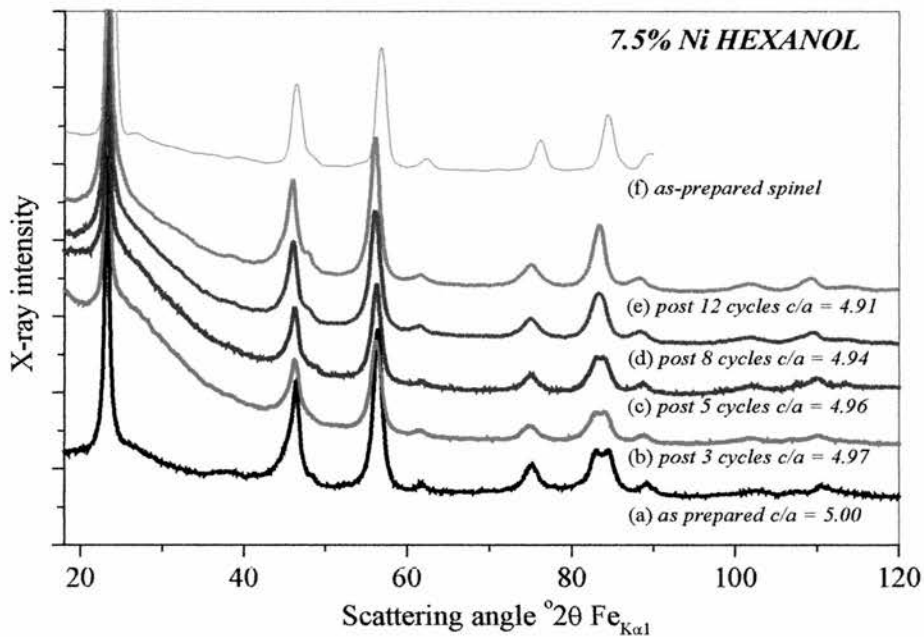


Figure 4.12 Powder x-ray diffraction patterns taken from cycled cathode materials for the composition $y = 0.075$, prepared by ion exchange in hexanol. Voltage range 4.8 to 2.4 V, current density 25 mA g^{-1} .

The x-ray diffraction patterns clearly indicate a change from the as-prepared layered structure after 8 cycles. In the as-prepared material, Figure 4.12(a) the 018 and 110 reflections are visible, and after only 8 cycles, Figure 4.12(d), these are seen to merge on cycling. The lattice parameters of the cycled materials in Figure 4.12 were refined, and the c/a ratios are presented. Closer examination suggests that after 8 cycles, with a lattice distortion of 4.94, the material is not entirely cubic, since this is still greater than 4.91, the lattice distortion after 12 cycles.

Electrochemistry is a sensitive probe of structural changes that extend over dimensions not easily accessible by x-ray diffraction. It is therefore not surprising that spinel formation is apparent at an earlier stage in the incremental capacity plot results, than is the case for x-ray diffraction.

It is thought that the evidence for spinel-like regions is progressively less for the higher Ni doping levels. The trend towards a less facile transition with higher Ni content is consistent with the fact that the Ni rich end member of this solid solution series LiNiO_2 is stable as a layered phase. To investigate this, the 5th cycle incremental capacity plots for various y , are correlated with the corresponding x-ray diffraction patterns.

The 5th cycle incremental capacity plots for all y , ($0 < y < 0.2$), are shown in Figure 4.13 in the region between 3.5 and 4.5 V. There are obvious spinel like characteristics evident in the 5th cycle for $y < 0.05$. For increased Ni contents, $y \geq 0.075$, the double 4 V peak is less pronounced, although it is present, very subtly even for $y = 0.2$. It is also interesting to observe that there is increased capacity for the higher Ni contents close to 4.37 V, indicating that Ni^{2+} ions are still active in the 5th cycle.

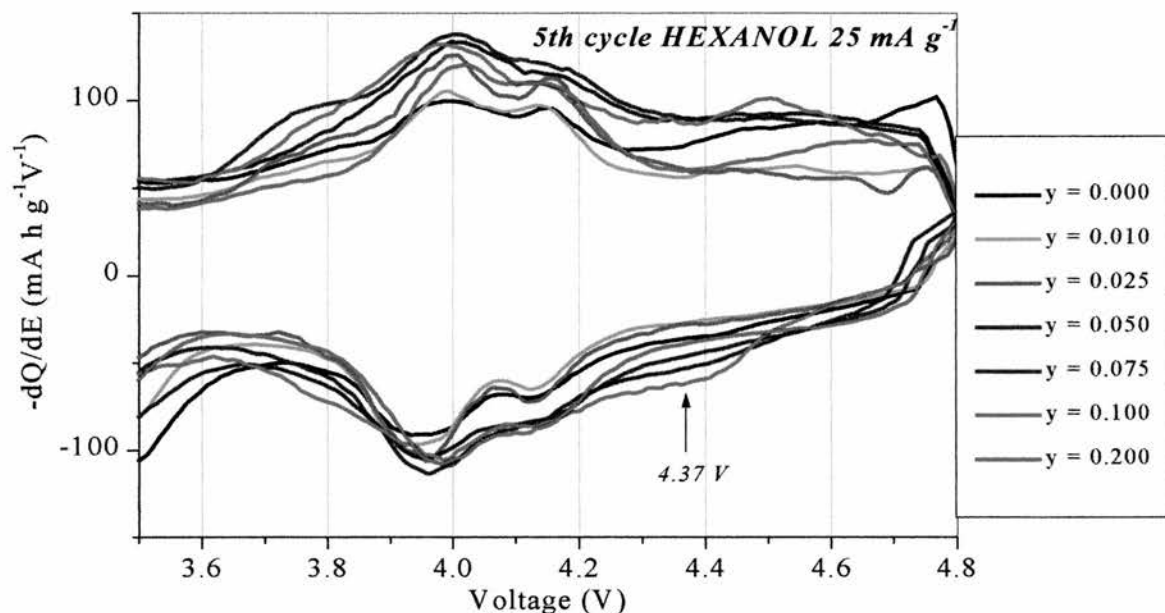


Figure 4.13 Incremental capacity plots corresponding to the 5th cycle of all $\text{Li}_x\text{Ni}_y\text{Mn}_{1-y}\text{O}_2$ materials prepared by ion exchange in hexanol. Voltage range = 4.8 to 2.4 V, current density = 25 mA g⁻¹.

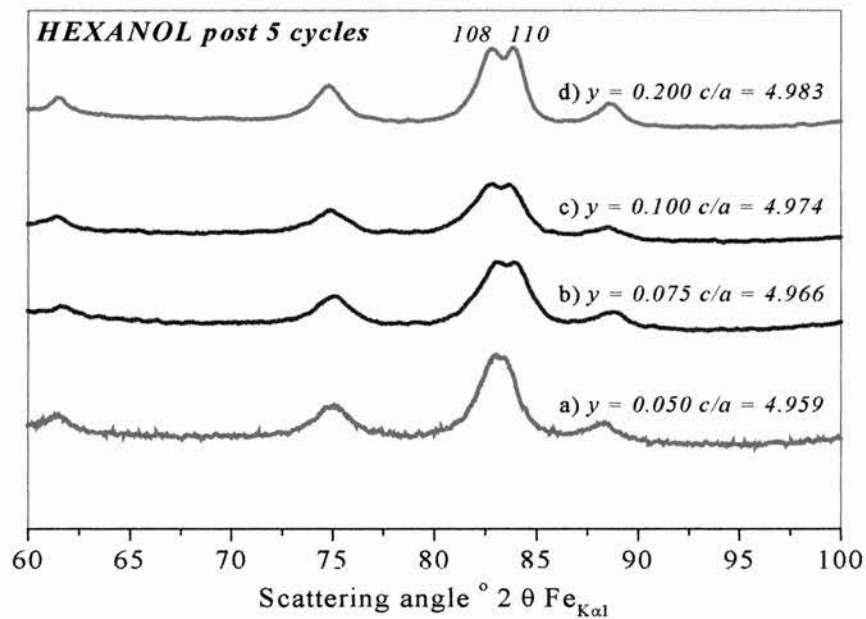


Figure 4.14 Powder x-ray diffraction patterns taken from cathode materials stopped at 3.5 V after 5 cycles at 25 mA g⁻¹, 2.4 to 4.8 V. a) 5% Ni, b) 7.5 % Ni, c) 10 % Ni and d) 20 % Ni, (hexanol).

The influence the Ni content has, on the conversion from the layered to spinel-like structure, has also been probed by examining the x-ray diffraction patterns for $y = 0.05, 0.075, 0.1$ and 0.2 after 5 cycles. Cycling is stopped at 3.5 V on charge, at which point the samples are single phase. The x-ray diffraction patterns are shown in Figure 4.14, and they agree well with the incremental capacity plots; the conversion to spinel is slower for higher Ni contents. The separation of the 018 and 110 peaks is much more defined for higher Ni contents after the same number of cycles. The c/a ratio after 5 cycles increases from 4.96 for $y = 0.05$, to 4.98 for $y = 0.2$.

Table 4.3 summarises the results of the lattice parameters obtained from cycled materials prepared in hexanol. Figure 4.15 presents these results in the form of a plot of c/a vs. cycle number, and shows that the largest lattice distortion clearly exists in the materials with the highest Ni contents. Figure 4.15 also shows that a c/a ratio of 4.90, the same as the cubic spinel lattice, is achieved after 50 cycles.

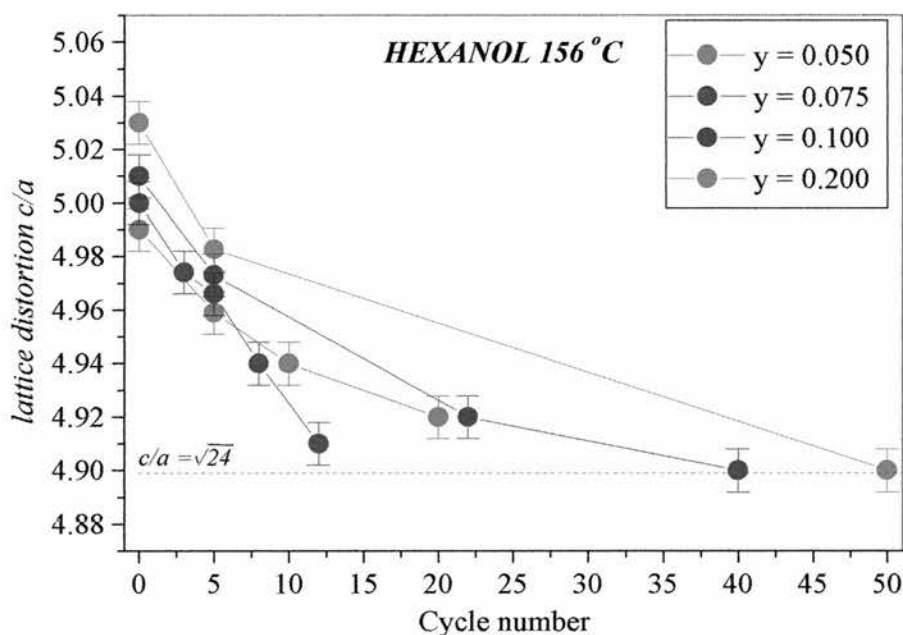


Figure 4.15 A plot of the lattice distortion with cycle number for $\text{Li}_x\text{Ni}_y\text{Mn}_{1-y}\text{O}_2$ prepared in hexanol. Cells were cycled at 25 mA g^{-1} and stopped at 3.5 V on oxidation.

Ni content y	Cycles	$a(\text{\AA})$	$c(\text{\AA})$	$c/a (\pm 0.01)$
0.050	0	2.8874 ± 0.0006	14.399 ± 0.002	4.99
	5	2.9052 ± 0.0004	14.407 ± 0.003	4.96
	10	2.9069 ± 0.0004	14.359 ± 0.002	4.94
	20	2.9052 ± 0.0003	14.279 ± 0.002	4.91
0.075	0	2.8841 ± 0.0003	14.415 ± 0.002	5.00
	3	2.8939 ± 0.0004	14.396 ± 0.002	4.97
	5	2.8953 ± 0.0005	14.378 ± 0.003	4.96
	8	2.9069 ± 0.0004	14.364 ± 0.002	4.94
	12	2.9131 ± 0.0006	14.305 ± 0.002	4.91
0.100	0	2.8761 ± 0.0004	14.418 ± 0.002	5.01
	5	2.9022 ± 0.0004	14.435 ± 0.002	4.97
	22	2.9090 ± 0.0003	14.313 ± 0.002	4.92
	40	2.9166 ± 0.0004	14.299 ± 0.003	4.90
0.200	0	2.8784 ± 0.0004	14.467 ± 0.002	5.03
	5	2.8980 ± 0.0003	14.440 ± 0.003	4.98
	50	2.9161 ± 0.0004	14.288 ± 0.002	4.90
0.200	0	2.8784 ± 0.0004	14.467 ± 0.002	5.03
	5	2.8980 ± 0.0003	14.440 ± 0.003	4.98
	50	2.9161 ± 0.0004	14.288 ± 0.002	4.90

Table 4.3 Lattice parameters obtained of cycled $\text{Li}_x\text{Ni}_y\text{Mn}_{1-y}\text{O}_2$ materials prepared by hexanol reflux.

4.3.3 $\text{Li}_x\text{Ni}_y\text{Mn}_{1-y}\text{O}_2$ PREPARED IN ETHANOL, 78 °C

4.3.3.1 AS-PREPARED MATERIAL

The main differences between the as-prepared materials from an ethanol reflux, compared to hexanol, were discussed in chapter three. They were found to have a higher c/a ratio (5.10 vs. 5.00), and more residual sodium and transition metal vacancies following exchange. As a result the manganese oxidation state for materials prepared in ethanol is slightly higher, (3.65 vs. 3.45).

4.3.3.2 ELECTROCHEMICAL PERFORMANCE AT 25 mA g⁻¹

The influence of the Ni content, on the variation of discharge capacities for materials prepared in ethanol at 78 °C is shown in Figure 4.16. Cycling was carried out under identical conditions as for the materials prepared in hexanol. The current density was 25 mA g⁻¹ and the potential range used was from 2.4 to 4.8 V. The discharge capacities display first, a decrease in capacity, and then, after cycle number n , a slight increase. Then the capacity continuously fades, the fade per cycle, after cycle number n , up to cycle 50 is presented in Figure 4.16.

For the lowest dopant levels, $0.01 < y < 0.05$, the capacity is always in excess of 200 mA h g⁻¹, and all fade rates have improved, compared to materials prepared in hexanol. The best performance is obtained for a dopant level of 2.5 % Ni. The first discharge capacity for this material is 220 mA h g⁻¹, with a fade rate of only 0.2 mA h g⁻¹ per charge/discharge cycle up to the 50th cycle. For the same material prepared in hexanol the first discharge capacity was around 203 mA h g⁻¹ with a fade rate of 0.7 mA h g⁻¹ cycle⁻¹. Given the performance of the material prepared in ethanol with 2.5 % Ni, coupled with the significant cost advantage of a minimal nickel content, this material represents an interesting intercalation compound in the context of new positive electrodes for lithium rechargeable batteries. It is a significant

improvement compared with the earlier stoichiometric LiMnO_2 which has a practical capacity of 130 mA h g^{-1} . Comparisons with the capacities and energy densities reported for LiCoO_2 and LiMn_2O_4 also shows that Ni doped LiMnO_2 prepared in ethanol also has promise for practical application in lithium ion batteries.¹⁰

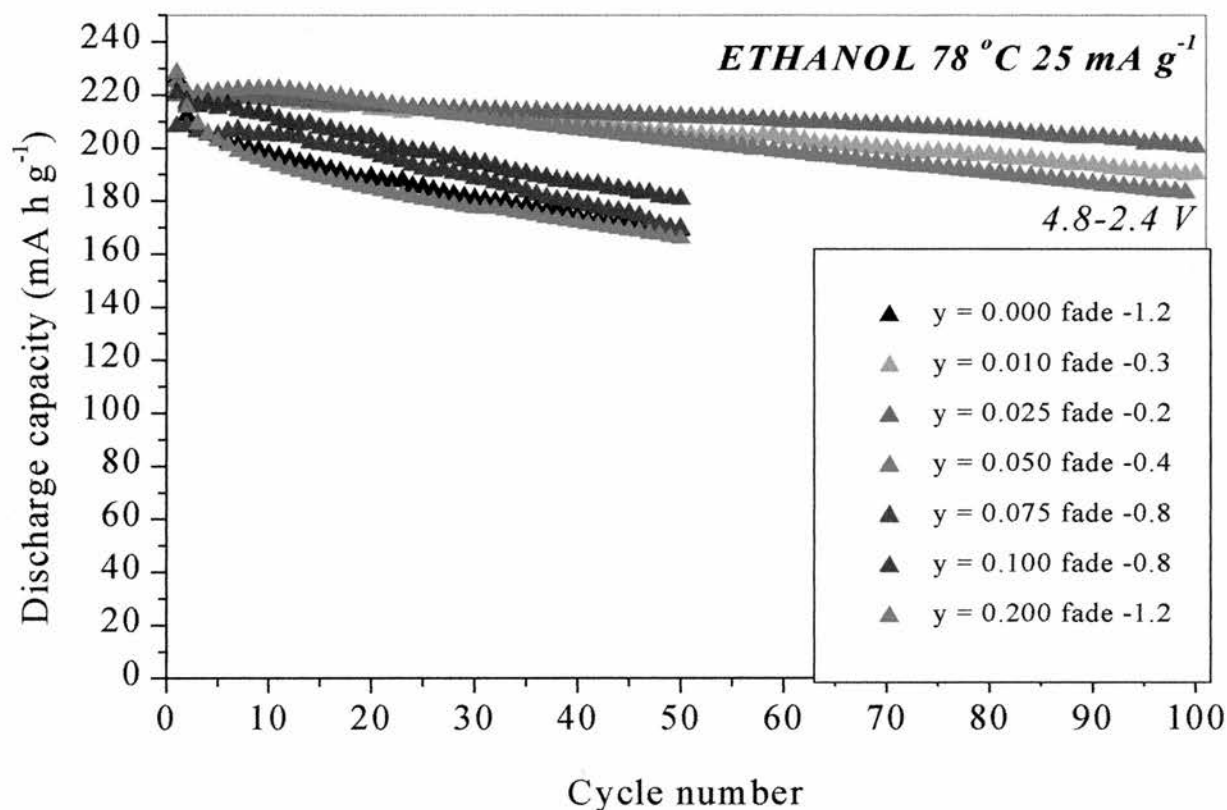


Figure 4.16 Comparison of discharge capacities for $\text{Li}_x\text{Ni}_y\text{Mn}_{1-y}\text{O}_2$ materials prepared in ethanol at 78 °C. Current density = 25 mA g^{-1} , potential range 2.4 to 4.8 V. The fade rate indicated is from the cycle number at maximum capacity n , to cycle 50.

Figure 4.17 compares the separate capacities over 3 V and 4 V for all Ni dopant levels prepared in ethanol. For all doped compositions the capacity trends behave differently above and below about cycle number ten. It is clear that Ni doping significantly improves the fade over 3 V and that for all materials, after the 10th cycle, the capacity is relatively stable.

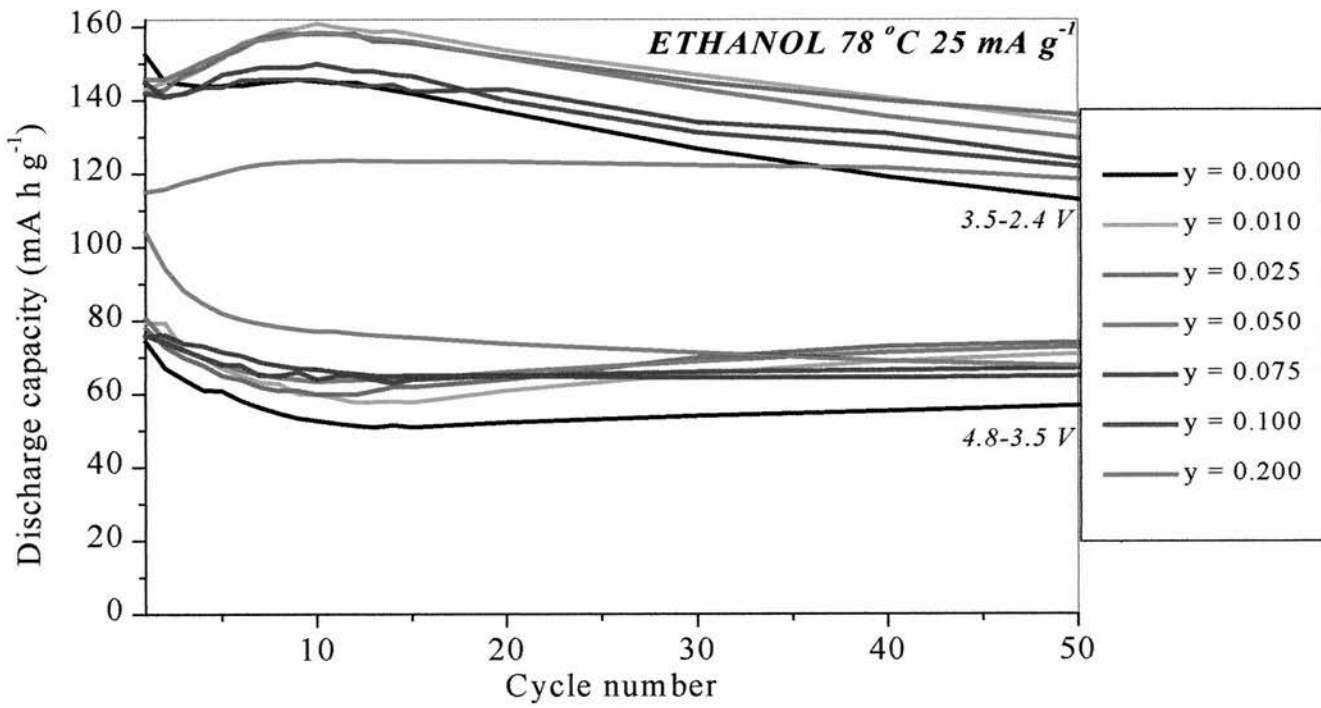


Figure 4.17 4 and 3 V plateau discharge capacities are shown by the coloured lines, derived from the data in Figure 4.16, in the potential ranges 4.8 to 3.5 V and 3.5 to 2.4 V respectively.

4.3.3.3 STRUCTURAL CHANGES ON CYCLING

Evolution of the structural changes during cycling the materials prepared in ethanol has been investigated by x-ray diffraction and incremental capacity plots. For the composition $y = 0.075$, Figure 4.18 shows that the 110 and 018 peaks merge between 15 and 24 cycles. This is in contrast to Figure 4.11 where for the same Ni dopant level, but prepared in hexanol, the merging of the peaks was clearly seen to occur between 8 and 12 cycles. Refinement of the lattice parameters has allowed the lattice distortion to be monitored and a reduction in c/a to 4.92 after 33 cycles is evidence for a spinel-like structure formation. Figure 4.12 shows the corresponding incremental capacity plots for the cycle numbers at which the x-ray diffraction patterns were obtained. Double 4 V characteristics are detected by cycle 24, in agreement with x-ray diffraction.

It appears therefore, that the conversion to a spinel-like structure is slowed for a lower ion exchange preparation temperature. Figure 4.12 also shows that the reduction peak at 4.37 V, thought to be due to Ni reduction, reduces on cycling.

The 20th cycle incremental capacity plots for all materials prepared in ethanol are shown in Figure 4.13. It is again confirmed that the conversion to spinel is slower for higher Ni contents, since after 20 cycles there is still no evidence of a double 4 V peak for $y = 0.1$ and 0.2 .

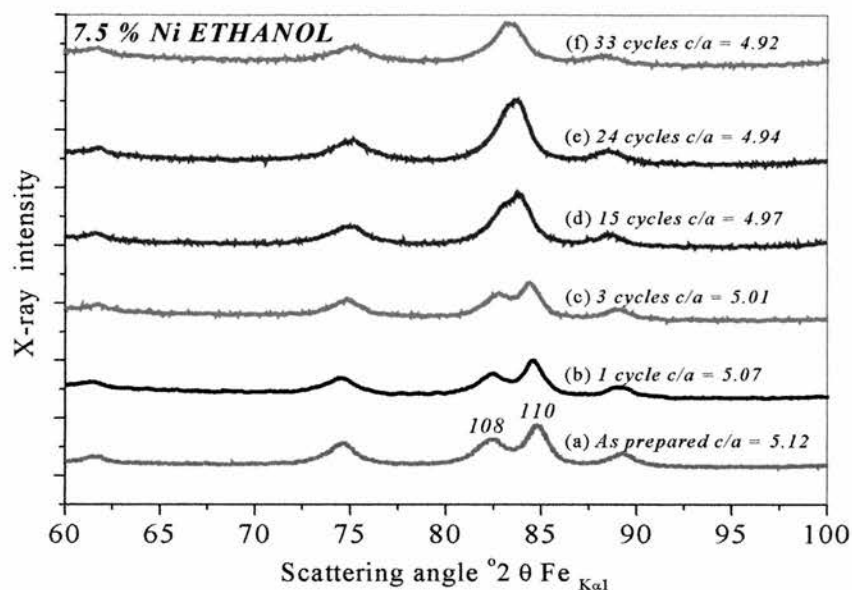


Figure 4.18 Powder x-ray diffraction patterns obtained from cycled cathode materials with the composition $y = 0.075$, prepared by ion exchange in ethanol at 78°C . (a) as-prepared, (b) post 1 cycle, (c) post 3 cycles, (d) post 15 cycles, (e) post 24 cycles and (f) post 33 cycles.

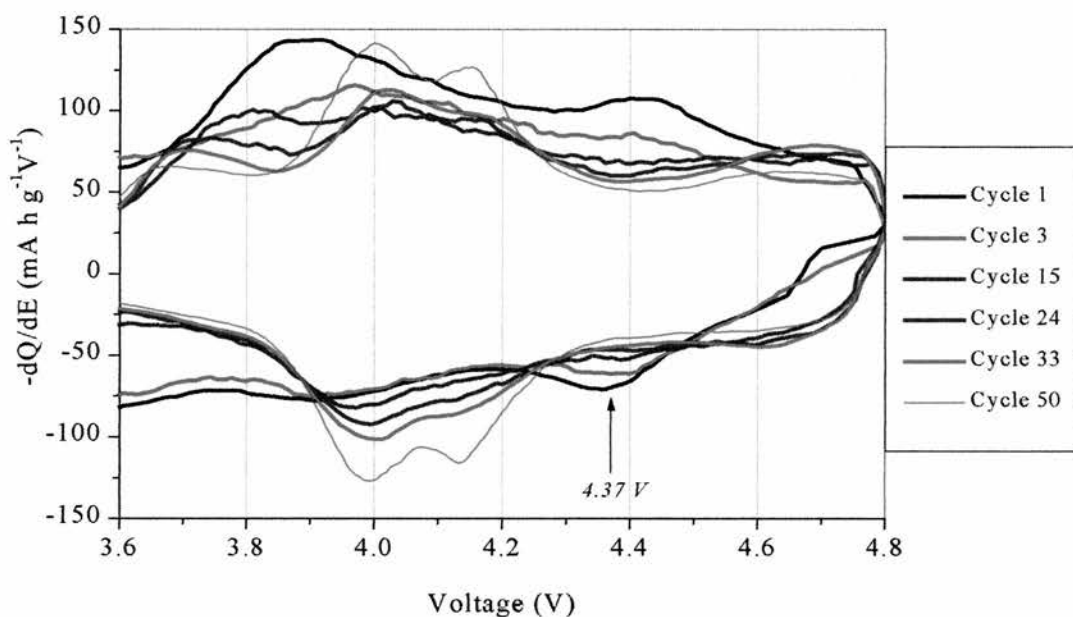


Figure 4.19 Incremental capacity plots corresponding to the cycling of 7.5% Ni doped material ion exchanged in ethanol. Data derived from Figure 4.16.

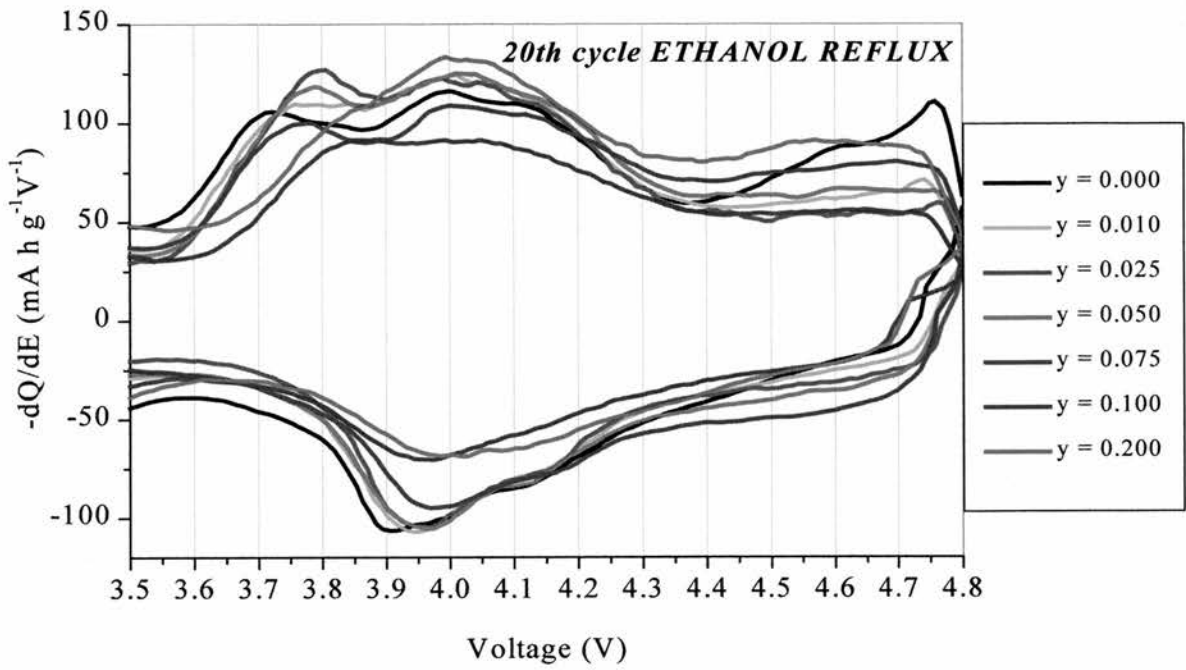


Figure 4.20 20th cycle incremental capacity plot for all Ni contents y .

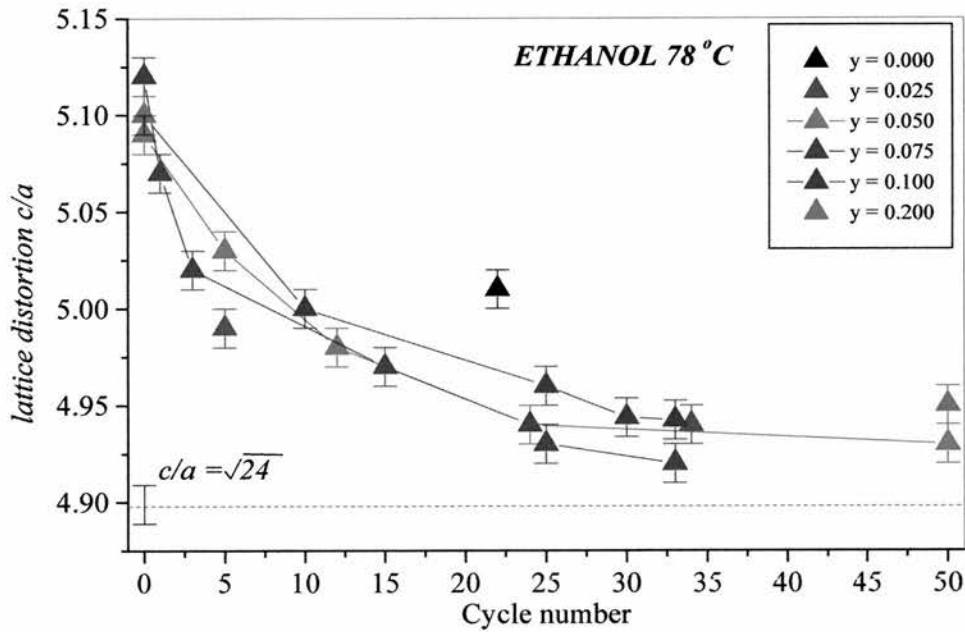


Figure 4.21 A plot of the lattice distortion with cycle number for $\text{Li}_x\text{Ni}_y\text{Mn}_{1-y}\text{O}_2$, prepared in ethanol at 78 °C. Cells were cycled at 25 mA g⁻¹ and stopped at 3.5 V on oxidation. Lattice parameters a and c were obtained from x-ray diffraction data.

Ni content y	Cycles	a (\AA)	c (\AA)	c/a ± 0.01
0.000	0	2.8605 ± 0.0005	14.635 ± 0.002	5.12
	22	2.8932 ± 0.0004	14.505 ± 0.002	5.01
0.025	0	2.8713 ± 0.0005	14.485 ± 0.002	5.04
	5	2.8957 ± 0.0003	14.451 ± 0.003	4.99
	34	2.9019 ± 0.0004	14.349 ± 0.003	4.94
0.050	0	2.8703 ± 0.0006	14.623 ± 0.002	5.09
	5	2.8882 ± 0.0003	14.520 ± 0.002	5.03
	12	2.8991 ± 0.0004	14.450 ± 0.002	4.98
	24	2.9066 ± 0.0004	14.357 ± 0.002	4.94
	50	2.9073 ± 0.0004	14.330 ± 0.002	4.93
0.075	0	2.8652 ± 0.0004	14.549 ± 0.002	5.08
	1	2.8766 ± 0.0005	14.588 ± 0.003	5.07
	3	2.8826 ± 0.0004	14.457 ± 0.002	5.02
	15	2.8975 ± 0.0006	14.404 ± 0.002	4.97
	24	2.9002 ± 0.0007	14.340 ± 0.002	4.94
	25	2.9018 ± 0.0005	14.316 ± 0.002	4.93
	33	2.9111 ± 0.0005	14.325 ± 0.003	4.92
	0.100	0	2.8683 ± 0.0004	14.628 ± 0.002
0.100	10	2.8957 ± 0.0006	14.459 ± 0.002	5.00
	25	2.8988 ± 0.0006	14.391 ± 0.002	4.96
	30	2.9070 ± 0.0007	14.371 ± 0.002	4.94
	33	2.9050 ± 0.0004	14.358 ± 0.002	4.94
	0.200	0	2.8710 ± 0.0004	14.600 ± 0.002
0.200	50	2.8985 ± 0.0005	14.349 ± 0.002	4.95

Table 4.4 Lattice parameters obtained by GSAS refinement of x-ray diffraction patterns taken from cycled $\text{Li}_x\text{Ni}_y\text{Mn}_{1-y}\text{O}_2$ prepared in ethanol at 78 °C.

Table 4.4 lists the full set of refined lattice parameters for cycled materials originally prepared in ethanol at 78 °C. The lattice distortion, c/a with cycle number has been plotted in Figure 4.21. Again it is greater for materials with higher Ni contents. Even after 50 cycles, a slight lattice distortion still exists, the c/a ratio is 4.93 and 4.95 for $y = 0.05$ and 0.2 respectively. This is in contrast to the materials prepared in hexanol where complete conversion to a cubic lattice displaying a c/a ratio of 4.9 was attained after 50 cycles.

4.3.4 $\text{Li}_x\text{Ni}_y\text{Mn}_{1-y}\text{O}_2$ PREPARED IN ETHANOL AT 25 °C

The results from cycling Ni doped $\text{Li}_x\text{Ni}_y\text{Mn}_{1-y}\text{O}_2$ materials prepared at the lowest temperature, in ethanol at 25 °C, show very similar trends to those observed previously, so an overview will be given. Figure 4.22 shows the evolution of the discharge capacities during galvanostatic cycling of materials prepared in ethanol at 25 °C. The voltage range used was again between 4.8 and 2.4 V at 25 mA g⁻¹.

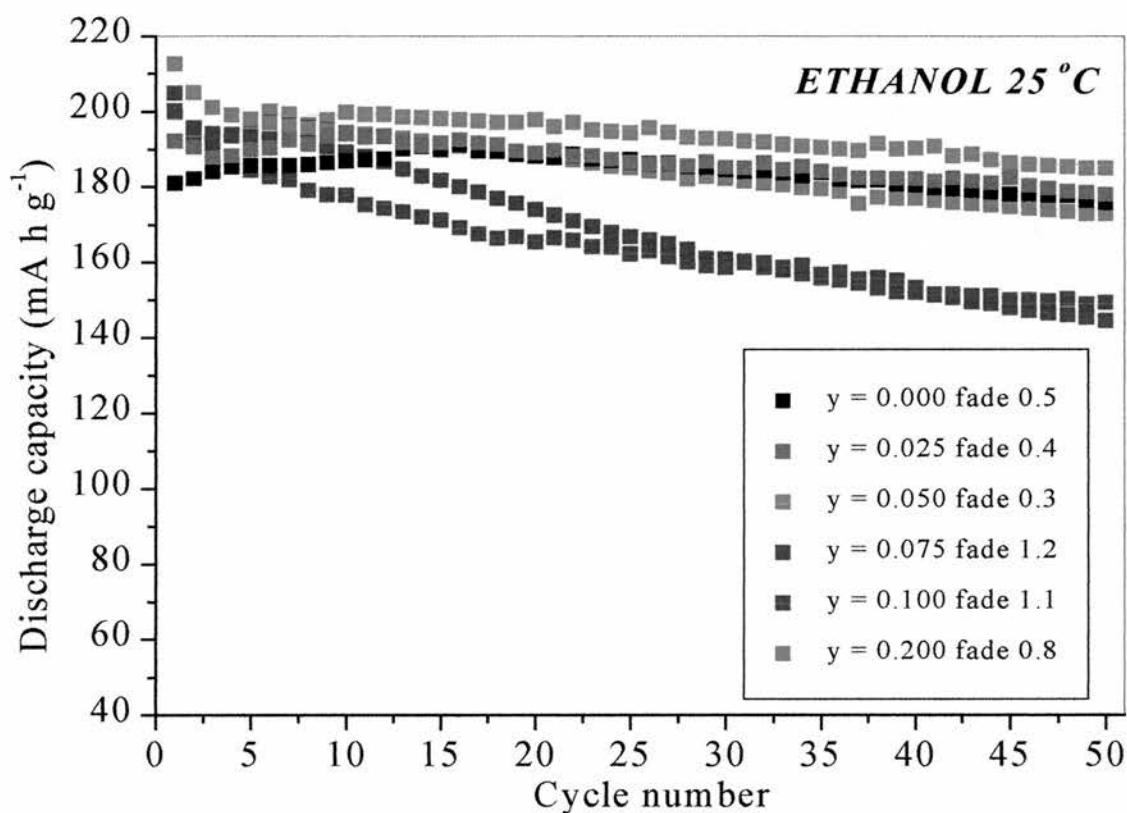


Figure 4.22 Discharge capacity vs. cycle number for $\text{Li}_x\text{Ni}_y\text{Mn}_{1-y}\text{O}_2$ prepared by ion exchange at 25 °C in ethanol.

It was shown in section 4.2.3 that only the materials prepared at 25 °C displayed a clear increase in first discharge capacity with increasing Ni content. The increase was attributed to the possible Ni oxidation/reduction which occurs close to 4 V. On subsequent cycling, the

discharge capacity increases over the first 12 cycles for $y \leq 0.05$. The capacity fade for all y , following the maximum capacity is indicated in Figure 4.22. Compared to materials prepared at 78 °C in ethanol, ion exchanging at 25 °C has not significantly improved the capacity retention.

Considering all the compositions exchanged at 25 °C in ethanol, the best performance is obtained for 5 % Ni. The first discharge capacity for this material is 199 mA h g^{-1} , which increases over the first 12 cycles, the fade rate after this is $0.3 \text{ mA h g}^{-1} \text{ cycle}^{-1}$. This is only a small improvement on the same composition prepared by reflux in either ethanol or hexanol. which displayed fade rates of 0.4 and 0.9 mA h g^{-1} respectively.

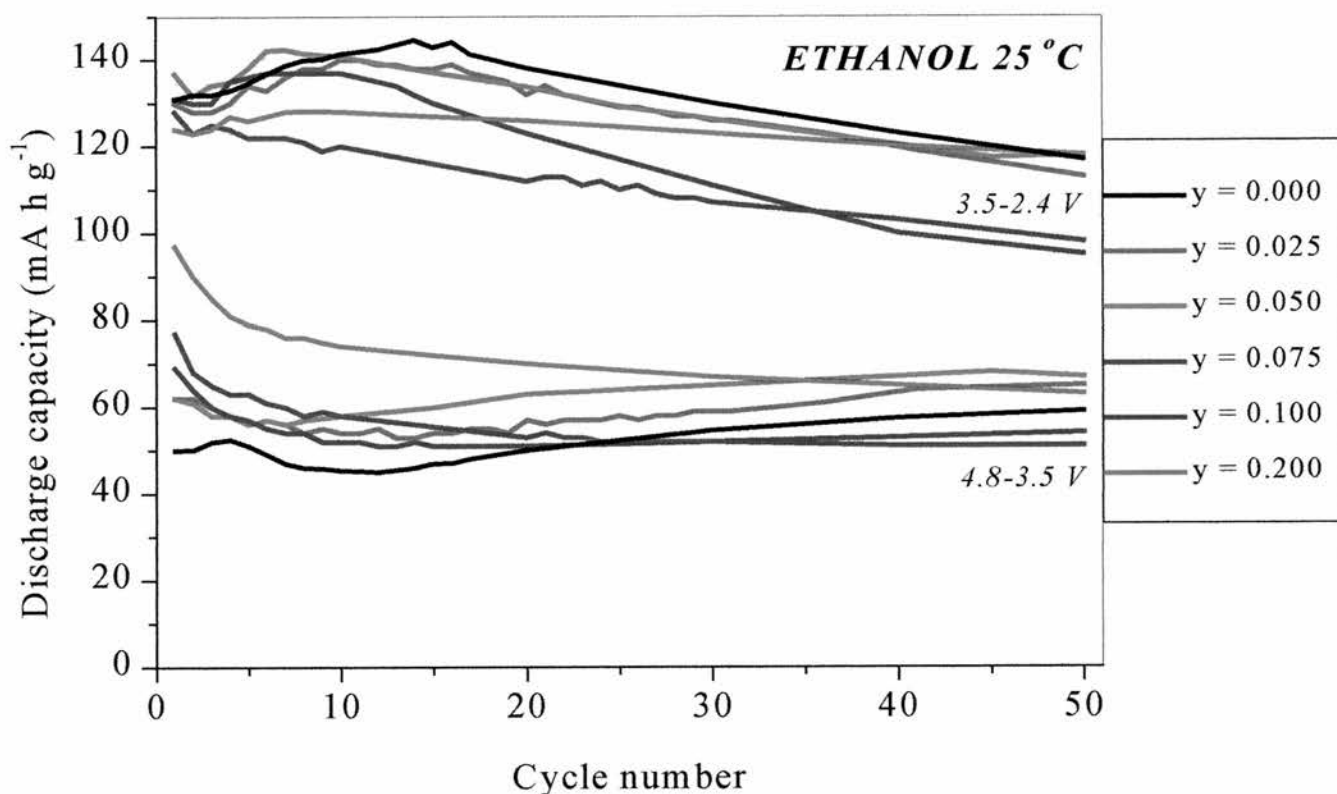


Figure 4.23 4 and 3 V plateau discharge capacities vs. cycle number for $\text{Li}_x\text{Ni}_y\text{Mn}_{1-y}\text{O}_2$ prepared at 25 °C. 4 and 3 V capacities were calculated in the voltage ranges of 4.8 to 3.5 V and 3.5 to 2.4 V respectively, Current density 25 mA g^{-1} .

Figure 4.23 compares the capacities of the 3 V and 4 V plateaus for all Ni dopant levels prepared in ethanol at 25 °C. The trends in capacity retention within each voltage range are the same as those seen for ethanol and hexanol materials. Again the capacity retention in the 3V region improves with Ni doping. There is clearly an anomaly in the 3 V capacity fade rate for $y = 0.075$ resulting in the poor performance of this composition.

The x-ray diffraction patterns obtained from two cycled materials, $y = 0.1$ and 0.2 , both prepared in ethanol at 25 °C, are shown in Figure 4.24, in the 2θ range 60° to 100° . As expected, the lattice distortion after 17 cycles is greater for the higher Ni doped material, despite both materials being subjected to 17 cycles under the same cycling conditions. The corresponding 17th cycle incremental capacity plots are presented in Figure 4.25 and show that both materials still display layered characteristics at this stage of cycling. However, spinel-like characteristics are observed electrochemically in both materials after 40 cycles.

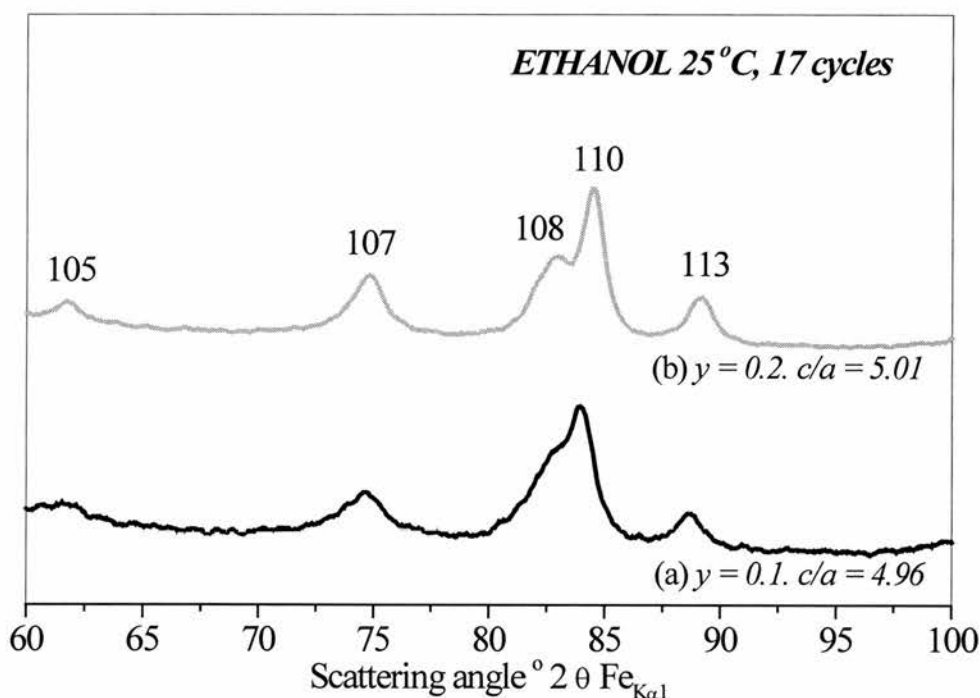


Figure 4.24 X-ray diffraction patterns of materials originally ion exchanged in ethanol at 25 °C after 17 cycles. a) 10% Ni, b) 20% Ni.

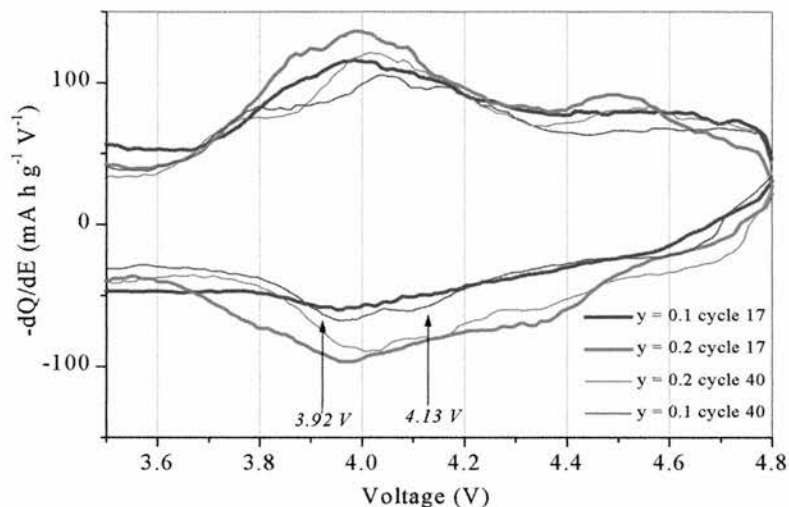


Figure 4.25 Incremental capacity plots showing no spinel characteristics up to 17 cycles for the 10 and 20 % Ni doped materials. After 40 cycles there is evidence for spinel-like characteristics.

Ni content y	Cycle number	a (Å)	c (Å)	c/a
0.025	0	2.8689 ± 0.0004	14.682 ± 0.002	5.12
	5	2.8981 ± 0.0003	14.487 ± 0.003	5.00
	50	2.9088 ± 0.0004	14.343 ± 0.002	4.93
0.050	0	2.8601 ± 0.0004	14.595 ± 0.003	5.10
	10	2.8969 ± 0.0006	14.500 ± 0.002	5.01
	20	2.9011 ± 0.0005	14.441 ± 0.002	4.98
	45	2.9099 ± 0.0006	14.301 ± 0.002	4.91
0.075	0	2.8626 ± 0.0006	14.652 ± 0.002	5.12
	30	2.9126 ± 0.0007	14.337 ± 0.002	4.92
	50	2.9152 ± 0.0006	14.285 ± 0.002	4.90
0.100	0	2.8633 ± 0.0006	14.636 ± 0.002	5.11
	17	2.9011 ± 0.0006	14.400 ± 0.002	4.96
	26	2.9116 ± 0.0005	14.327 ± 0.002	4.92
0.200	0	2.8698 ± 0.0005	14.647 ± 0.002	5.10
	17	2.8827 ± 0.0004	14.459 ± 0.002	5.01

Table 4.5 Lattice parameters obtained from cycled $\text{Li}_x\text{Ni}_y\text{Mn}_{1-y}\text{O}_2$ cathode materials, prepared by ion exchange in ethanol at 25 °C.

Table 4.5 lists the full set of refined lattice parameters for cycled materials prepared in ethanol at 25 °C. The lattice distortion is again greater for higher Ni contents, and the c/a ratio reduces as far as 4.9 after 50 cycles.

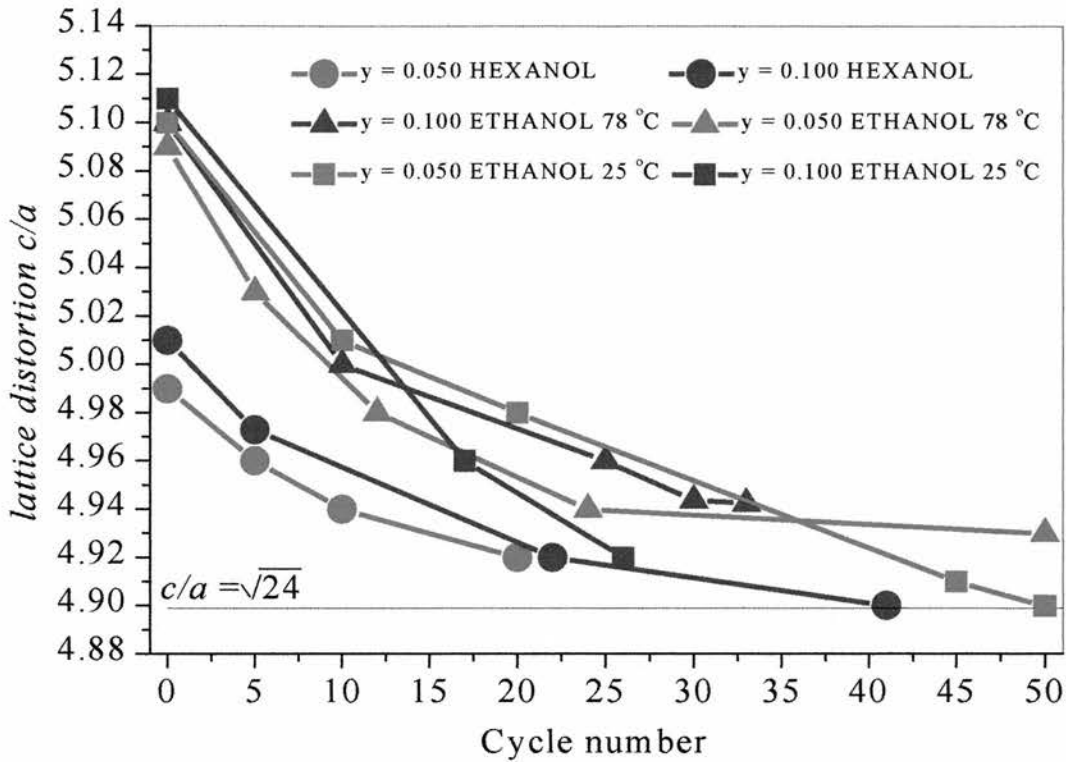


Figure 4.26 Change in lattice parameters during cycling for Ni doped materials, $y = 0.05$ (red) and $y = 0.1$ (blue), for all ion exchange conditions. (circles = hexanol, triangles = ethanol 78 °C, squares = ethanol 25 °C).

Figure 4.26 summarises the lattice distortion results obtained after cycling two Ni compositions. The lattice distortion of materials doped with 5% Ni has been plotted in red, and 10 % Ni in blue. Results are shown for both compositions ion exchanged under each of the three conditions. Circles represent materials prepared in hexanol, triangles represent materials prepared in ethanol at 78 °C and squares represent materials prepared in ethanol at 25 °C, the lines have been put in to show the trends more clearly

As expected the lattice distortion reduces with cycle number, and as shown earlier, it is always smallest for materials prepared in hexanol (circles). For materials prepared in ethanol at either temperature, (squares and triangles), the lattice distortions at each stage of cycling are very

similar. At all cycle numbers the lattice distortion for each ion exchange condition is generally slightly greater for 10 % Ni (blue) compared to 5 % Ni (red). The behaviour observed here is consistent with the fact that materials prepared in hexanol, and materials with low dopant levels, display higher fade rates and more spinel-like character.

4.3.5 RATE CAPABILITY OF $\text{Li}_x\text{Ni}_{0.05}\text{Mn}_{0.95}\text{O}_2$ ETHANOL REFLUX

For applications it is desirable to have the lowest possible capacity fade rate on cycling. An important practical feature of any lithium intercalation cathode for rechargeable lithium batteries is the extent to which capacity decreases on cycling at higher current densities. To illustrate the rate capability of the material prepared in ethanol, discharge capacities at four different rates are presented for one of the optimum materials (5 % Ni, prepared in ethanol at 78 °C) in Figure 4.27. The initial discharge capacity at 25 mA g⁻¹ is 225 mA h g⁻¹ and after an initial gain in capacity this fades by only 0.4 mA h g⁻¹ per charge/discharge cycle over 100 cycles. The initial discharge capacity at 100 mA g⁻¹ has reduced to 192 mA h g⁻¹. The variation of discharge capacity with cycle number over the first few cycles is strongly dependent on current density. At higher cycle numbers, (higher than 50), the capacity fade appears to be almost unaffected by the current density. The convergence of the fade at higher cycle numbers is reflected in the curves for each voltage region, Figure 4.27.

As well as the absolute discharge capacity it is instructive to consider the voltage the capacity is delivered at, as a function of the state of charge, and how the voltage curve might be influenced by the current density. In Figure 4.28 the 30th cycle load curves for four current densities are shown. The basic shape of the curve is invariant with rate.

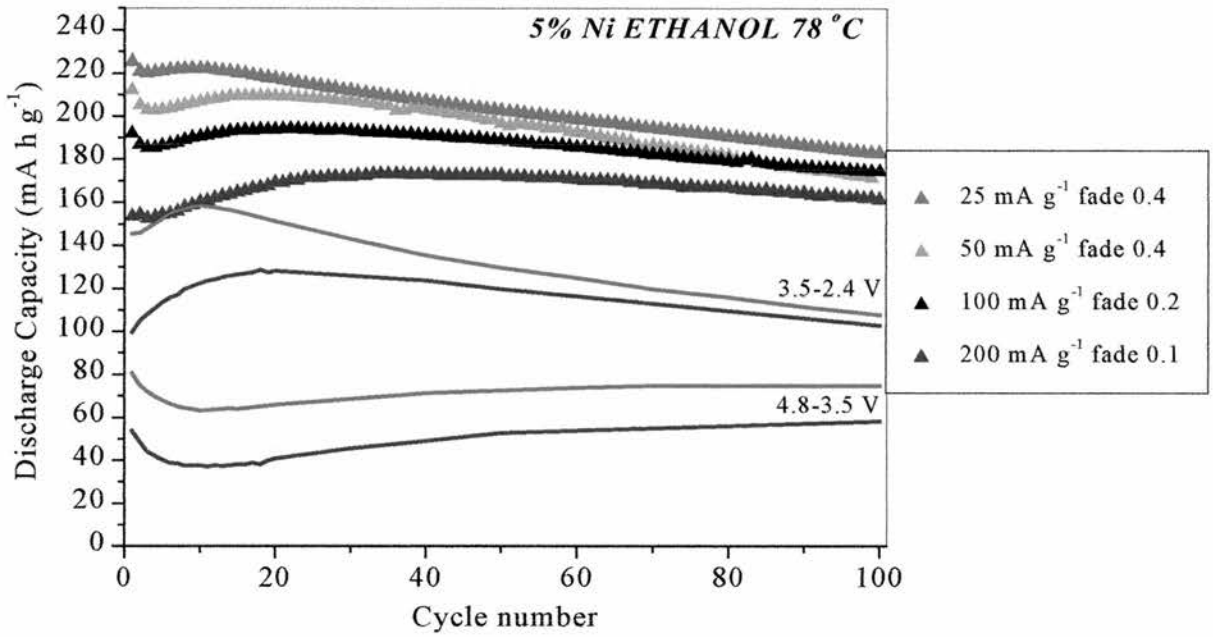


Figure 4.27 Discharge capacities plotted vs. cycle number for $\text{Li}_x\text{Ni}_{0.05}\text{Mn}_{0.95}\text{O}_2$ ethanol reflux at different cycling rates.

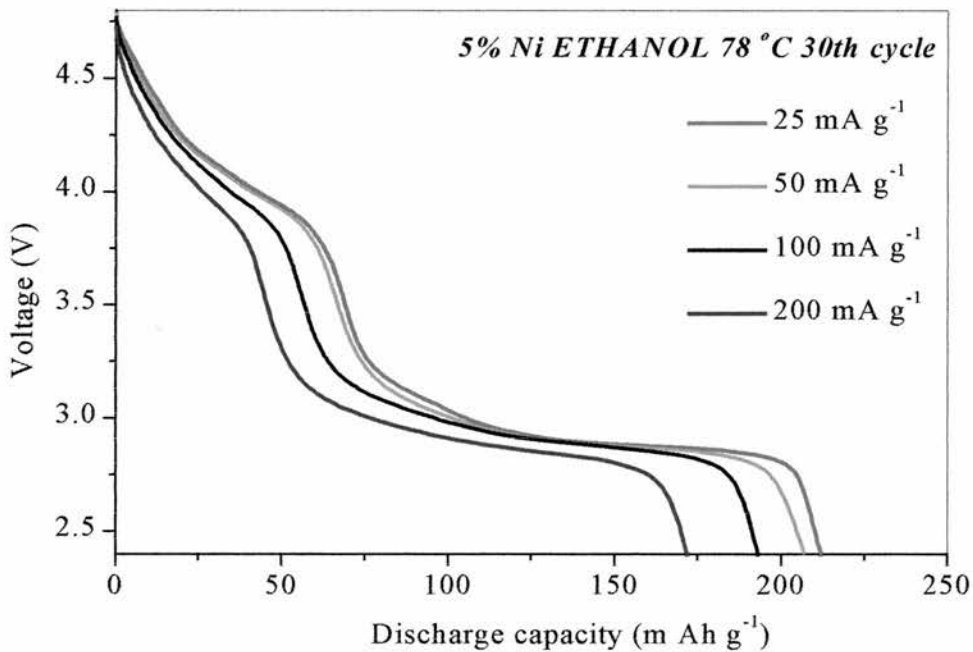


Figure 4.28 30th cycle load curves of 5% Ni doped, ethanol reflux materials at four different current densities.

Figure 4.29 demonstrates the slightly larger lattice distortion, $c/a = 4.96$, at the higher current density of 50 mA g^{-1} , compared to $c/a = 4.93$ at 25 mA g^{-1} , for the same material after 50 cycles.

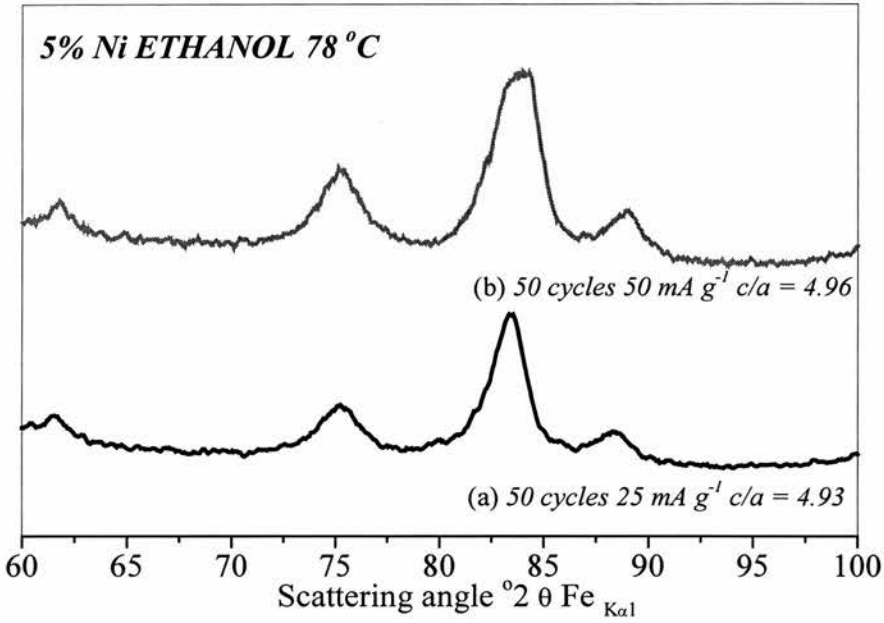


Figure 4.29 X-ray diffraction patterns showing the slower change to spinel like characteristics for cells cycled at a faster density of 50 mA g^{-1} compared to 25 mA g^{-1}

4.4 CONCLUSIONS

The layered lithium intercalation compounds $\text{Li}_x\text{Ni}_y\text{Mn}_{1-y}\text{O}_2$ with the O3 ($\alpha\text{-NaFeO}_2$) structure exhibit high capacities to cycle lithium. The ion exchange conditions used, as well as the level of Ni dopant, significantly influence the electrochemical performance of these materials. The lowest capacity fade rate on cycling is displayed by $\text{Li}_x\text{Ni}_y\text{Mn}_{1-y}\text{O}_2$ prepared by refluxing in ethanol, at a temperature of 78 °C. 2.5 % Ni doped layered lithium manganese oxide, prepared in this way, exhibits a capacity to store lithium equivalent to 220 mA h g⁻¹, and this fades by only 0.2 mA h g⁻¹ cycle⁻¹ at 25 mA g⁻¹.

The evolution of the incremental capacity plots, derived from the cycling data, have been examined together with x-ray diffraction patterns taken of cycled materials. During electrochemical cycling, all compounds develop two voltage plateaus (4 and 3 V vs. a lithium anode), suggesting spinel-like cation ordering. It has been observed that this conversion can be slowed significantly by reducing the ion exchange temperature, or by the addition of Ni.

4.5 REFERENCES

- ¹ M. M. Thackeray, W. I. F. David, P. G. Bruce and J. B. Goodenough, *Mat. Res. Bull.*, **18**, (1983), 461.
- ² W. R. McKinnon, Ed. P. G. Bruce, *Solid State Electrochemistry*, Cambridge University Press, (1995).
- ³ Q. Zhong, A. Bonakdarpour, M. Zhang, Y. Gao and J. Dahn, *J. Electrochem. Soc.*, **144**, (1997), 205.
- ⁴ M. M. Thackeray, P. J. Johnson, L. A. de Picciotto, W. I. F. David, P. G. Bruce and J. B. Goodenough, *Mater. Res. Bull.*, **19**, (1984), 179.
- ⁵ M. M. Thackeray, L. A. de Picciotto, W. I. F. David, P. G. Bruce and J. B. Goodenough, *J. Solid State Chem*, **67**,(1987), 285.
- ⁶ A. C. Larson and R. B. von Dreele, General Structure Analysis System, Los Alamos National Laboratory, (1995).
- ⁷ R. D. Shannon, *Acta Crystallogr. A*, **32**, (1976), 751.
- ⁸ J. Barker, K. West, Y. Saidi, R. Punenburg, B. Zachau-Christiansen, and R. Koksang, *J. Power Sources*, **54**, (1995), 475.
- ⁹ Tarascon, *J. Electrochem. Soc.*, **138**, (1991), 2859.
- ¹⁰ R. Koksang, J. Barker, H. Shi, and M Saidi, *Solid State Ionics*, **84**, (1996), 1.

CHAPTER 5. STRUCTURE AND ELECTROCHEMISTRY OF $\text{Li}_x\text{Mg}_y\text{Mn}_{1-y}\text{O}_2$

5.1 INTRODUCTION

Compared with Ni as a dopant, magnesium yields lower weight, cost and toxicity. It will not take part in the redox process because it has no remaining valence electrons, as a result it will reduce the capacity.

Magnesium doped sodium manganese oxide precursor materials, $\text{Na}_x\text{Mg}_y\text{Mn}_{1-y}\text{O}_2$ with $0 < y < 0.4$, were synthesised by the coprecipitation method, and quenched from 600 °C. Subsequent ion exchanges at 25 °C, 78 °C and 156 °C with LiBr yielded $\text{Li}_x\text{Mg}_y\text{Mn}_{1-y}\text{O}_2$. The experimental details are described in chapter two. All materials were characterised by x-ray diffraction and several by chemical analysis and SEM. The cycling performance and corresponding structural changes will be investigated for these new materials, and the results compared to the nickel doped system described in Chapter four.

5.2 SODIUM PHASES $\text{Na}_x\text{Mg}_y\text{Mn}_{1-y}\text{O}_2$

5.2.1 X-RAY DIFFRACTION

Powder x-ray diffraction patterns were obtained to demonstrate preparation of the layered phase, and to obtain lattice parameters. The x-ray diffraction patterns, Figure 5.1(b) to (f), show, by comparison with the black tic marks of the simulated model, that it is possible to synthesise layered

$\text{Na}_x\text{Mg}_y\text{Mn}_{1-y}\text{O}_2$ compounds. It is also evident that the crystallinity increases with Mg content. The set of hkl Miller indices are characteristic of an $\alpha\text{-NaFeO}_2$ -type structure, space group R-3m. Peaks due to unreacted Na_2CO_3 are also present, identified by the grey tic marks and this immediately suggests the presence of vacancies on the sodium sites.

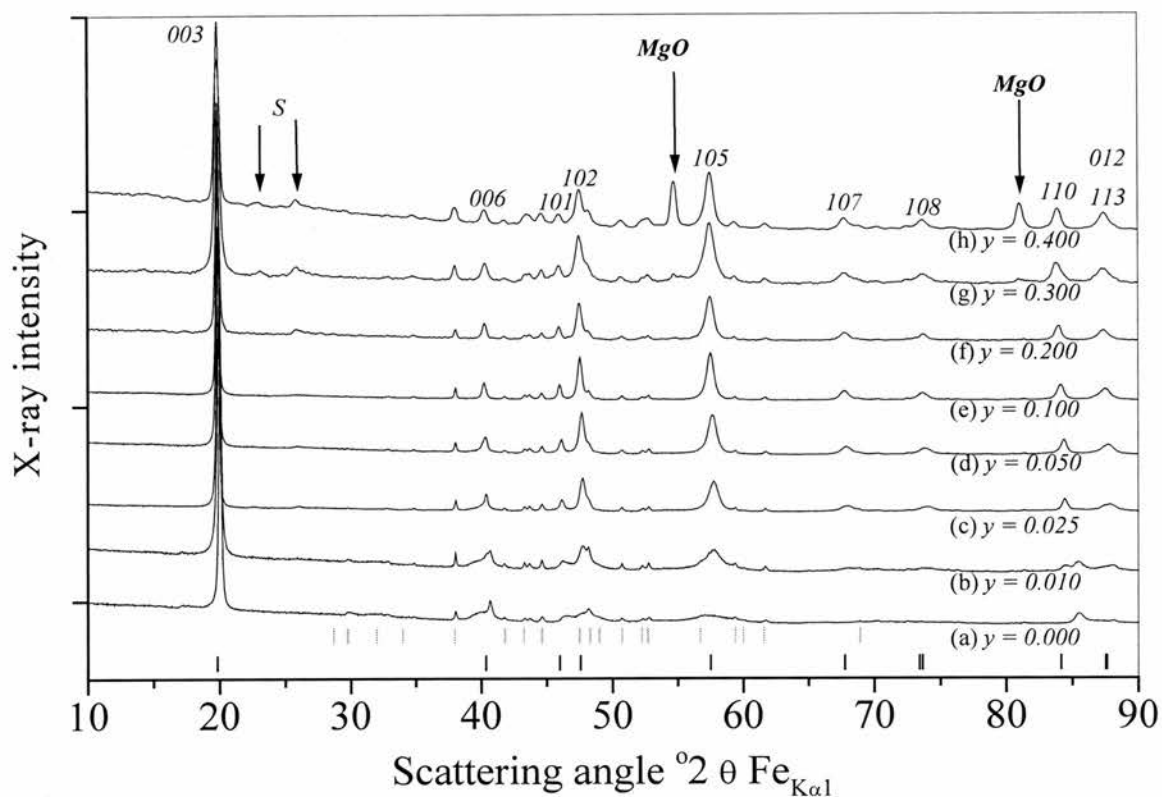


Figure 5.1 X-ray diffraction patterns of magnesium substituted $\text{Na}_x\text{Mg}_y\text{Mn}_{1-y}\text{O}_2$ phases, prepared at 600 °C. The set of hkl Miller indices are characteristic $\alpha\text{-NaFeO}_2$ type structure. **MgO** arrows indicate the positions of magnesium oxide peaks, **S** indicates the positions of superlattice peaks. The black and grey tic marks represent the peak positions for the R3m layered phase and Na_2CO_3 respectively.

The x-ray diffraction patterns taken from materials with magnesium compositions, $y > 0.2$, Figure 5.1(g) and (h), display peaks corresponding to impurity MgO, their positions are indicated at 55° and 81° in 2θ .

The x-ray diffraction patterns obtained from materials with $0.2 < y < 0.4$ display new peaks at scattering angles of 23° and 26° in 2θ . The 'S' indicates them in Figure 5.1, on patterns (f) to (h), and they correspond to a d -spacing of 4.85 and 4.33 Å respectively. Figure 5.2 enlarges the region of for $19^\circ < 2\theta < 30^\circ$, the peaks have an asymmetric shape with a tail to high angles.

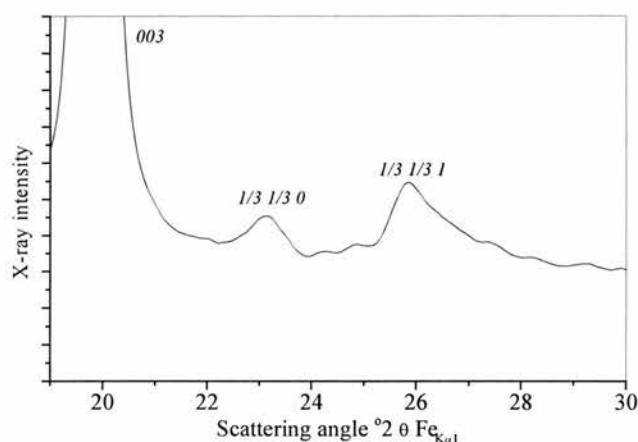


Figure 5.2 X-ray diffraction pattern for $\text{Na}_x\text{Mg}_{0.3}\text{Mn}_{0.7}\text{O}_2$.

Peaks with very similar characteristics have been observed before, for example in $\text{O}3 \text{Li}_2\text{MnO}_3$. When expressed instead as $\text{Li}[\text{Li}_{1/3}\text{Mn}_{2/3}]\text{O}_2$, it is clear that there are two different cations present in the host cation layer, Li^+ and Mn^{4+} . The peaks observed are due to the ordering of these cations, and this produces a superlattice. Li_2MnO_3 is the prototypical layered bronze that displays this ordering and the observed superstructure peaks can be indexed as $(1/3, 1/3, l)$.¹ The unusual peak shape was attributed to the ordered cation layers being stacked in an uncorrelated manner.

In $\text{Na}_x\text{Mg}_y\text{Mn}_{1-y}\text{O}_2$ the host cation layer is analogous to a two-dimensional triangular lattice gas. The cations involved are Mg^{2+} , Mn^{3+} and Mn^{4+} , and the nearest neighbour screened Coulomb repulsion between adjacent pairs of Mn^{4+} ions should be larger than that between any other pair. Therefore, the atoms will naturally try to form an arrangement where the number of Mn - Mn near neighbour contacts is minimised. Since Mg and Mn have such different x-ray scattering powers the superlattice peaks due to this ordering would be easily visible in these samples by x-ray diffraction. The ionic radius of Mg^{2+} (0.72 Å) compared to $\text{Mn}^{3+/4+}$ (0.645 Å and 0.53 Å) also plays a part in this ordering phenomena. The corresponding superlattice peaks are not observed at all by x-ray diffraction in the Ni doped sodium materials of Figure 3.7, it is thought that this is because Ni and Mn are indistinguishable by x-ray diffraction.

Even for $0.025 < y < 0.1$ there is evidence for weak short range ordering among the transition metal cations since weaker, broader superstructure peaks are observed compared to $y = 0.2$ and 0.3 . When $y = 0$ or 0.01 the superstructure peaks are absent completely.

5.2.2 RIETVELD REFINEMENT AND LATTICE PARAMETERS

The same refinement strategy as for the Ni doped materials, based on space group R3m, was adopted for all the samples, *i.e.* a two phase refinement was used, incorporating the layered phase and Na_2CO_3 . Table 5.1 shows the crystallographic parameters used to initiate the refinement of the layered phase with nominal Mg composition $y = 0.05$. The starting compositions were based on analogous Ni materials. The x-ray diffraction patterns obtained from materials with $y = 0.2$ and 0.3 were also fitted a three phase model including MgO. The crystallographic parameters for MgO are shown in Table 5.2 and those for Na_2CO_3 were shown in Table 3.6.

The occupancies of sodium, magnesium and manganese in $3b$ and $3a$ sites were then allowed to vary. The lattice parameters, the oxygen positional parameters, five thermal factors, and several parameters describing the background function were also allowed to vary. Two parameters, $G(w)$ and $L(y)$, for each phase, describing the variation of the half-width of the pseudo-Voigt peaks with scattering angle, were also refined, as well as the phase fractions.

Atom	Wyckoff symbol	x/a	y/b	z/c	Occupancy
Na	$3b$	0	0	0.8300	0.45
Mn	$3a$	0	0	0	0.9
Mg	$3a$	0	0	0	0.05
O1	$6c$	0	0	0.5996	1
O2	$6c$	0	0	0.3548	1

Table 5.1. Crystallographic details for the layered sodium phase with nominal Mg composition $y = 0.05$, space group $R3m$.

Atom	Wyckoff symbol	x/a	y/b	z/c	Occupancy
Mg	$4a$	0	0	0	1
O	$4b$	0.5	0.5	0.5	1

$a = 8.12 \text{ \AA } Fm3m$

Table 5.2 Crystallographic details for cubic MgO, space group, $Fm3m$.²

The measured x-ray diffraction pattern, the calculated pattern and their difference are shown in Figure 5.3 for the two-phase refinement of the sample with nominal composition $\text{Na}_x\text{Mg}_{0.05}\text{Mn}_{0.95}\text{O}_2$, and unreacted Na_2CO_3 . The refined composition was in good agreement with expected values, $\text{Na}_{0.60}\text{Mg}_{0.04}\text{Mn}_{0.87}\text{O}_2$. Other samples gave similar fits and the lattice parameter results are presented in Table 5.3 and as a plot in Figure 5.4.

y	a (Å)	c (Å)
0.000	2.8779 ± 0.0007	16.748 ± 0.003
0.010	2.8776 ± 0.0006	16.757 ± 0.002
0.025	2.8805 ± 0.0004	16.822 ± 0.002
0.050	2.8841 ± 0.0003	16.843 ± 0.002
0.075	2.8920 ± 0.0008	16.861 ± 0.004
0.100	2.8954 ± 0.0002	16.851 ± 0.001
0.200	2.8964 ± 0.0003	16.853 ± 0.002

Table 5.3 Summary of x-ray Rietveld refinement results for $\text{Na}_x\text{Mg}_y\text{Mn}_{1-y}\text{O}_2$ on the basis of a layered, $\alpha\text{-NaFeO}_2$ -type model. Rhombohedral cell $R3m$.

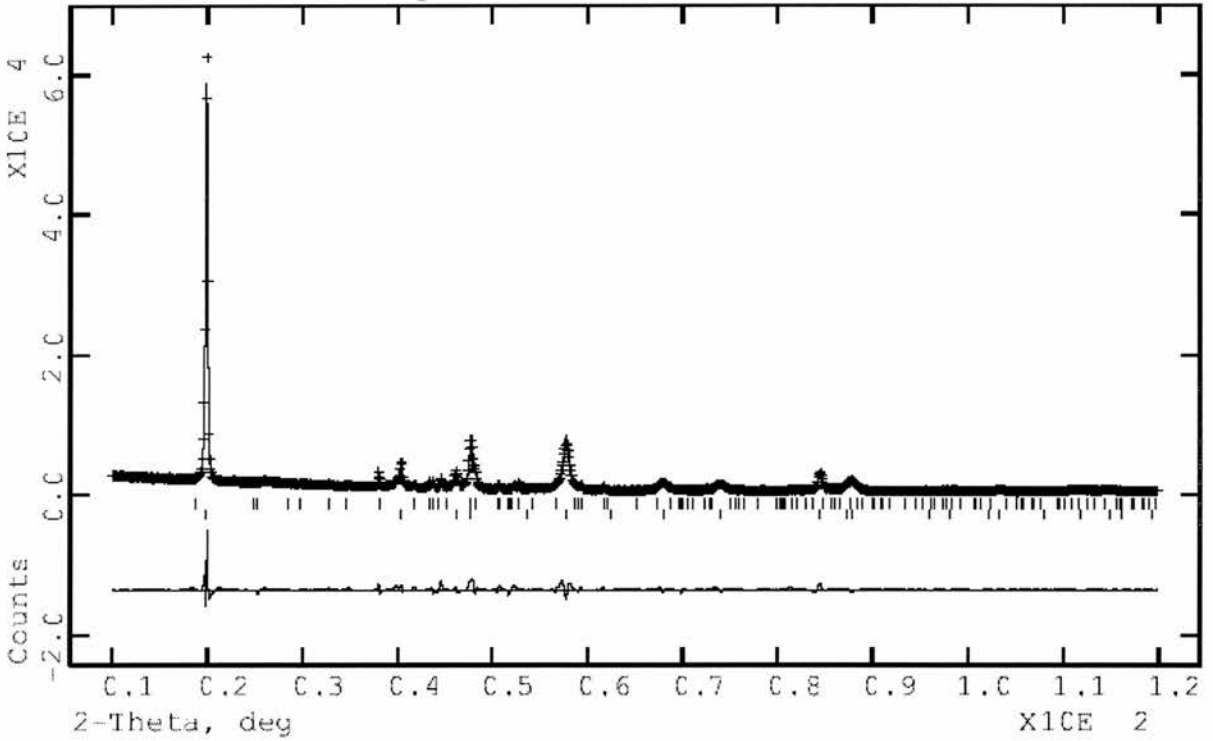


Figure 5.3 Powder x-ray diffraction pattern for 5% Mg doped layered sodium manganese oxide.

Crosses: experimental points, solid line: best fit, lower curve: difference plot, $\chi^2 = 17$. The tick marks show the allowed reflections for sodium carbonate and for the layered phase.

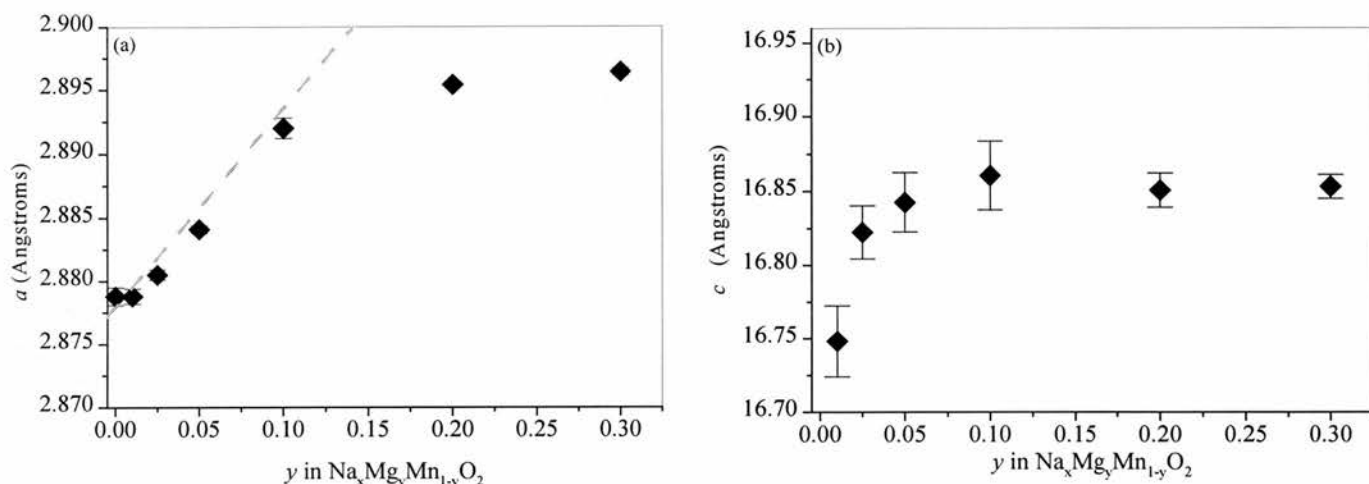


Figure 5.4. Lattice parameters a and c (in Angstroms) for rhombohedral $\text{Na}_x\text{Mg}_y\text{Mn}_{1-y}\text{O}_2$ for $0 < y < 0.3$. The dotted line is a plot of the average (Mn/Mg)-O bond expansion as a function of the nominal Mg content.

Variation of the lattice parameters a and c , obtained from refinement of the x-ray patterns of Figure 5.1, are shown in Figure 5.4 for $0 < y < 0.3$. The substitution mechanism is $2\text{Mn}^{3+} \rightarrow \text{Mn}^{4+} + \text{Mg}^{2+}$.

There are two competing forces at work here, Mg^{2+} (0.72 \AA), is larger than Mn^{3+} (0.645 \AA), and this is expected to lead to an increase in a . However, for each replacement of Mn^{3+} a second Mn^{3+} is oxidised to the smaller Mn^{4+} (0.53 \AA).

From chemical analysis, Table 3.4, the sample with $y = 0$, has a manganese composition $\text{Mn}^{3+}_{0.27}\text{Mn}^{4+}_{0.63}$. The average size of a manganese ion in the undoped composition is therefore 0.564 \AA . Assuming the above replacement mechanism, an expansion of the a -axis and, more particularly the average (Mg/Mn)-O bond is anticipated. A plot comparing the expected expansion

of the (Mg/Mn)-O bond, with the observed variation, is shown in Figure 5.4(a) by the straight dotted grey line. The bond length expansions use the $y = 0$ material as the base line, and the variation is consistent with the observed bond length changes up to $y = 0.1$. For Ni doped materials such a clear trend was not seen, probably due to its smaller size.

5.3 LITHIUM PHASES $\text{Li}_x\text{Mg}_y\text{Mn}_{1-y}\text{O}_2$

5.3.1 ION EXCHANGE

Six sodium precursors with Mg dopant levels $0 < y < 0.2$, were ion exchanged by refluxing in ethanol at 78 °C. The composition with $y = 0.05$ was also ion exchanged under four different conditions, including ion exchange at 82 °C in acetonitrile. This is a preparation temperature very close to that of an ethanol reflux, and so it will be interesting to compare the cycling performance of these materials. Table 5.4 shows the full set of Mg doped materials prepared by each ion exchange condition. (✓ = compositions prepared, ✗ = not attempted).

Mg content y	Ethanol 25 °C 1 week	Ethanol 78 °C 8 hours	Acetonitrile 82 °C 8 hours	Hexanol 156 °C 8 hours
0.000	✓	✓	✗	✓
0.010	✗	✓	✗	✗
0.025	✓	✓	✗	✓
0.050	✓	✓	✓	✓
0.100	✗	✓	✗	✓
0.200	✗	✓	✗	✗

Table 5.4 Ion exchange conditions for preparation of various $\text{Li}_x\text{Mg}_y\text{Mn}_{1-y}\text{O}_2$.

5.3.2 X-RAY DIFFRACTION

Powder x-ray diffraction patterns were obtained to measure completion of the ion exchange, to confirm phase purity and to obtain lattice parameters. The x-ray diffraction patterns of $\text{Li}_x\text{Mg}_y\text{Mn}_{1-y}\text{O}_2$ prepared by ion exchange in ethanol at 78 °C are shown in Figure 5.5. The x-ray diffraction patterns from materials prepared in hexanol at 156 °C, and in ethanol at 25 °C are shown in Figures 5.6 and 5.7 respectively.

Comparison of the x-ray patterns with the tic marks in Figure 5.5 confirms that these phases can be identified as being of the O3 structure, R-3m. All x-ray diffraction patterns exhibit 018 and 110 peaks, and as seen in x-ray diffraction patterns for the Ni doped materials, the separation of these is least prominent for materials ion exchanged in hexanol, Figure 5.6.

For $y \geq 0.025$, the most intense superlattice peak is present, indicated by 'S,' at a d -spacing of 4.33 Å, this shows that the Mg - Mn cation ordering is preserved on ion exchange under all conditions.

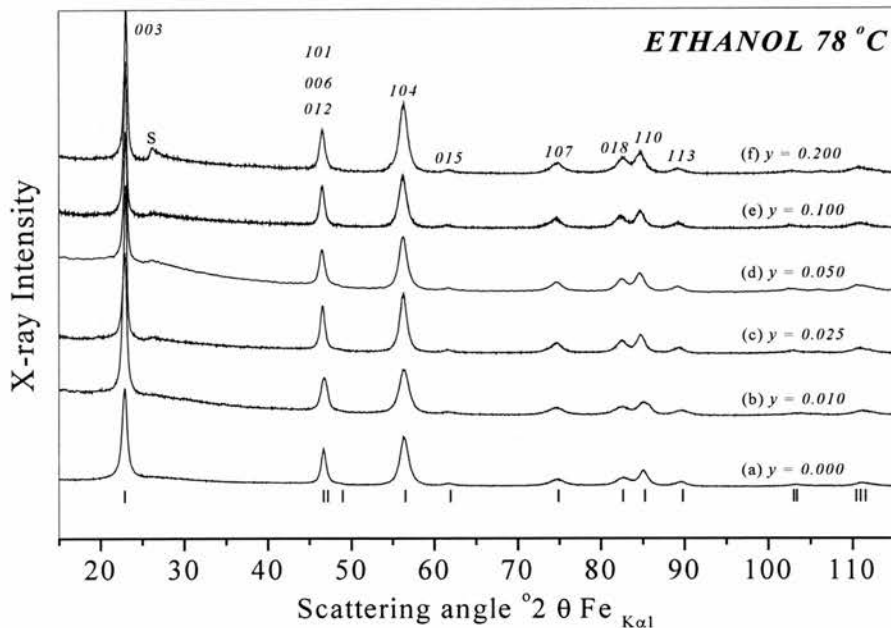


Figure 5.5 X-ray diffraction patterns of magnesium substituted materials $\text{Li}_x\text{Mg}_y\text{Mn}_{1-y}\text{O}_2$, ion exchanged by refluxing in ethanol at 78°C for eight hours. Space group $R\text{-}3m$.

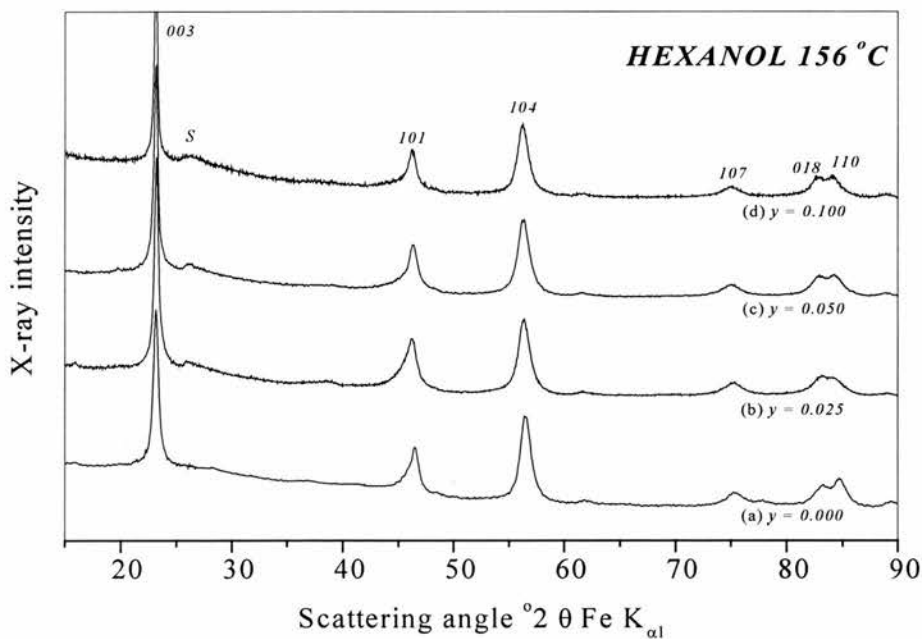


Figure 5.6 X-ray diffraction patterns of magnesium substituted materials $\text{Li}_x\text{Mg}_y\text{Mn}_{1-y}\text{O}_2$, ion exchanged by refluxing in hexanol at 156°C for eight hours.

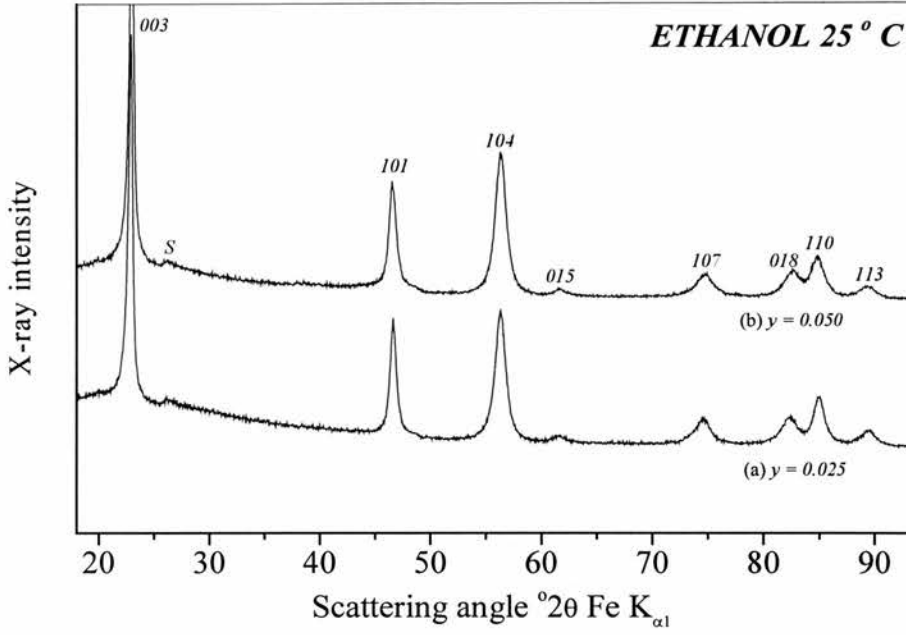


Figure 5.7 X-ray diffraction patterns of magnesium substituted materials $\text{Li}_x\text{Mg}_y\text{Mn}_{1-y}\text{O}_2$, ion exchanged by stirring in ethanol at 25 °C for 1 week.

The variation in the peak widths as a function of hkl value is well demonstrated in Figure 5.7. The effect is dependent on the l component of the reflection, this is evidence for more disorder in the c direction for materials prepared in ethanol at 25 °C.

5.3.3 CHEMICAL ANALYSIS

Elemental and oxidation state analysis of three materials refluxed in ethanol will be used to confirm the composition, and the occupancies will be used in the corresponding refinements. The results of chemical and oxidation state analysis, for several Mg doped materials, prepared in ethanol at 78°C, are reported in Table 5.5. The notation Mn_{1-y} is used to indicate that the dopant ions are substituting for Mn, however, it is realised that there are vacancies in these materials.

Mg content y in $\text{Li}_x\text{Mg}_y\text{Mn}_{1-y}\text{O}_2$	Stoichiometry	Mn oxidation state	TM vacancies
0.000	$\text{Na}_{0.06}\text{Li}_{0.59}[\]_{0.34}\text{Mn}^{3+}_{0.40}\text{Mn}^{4+}_{0.54}[\]_{0.06}\text{O}_2$	3.58	7 %
0.025	$\text{Na}_{0.04}\text{Li}_{0.58}[\]_{0.38}\text{Mg}_{0.03}\text{Mn}^{3+}_{0.33}\text{Mn}^{4+}_{0.58}[\]_{0.06}\text{O}_2$	3.64	6 %
0.050	$\text{Na}_{0.05}\text{Li}_{0.65}[\]_{0.30}\text{Mg}_{0.05}\text{Mn}^{3+}_{0.37}\text{Mn}^{4+}_{0.52}[\]_{0.06}\text{O}_2$	3.58	6 %
0.100	$\text{Na}_{0.03}\text{Li}_{0.64}[\]_{0.33}\text{Mg}_{0.09}\text{Mn}^{3+}_{0.30}\text{Mn}^{4+}_{0.56}[\]_{0.05}\text{O}_2$	3.65	5 %

Table 5.5 Chemical analysis for $\text{Li}_x\text{Mg}_y\text{Mn}_{1-y}\text{O}_2$ doped with $y = 0, 0.025, 0.05$ and 0.10 , prepared by reflux in ethanol at 78°C.

All the materials are alkali metal deficient, with about 33 % vacancies, originating from the sodium deficiencies of the precursor phases prior to exchange. As was seen in Table 3.13 for materials also prepared by ion exchange in ethanol, the amount of residual sodium is about 4 %. There are also a number of transition metal vacancies, about 6 %. The vacancies will significantly affect the Mn oxidation state, while the increased Mg content appears to have no effect on this.

5.3.4 RIETVELD REFINEMENT AND LATTICE PARAMETERS

The lattice parameters of the magnesium doped materials were refined by Rietveld refinement of the x-ray data in Figures 5.5 to 5.7. The crystallographic parameters of the lithium phase are shown in Table 5.6, space group R-3m. The Rietveld refinement for materials prepared in ethanol at 78 °C

was carried out with the Na, Li, Mn and Mg contents fixed at the values obtained from chemical analysis where possible, (Table 5.5). For the remaining materials, and those prepared at other temperatures, the occupancies were varied. In addition, thermal factors and parameters describing the background function were also allowed to vary. The layer and MgO, (where applicable), phase fractions, along with their respective peak shapes were also allowed to vary. The measured x-ray diffraction pattern, the calculated pattern and their difference are shown in Figure 5.8 for the sample with composition $y = 0.05$ prepared by ion exchange in acetonitrile at 82 °C. All other samples gave similar fits and the results from refining all lattice parameters for $\text{Li}_x\text{Mg}_y\text{Mn}_{1-y}\text{O}_2$, as well as the lattice distortion c/a , are presented in Table 5.7 and as plots in Figures 5.9(a), (b) and (c). Since the refinements for x-ray diffraction data in chapter three were previously in good agreement with neutron data, it is assumed that these results are also reliable.

Atom	Wyckoff symbol	x/a	y/b	z/c	Occupancy
Li	$3b$	0	0	0.5	x
Mg	$3a$	0	0	0	y
Mn	$3a$	0	0	0	$1-y$
O	$6c$	0	0	0.25	1

Table 5.6 Crystallographic details of the lithium phase, space group $R-3m$.

Figures 5.9(a) and (b) show the results from refinement of lattice parameters for four different ion exchange conditions and six magnesium contents. Circles represent materials prepared in hexanol at 156 °C, grey squares acetonitrile at 82 °C, triangles ethanol at 78 °C and black squares ethanol at 25 °C.

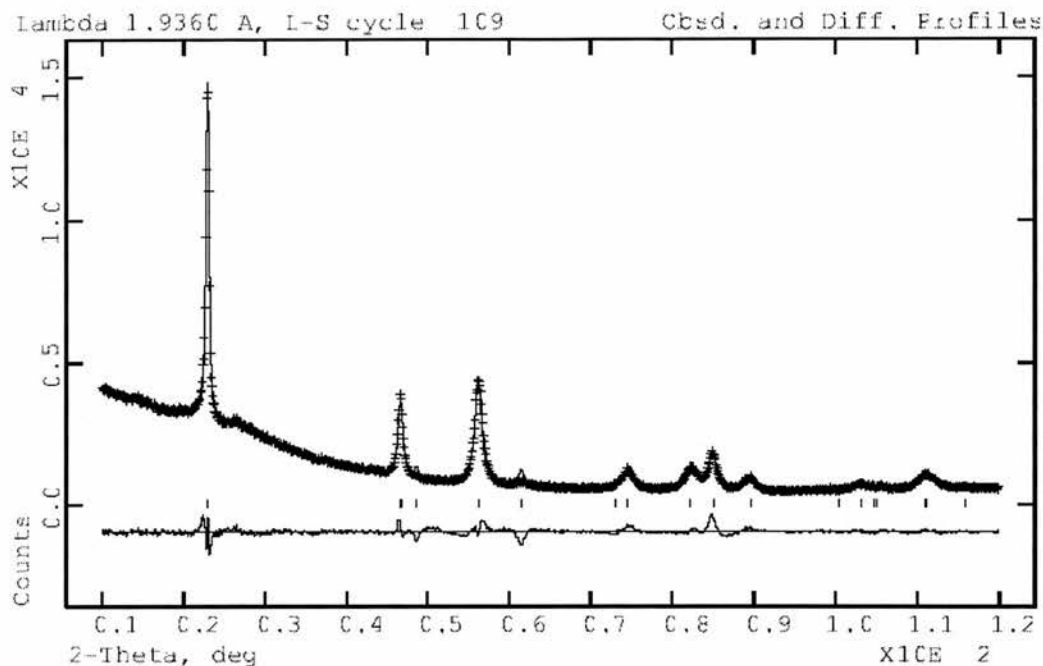


Figure 5.8 Powder x-ray diffraction pattern for 5 % Mg doped layered lithium manganese oxide ion exchanged by reflux in acetonitrile at 82 °C. Crosses: experimental points, solid line: best fit, lower curve: difference plot, $\chi^2 = 6.7$. The tic marks show the allowed reflections for the layered phase.

Mg content, y	Ion exchange conditions	$a/\text{\AA}$	$c/\text{\AA}$	c/a (± 0.01)
0.000	Ethanol 25 °C	2.8511 ± 0.0006	14.634 ± 0.002	5.14
	Ethanol 78 °C	2.8605 ± 0.0006	14.634 ± 0.002	5.12
	Hexanol 156 °C	2.8689 ± 0.0005	14.438 ± 0.002	5.03
0.010	Ethanol 78 °C	2.8575 ± 0.0003	14.654 ± 0.002	5.13
	0.025	Ethanol 25 °C	2.8632 ± 0.0009	14.645 ± 0.002
0.025	Ethanol 78 °C	2.8697 ± 0.0007	14.588 ± 0.002	5.08
	Hexanol 156 °C	2.8859 ± 0.0004	14.419 ± 0.003	5.00
	0.050	Ethanol 25 °C	2.8665 ± 0.0004	14.580 ± 0.002
0.050	Ethanol 78 °C	2.8723 ± 0.0005	14.575 ± 0.003	5.07
	Acetonitrile 82 °C	2.8642 ± 0.0007	14.633 ± 0.003	5.11
	Hexanol 156 °C	2.8850 ± 0.0003	14.459 ± 0.002	5.01
0.100	Ethanol 78 °C	2.8702 ± 0.0008	14.605 ± 0.002	5.09
	Hexanol 156 °C	2.8843 ± 0.0008	14.464 ± 0.003	5.02
0.200	Ethanol 78 °C	2.8694 ± 0.0006	14.548 ± 0.003	5.07

Table 5.7 Lattice parameters for layered $\text{Li}_x\text{Mg}_y\text{Mn}_{1-y}\text{O}_2$ obtained from Rietveld refinement of the x-ray diffraction patterns in Figures 5.4 to 5.6.

As observed in the Ni doped materials of chapter three, there is a significant variation in lattice parameters with ion exchange conditions. The trends are most clearly seen if the lattice parameters of materials prepared in hexanol are compared with those prepared in ethanol, a increases and c decreases with increasing ion exchange temperature. There is very little difference in the lattice parameters of materials prepared at 25 °C, 78 °C and 82 °C.

An indication of the origins of the variations was obtained in chapter three, by considering the results of chemical analysis. It was found that during the lower temperature ion exchanges some sodium remains in the layers. The greater sodium ion content in these samples contributes to the larger c axis, since sodium ions have a larger ionic radius than lithium ions. The number of cation vacancies was also found to be greatest for the lower temperature reflux, producing samples with a higher average manganese oxidation state. As a result a shorter average host cation-O bond length is expected, with an associated reduction in the a lattice parameter, as observed for materials prepared at lower temperatures.

The a parameter increases slightly with Mg content for $0 < y < 0.05$ for all ion exchange conditions. This is close to the observed trend in the sodium precursor materials, Figure 5.4(a). However, the c parameter, Figure 5.9(b), does not reflect the same trend.

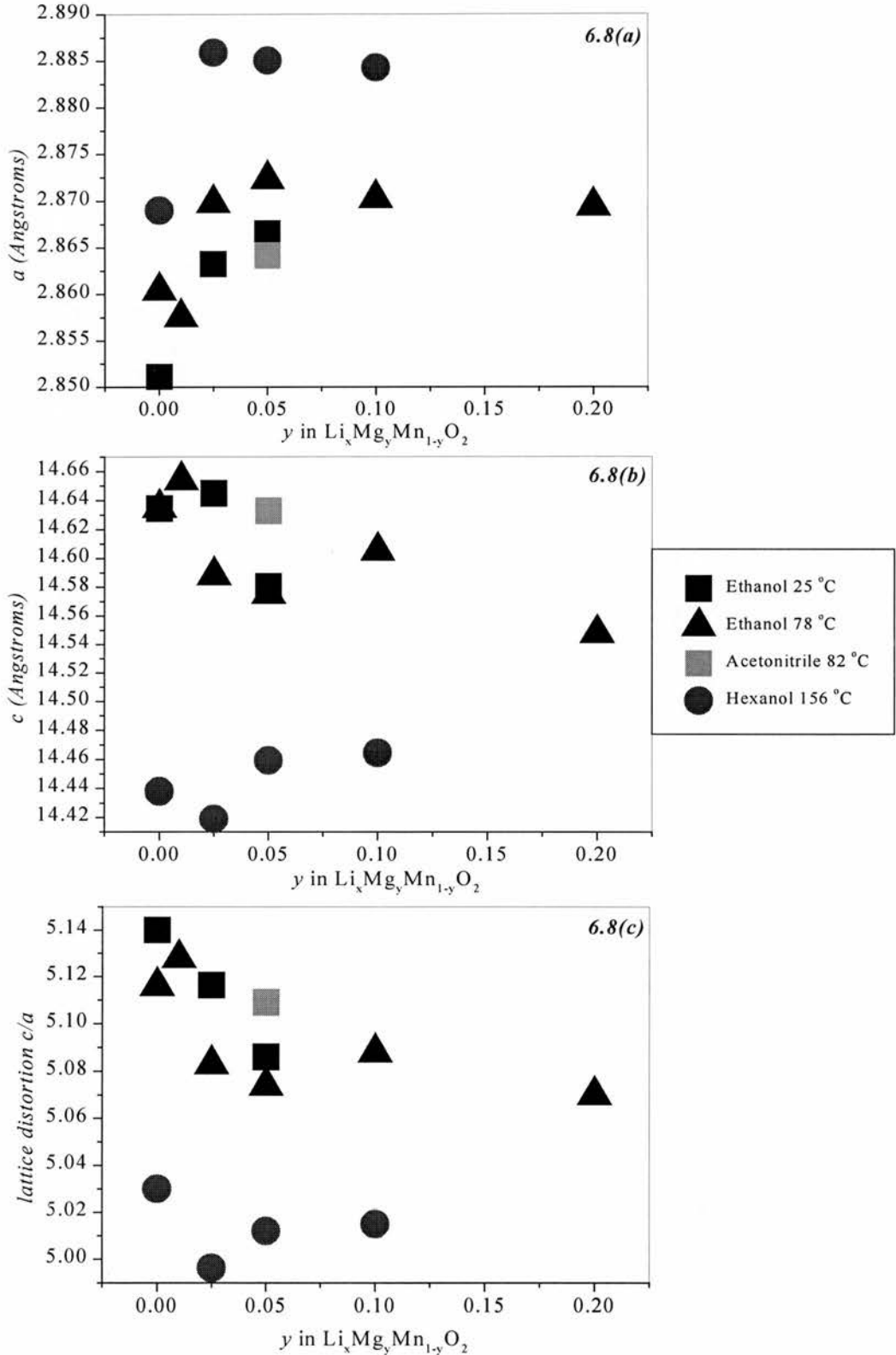


Figure 5.9. a) and b) Refined lattice parameters of magnesium doped materials $\text{Li}_x\text{Mg}_y\text{Mn}_{1-y}\text{O}_2$. c)

Effect of lattice distortion, c/a ratio, with magnesium doping.

5.3.5 PARTICLE MORPHOLOGY

The particle morphology of magnesium doped layered lithium manganese oxides was investigated by scanning electron microscopy. Figure 5.10 shows the scanning electron micrographs obtained from $\text{Li}_{0.64}\text{Mg}_{0.09}\text{Mn}_{0.86}\text{O}_2$, ion exchanged in ethanol at 78 °C, and magnified 250, (top), and 1500, (bottom), times. The same porous agglomerate morphology is seen as for the Ni doped materials of Figures 3.28 and 3.29.

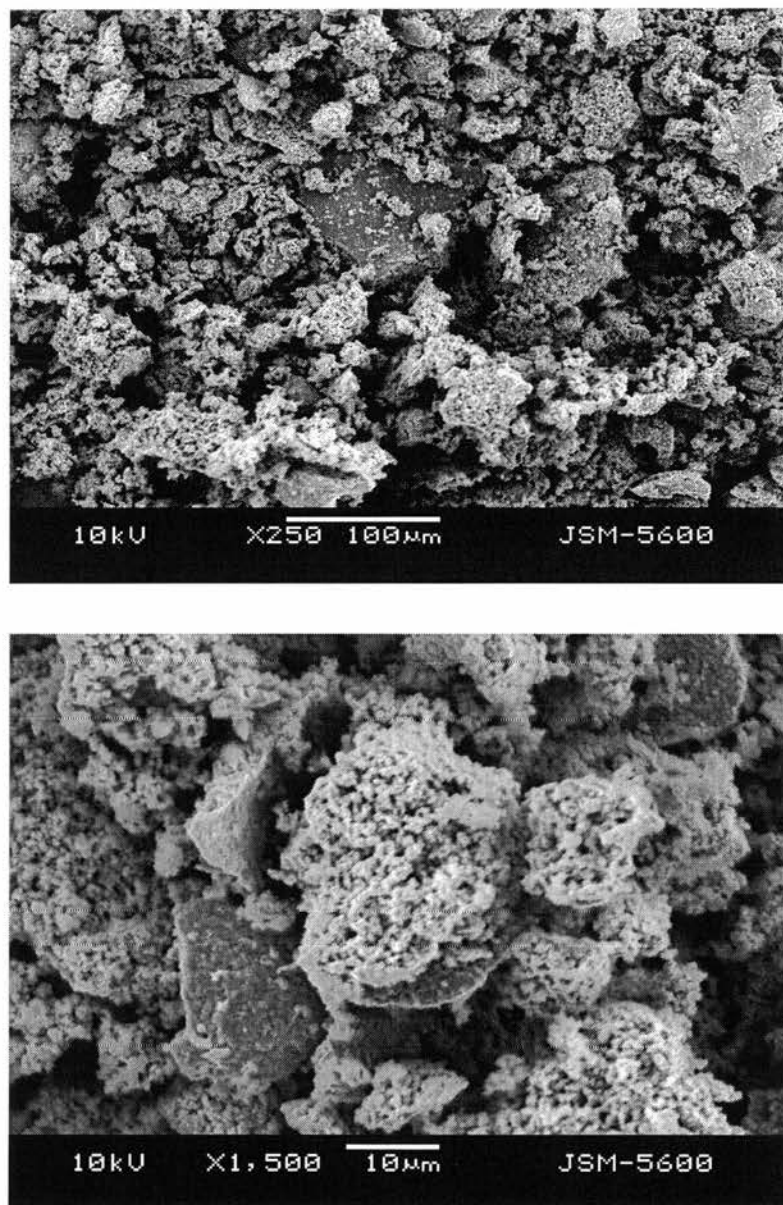


Figure 5.10. SEM micrographs of $\text{Li}_x\text{Mg}_{0.1}\text{Mn}_{0.9}\text{O}_2$, prepared in ethanol at 78°C, and magnified 250 and 1500 times, top and bottom respectively.

5.4 ELECTROCHEMICAL PERFORMANCE OF $\text{Li}_x\text{Mg}_y\text{Mn}_{1-y}\text{O}_2$.

5.4.1 INTRODUCTION

An electrochemical study was carried out to test the cycling performance of the single phase, layered $\text{Li}_x\text{Mg}_y\text{Mn}_{1-y}\text{O}_2$ materials. The aim is to find the optimum Mg^{2+} concentration that will improve the capacity retention while also yielding a high initial reversible capacity. The voltage range to be investigated includes, as in Chapter 5 for Ni doped materials, both the 3 and 4 V regions.

5.4.2 FIRST CYCLE - PRACTICAL CHARGE AND DISCHARGE CAPACITIES

5.4.2.1 INTRODUCTION

To investigate the amount of lithium extracted and reinserted from $\text{Li}_x\text{Mg}_y\text{Mn}_{1-y}\text{O}_2$ during the first cycle, a constant current of 25 mA g^{-1} is used and cells are charged to up to 4.8 V and discharged to 2.4 V.

5.4.2.2 EFFECT OF MAGNESIUM SUBSTITUTION LEVEL

The first cycle variation of cell voltage vs. capacity for magnesium doped compositions, ($0 < y < 0.2$), prepared by ethanol reflux, is shown in Figure 5.11. There is no clear trend in the charge capacity, however, as predicted theoretically, the practical first discharge capacity decreases with increasing magnesium content. This is attributed to a reduction of Mn content. For $y = 0$ the practical discharge capacity is 226 mA h g^{-1} , and for $y = 0.2$ this has reduced to 87 mA h g^{-1} . The first charge and discharge capacities for these Mg doped materials are displayed in Table 5.8.

Using the manganese compositions obtained from chemical analysis, Table 5.5, the percentage of each theoretical capacity can be expressed, and this is shown in brackets.

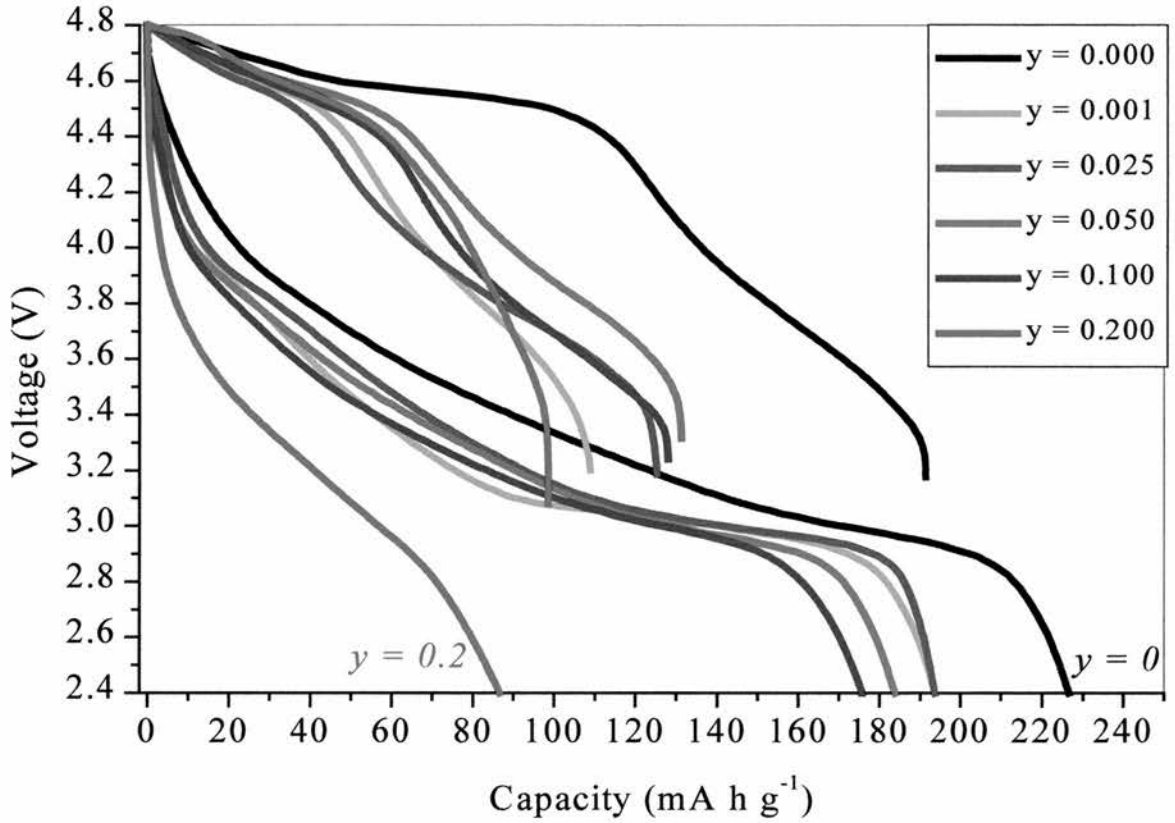


Figure 5.11 The first cycle charge and discharge voltage vs. state of charge curves for $\text{Li}_x\text{Mg}_y\text{Mn}_{1-y}\text{O}_2$, samples refluxed in ethanol at 78 °C, 25 mA g⁻¹.

Magnesium content y	Capacity (mA h g^{-1})				
	1 st charge	1 st discharge			
	OCV-4.8 V	4.8-2.4 V	Theoretical	3.5-2.4 V	4.8-3.5 V
0.000	191	226	(84 %)	154	72
0.010	109	194		147	47
0.025	125	194	(75 %)	136	58
0.050	131	187	(74 %)	135	52
0.100	128	176	(72 %)	132	44
0.200	99	87		68	19

Table 5.8 First cycle charge and discharge capacities of $\text{Li}/\text{Li}_x\text{Mg}_y\text{Mn}_{1-y}\text{O}_2$ cells, ethanol reflux
Current density = 25 mA g^{-1} , voltage range: 2.4 to 4.8 V. The theoretical capacity was calculated from the Mn compositions in Table 5.5 and is indicated in brackets. The first discharge capacity is also split, in the last two columns, into two voltage ranges.

5.4.2.3 EFFECT OF ION EXCHANGE CONDITIONS

The first cycles of magnesium doped materials prepared in hexanol at 156°C and ethanol at 25°C were also examined. The cycling conditions were exactly the same as for the previous section and the results are shown in Tables 5.9 and 5.10 respectively.

Comparing the first charge capacities for all materials, the highest values are obtained for materials prepared in hexanol. This is in agreement with the fact that these materials are expected to have a significantly lower Mn oxidation state and therefore a greater proportion of Mn^{3+} ions, allowing a higher level of lithium extraction.

Magnesium content y	Capacity (mA h g^{-1})			
	1 st charge	1 st discharge		
	OCV-4.8 V	4.8-2.4 V	2.4-3.5 V	4.8-3.5 V
0.000	198	223	141	82
0.025	162	192	120	72
0.050	164	189	121	68
0.100	189	166	110	56

Table 5.9 First cycle charge and discharge capacities of $\text{Li}_x\text{Mg}_y\text{Mn}_{1-y}\text{O}_2$ prepared by hexanol reflux. The first discharge capacity is also split, in the last two columns, into two voltage ranges.

Magnesium content y	Capacity (mA h g^{-1})			
	1 st charge	1 st discharge		
	OCV-4.8 V	4.8-2.4 V	3.5-2.4 V	4.8-3.5 V
0.000*	70	181	131	50
0.025	112	176	128	48
0.050	126	177	131	46

Table 5.10 First cycle charge and discharge capacities of $\text{Li}/\text{Li}_x\text{Mg}_y\text{Mn}_{1-y}\text{O}_2$ cells, 25 °C ion exchange, (*4.6 to 2.4 V). The first discharge capacity is also split, in the last two columns, into two voltage ranges.

The first cycle discharge capacity variation with Mg is summarised in Figure 5.12. Circles, triangles and squares represent the materials prepared in hexanol at 156 °C, ethanol at 78 °C and ethanol at 25 °C respectively. The Figure also shows, using corresponding open shapes, the contribution from each potential range as indicated. With increasing magnesium content y , a decrease in first discharge capacity (4.8 to 2.4 V, solid shapes) is observed for all ion exchange conditions.

Comparison with materials prepared in hexanol and ethanol shows that the level of first discharge capacity at each Mg content is very similar. However, the 4 V capacity is always highest for the higher ion exchange temperature, yet the 3 V capacity is generally lowest. This is in agreement with the charge capacity results which showed an increased amount of Li extracted at 4 V for materials prepared in hexanol, the discharge capacity demonstrates that more lithium is also reinserted at 4 V in these materials.

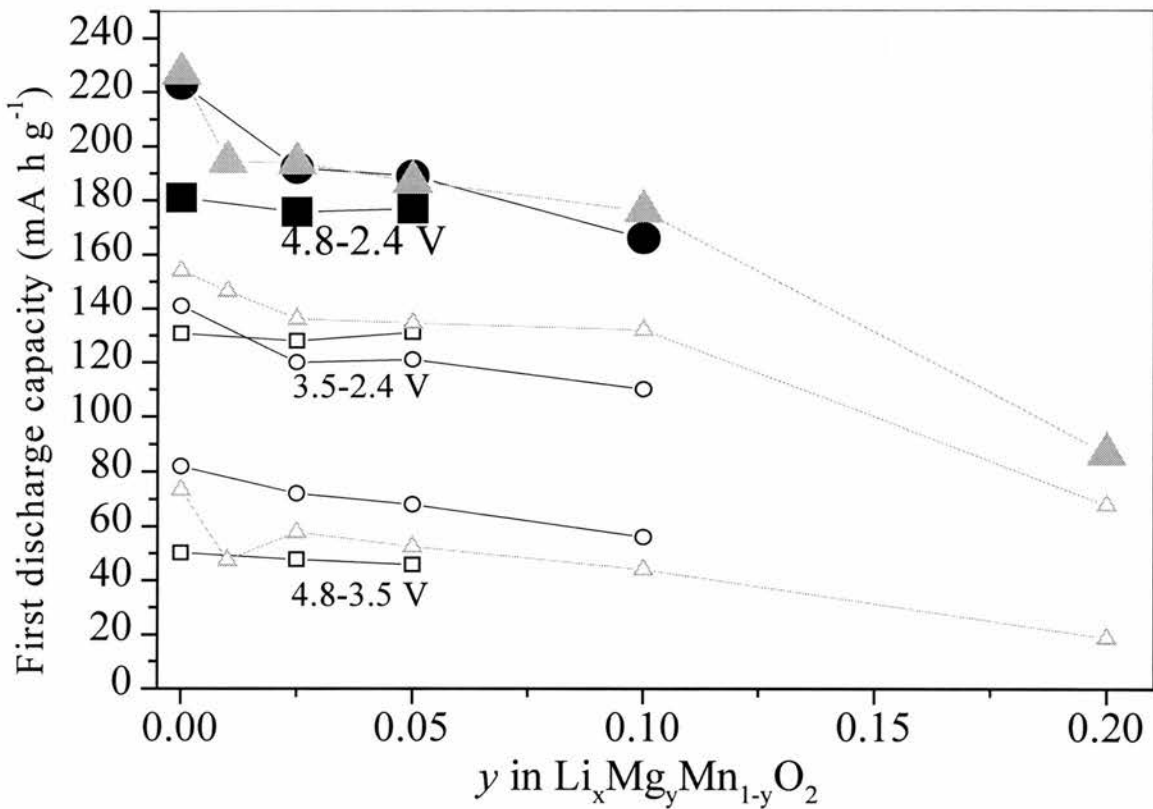


Figure 5.12 First cycle discharge capacities for $\text{Li}_x\text{Mg}_y\text{Mn}_{1-y}\text{O}_2$ as a function of Mg content.

Voltage range 4.8 to 2.4 V, current density = 25 mA g^{-1} . Circles = hexanol 156°C , triangles = ethanol 78°C and squares = ethanol 25°C . The contribution of first discharge capacity from each voltage range is also shown by the corresponding smaller open shapes.

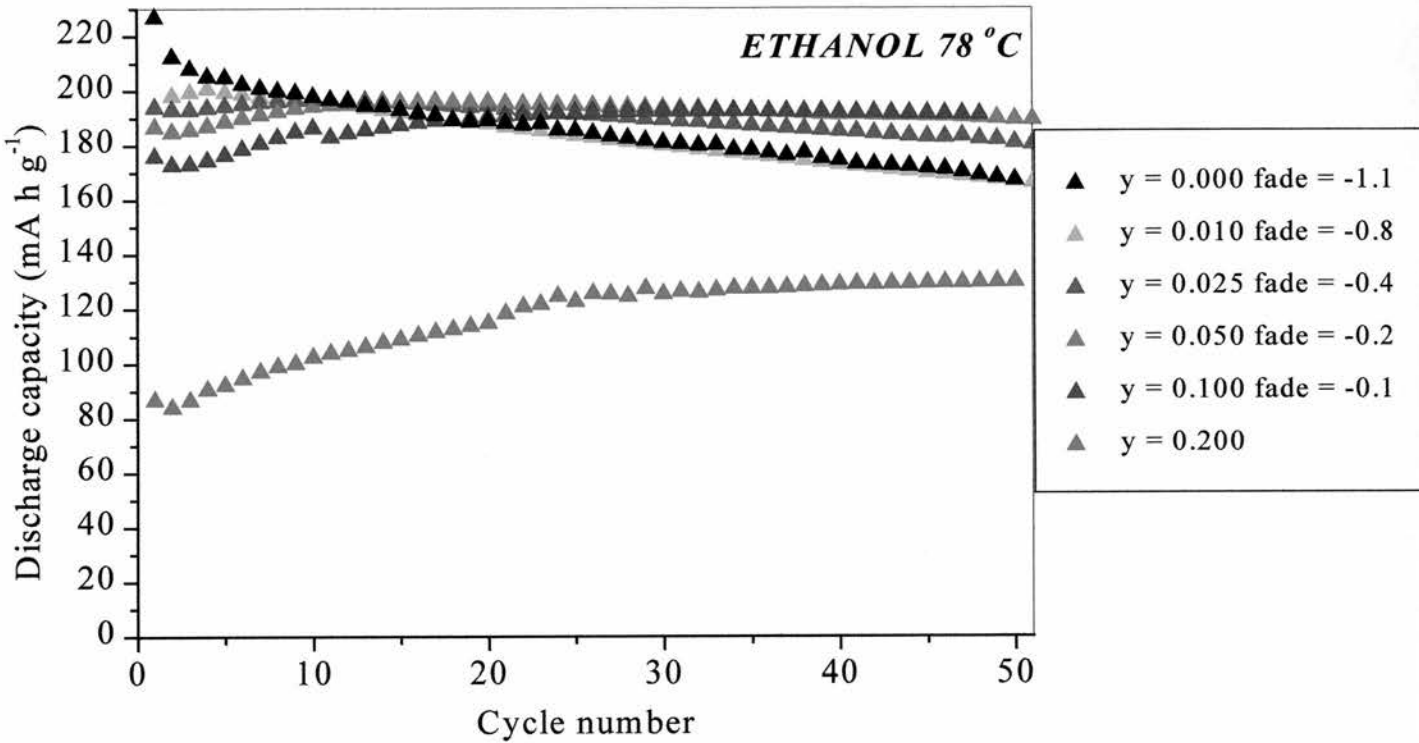
5.4.3 EXTENDED CYCLING OF $\text{Li}_x\text{Mg}_y\text{Mn}_{1-y}\text{O}_2$ 5.4.3.1 $\text{Li}_x\text{Mg}_y\text{Mn}_{1-y}\text{O}_2$ PREPARED IN ETHANOL AT 78°C

Figure 5.13 Comparison of discharge capacities for $\text{Li}_x\text{Mg}_y\text{Mn}_{1-y}\text{O}_2$ materials prepared in ethanol at 78 °C. Current density = 25 mA g⁻¹, potential range 2.4 to 4.8 V.

The extended cycling performance of $\text{Li}_x\text{Mg}_y\text{Mn}_{1-y}\text{O}_2$ ($0 < y < 0.2$) prepared in ethanol at 78 °C was investigated and the variation of discharge capacity with cycle number is shown in Figure 5.13. All cells were cycled under identical conditions between the potential limits of 2.4 and 4.8 V with a current density of 25 mA g⁻¹.

The discharge capacity fade rate is significantly improved for Mg doped materials with $y \geq 0.025$, compared with the undoped material. For all doped materials, the capacity increases initially to a maximum capacity, after which it fades. For $y \geq 0.025$ there is a slight drop in capacity in the first two cycles, prior to the rise. The maximum capacity attained occurs at a higher cycle number, n , for a higher Mg dopant level, y . Due to this significant rise and then fall in capacity, the fade rate is calculated between cycle number n and cycle 50, *i.e.* after the peak and in the region of a continuous fall in capacity.

The capacity fade rate per cycle for each dopant level is indicated in Figure 5.13 and in Table 5.11. The table also shows how n increases and the maximum discharge capacity decreases with increasing magnesium content. Such discharge capacity characteristics were not so clearly dependent on dopant level for the Ni doped materials, prepared at 78°C , of chapter four, (see Figure 4.16). Instead the maximum capacity was always displayed around the 10th cycle.

From Figure 5.13 and Table 5.11 it can be seen that the capacity fade rate is improved, with the addition of more Mg, from $-1.1 \text{ mA h g}^{-1} \text{ cycle}^{-1}$ for $y = 0$ to $-0.1 \text{ mA h g}^{-1} \text{ cycle}^{-1}$ for $y = 0.1$, but at a modest cost of capacity. For the composition with $y = 0.2$, significantly less lithium can be reinserted initially, up to 50 cycles are required before the maximum capacity is attained.

Mg content y	Maximum discharge capacity (mA h g^{-1})	Cycle number at maximum capacity n .	Capacity loss per cycle between cycle n and 50. 4.8-2.4 V. ($\text{mA h g}^{-1} \text{ cycle}^{-1}$)
0.000	227	1	-1.1
0.010	200	4	-0.8
0.025	197	11	-0.4
0.050	197	17	-0.2
0.100	192	35	-0.1
0.200	130	50	-

Table 5.11. Results from cycling $\text{Li}_x\text{Mg}_y\text{Mn}_{1-y}\text{O}_2$ prepared in ethanol at 78°C .

The effect of Mg doping on the capacity retention has been investigated further by considering the discharge capacity over 3.5 to 2.4 V and 4.8 to 3.5 V separately. Figure 5.14 shows the discharge capacity variation within each of these voltage regions. In all doped samples, except $y = 0.2$, the 3 V capacity increases then decreases, whereas the 4 V capacity exhibits a decrease then an increase. It can be seen that maximum and minimum values of 3 V and 4 V discharge capacities occur within the first 10 to 20 cycles.

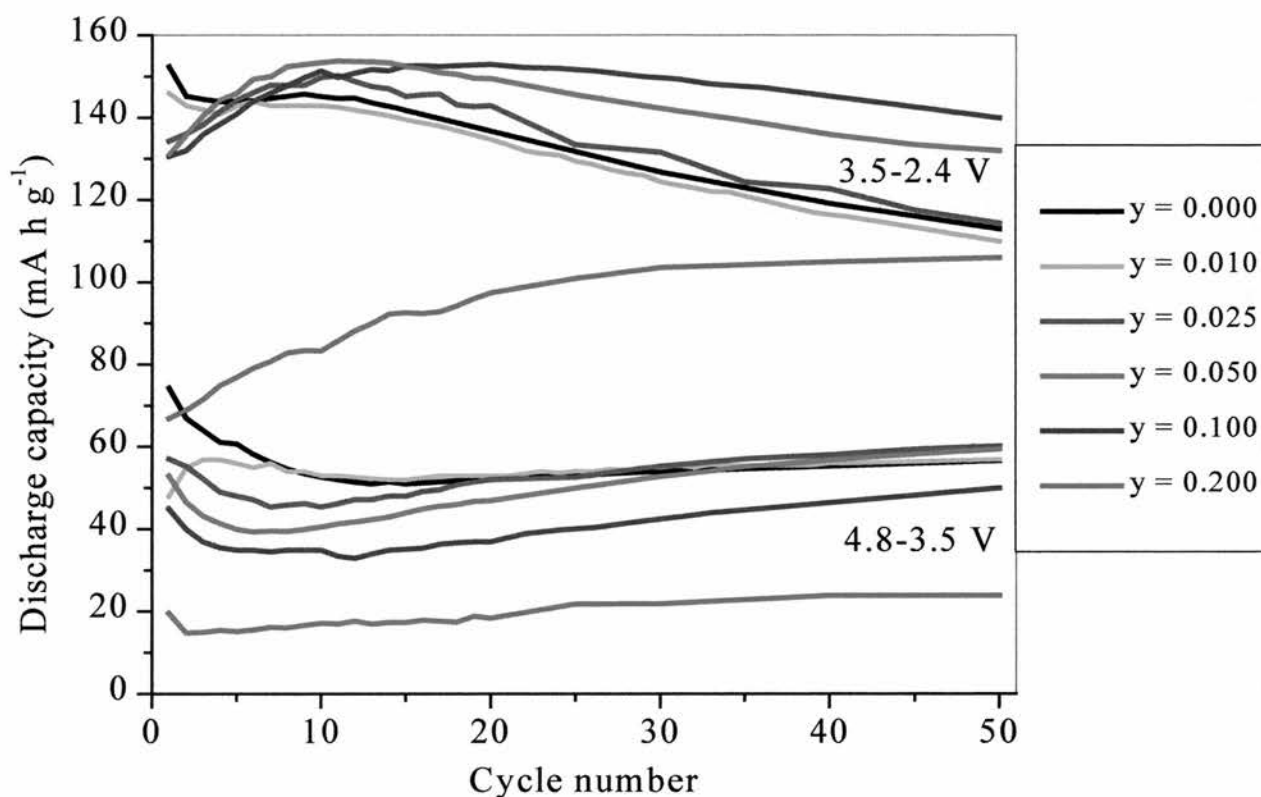


Figure 5.14 Line graphs showing the separate trends in discharge capacity for the two voltage regions, 4.8 to 3.5 V and 3.5 to 2.4 V, for $\text{Li}_x\text{Mg}_y\text{Mn}_{1-y}\text{O}_2$ prepared in ethanol. Current density = 25 mA g^{-1} , data derived from Figure 5.13.

After this unusual variation a more steady state appears to exist where the capacity is seen to fade over 3 V for all materials. Meanwhile the capacity of the 4 V region remains essentially unchanged for the lowest dopant level, while gaining slightly for higher Mg dopant levels; it takes over 50 cycles for these 4 V profiles to become flat. This behaviour suggests that some type of slow structural or compositional change is occurring in the cathode throughout cycling. It appears therefore that the change is consistently slowed as the Mg dopant level is increased.

5.4.3.2 STRUCTURAL CHANGES ON CYCLING

As described in chapter four, the Ni doped materials convert to spinel on cycling. To investigate this for the Mg doped materials x-ray and incremental capacity data were collected. The formers are presented in Figure 5.15 and the latter in Figure 5.16. Cells were subjected to 5, 10, 15 and 50 cycles under exactly the same cycling conditions as previous Mg doped materials. Cycling terminated at 3.5 V on charge and x-ray data were collected of the cycled cathode material. For each trace in Figure 5.15, the lattice parameters were refined, and the c/a ratios obtained as indicated on the Figure. Coalition of the 018 and 110 peaks occurs between 20 and 50 cycles indicating that the long range order is, as expected, becoming spinel-like and the c/a ratio is decreasing towards $\sqrt{24}$ (4.898).

The incremental capacity plots for the corresponding cycle numbers are shown in Figure 5.16. The electrochemistry has detected spinel-like characteristics, (double 4 V peak), by about cycle 20, which is slightly sooner than was detected by x-ray diffraction. These results are similar to those obtained from Ni doped materials. A material doped with 5 % Ni and prepared by reflux in ethanol displayed spinel-like characteristics by cycle 24 from x-ray diffraction, and by cycle 17 in the incremental capacity plots.

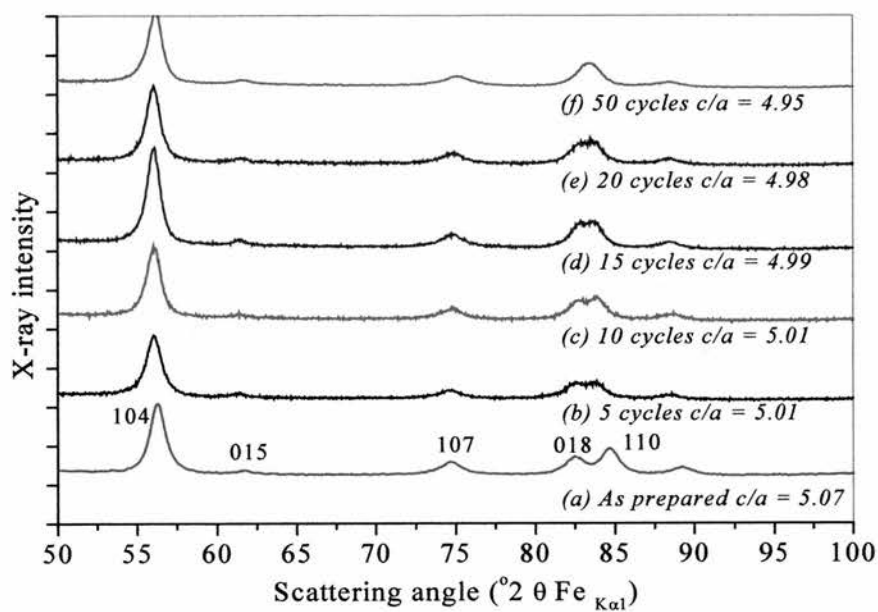


Figure 5.15 Powder x-ray diffraction data collected after 5, 10, 15, 20 and 50 cycles on a 5 % Mg doped material prepared by ethanol reflux.

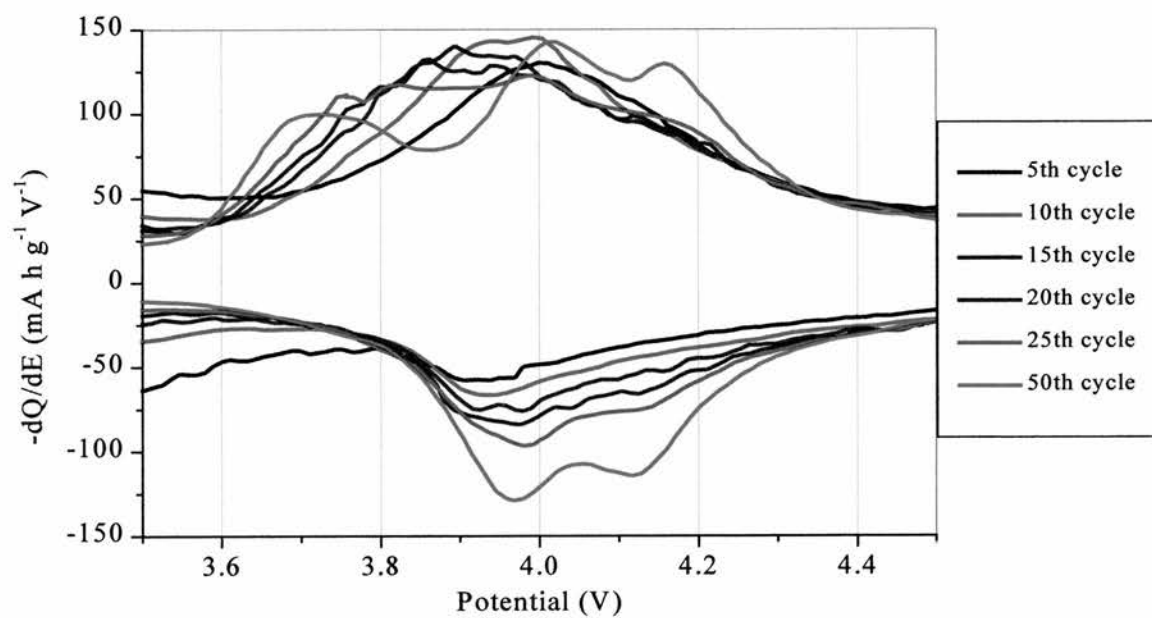


Figure 5.16 Incremental capacity plots of $\text{Li}_x\text{Mg}_{0.05}\text{Mn}_{0.95}\text{O}_2$, prepared by an ethanol reflux.

5.4.3.3 EFFECT OF ION EXCHANGE CONDITIONS

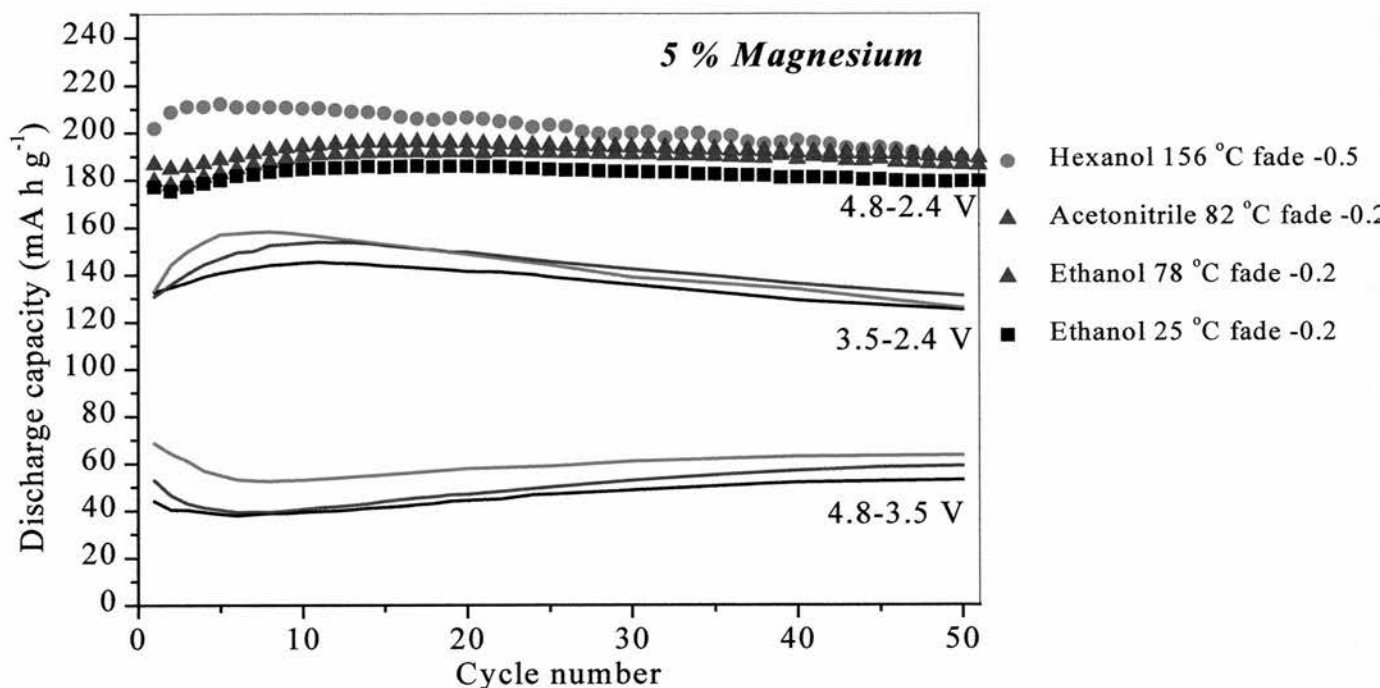


Figure 5.17 Discharge capacity variation as a function of cycle number for the 5 % magnesium doped material exchanged under four different conditions and cycled between 4.8 and 2.4 V.

The lines show the capacity trends existing for three ion exchange conditions within the voltage ranges 4.8 to 3.5 V, and 3.5 to 2.4 V. Current density = 25 mA g^{-1} .

The sodium precursor phase with Mg composition $y = 0.05$ was ion exchanged under four different ion exchange conditions. The variation of discharge capacity for each material is displayed by the solid symbols in Figure 5.17. The red circles are the cycling results from materials prepared in hexanol at 156 °C, green triangles in acetonitrile at 82 °C, blue triangles in ethanol at 78 °C and black squares in ethanol at 25 °C.

The material prepared in hexanol at 156 °C loses capacity more rapidly than those synthesised at lower temperatures. The maximum value of discharge capacity for the material prepared in hexanol

is 211 mA h g^{-1} , occurring at cycle $n = 3$, after this the capacity fades at a rate of $0.5 \text{ mA h g}^{-1} \text{ cycle}^{-1}$. For the material prepared in ethanol at $78 \text{ }^\circ\text{C}$ the maximum capacity attained is 197 mA h g^{-1} at cycle $n = 17$, with a fade rate of $0.2 \text{ mA h g}^{-1} \text{ cycle}^{-1}$ between cycle 17 and 50. For the material prepared at $25 \text{ }^\circ\text{C}$ the maximum capacity attained is slightly lower at 186 mA h g^{-1} and occurs slightly later, at cycle 20, the fade rate is also $0.2 \text{ mA h g}^{-1} \text{ cycle}^{-1}$. It is clear that the maximum value in capacity occurs after fewer cycles for the material prepared at the highest temperature, an indication that the conversion to spinel-like characteristics has probably occurred earlier.

The discharge capacity results displayed by the material prepared in acetonitrile at $82 \text{ }^\circ\text{C}$ are very similar to those of the material prepared in ethanol at $78 \text{ }^\circ\text{C}$. This is confirmation that the temperature of ion exchange is probably the key factor governing the differences between these materials.

The lines in Figure 5.17 display the separate capacity contribution from each voltage range. The colours correspond to the same ion exchange conditions as described previously. The separated capacities show the increasing 3V and decreasing 4V trends over the first 5 to 15 cycles. The trends appear to be most exaggerated, and to occur sooner, for the material prepared in hexanol. The material prepared in ethanol at $25 \text{ }^\circ\text{C}$ clearly displays the least variation in 3 and 4V discharge capacity behaviour.

The highest fade in the 3 V capacity region is displayed by the material prepared in hexanol. However, over 4 V there is no further loss in capacity, only a slight gain which reduces to a plateau by cycle 40. In contrast the 3 V capacity fade is reduced for materials prepared at the lower temperatures while over 4 V the capacity continues to increase suggesting that the structural changes are still occurring beyond the 50th cycle.

On comparing incremental capacity plots it has been shown that the behaviour of these Mg doped materials is very similar to the Ni cycling results. The same trends are evident such as the double 4 V process occurring sooner for the materials prepared in hexanol. These results, together with the more rapid reduction in c/a ratio confirm that the conversion to a spinel-like material occurs sooner for materials prepared in hexanol.

5.4.3.4 RATE CAPABILITY

Cycling of Mg doped materials showed that the cathode material with $y = 0.05$ prepared in ethanol presents good cycling properties. The variation of capacity with cycle number for the nominal composition, $\text{Li}_x\text{Mg}_{0.05}\text{Mn}_{0.95}\text{O}_2$, at four different current densities is shown in Figure 5.18. At 10 mA g^{-1} the first discharge capacity is 200 mA h g^{-1} . At 25 mA g^{-1} the first discharge has reduced to 187 mA h g^{-1} . At the higher current densities of 50 and 100 mA g^{-1} the specific capacities on the first discharge are 170 and 140 mA h g^{-1} respectively. The variation of discharge capacity with cycle number over the first few cycles is strongly dependent on current density. At higher cycle numbers, (higher than cycle 40), the capacity fade appears to be almost unaffected by current density. The convergence of fade at higher cycle numbers is reflected in the curves for each voltage region, Figure 5.18.

Tenth discharge voltage profiles for $y = 0.05$ at the four different current densities are shown in figure 5.19. A capacity of around 196 mA h g^{-1} is delivered at 25 mA g^{-1} . Doubling the rate leads only to a modest reduction in the discharge capacity with the material still delivering 177 mA h g^{-1} in the voltage range 4.8 to 2.4 V. Doubling the rate again and the material delivers 149 mA h g^{-1} .

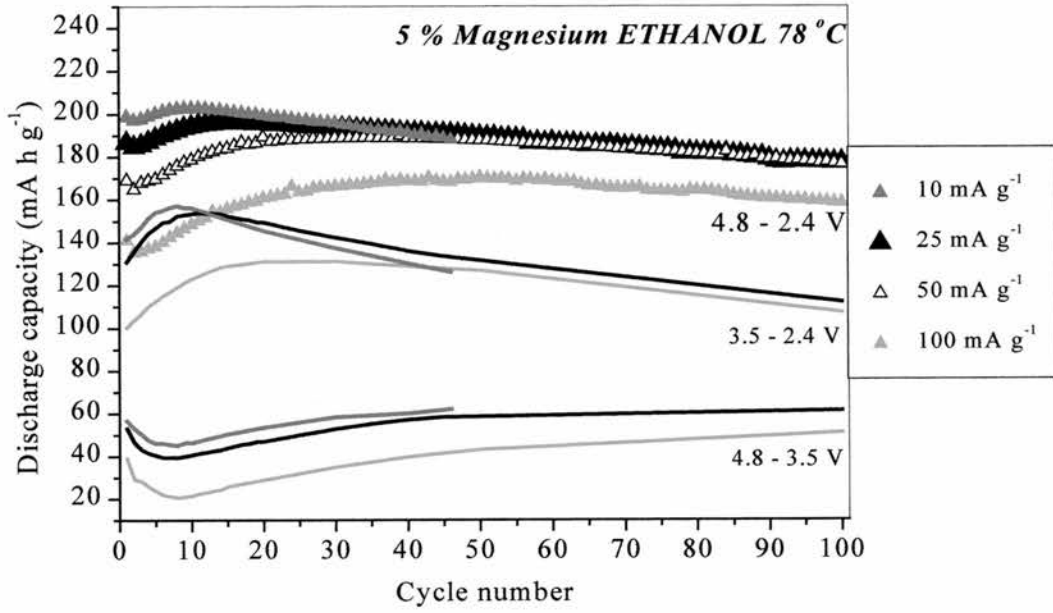


Figure 5.18 Rate capability data for $\text{Li}_x\text{Mg}_{0.05}\text{Mn}_{0.95}\text{O}_2$ prepared by ethanol reflux at 78°C .

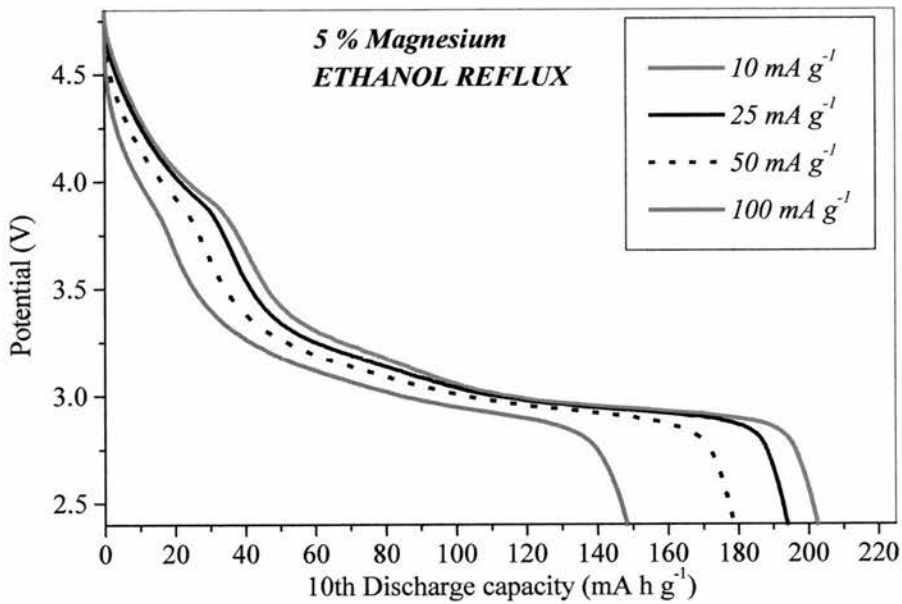


Figure 5.19 Tenth cycle discharge voltage vs state of charge at four different current densities for 5 % Mg doped material refluxed in ethanol at 78°C .

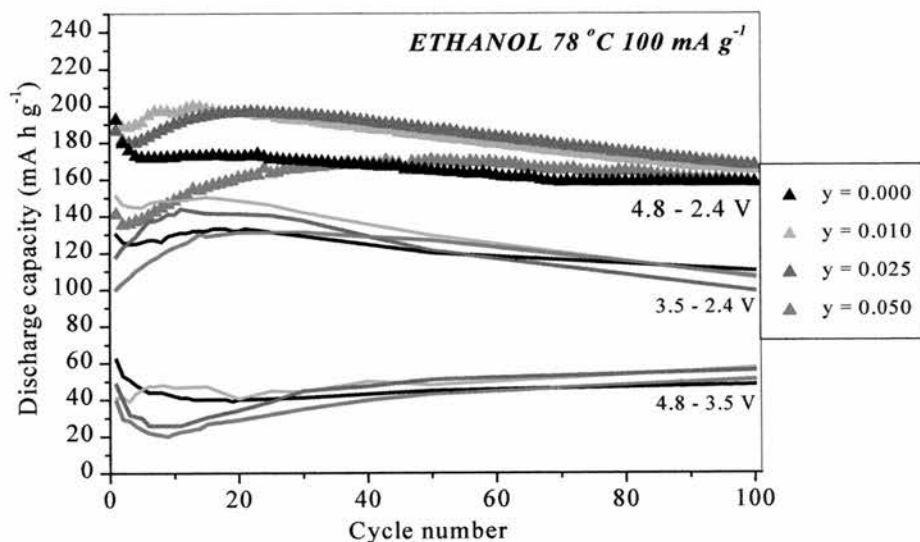


Figure 5.20 Discharge capacity profiles of the $\text{Li}_x\text{Mg}_y\text{Mn}_{1-y}\text{O}_2$ cells with $y = 0, 0.01, 0.025$ and 0.05 cycled at a current density of 100 mA g^{-1} , voltage range 2.4 to 4.8 V . The separate capacities are also shown in the potential regions 4.8 to 3.5 V and 3.5 to 2.4 V .

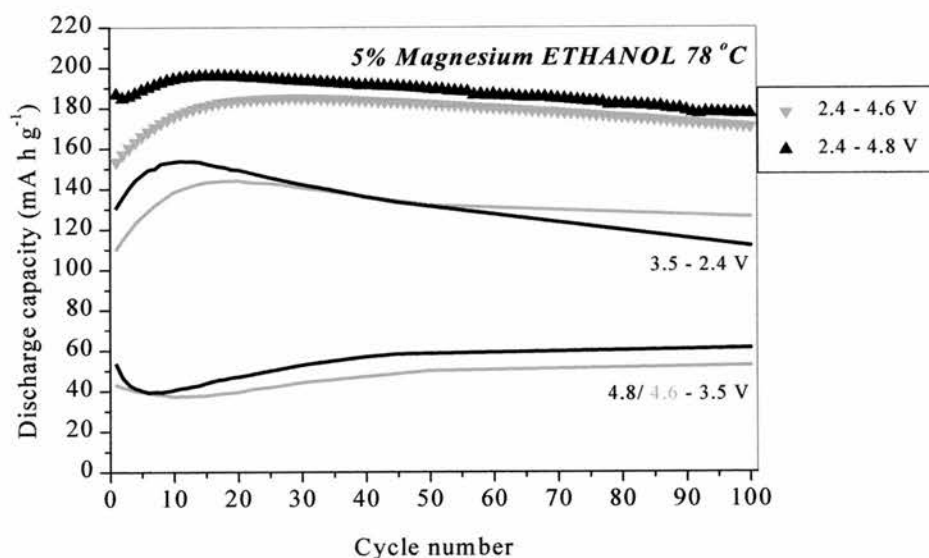


Figure 5.21 Discharge capacity profiles of the $\text{Li}_x\text{Mg}_{0.05}\text{Mn}_{0.95}\text{O}_2$ cells cycled at a current density of 25 mA g^{-1} , voltage ranges = 2.4 to 4.8 V (black), 2.4 to 4.6 V (grey). The separate capacities are also shown in the potential regions $4.8(4.6)$ to 3.5 V and 3.5 to 2.4 V .

Figure 5.20 shows the performance of cathode materials with $y = 0, 0.01$ and 0.025 at 100 mA g^{-1} and these also show very promising stability at such a high rate.

5.4.3.5 COMPARISON OF DIFFERENT VOLTAGE WINDOWS

On reducing the upper cutoff voltage from 4.8 to 4.6 V the initial discharge capacity is reduced and the rise in capacity within the first 20 cycles increases. However, it is noteworthy that the fade at higher cycle number is unaffected. Analysis of the capacities in the 3 and 4 V regions, Figure 5.21, shows that the reason for this is that the 3 V capacity fades while the 4 V capacity increases for the 4.8 V cut off. These cancel, giving a 'flatter' overall curve.

5.5 COMPARISON WITH NI DOPING

Figure 5.22 compares the overall capacity retention from cycling Mg and Ni doped materials. The performance appears to be slightly better for Ni doped materials only for $y \leq 0.025$, yet for higher doping levels the Mg doped materials have the better performance. This is also summarised in Figure 5.23, on comparing the compositions with $y = 0.01, 0.025$ and 0.05 , the capacity retention is improved for Mg doping only for $y = 0.05$.

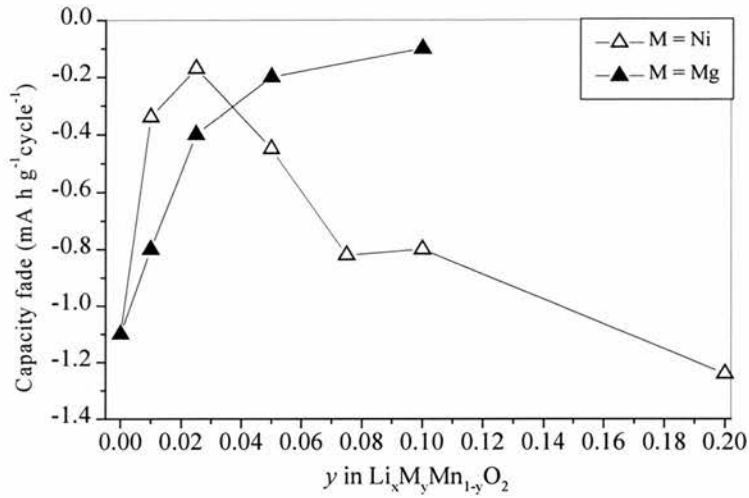


Figure 5.22 Capacity fade per cycle for materials prepared at 78 °C as a function of M content y ($M = \text{Ni}, \text{Mg}$), in the voltage range 4.8 to 2.4 V. Derived from Figures 4.16 and 5.13.

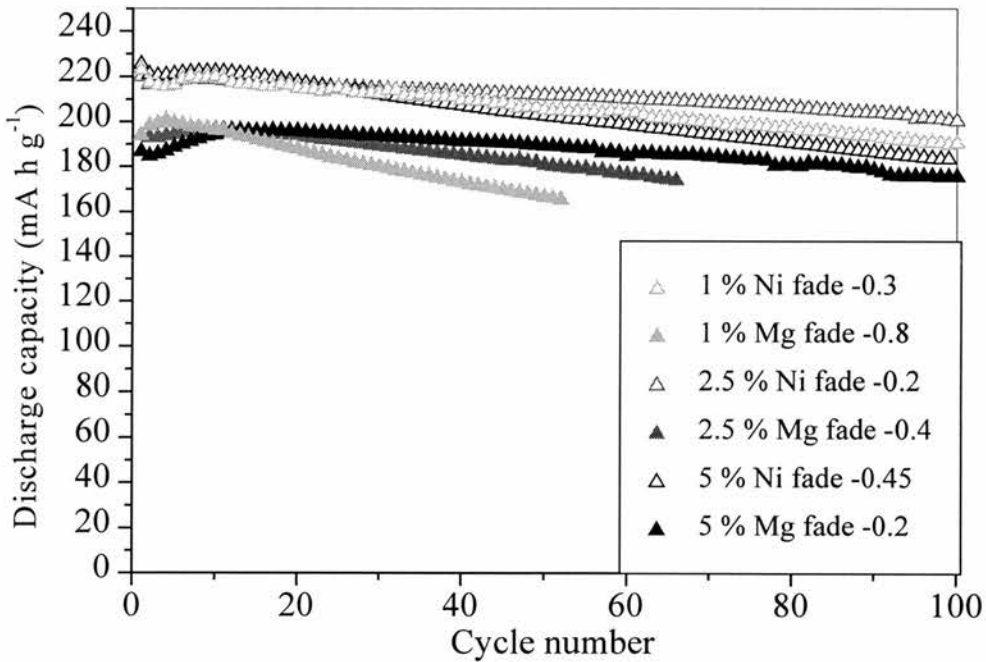


Figure 5.23 Cycling data showing that for $y \leq 0.025$ Ni doping has the better performance, and for $y = 0.05$ Mg doping has the better performance. All materials prepared in ethanol at 78 °C, Voltage range 2.4 to 4.8 V, current density 25 mA g⁻¹.

5.6 CONCLUSIONS

Single phase Mg doped $\text{Li}_x\text{Mg}_y\text{Mn}_{1-y}\text{O}_2$ ($0 < y < 0.2$) layered materials have been synthesised by ion exchange from sodium precursors at several different temperatures. In the first cycle the amount of lithium extracted/inserted decreases on increasing the Mg content due to the corresponding reduction in Mn content.

The capacity retention on cycling can be greatly improved by doping with small amounts of Mg. The material with composition $\text{Li}_x\text{Mg}_{0.025}\text{Mn}_{0.975}\text{O}_2$ shows good performance with a reversible capacity of 190 mA h g^{-1} . Higher dopant levels reduce the capacity loss further by slowing the conversion to a spinel-like material, but at the cost of capacity.

5.7 REFERENCES

¹ Jansen and Hoppe, *Z. Anorg. Allg. Chem.*, **397**, (1973), 279.

² PDF number 30-0794 JCPDS ICDD International Centre for Diffraction Data, Version 2.16.

CHAPTER 6

CONCLUSIONS AND FURTHER WORK

6.1 INTRODUCTION

The work presented in this thesis has shown that it is possible to prepare single phase, Ni and Mg doped, layered LiMnO_2 . Cycling these materials showed a high capacity for lithium and good reversibility. The purpose of this chapter is to provide a brief summary of the main conclusions of this work. The conclusions are grouped into the following themes: sodium phases, lithium phases and electrochemistry. Following the summary, suggestions for further work are given.

6.2 SODIUM PHASES

As observed by x-ray diffraction, a layered rhombohedral sodium phase, $\text{Na}_x\text{M}_y\text{Mn}_{1-y}\text{O}_2$, ($\text{M} = \text{Ni}, \text{Mg}$), with P3 structure can be formed at 600 °C in air. Quenching from this temperature after one hour is critical to the success of the synthesis, because at higher temperatures or longer times, the P3 phase is unstable when prepared with a composition $x = 1$. Unreacted sodium carbonate was also present in all samples, an indication that the layered phase is deficient in sodium, *i.e.* $x < 1$. Chemical analysis confirmed the existence of sodium vacancies, (about 50 %) and also a small number, (about 4 %), of transition metal vacancies. Scanning electron micrographs displayed irregularly shaped particles consisting of porous agglomerates about 10-100 μm in size.

For $\text{M} = \text{Ni}$ with $y > 0.2$, a NiO impurity was present which gives the limit of the solid solution.

For $y \leq 0.2$ it was possible to eliminate the NiO impurity by stirring the precursor acetates at

80 °C prior to rotary evaporation of the acetate solution. The lattice parameters of $\text{Na}_x\text{Ni}_y\text{Mn}_{1-y}\text{O}_2$ did not change significantly with nickel content, $a \approx 2.88 \text{ \AA}$ and $c \approx 16.80 \text{ \AA}$. This is probably due to the invariance of the average transition metal radius on substitution of 2Mn^{3+} with a Ni^{2+} and a Mn^{4+} , (0.645 Å vs. 0.61 Å).

For $M = \text{Mg}$ the lattice parameters display a variation more dependent on dopant level compared to the corresponding Ni doped materials. Both lattice parameters increase, probably due to the increased size of magnesium. In addition, For magnesium doped materials with $y \geq 0.1$, superlattice peaks were observed at around 21° in 2θ . It is thought that these are due to Mn and Mg cations ordering in each host cation layer, and are clearly observed by x-ray diffraction because of the different scattering powers of Mn and Mg.

6.3 LITHIUM PHASES

Ion exchange of all sodium precursors was performed, and three different conditions were used; hexanol at 156 °C, ethanol at 78 °C and ethanol at 25 °C. As observed by x-ray and neutron diffraction, a single-phase, (R-3m), layered rhombohedral lithium phase, $\text{Li}_x\text{M}_y\text{Mn}_{1-y}\text{O}_2$, with O3 structure is formed under all conditions. The main observable difference in the x-ray diffraction patterns was an increased separation of the 018/110 peak pair as the temperature of ion exchange decreased.

The refined lattice parameters were dependent on ion exchange temperature. An increased c lattice parameter and a reduced a lattice parameter was observed with decreasing ion exchange temperature. The c/a ratio increased from 4.96 to 5.13, indicative of increasing layered character. Chemical analysis of all the lithium phases showed that the number of alkali metal vacancies originally present in the sodium phase, was reduced by ion exchange. Materials prepared by reflux at 156 °C in hexanol displayed only 33 % alkali vacancies, while materials

prepared in ethanol contained slightly more, about 38 % vacancies on these sites. There is essentially no residual sodium in the case of the hexanol samples but about 4 % remains in the case of the material prepared in ethanol. The Mn vacancies on Mn sites also vary with ion exchange, more vacancies remain after exchange in ethanol whereas in the case of hexanol at 156 °C almost all the vacancies are eliminated. These variations in alkali metal content and transition metal vacancies are in agreement with the increasing a lattice parameter on increasing the ion exchange temperature. For materials with $M = \text{Ni}$, analysis of XPS measurements showed that the only nickel valence state present in these materials was Ni^{2+} .

Analysis of SEM micrographs showed that the particle morphology changes little during the ion exchange reaction. The structure change during ion exchange was observed at 25 °C by x-ray diffraction. A two-phase region comprised of the sodium phase P3, and lithium phase O3, clearly exists for at least one hour, and by x-ray diffraction ion exchange appears to be complete after two hours.

Overall it is evident that the ion exchange process is not restricted to the anticipated simple exchange of sodium by lithium. It also plays a critical role in controlling the defect chemistry/non-stoichiometry of the transition metal host. In addition the defect chemistry was also significantly affected by the conditions of ion exchange which in turn affect the lattice parameters.

6.4 ELECTROCHEMISTRY

Cycling lithium between 2.4 and 4.8 V vs. a lithium anode, in $\text{Li}_x\text{M}_y\text{Mn}_{1-y}\text{O}_2$ materials, with $\text{M} = \text{Ni}$ and Mg , displayed significant capacity at 3 V, and some capacity at higher voltages.

6.4.1 NICKEL DOPED MATERIALS

The Ni ions were thought to be active in this potential region, incremental capacity plots displayed increased capacity at 4.37 and 3.92 V for the higher Ni doped materials, ($y > 0.05$). The variation in discharge capacity with y was best observed in the first discharge capacity of materials prepared by ion exchange at 25 °C, where the capacity increased from 192 mA h g⁻¹ for $y = 0$ to 223 mA h g⁻¹ for $y = 0.2$. This was in good agreement with the redox process involving two electrons i.e. $\text{Ni}^{2+} \rightarrow \text{Ni}^{4+} + 2\text{e}^-$.

The ion exchange conditions were also found to influence the first cycle behaviour. In materials prepared in hexanol at 156 °C with low $y \leq 0.05$, a subtle double 4 V process was observed, suggesting that there is some lithium in the tetrahedral sites within the first cycle. *i.e.* conversion to a spinel structure has already begun. This process was not observed in the first cycle of the same materials prepared in ethanol at 78 °C.

Structural changes observed in the first cycle of a material with Ni composition $y = 0.066$, (nominal 0.075), and prepared in ethanol at 78 °C, show a rhombohedral phase at all lithium compositions. The unit cell parameters are highly reversible throughout the first cycle charge-discharge process.

Layered $\text{Li}_x\text{Ni}_y\text{Mn}_{1-y}\text{O}_2$ have shown good capacity retention on lithium cycling compared to the undoped material with $y = 0$. In particular, low Ni dopant levels display the best performance. For materials prepared in hexanol, the compositions with $0.025 < y < 0.075$ have capacities

over 200 mA h g^{-1} and fade by about 0.8 mA h g^{-1} per cycle at 25 mA g^{-1} . This capacity fade can be improved on cycling the materials prepared by ion exchange at lower temperature, in ethanol. The materials prepared at $78 \text{ }^\circ\text{C}$ displayed the best performance. 2.5 % Ni doped layered lithium manganese oxide, prepared by refluxing in ethanol, exhibits a capacity to store lithium equivalent to 220 mA h g^{-1} which fades by only $0.2 \text{ mA h g}^{-1} \text{ cycle}^{-1}$ at 25 mA g^{-1} .

The discharge capacity behaviour could be observed after the amount of capacity originating from the high and low voltage ranges separately was calculated, (4.8 to 3.5 V and 3.5 to 2.4 V respectively). The general trend observed for doped materials beyond the 10th cycle, was a relatively constant 4 V capacity, while the 3 V capacity faded. The combination of these trends resulted in the cycling behaviour described previously.

During electrochemical cycling all compounds develop two voltage plateaus (4 and 3 V), suggesting spinel-like cation ordering, as previously observed for orthorhombic LiMnO_2 and monoclinic layered LiMnO_2 . Evidence for spinel-like characteristics has also been observed by *ex situ* x-ray diffraction taken of cycled materials. It is thought that the discharge capacity behaviour observed in the first 10 to 20 cycles, over separate 3 V and 4 V regions, is due to the spinel transformation stage. This takes longer in the materials prepared in ethanol compared to hexanol, and in materials with the highest dopant contents. The conversion to a spinel-like material can be slowed further by reducing the voltage window to 2.4 to 4.6 V, or by increasing the current density. In all cases, the resulting indirectly prepared spinel-like material shows good cyclability and high reversible capacity when cycled over both voltage plateaus, unlike the directly prepared LiMn_2O_4 spinels.

6.4.2 MAGNESIUM DOPED MATERIALS

The first cycle discharge capacity of layered $\text{Li}_x\text{Mg}_y\text{Mn}_{1-y}\text{O}_2$ decreases with increasing Mg content due to the reduced Mn content and the electrochemical inactivity of Mg. Layered $\text{Li}_x\text{Mg}_y\text{Mn}_{1-y}\text{O}_2$ have shown good capacity retention on lithium cycling compared to the undoped material with $y = 0$. On extensive cycling Mg doping significantly improves the capacity fade, but at the cost of capacity. For materials prepared in ethanol, the compositions with $0.025 < y < 0.05$ have capacities over 200 mA h g^{-1} and fade by about 0.8 mA h g^{-1} per cycle at 25 mA g^{-1} . Again, the capacity fade is best for the materials prepared by ion exchange in ethanol. Evidence for spinel-like characteristics has also been observed by incremental capacity plots and *ex situ* x-ray diffraction taken of cycled materials.

6.5 SUGGESTIONS FOR FURTHER WORK

Additional work is needed to confirm the activity of Ni on cycling. The recommended technique for obtaining this information is XPS from a material stopped at full charge. All these cycling studies have been carried out at $30 \text{ }^\circ\text{C}$; however, investigation at higher temperatures up to $55 \text{ }^\circ\text{C}$ should be carried out. It would be interesting to obtain neutron diffraction data on cycled materials to investigate the possible migration of Ni and Mg into the lithium sites in addition to Mn. This may lead to an explanation for the role of the dopant ions in slowing the conversion to spinel.